Global identification and characterization of drivers of shoreline evolution

A novel method using Satellite Derived Shorelines and spatiotemporal characteristics

D.D.C. van der Heijden

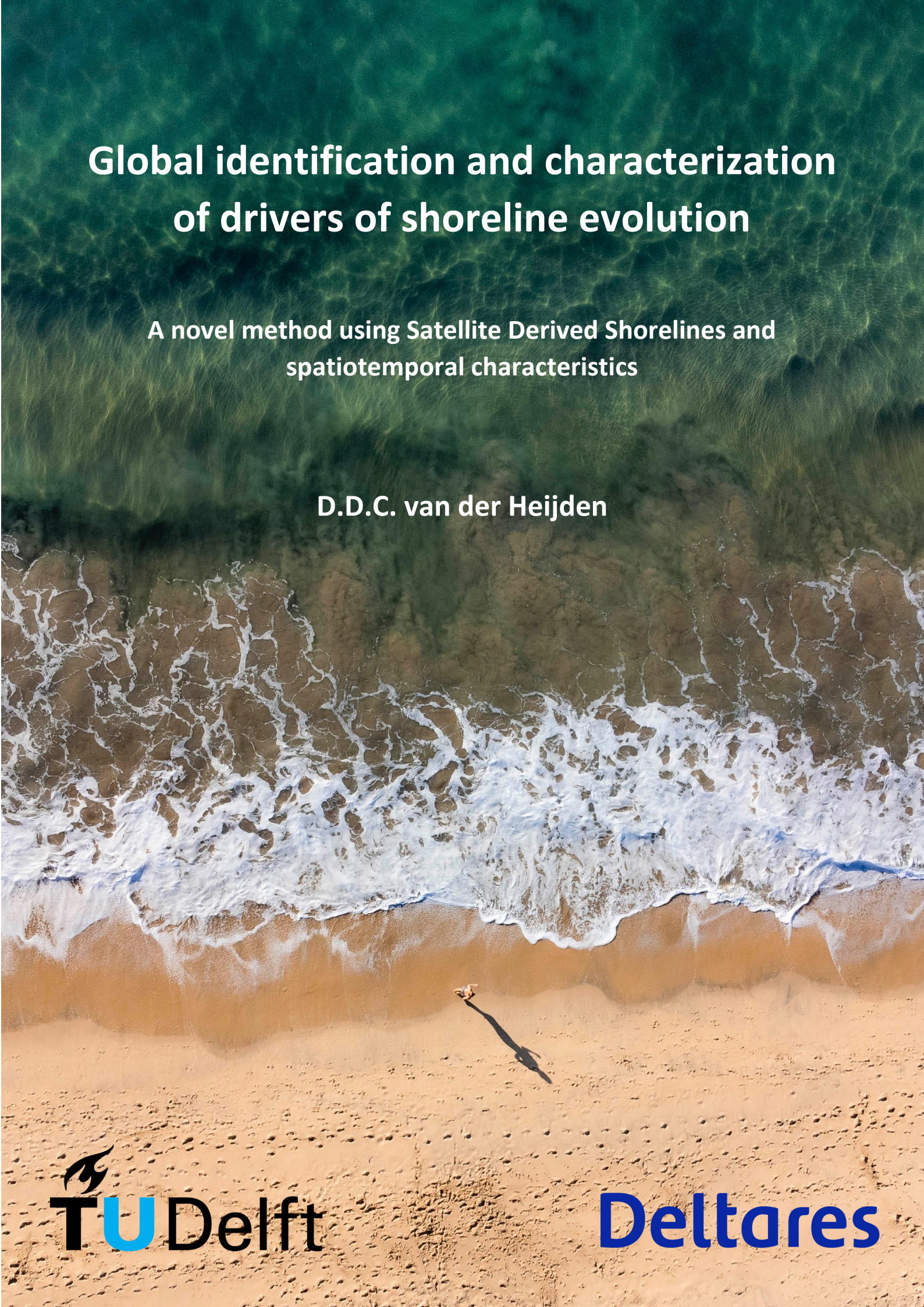

TU Delft

Deltares

Global identification and characterization of drivers of shoreline evolution

A novel method using Satellite Derived Shorelines and spatiotemporal characteristics

by

D.D.C. van der Heijden

Student number: 4563697
Study: MSc Hydraulic Engineering

Project duration: February 8, 2022 - December 20, 2022

Thesis committee:

Prof. dr. ir. S. G. J. Aarninkhof,	TU Delft
Dr. Ir. A. P. Luijendijk,	TU Delft / Deltares (supervisor)
Ir. E. C. Kras,	Deltares
Dr. Ir. J. E. A. Storms,	TU Delft

An electronic version of this thesis is available at http://repository.tudelft.nl/.

Cover: Aerial. Mazunte Beach. Mexico. (Photo made by David Arenas from Pexels)

TU Delft

Deltares

Preface

Before you lies the thesis “Global identification and characterization of drivers of shoreline evolution”. It has been written to fulfill the graduation requirements of the Masters program Hydraulic Engineering at Delft University of Technology. This work was performed at Deltares, an independent knowledge institute in the field of water and research, over the period of 11 months from February to December 2022.

During my early studies, I became increasingly interested in the field of data science. In this thesis, I was able to combine it with my study direction, coastal engineering. Since big data is still relatively new, especially in the field of coastal engineering, it has been a challenging but educational and contentment road to contribute to this developing approach.

First, I would like to thank my thesis committee for helping me deliver this master thesis. Thank you, Stefan Aarninkhof for your critical comments and observations during our meetings. Secondly, a special acknowledgement to my daily supervisors at Deltares, Arjen Luijendijk and Etienne Kras. Thanks, Arjen, for sharing your expertise, ideas and interpretations with me. Thank you Etienne for your sharp insights, for always making time to help and your contagious positive energy. Also, I would like to thank Joep Storms for taking a final seat in my committee and reviewing this thesis.

Finally, I want to thank my family and friends for your support and help. I would also like to thank you, my reader: enjoy!

Dante van der Heijden
Delft, December 2022

Abstract

Since early history, humans have been attracted to coastal areas. This can be related to the economic benefits of these areas due to access of ocean navigation, coastal fisheries, tourism and recreation (Seas and Plans, 2011). Around 40% of the world's population lives within 100 km of the coast (Seas and Plans, 2011). People are drawn to sandy beaches in particular because of its aesthetics and value for specific economic amenities (Luijendijk et al., 2018). Nevertheless, as these beaches are dynamic both in time and space, proper coastal management is required to prevent loss of land and secure future coastal life.

Up till now, studies into coastal erosion have been conducted locally, resulting in site specific observations. However, the promising results of using satellite imagery in the field of coastal engineering allowed studies to be performed at larger spatial scales. This can lead to the identification of areas with similar characteristics, resulting in methodological standardization of approaching a specific problem. A first step toward this new approach of studying shoreline evolution was taken by Luijendijk et al. (2018) who presented a global dataset of annual shoreline positions for sandy beaches over the period 1984-2016 using satellite derived shorelines (SDS). However, the drivers (causes) of shoreline evolution on a global scale were still unknown, making it only suitable for identifying areas of structural shoreline change, but less suitable for deriving coastal management solutions. Therefore, the research objective in this study is to identify and characterize drivers of shoreline evolution on a global scale using SDS.

This study focused on dynamic sandy beaches, or hotspots, extracted using a method developed by Kras (2019). In this method, using a 2.5-kilometer moving window, transects showing structural shoreline changes and similar characteristics both in space and time were grouped. The small size of the moving window led to locally created hotspots, 95% of which had a spatial extent of less than 10 kilometers, allowing to study shoreline drivers with small to moderate spatial scales (~10 kilometer). Therefore, the main focus in this study lies on seasonality as a natural driver of shoreline evolution and three anthropogenic drivers: reclamations, nourishments and littoral drift barriers. As seasonality shows inter-annual variability, the temporal resolution of the SDS is increased from annual to monthly.
Using time series decomposition methods, different parameters are extracted that can be used to link the drivers to the SDS. Besides temporal parameters, also parameters related to spatial characteristics are considered. These parameters can be split into identification parameters, used for identifying a driver, and informative parameters, providing knowledge on the behaviour of the driver. These parameters were developed and tested using local case studies. Results from these local case studies showed that the identification parameters showed similar behaviour along the case studies. This implies that the identification parameters correctly reflect a driver's behavior.
Next, identification of the drivers was verified on a larger scale, all transects within hotspots on West-European coastlines. Verification was done on hundreds of samples using literature or manual inspection of satellite images. Using precision scores, the fraction of true positives to the total identified cases, optimal settings were derived for identification of the drivers. These settings resulted in a pattern of driver identification and characterization along the West-European coastline that is supported by literature.

With the optimal settings for identification determined, the methods were deployed on a global scale. The global dataset consisted out of 3033 prograding and 2121 retreating hotspots containing over 58 thousand transects in total. For these hotspots, SDS were generated over the period 1984-2021 with a monthly temporal resolution. This resulted in a global dataset of more than 26 million monthly shoreline positions.
Two other processes, in addition to a seasonal change in wave height, were found to be able to generate seasonal variations in coastline positions from this global dataset. At the Red Sea, even though the wave climate is low in energy (Langodan et al., 2017), the coast is characterized by seasonal behaviour. However, in this basin, seasonal variations in water levels rather than the wave climate best described this pattern. In addition to varying wave height and water level, seasonal beach morphology can also be caused by a shift in wave direction. This was observed in southern and western parts of Australia. Furthermore, non-seasonal beaches were primarily seen in low-energetic wave regions where neither of these other two processes occurred, as

is the case in the Mediterranean. In regions where seasonal shoreline fluctuations are caused by differences in wave energy, minimum shoreline positions were found at the start of the summer. However, the period in which minimal shoreline positions are observed may be observed at a different time of the year in regions where seasonal shoreline behavior is driven by water level variations or a shift in wave direction.
The identification of reclamations pointed out that this driver was especially linked to shoreline evolution in the Middle East and East-Asia. Furthermore, while the amount of constructions of reclamations remained constant on a global level over the period 1987-2017, in these two areas an increase was observed. Opposite behaviour was found by the identification of nourishments, as this driver was identified more often in the period 2007-2017 compared to the two decades before that. Moreover, nourishments were mostly observed in Western countries, for example the USA and the Netherlands. Nevertheless, also in Non-Western countries, an increment over time in the amount of nourishments could be detected. This indicates that throughout the entire world the use of nourishments as a measure to prevent coastal erosion is increasing. Shoreline evolution linked to littoral drift barriers was mostly observed in North-America, Europe and Africa. Downdrift (erosive) hotspots were mostly observed in Africa while in North-America and Europe mostly updrift (accreting) hotspots were linked to littoral drift barriers. On a global level, a combination of an updrift and downdrift hotspots (a pair) was observed in only 2% of all hotspots.

The outcomes above can support local-scale studies by identifying the drivers of shoreline evolution, describing their characteristics and even create standardization by analyzing areas with similar behavior. Hence, it can be concluded that spatiotemporal parameters describing the behavior of a driver can be used to identify and characterize drivers on a global scale using SDS. Nevertheless, not all drivers of shoreline evolution were included in this study. Therefore, to include drivers with larger spatial scales, hotspots should be extracted by using a larger moving spatial window. Furthermore, by increasing the spatiotemporal resolution on which this extraction is based, accuracy of the spatial extent of the hotspots is expected to increase. The small proportion of pairs identified for littoral drift barriers can be partly explained by the erroneous spatial extent of some hotspots. Finally, drivers are identified independently from each other neglecting their interactions. Even though interactions might be complex, drivers should not be identified independently as this will rather require local studies than support them. Still, even though refinement and further development of the methods is required, this research has shown that identifying the drivers of shoreline development on a global scale using SDS has great potential for sustainable coastal management in the face of future challenges.

Contents

Acronyms

AOI Area of Interest.

CART Classification and Regression Tree.

DFT Discrete Fourier Transform.

EMD Empirical Mode Decomposition.
ENSO El-Niño-Southern Oscillation.

FFT Fast Fourier Transform.

GEE Google Earth Engine.

KNN K-Nearest Neighbour.

LR Logistic regression.

NAO North Atlantic Oscillation.
NDWI Normalized Difference Water Index.
NIR Near InfraRed.

OLS Ordinary Least Squares.
OSM Open Street Map.

R^2 Coefficient of Determination.

SDS Satellite Derived Shorelines.
STL Seasonal-Trend decomposition with LOESS.

TOA Top of Atmosphere.

WGS World Geodetic System.

1

Introduction

Since ancient times, people have been fighting coastal erosion to prevent land loss. The Dutch, who live in one of the world's lowest lying countries (Katsman et al., 2011), have been battling the ocean for over a thousand years (Charlier et al., 2005). In older times, these protections were mostly built without proper knowledge of coastal processes, which could result in only more negative effects, either for the location itself or for its surroundings. As was stated by Reeve and Spivack (2001):

'Strategic planning for the management of our coasts relies implicitly upon an understanding of the physical processes responsible for shaping coastal morphology'

Nowadays, research has greatly increased understanding of coastal processes. Detailed local studies and the application of models can reveal the processes that shape the coast. These processes are driven by nature and anthropogenic (human) influences to the coast and result in a changed sediment budget affecting shoreline evolution. Shoreline evolution is defined as the movement of the shore over time, which can be either seaward (accretion) or landward (erosion). Process-driven models lay the foundation of these local-scale studies by solving a set of mathematical equations based on the physical behaviour of the processes shaping the coasts. With the increased availability of high-quality data on coastal morphology, a new method of analyzing coastal processes has emerged: data-driven modeling (Larson et al., 2003). These models, in essence, consist of decomposing the analyzed signal into patterns that represent key system dynamics (Larson et al., 2003). The interpretation of the identified behavior is sought from those patterns. Using this strategy, the effects are examined into order to identify, describe and quantify their causes (Larson et al., 2003).

Various studies have employed these data-driven models to study shoreline evolution on a small scale (Seale et al., 2022; Taveneau et al., 2021). However, with the promising results of satellite imagery to study shoreline evolution (Di et al., 2003; Turner et al., 2021), these data-driven models can also be applied to bigger scales. Nevertheless, up till know only the magnitude of shoreline evolution have been examined on a larger (global) scale (Luijendijk et al., 2018), while the identification, description and quantification of their causes still remains unknown. In this study, the causes of shoreline evolution will be referred to as drivers.

1.1. Coastal communities

Human settlements are often more concentrated in the coastal zone than elsewhere due to the economic benefits of access to ocean navigation, coastal fisheries, tourism, and recreation (Seas and Plans, 2011). Nearly 2.4 billion people, around 40% of the world's population, lives within 100 km of the coast. From these 2.4 billion, 600 million people live in coastal areas which are less than 10 meter above sea level (Seas and Plans, 2011). Most people live near sandy beaches as sandy coasts are aesthetic and important for certain economic amenities. On the other hand, sandy beaches are very dynamic both in space and time (Luijendijk et al., 2018). As a result, especially in these areas, people's lives may be seriously compromised due to coastal erosion.
Coastal erosion can have a sizable negative effect due to loss of land, lost or damage property and impacts on trade and industry in general. Also, as a result of coastal erosion, biodiversity and other ecological factors suffer, for example from coastal devegatation or an increase in certain mineral particles (Shadrin et al., 2013). Indirect negative effects of erosion to biodiversity can be the result of human interventions to prevent erosion, such as nourishments or land reclamations (Shadrin et al., 2013). Furthermore, as a result of global warming, the causes of coastal erosion will become more prominent, amplifying the negative effects. Not counteracting this erosion will result in direct and indirect consequences for not only coastal communities, but the entire world. Direct consequences include economic loss, but people will also suffer long-term consequences as a result of loss of biodiversity. Therefore, to minimize future negative effects, effective measures to prevent erosion or restore coastal communities are required.

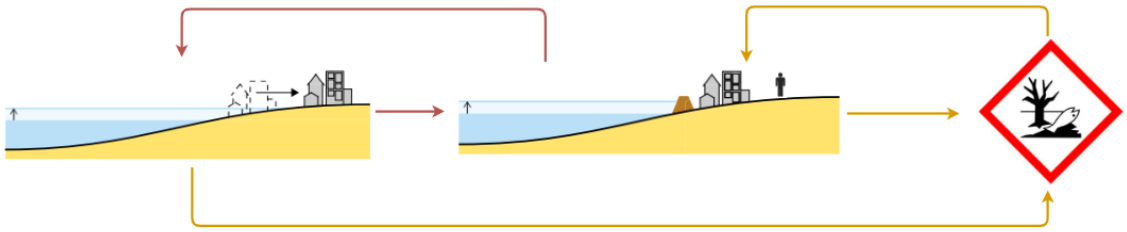

Figure 1.1: Direct link (red arrows) between coastal erosion and jeopardized (coastal) communities and an indirect link between the two (orange arrows). Erosion directly affects the coastal communities while an indirect link exists between jeopardized coastal communities and a loss of biodiversity due to erosion. Furthermore, human interventions can also lead to erosion which then also affect coastal communities directly or indirectly through endangered biodiversity.

1.2. Shoreline monitoring

Many studies have been conducted locally to identify the causes of shoreline evolution. These studies are usually based on local field measurements resulting in site-specific observations. Besides that, retrieving field measurement data can be time consuming and expensive (Davidson et al., 2010). A cheaper solution to field measurement to study shoreline evolution is the use of satellite imagery. For example, Quang et al. (2021) used satellite images to study long-term shoreline evolution in the Quan Nam Province in Vietnam. Wang (2018) explored to what extent drivers of shoreline evolution could be exposed through satellite imagery by using satellite derived shorelines (SDS). As research shows promising results, the use of satellite imagery in coastal engineering is increasing in popularity.

1.3. Research objective and scope

As previously stated, due to the increasing availability of high-quality data of coastal morphology, data-driven models are becoming increasingly popular in the field of coastal engineering (Larson et al., 2003). However, data-driven models are still mostly used in detailed local studies. Rather than assessing problems on a local scale, shoreline evolution can be studied on a larger scale. Since similar characteristics can be identified for different locations, this can result in methodological standardization of the approach to a specific problem. In coastal management, standardization is not always used. This is because of the complexity and variability of coastal systems, as well as a lack of knowledge. The research objective in this study is to identify and characterize drivers of shoreline evolution on a global scale using SDS. The drivers of shoreline evolution are visualized in Figure 1.2.

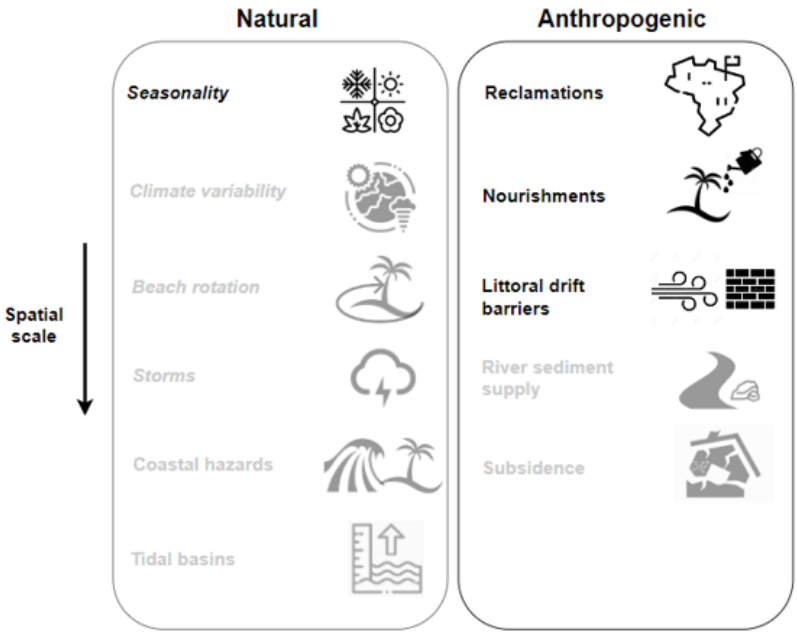

Figure 1.2: Natural and anthropogenic drivers of shoreline evolution. The drivers are sorted from bottom to top according to their spatial scales. The drivers indicated with a grey transparent colour will not be treated in this study. Primary (secondary) drivers are indicated with a normal (italic) font.

Drivers are identified on stretches of coasts with high variability showing similar characteristics, or in other words; hotspots. Hotspots are extracted based on a method developed by Kras (2019). The foundation of this method is a dataset called the Shoreline Monitor (Luijendijk et al., 2018). This is an application that identifies sandy beaches and annual SDS for these sandy beaches on a global scale using a 500-m spaced transect system for the period 1984 to 2016. Hotspots are extracted from this dataset by capturing transects with high shoreline variability showing similar characteristics using a 2.5-kilometer spatial moving window. The small extent of the moving window results in local generated hotspots, allowing to study shoreline drivers with small to moderate spatial scales (~10 kilometer). Furthermore, storms are difficult to study if a survey is conducted a long time after the event, as may be the case with satellite imagery. Therefore, this driver of shoreline evolution is also ignored. That leaves the following natural drivers of shoreline development that will be considered in this study: Seasonality, beach rotation and climate variability, and three anthropogenic (human) drivers: nourishments, reclamations and littoral drift barriers. Besides classifying drivers as caused by natural or anthropogenic influences, a distinction can be made between primary drivers and secondary drivers. Primary drivers have major structural effects on shoreline development, while secondary drivers do not lead to long-term changes in the coastal system. This classification is also indicated in Figure 1.2. Real life examples of shoreline response to some of the drivers that are considered in this study can be found in Figure 1.3.

(a) Beach erosion in Oartley Beach (USA) during energetic winter wave conditions. (source: Doug Hood).

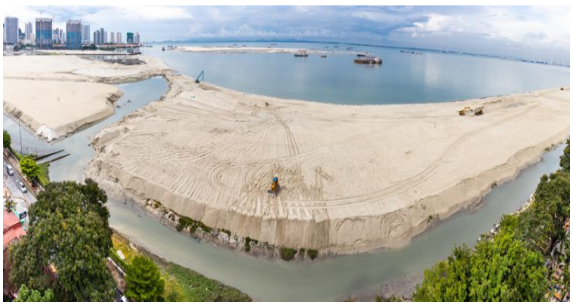

(b) Land reclamation under construction in Malaysia to meet the demand of population increase. (source: DHI).

(c) Beach nourishment under construction along the coast of Lincolnshire, UK. (source: Van Oord).

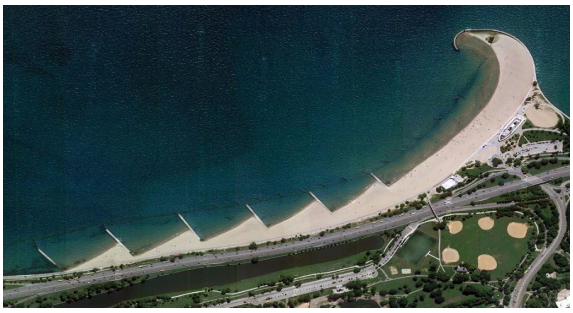

(d) Sand accumulation at a system of groynes at North Avenue Beach in Chicago, USA. (source: pruned.blogsplot.com)

Figure 1.3: Shoreline evolution at beaches caused by natural processes or anthropogenic interventions.

1.4. Research question

Section 1.3 states the research objective and scope of this thesis. From this objective a main research question and three supportive sub-questions are formulated. The main research question is:

How can satellite derived shorelines be used to identify and characterize drivers of shoreline change on a global scale?

1. ***To what extent can existing methods be applied to link drivers to SDS?***
   This sub-question will explain how various methods are used to decompose time series of SDS and link them to drivers. Parameters are extracted from these decompositions and validated as well as verified for several case studies.

2. ***What are the optimal method settings to identify drivers using regional verification?***
   This sub-question will elaborate on the optimal settings for the methods explored in the previous sub-question. This will be done by increasing the spatial extent of the study to all hotspots within West-Europe. Next, driver identification will be verified for this region.

3. ***What is the global distribution and characterization of drivers?***
   In this sub-question, results from the previous two sub-questions will be used to identify and characterize the drivers on a global scale.

1.5. Research outline

This report is divided into nine major chapters. Background information relevant to this study will be provided in Chapter 2. This chapter will focus on the Shoreline Monitor, satellite derived shorelines, and shoreline evolution drivers, as these three components form the foundation of this research. The research methods will then be discussed in Chapter 3. In the Chapters 4, 5, and 6, results from research methods on a local, regional, and global scale will be presented respectively. Each of these chapters can be used to answer a single sub-question. Chapter 7 reflects on and discusses these findings. The research's limitations are outlined, with a focus on assumptions, decisions, and constraints, as well as the applicability of current and future directions. Based on the results of the three sub-questions the main research question is answered in Chapter 8. Finally, future directions and improvements for further research are outlined in Chapter 9. Before the start of each section, the key points that are treated or arised in this part of the report are stated. Furthermore, at the end of each chapter, a summary is provided. Figure 1.4 shows a schematic visualization of the outline of this research.

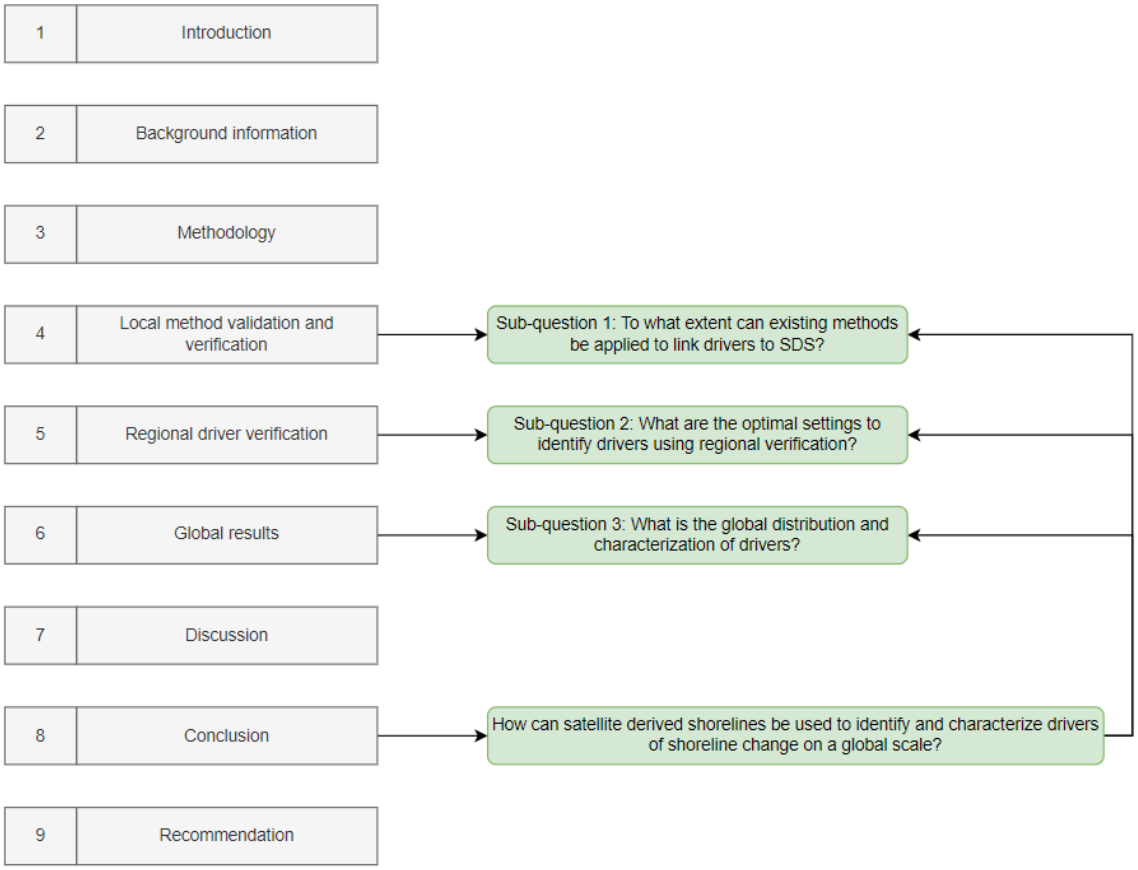

Figure 1.4: Schematic visualization of the chapters (grey boxes) in this research. The research questions answered in a particular chapter are indicated with green boxes.

2

Background Information

2.1. The Shoreline Monitor

With the use of satellite images, Luijendijk et al. (2018) presented a global-scale assessment of the occurrence of sandy beaches and their annual shoreline positions from 1984 to 2016. Using the Google Earth Engine (GEE, Section 2.1.1) for image processing, sandy beaches were identified on a global scale with a 500 m spacing (Section 2.1.2) using a supervised classification to cloud-free satellite images (Section 2.1.3). Next, for these sandy beaches, an algorithm presented by Hagenaars (2017) was applied to identify annual Satellite Derivered Shorelines (SDS) for the period 1984-2016 (Section 2.1.4).

Key points

- The Shoreline Monitor is a dataset that identifies on a global scale, with a 500-m spaced transect system, sandy beaches and annual satellite derived shorelines (SDS) for these sandy beaches over the period 1984-2016.
- The SDS detection algorithm can be used to extract shorelines from satellite images. Accuracy of these extracted shorelines depends on the satellite mission. Shoreline positions can have various temporal resolutions such as annual, monthly etc.
- Using an 'along-the-shore' analysis, 3033 prograding and 2121 retreating hotspots were identified from the Shoreline Monitor dataset. Hotspots are regions with high shoreline variability and similar characteristics in time and space.

2.1.1. The Google Earth Engine

The GEE is a cloud-based platform for global scale geospatial analysis that can be used to study environmental or societal issues such as deforestation or spread of diseases (Gorelick et al., 2017).
This Engine contains a freely available data catalog with data already corrected and preprocessed (Gorelick et al., 2017). Examples of frequently used datasets in the Earth Engine catalog are Landsat, Sentinel and MODIS images. Performances in the GEE are carried out with a Java Just-in-Time (JIT) compiler which is 50% more efficient than similar dynamic graph-based computations in C++ (Gorelick et al., 2017).

2.1.2. Global transects

The Shoreline Monitor provides global data for sandy coasts with up to 500 meter spaced transects. These transects extend 1000 meter land- and seaward perpendicular to highest resolution (z8) shorelines from OpenStreetMap (OSM) (Luijendijk et al., 2018). The OSM shorelines consist of 30374 pieces in total and are presented in the World Geodetic System (WGS) 84 or its equivalent European Petroleum Survey Group

() 4326. By summing straight intercepts between transects, the total length of the world's ice free shoreline is estimated at 1.11 million kilometer, which is comparable to other reported values of 1 million kilometer (Hinkel et al., 2013), 1.16 million kilometer (Agency, 2016) and 1.47 million kilometer (Burke et al., 2001). This ice free shoreline eventually consisted of 2.2 million transects. After applying a latitude filter (50°N - 50°S), only 1.8 million transects remained. To speed up computations, transects were labeled with id's according to their location (see Appendix A.1.1 for the details).
Errors in the results of the Shoreline Monitor can be caused by transects with a length larger than the width of the coast, see Figure 2.1. This arises in the erroneously identification of two coastlines (Van Leeuwen, 2018). At these locations, a land- and seaward extension of the transects smaller than 1000 meter is recommended (Van Leeuwen, 2018).

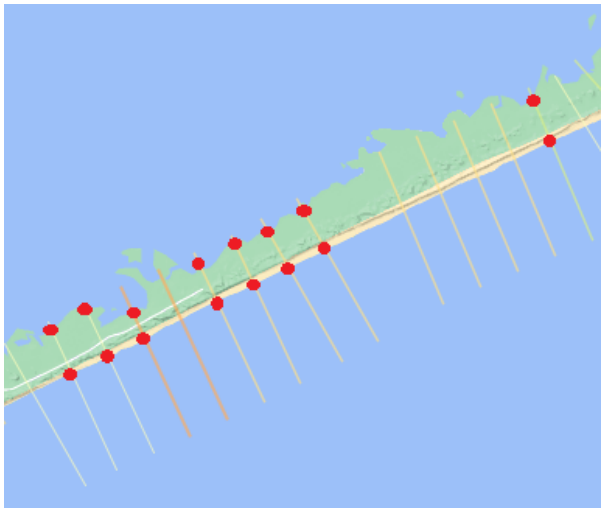

Figure 2.1: Example of a location (Fire Island, US) where the length of the transect exceeds the width of the coast. The red dots indicate the identification of a coastline at a transect with a length exceeding the width of the barrier island.

To reduce the amount of errors caused by the transects system, Van Leeuwen (2018) recommended to employ a built-in fault detector to consecutive transects (see Appendix A.1.1). Besides that, another recommendation was done for plotting of the transects on the SDS instead of OSM.

2.1.3. Sandy beaches

Changes on sandy coasts are continuous and occur at different spatial and temporal scales, resulting in highly dynamic beaches (Absalonsen and Dean, 2011). Since sandy coasts are highly developed and populated, the erosion of these coasts in recent decades has resulted in coastal squeeze (Pontee, 2013). Therefore, mapping of sandy coasts is necessary for spatial planning and proper coastal management (Luijendijk et al., 2018).

Detection

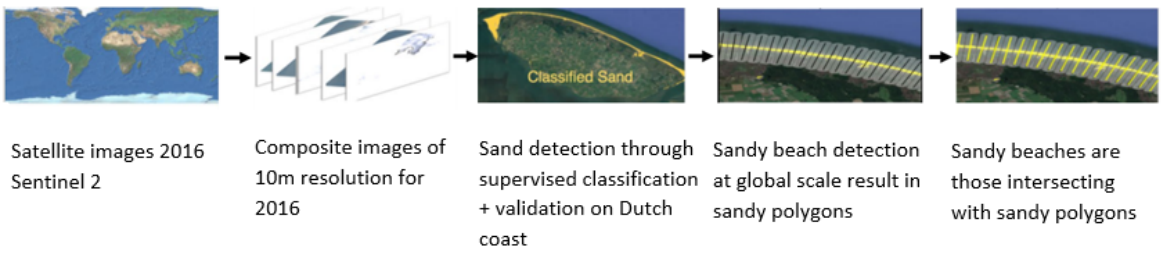

Figure 2.2: Work-flow to assess sandy beach occurrence on a global scale (source: Luijendijk et al., 2018).

To detect sandy beaches, a pixel-based supervised classification was applied. This classification was applied

to a global Top of Atmosphere (TOA) reflectance percentile composite image for the year 2016 using Sentinel-2 images (Luijendijk et al., 2018). First, to train the algorithm, a beach area consisting entirely of sand (at the Dutch Island of Texel) was selected together with training areas representing different types of land use. Four classification algorithms were considered and their results were validated against the sandy beach feature in OSM. The Classification and Regression Tree (CART) classifier resulted in the lowest omission error and the highest percentage of true positives (97%) by validating on a 100 kilometer stretch along the Dutch coast (Luijendijk et al., 2018).
To apply this classifier on a global scale, the world has been divided into boxes of 20km x 20km. Only boxes that intersected with the 2016 OSM shoreline were selected, resulting in about 24,000 boxes to be analysed. This global upscaling was necessary as the OSM sandy beach feature is not available on a global scale. The result was a series of polygons encapsulating all sandy beaches worldwide, including both quartz and carbonate sands and gravel. Validation through visual inspection on more than 50 locations, randomly spread accross the world, resulted in 96% accuracy (Luijendijk et al., 2018). See Figure 2.4 for a overview of the workflow to assess sandy beach occurence.
Transects with an intersection with a sandy polygon are defined as 'sand' and the others as 'non-sand'. Whenever a composite image could not be constructed and hence no input for the classification algorithm was available, transects were labelled as 'undetermined sand composition'. The percentage of sandy beaches is 31% ± 1.5%, assuming that undetermined areas behave similar to the global mean (Luijendijk et al., 2018).

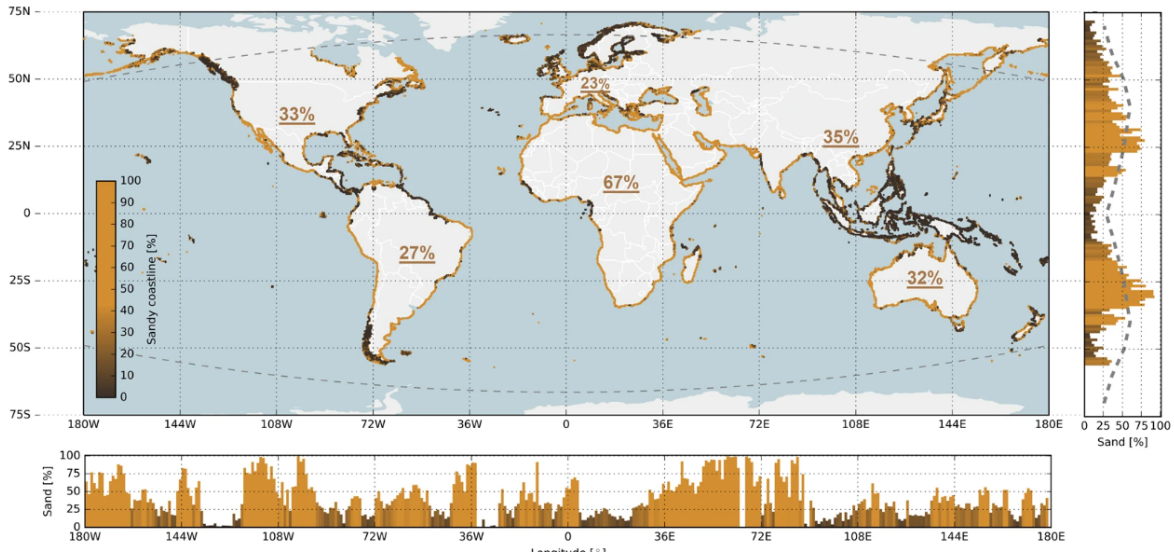

Figure 2.3: Distribution of sandy shorelines at a global scale. The colored dots along the shoreline represent the local percentage of sandy shorelines (yellow is sand, dark brown is non-sand). The subplot on the bottom and on the right indicate per degree longitude and latitude the relative occurrence of sandy beaches. The dashed line in the right subplot shows the Hayes distribution. The numbers in the main plot indicate the percentage of sandy beach occurrence per continent. Latitude filters are shown with dashed lines in the main plot. (source: Luijendijk et al., 2018).

2.1.4. Satellite derived shorelines

Locations of the shoreline and rates of change can provide important information for coastal management (W.-W. Chen and Chang, 2009; Hanson et al., 1989). Idealistically, a shoreline is defined as the interface of land and water (Dolan et al., 1980; Horikawa, 1988). Within time, shoreline positions change on a large timescale due to sediment fluxes. On a shorter scale, shoreline position varies because of the dynamic nature of water levels such as waves and tides (W.-W. Chen and Chang, 2009). The shoreline extracted from a satellite image is a position that describes the instantaneous land-water boundary at the time of the image taken (Foody et al., 2005; Zhao et al., 2008).

Image processing

Hagenaars et al. (2018) developed and tested an algorithm able to extract shoreline positions from satellite images. First, following McFeeters (1996), the Normalized Difference Water Index (NDWI) is calculated per pixel. The result is a greyscale image with NDWI values ranging from -1 to 1. Using the method proposed by Otsu (1979) this greyscale image is classified into a binary water-land image. The optimal threshold value to seperate the NDWI values into distinct regions of land and water is -0.16 (Hagenaars et al., 2018).
By applying a region growing algorithm, a coherent water mask is created from pixels identified as water (Kamdi and Krishna, 2012). The location of the SDS is defined as the outer edge of the water mask. By applying a 1D Gaussian smoothing operation, a gradual shoreline is obtained from the saw-tooth SDS vector following the image pixel edges (Hagenaars et al., 2018).

Figure 2.4: NDWI greyscale image (left) and resulting binary image (middle) for a Sentinel 2 image acquired on 12-03-2015 10:33:27 (GMT). The right image shows the same satellite image with the derived SDS plotted in black. (source: adjusted from Hagenaars et al., 2018).

Hagenaars et al. (2018) identified six factors that cause deviations at the SDS compared to the actual shoreline. Three factors could be related to the environmental conditions:1) cloud cover, 2) waves (surface roughness and foam) and 3) soil moisture and grain size (D_{50}). The remaining factors are related to the satellite instruments: 1) sensor corrections, 2) georeferencing and 3) image pixel resolution.

Composite windows

To reduce the effects of inaccuracies caused by cloud cover, waves, soil moisture and sensor correction, an image composite processing technique developed by Donchyts et al. (2016) was applied. With this technique a single composite image is acquinted from a sequence of satellite images. Pixels in the composite image are obtained from the 15th percentile value of the TAO green and Near InfraRed (NIR) reflectance values of the concurrent pixels within a sequence of individual images. By increasing this composite time window, the average offset reduces (Hagenaars et al., 2018). By applying a composite window of 90 days, the average offset reduces from 56.5 m to 14.9 m compared to the case of an individual image (Hagenaars et al., 2018).The offset was defined by comparing the SDS position to in-situ data for a case study (The Sand Engine, Hagenaars et al., 2018). The accuracy of composite windows is below subpixel precision (half a pixel size, i.e. 15 meter for Landsat and 5 meter for Sentinel 2). Therefore, to analyse reliable shoreline changes, the displacement of the SDS should be larger than 15 meter for Landsat or 5 meter for Sentinel 2 (Hagenaars et al., 2018). A disadvantage of this described technique is that shoreline variability below the composite window is lost tot some extent (Hagenaars et al., 2018). Studying intra-annual shoreline variability is thus not possible by applying a composite window of 360 days.

Temporal resolution

Composite windows should not be confused with the temporal resolution of the SDS. A composite window of 360 days does not correspond to annual shoreline positions, but a yearly averaged shoreline position for a certain moment in time. To emphasize this, Figure 2.6 shows various combinations of temporal resolution and composite windows. Luijendijk et al. (2018) performed his analysis with an yearly resolution and a composite window of 360 days (Figure 2.6a).

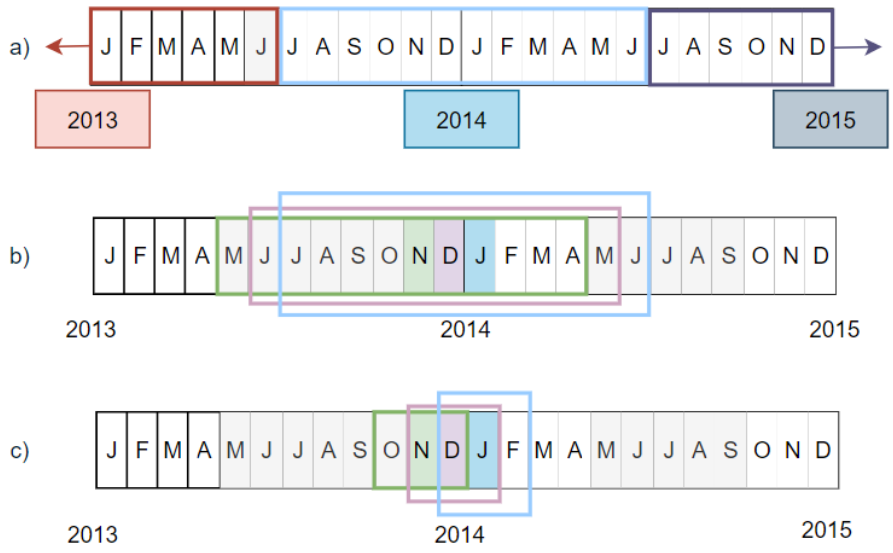

Figure 2.5: Various combinations of temporal resolution and composite windows. The colored boxes correspond to the composite window of the moment in time with the same color. a) yearly resolution with a composite window of 360 days. b) monthly resolution with a composite window of 360 days. c) monthly resolution with a composite window of 90 days.

Coastline trends

To monitor shoreline evolution by a time series of SDS positions, SDS vectors are projected along the global transects. The shoreline position is defined as the distance between the transect center (origin) and the intersection point of the SDS. Trends in shoreline positions are quantified by means of a Ordinary Least Squares (OLS) fit:

$$y(t) = at + b \tag{2.1}$$

where	$y(t)$	:	distance between the transect origin and the SDS intersection at time t	(m)
	a	:	an indicator for the structural rate of change	(m/y)
	b	:	distance between transect origin and the SDS at t = 0	(m)

Luijendijk et al. (2018) found that 24% of the world's sandy beaches are eroding at a rate exceeding 0.5 m/yr over the study period (1984-2916), while 27% are accreting. More severe erosion, with a changerate exceeding 1 m/yr, occurs at 16% of the sandy beaches.

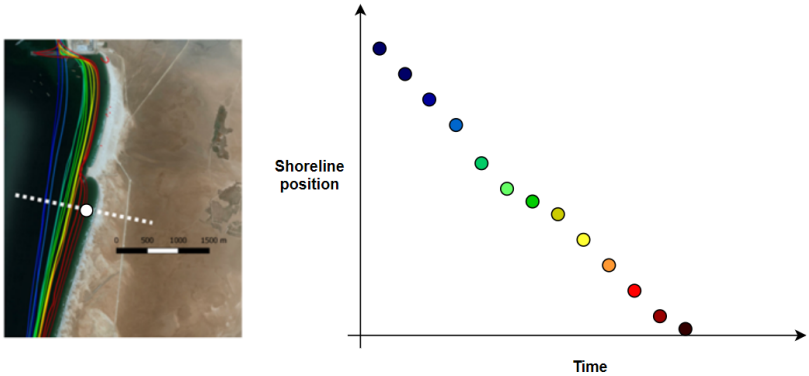

Figure 2.6: Visualization of how shoreline positions are derived from SDS-vectors. The white dot in the left image shows the center of the transect. The coloured markers on the right figure correspond to a shoreline position from the vector with the same colour on the left image.

2.1.5. Dynamic sandy beaches

Kras (2019) developed an algorithm that identifies coastal stretches with high variability containing ajdacent transects with similar characteristics both in time and space. These coastal stretches were defined as so called features. In this research, instead of feature, the term dynamic sandy beach or hotspot will be used for such a region. This hotspot identification method is called an 'along-the-shoreline'-analysis and was based on the data behind the Shoreline Monitor. Transects in this dataset are ordered as outlined in Appendix A.1.1, making a global 'along-the-shoreline'-analysis impossible. To do so, the transects needed to be reordered based on alongshore distance to each other. The 30374 small pieces of OSM shoreline (see section 2.1.2) were welded together, resulting in 33 stretches of continuous shoreline. Only areas larger than 25 thousand km^2 and within latitude filters were considered. Starting at the most upper left point of each continuous stretch of shoreline, the transect were reordered based on the smallest linear distance between two transect intersections in the WGS3857 projection (Kras, 2019).
Similar to Luijendijk et al. (2018), transects labelled as 'non-sandy' and with an 'undetermined sediment composition' were excluded. Three other filters reject transects with a linear change rate above 100 m/yr, containing less than 5 out of 33 or with a temporal coverage below seven years. Furthermore, based on recommendations of Van Leeuwen (2018) an additional rejection filter was applied by Kras (2019). This filter rejects transects with big changerate differences compared to adjacent ones. See Appendix A.1.1 for an overview of this rejection filter.
The algorithm developed by Kras (2019) could be used to quantify shoreline evolution at different scales. Using moving windows of various spatial scales, for each transect a moving average linear change rate is calculated, referred to as the rolling mean. This is done using different moving windows of 2.5, 10, 20, 50 and 100 km. The rolling mean is based on the summation of the changerates of all transects closest to a window, divided by the total summed length of these transects. The rolling mean is appointed to the approximate center transect of the moving window, determined by the floored position of the first moving window on the shoreline.
With the help of the rolling means, the hotspots are identified. First of all, rolling means in the stable regime (< 0.5 m/yr) are excluded. Next, all the tops and bottoms are identified. A top (bottom) is a transect with a rolling mean higher (lower) than both its adjacent transects. This so called top-bottom approach leads to many tops and bottoms. A top-bottom fit is created by connecting these tops and bottoms by means of a linear fit. By applying several threshold to this top-bottom fit, the amount of tops and bottoms is reduced and a new fit is created. All transects between two bottoms in this final fit represent a hotspot. See Appendix A.1.1 for a more in-depth understanding of this along-the-shore analysis.
Using a moving window of 2.5 kilometer, Kras (2019) applied the along-the-shore analysis on global scale. The 33 considered continuous shorelines contained 985 thousand transects. After applying the filters on these transects, 400 thousand transects remained and 585 thousand transects were excluded. The top-bottom approach resulted in 3033 prograding and 2121 retreating hotspots. The prograding and retreating hotspots combined incorporate approximately 224 thousand transects, or 22 thousand kilometer of shoreline. This indicates that somewhat less than 22% of the transects formed a hotspot. Of all these hotspots, 95% has a length below 10 kilometer, see Figure A.6.
A large amount of prograding hotspots is seen at the coast of China, Japan and the UAE, which is possibly related to land reclamation, see Figure 2.7 (Kras, 2019). This might explain why in Asia the amount of prograding hotspots almost exceeds the amount of retreating hotspots by a factor 2. In Europe, the number of prograding hotspots is larger than the retreating ones. This could be caused by a high number of human interventions. South America experiences more prograding than retreating hotspots as well, this is especially noted at the west coast. This seems to be caused by natural drivers. The remaining continents have a balanced number of prograding and retreating hotspots (Kras, 2019).

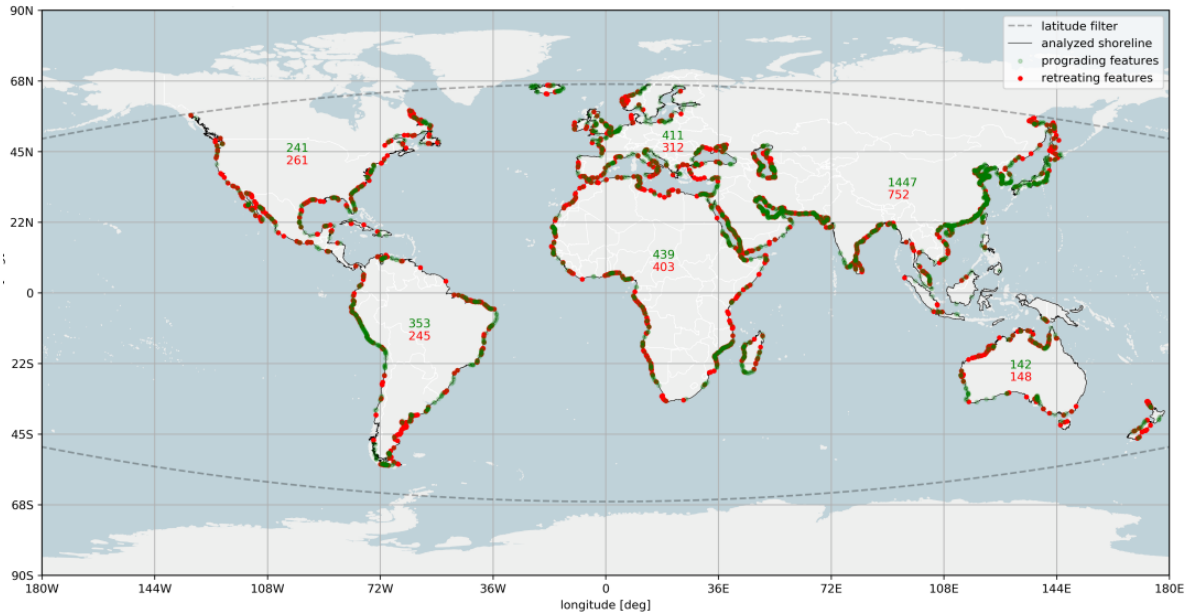

Figure 2.7: Global map of locations of hotspots for 33 continuous shorelines with 3033 prograding (green dots) and 2121 retreating hotspots (red dots). The green (red) numbers on the map indicate the amount of prograding (retreating) hotspots per continent. (source: Kras, 2019).

2.2. Drivers of sandy shoreline evolution

In this section, the mechanisms behind the drivers of sandy shoreline evolution are described. For all drivers that could be identified using SDS, following Wang (2018), characteristics in time as well as in space will be explained. Furthermore, examples of typical case studies will be provided for each driver, emphasizing these characteristics. The drivers are split into anthropogenic (human) induced and natural ones, see Figure 2.8. The natural and anthropogenic drivers are treated in Section 2.2.1 and Section 2.2.2 respectively in order of their spatial scales.

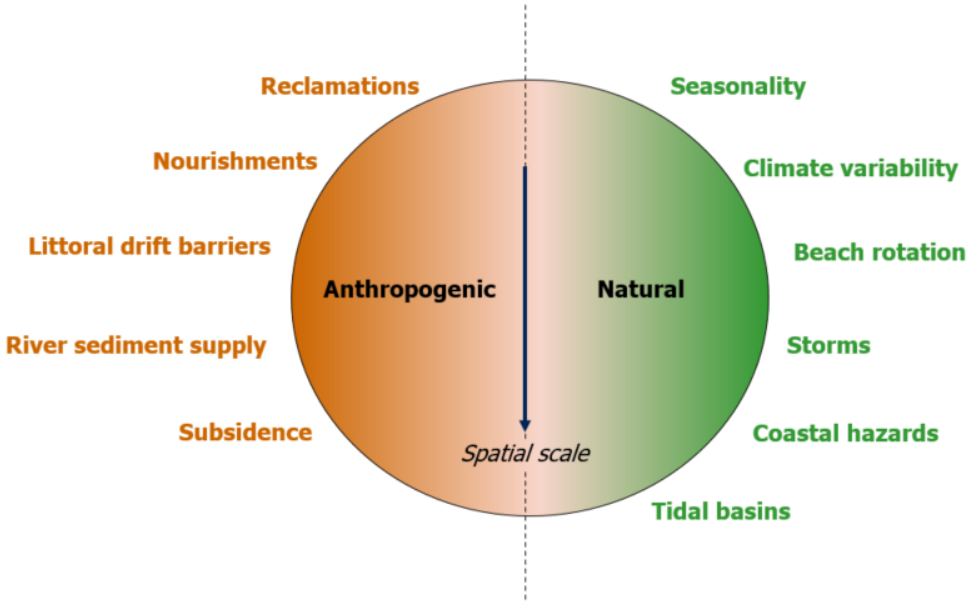

Figure 2.8: Natural and anthropogenic drivers of shoreline evolution. The drivers are sorted from bottom to top according to their spatial scales.

2.2.1. Natural drivers

The following six natural drivers are considered:

1. Seasonality
2. Climate variability
3. Beach rotation
4. Storms
5. Coastal hazards
6. Tidal basins

Seasonality (SN)

Seasonality is a phenomenon where during the winter period energetic waves combined with higher water levels cause erosion and during the summer period accretion occurs under calmer conditions. In winter, waves move sediment into the surf zone, creating a narrow beach. In summer, in response to milder wave conditions, the sandbars formed in the winter period move back to shore and eventually attach to the beach resulting in a wider beach again (Bosboom and Stive, 2012). This gives an oscillating behavior with narrow beaches at the end of the winter and wide beaches at the end of the summer. Theoretically, there is no net change in shoreline position due to seasonality, except in cases where sediment is deposited in offshore canyons, transported to the hinterland by aeolian transport or lost in the alongshore direction.

As indicated, seasonality is caused by variations in wave climate on the beach and therefore can vary at small spatial scales. The presence of reefs and bars can cause wave dissipation and thus affect wave action at the

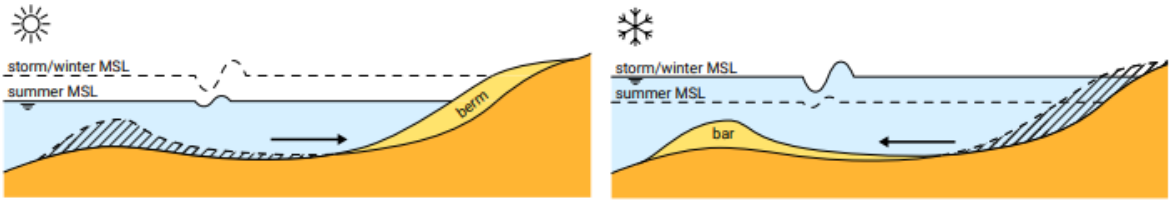

Figure 2.9: Summer and winter profiles showing the annual changes in beach profile. (source: Bosboom and Stive, 2012).

beach. Therefore, reefs and bars influence seasonal variations. Furthermore, the magnitude of the wave height is determined by three factors; wind speed, wind duration and fetch, which is the distance over which the wind blows. Large waves occur only when all three factors combine (Duxbury et al., 1997).

Perth North City Beach, Australia

Perth is the capital of Western Australia with coastlines characterized by sandy beaches punctuated by rocky outcrops. Wave energy varies along the coastline due to variation in wave exposure because of sheltering effects or the presence of reefs and sandbars. This results in a varying seasonal beach behaviour along the coast. Masselink and Pattiaratchi (2001) used standard survey techniques to examine seasonal changes in shoreline position in Perth from November 1995 to October 1997, see Figure 2.11. At this location, the morphological changes are better explained by a seasonal reversal in the littoral drift direction than by variations in the incident wave energy conditions. Minimum shoreline positions are observed around July. Seasonal shoreline displacement are of the order of 100 meters.

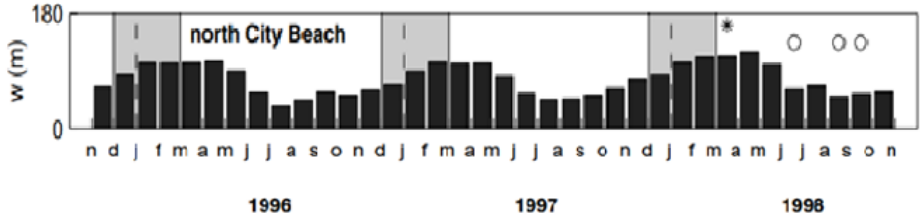

Figure 2.10: shoreline positions at North City Beach in Perth during November 1995 to October 1996. The shading indicated the summer months (December - February). Circles and asterixes represent the presence of nearshore bar morphology and a scarped beach face, respectively. (source: Masselink and Pattiaratchi, 2001).

San Francisco Ocean Beach, USA

San Francisco is a city on the east coast of the United States. San Francisco's beach, Ocean Beach (OB), is a sandy beach of about seven kilometers stretching from a rocky headland at Point Lobos to the bluffs at Fort Funston. Using All Terrain Vehicle Surveys (ATVs) measurements with an accuracy of +/- 3 cm, Barnard et al. (2007) found that during a fairly typical winter, as observed in 2004-2005 the shoreline retreated up to 40 meters, depending on the exact location at the beach. Beach volume maxima are reached around the end of summer in the months of September/October, while minimum shoreline positions occurs at the end of spring (Barnard et al.).

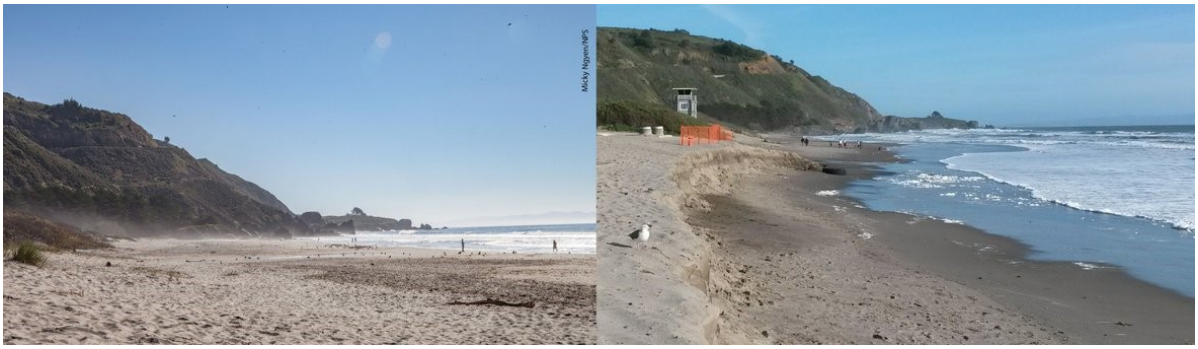

Figure 2.11: Summer (left) and winter (right) beach at Stinson, 10 kilometer north of San Francisco. In the summer the beach is rich in sediment which is eroded in the winter months.

Climate variability (CV)

When aspects of climate such as temperature, precipitation or wind speeds differ from an average, one speaks of climate variability. These aspects occur due to changes in the circulation of air, ocean or other factors (UCAR, n.d.). The best known globally climate variations are the El-Niño-Southern Oscillation (ENSO) and the North Atlantic Oscillation (NAO) (De Viron et al., 2013).
ENSO explains much of interannual variability in sea surface temperate, sea-level pressure and atmospheric forcing accros the equatorial Pacific. It has a period fluctuation of around 2-7 years. One way to measure the intensity of this fluctuation is the Southern Oscillation Index (SOI), which is based on the observed sea level pressure (SLP) differences between Tahiti and Darwin, Australia. A prolonged negative (positive) phase of the SOI coincide with abnormally warm (cold) waters accross the eastern Pacific and are called El Niño (La Niña) episodes (NOAA, n.d.).

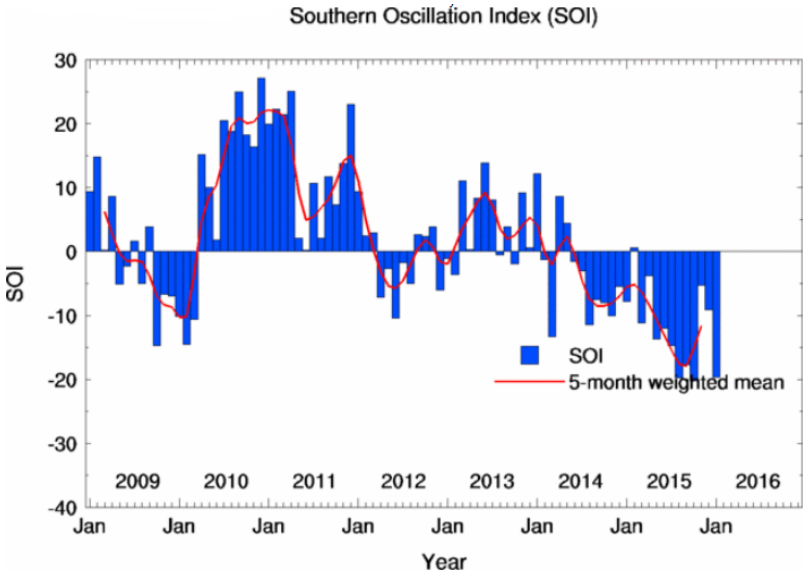

Figure 2.12: SOI values from 2009 to 2016. When the SOI has a value -7 (+7) of 5 consecutive months an El Niño (La Niña) episode occurs. (source: NOAA, n.d.).

El Niño events result in seasonally elevated water levels, higher wave energy and southerly wave directional shifts along the North American coast resulting in severe erosion during the winter especially in the years 1982-1983, 1997-1998, 2009-10 and 2015-2016 (Barnard et al., 2015). For the Eastern North Pacific, Pacific Northwest and Southwestern Pacific, El Niño and La Niña have been linked to elevated coastal hazards, particularly during boreal winter (December-February) (Barnard et al., 2015; Allan and Komar, 2006; Bryant, 1983).
The Northern Atlantic Oscillation (NAO) is a phenomenon over the North Atlantic Ocean of fluctuations in

SLP between the Icelandic Low and Azores High (Hurrell et al., 2003). It is one of the most important manifestations of climate fluctuations in the North Atlantic and surrounding humid climates (Hurrell, 1995a). On inter-annual and shorter timescales, the NAO only has variability in the atmospheric circulation as a consequence. The NAO controls the strength and direction of westerly winds and frequency and intensity of storm tracks accross the North Atlantic (Hurrell et al., 2003; Hurrell, 1995a).

Narrabeen and Palm beach, Australia

Beach rotation for these two pockets beaches as described in Section 2.2.1, is likely to be caused by ENSO (A. Short et al., 1995,). A study was undertaken to establishing the causes of the erosion at these beaches by linking its beach evolution to the SOI. By investigating the lagged correlation between the beach width and the SOI, Ranasinghe et al. (2004) found that for Narrabeen the northern part and the SOI were correlated by around -0.45 with a lag of 3 months. On the other hand, the southern part of the beach was correlated with the SOI by 0.3 with a lag of 17 months. In the 1986-1987 El Niño, the northern part of the beach accreted 14 meter where the southern part eroded 10 meter, causing a clockwise rotation of the beach. In the consecutive La Niña phase of 1988-1989, the northern part eroded 12 meter where the southern end accreted 15 meter (Ranasinghe et al., 2004), see also Figure A.8. Similar results for the lagged correlations between SOI and the beach width where found for the Northern and Southern part of Palm beach.

San Francisco Ocean Beach, USA

During the intense El Nino between October 1997 and April 1998, shoreline retreat was far more than the normal winter retreat with localized pockets of shoreline retreat of over 70 m (Barnard et al., 2007). This was especially encountered in the Northern section of the beach, see Figure 2.13.

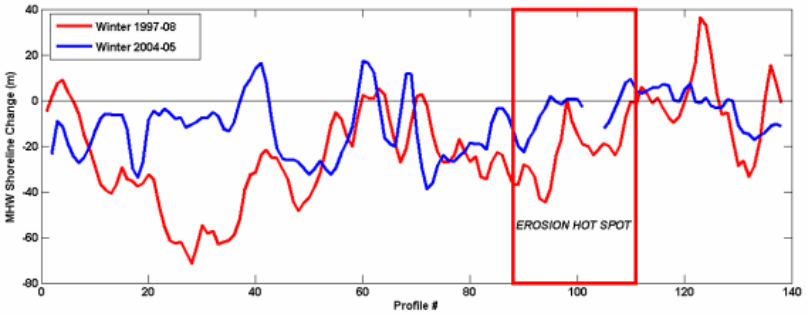

Figure 2.13: Winter change (MWH line) during the 1997-98 El Nino compared to a typical normal winter of 2005-05. Profiles are spaced 50m apart and numbering increases from north to south. (source: Barnard et al., 2007).

Danube Delta, Romania

The Danube Delta is a 162 kilometer long low-lying area in Romania of which most parts are dominated by erosion. Vespremeanu-Stroe et al. (2007), assesses the influence of NAO via storms on coastal processes by using shoreline positions covering the period 1961 - 2006 obtained from survyes, maps, aerial photos and sattelite images, and the NAO index defined as the difference of SLP between Lisbon, Portugal and Stykkisholmur, Iceland (Hurrell, 1995b). For this data the annual mean was first calculted and then normalized by extracting from each value the mean for the entire study period (1961-2006) and dividing it by the standard deviation. These annual normalized annomalies were smoothed with a three-year running mean filter to obtain an multi-annual component of the series. For three representative sectors of the study area it was found that the coastline changes on the medium-term (decadal) evolution are controlled by the NAO phases and there is a negative correlation between NAO and the evolution of the shoreline on the medium term (see Figure A.9) (Vespremeanu-Stroe et al., 2007).

Beach Rotation (BR)

Beach rotation can be defined as the lateral movement of sand along the beach in response to a modification in the indicident wave direction (A. D. Short et al., 2001) and is observed in embayed beaches. It causes localized retreat or accretion of the beach, although it does no lead to long-term loss of sediment because the beach often returns to it's initial state when wave direction shifts again (da Fontoura Klein et al., 2002).

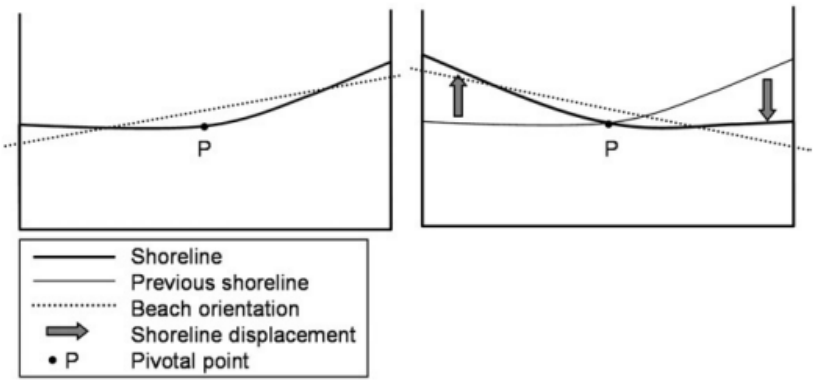

Figure 2.14: Illustation of beach rotation. (source: Ojeda and Guillén, 2008).

Narrabeen and Palm beach, Australia

Narrabeen and Palm beach are two embayed beaches (pocket beaches) located 20 and 30 kilometre north of Sydney, respectively. Many of these types of embayed beaches experienced severe erosion at their southern end over the last decade (Ranasinghe et al., 2004). Ranasinghe et al. (2004) used shoreline positions from April 1976 to October 2000, filtered using a low-pass filter to remove high-frequency signals, to investigate beach rotation at these beaches. Correlation between the shoreline positions at the southern and northern end for Narrabeen and Palm beach resulted in negative values of -0.18 and -0.6, respectively. Furthermore, correlations between the shoreline positions at locations at the same side of the pivotal point were positive for both pocket beaches. The shoreline positions at the two northern most profiles at Narrabeen had a correlation of 0.82. The two most southern profiles were correlated by 0.67. At palm beach, the two most northern profiles were correlated by 0.62 and the two most southern profiles by 0.76 (Ranasinghe et al., 2004). From these results, both beaches can be classified as rotational beaches.

Storms (S)

Storms are events in which atmospheric pressure and high wind speeds cause high water levels, also called surge, and high energetic waves. During storms, the beach is eroded and sediment is deposited in the surf zone. After the storm, when the sea conditions are calmer, this sediment is brought back onshore. The beach recovers to its original state after the storm. The post-storm profile is characterized by a narrow beach profile that slowly returns to its normal width. This is similar to the seasonal behavior of beaches described in Section 2.2.1. Yet, different from seasonality, storms are characterized by a random occurrence and duration.
During heavier storms, the beach is completely submerged and waves can reach the dunes, see Figure 2.20. The beach is not in equilibrium with the higher water levels and sediment from the dunes is transported to the lower beach. In contrast, this results in a wider beach width after the storm. After the water level drops, waves and alluvial processes return the beach to its original state. During storms, similar to seasonal behavior, there is no net change in beach width. Exceptions are very heavy storms where the water level exceeds the dune height and overwash occurs, transporting sediment across the dunes. Heavy storms can also cause sediment to be deposited far offshore, which is not returned to the beach. During these extreme events, beaches do not always recover to their original state.

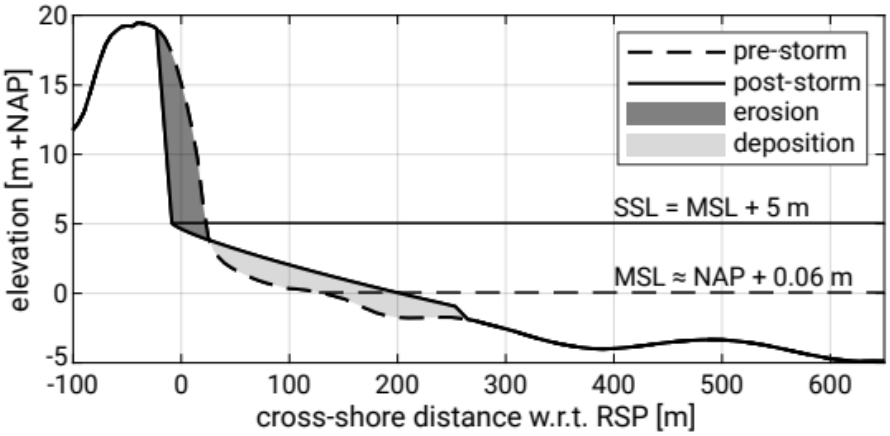

Figure 2.15: Illustration of a storm impact on the cross-shore profile. The dunes are eroded and the sediment is deposited on the foreshore resulting in a wider beach profiel. (source: Bosboom and Stive, 2012).

Fire Island, USA

Fire Island is a narrow barrier Island, located along the Southern shore of Long Island (New York). The majority of the width of this island is less than 1 km wide. Extra-tropical storms and hurricanes reach the Island in the mid-summer to late fall and nor'easter cyclonic storms in the late fall and the winter. As the Island has a large alongshore variability in bathymetry, the beach response differs along the island from beach and dune erosion to inundantion of the dunes and even a breach of the Island (Nelson and Hapke, 2015). Over the years, the Island experienced several large storms with mostly erosive consequences (2018; Lentz et al., 2013; Nelson and Hapke, 2015). The largest retreat of the shore was seen after Hurricane sandy in 2012. This event led to severe levels of coastal inundation and beach erosion. It even led to extensive dune overwashing and complete Island breaching (Nelson and Hapke, 2015). Table A.1 lists the large storms together with beach responses at Fire Island in the period 2005-2012.

Figure 2.16: Erosion after a nor'easter storm at Fire Island in 2016. (source: USGS).

San Francisco Ocean Beach, USA

Besides its seasonal behavior, Ocean Beach in San Francisco also experiences shoreline changes due to storm events. In 2005, a single storm removed over 40.000 m^3 sediment from the shores and resulted in up to 20 m of shoreline erosion. In December of the same year another storm resulted in shoreline retreat of 22 meter. This was particularly observed in the Northern part of the coastal stretch, see Figure 2.17 (Barnard et al., 2007).

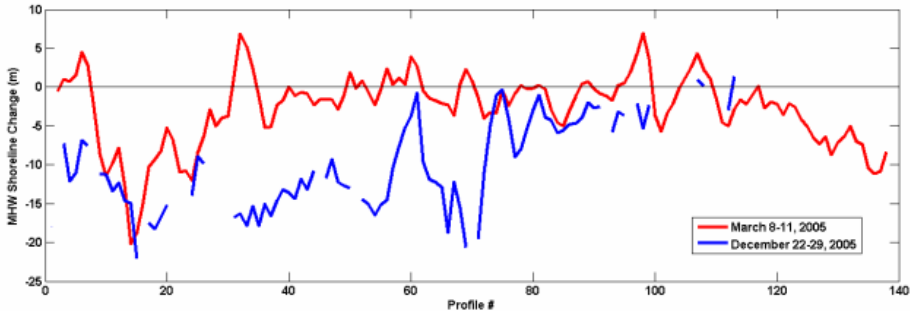

Figure 2.17: Alongshore shoreline change from two storms in 2005 at San Francisco Ocean Beach. Gaps in the data indicate no data and/or no MHW shoreline accessible. Profile 0 corresponds to the North of the beach and profile 140 to the south. (source: Barnard et al., 2007).

Coastal hazards (CH)

Events not caused by atmospheric pressures and wind are here classified as coastal hazards. An example of this is a tsunami. Tsunami's are sets of long shallow water waves, usually observed in oceans or large lakes. They are associated with earthquakes, volcanism or atmospheric disturbances (Röbke and Vött, 2017). Tsunami's are known to have sedimentary responses on the beaches, offshore as well as onshore. This type of coastal hazard can, similar to severe storms, gravely erode beaches by removing sediment from the coast and deposit it behind dunes or move it far offshore. Similar to storms, beach recovery will occur in the post-tsunami period.

Sumatra Aceh Coast, Indonesia

On 26 december 2004, a huge Indian Ocean tsunami devastated 175 km of the Aceh coast of northwestern Sumatra. At certain areas, the coast was eroded by 500 meter. At many locations the erosive effect of the tsunami was recovered within a very brief period. However, in locations where the coast was altered earlier by sinking large fish tanks into the wetlands behind the coasts, the destructive effects remained (Liew et al., 2010).

Figure 2.18: Satellite images at Banda Aceh City before the 2004 Indian Ocean tsunami (left) and after the tsunami (right). (source: Georgia Tech).

Tidal Basins (TB)

Tidal basins represent 10-13% of the world's continental coastlines (Schwartz, 1973) being an important feature considering coastal systems on a global scale. The main morphological elements in an basin are the inlet, the tidal delta's, the channels and the flats. At the inlet, the part where the water flows from the ocean inside the basin, tidal discharges and velocities are large resulting in a strong sediment exchange between the basin and the outside area. Especially in constricted inlets, this leads to deposition at both sides of the entrance, which are called the outer and inner delta. These deltas are also called the ebb-tidal and flood-tidal

delta respectively. An important hydraulic control for a basin is the tidal prism, the volume of water that flows in and out the inlet during one tidal cycle. For short basins, this tidal prism can approximated as following:

$$P = A_b \cdot H \tag{2.2}$$

where A_b : the surface area of the basin (m^2)
H : the mean tidal range (m)

An empirical relation exists between the sand volume stored in the outer delta and the tidal prism:

$$V_{od} = C_{od} P^{1.23} \tag{2.3}$$

C_{od} is an empirical coefficient dependent on the wave climate (Bosboom and Stive, 2012).
The morphologically active part of a basins consists of a deeper part where the flow concentrates during ebb, and of tidal flats which are exposed during low water and covered during flood. There is an empirical relation between the volume of this deeper part below MSL, the channels, and the tidal prism:

$$V_c = C_v \cdot P^{\frac{3}{2}} \tag{2.4}$$

C_v is a location dependent empirical coefficient.
The area of the flats can be approximated by the following equation:

$$A_f = A_b - \frac{V_c}{D_c} \tag{2.5}$$

where V_c : volume of the channels (m^3)
D_c : typical depth of the channels (m)

Basins that are not in equilibrium are either flood or ebb dominance, referring to net sand import or sand export. During equilibrium conditions, the geometrical characteristics of the basin are such that the duration of ebb and flood are approximately equal. A large ratio of tidal amplitude over water depth enhances flood dominance. In that case the propagation of the flood is faster than ebb and thus velocities are larger and the rising period is shorter. Since sediment transport responds non-linear to velocity higher flood velocity result in residual transport in flood direction and a basin is said to be flood dominant.

Terschelling, Netherlands

In 1932, the Afsluitdijk, closed of a part of the Wadden Sea reducing the area of the tidal basin. Equation 2.2 illustrates that this also reduces the tidal prism. Empirical relations 2.3 and 2.4 show that this closure results in a reduction of the volume of the outer delta and a decrease of volume of the channels. In other words, sediment is moved from the ebb-tidal delta to the channels. If sediment supply from the ebb-tidal delta is not sufficient, sediment will be supplied from the adjacent coasts.
After closure of the Zuiderzee 600 million m3 accumulated in the western part of the Wadden Sea. In the same period that sediment accumulated in the Wadden Sea, the adjacent North Holland coast, barriers island coasts and ebb-tidal deltas strongly eroded. Besides the closure of the Zuiderzee sea, level rise and subsidence due to gas extraction have played a role in the erosion Elias et al. One of the barrier islands subject to heavy erosion is Terschelling. Based on annual SDS and a linear regression, Luijendijk et al. (2018), estimated the retreat at the eastern tip of Terschelling to be 41 m/yr.

Figure 2.19: Aerial view of Terschelling island in the Dutch Wadden Sea. (source: photo from Marco van Middelkoop).

Dongkengtuo Sand Island, China

In the Loalonggou sea area, located in Bohai Bay in China, lies the delta of the Luan River. This sea area includes several coastal barrier islands, a lagoon and inlet channels. One of the outer barrier islands is the Dongkengtuo Sand Island (DSI) with a length of 6.8 kilometers and a width of 0.4 to 3.2 kilometers. The barrier islands obstruct wave action and deflect flood tide into the two channels on either side of the island. (Zhu et al., 2020). Suspended sediment from the bottom of the neritic zone at DSI is carried into the lagoon by tidal currents and deposited southwest of the island as a result of greatly reduced flow velocity. This results in westward movement of the island. This westward extension of DSI narrows the deep channel to the east, increasing flow velocity and increasing erosion on the eastern part of the island (Zhu et al., 2020). While the western part of the Island accretes this means erosion of the eastern part of DSI.

2.2.2. Anthropogenic drivers

Five human induced drivers are considered:

1. Reclamations
2. Nourishments
3. Littoral drift barriers
4. River sediment supply
5. Subsidence

Reclamations (RM)

Land reclamation is the process of creating new land. For the construction of a reclamation first a vertical or mound sea dyke is build after which the inner zone is filled with sand (Stauber et al., 2016). As the coast after reinforcement is protected by a hard structure it does not experience any coastline change.

Caofeidian port, China

In 2004 a project was launched in which 310 km^2 of land was reclaimed in the Caofeidian Industrial Complex of the Hebei Province (Elsayed et al., 2005; Frihy et al., 1994; W. Wang et al., 2014). The new reclaimed land was used as a deep water port for steel, chemical, electric works and nuclear power industries (Yin, 2007). Figure A.10 indicates the reclaimed areas between 2005 and 2010 at the Port of Caofeidian.

Jebel Ali, United Arab Emirates

The port Located in Jebel Ali, Dubai, is the largest and busiest port in the Middle-east and the ninth busiest in the world ("The Economist", n.d.). In 2005, the expansion of Terminal 2 started which was completed at the end of 2007. A second phase expansion was finished in 2015 ("Ship Technology", 2019).

Figure 2.20: Expansion of the Jebel Ali Port. The construction is protected by a rubble mound breakwater to prevent erosion. (source: Logistics Middle East).

Nourishments (NM)

Nourishment is the placement of sand in the coastal zone to maintain the volumes of sand in the littoral system. It is a measure to stabilize the shoreline and counter erosion (Wesenbeeck et al., 2012). Nourishments can be placed directly on the sub aerial beach, these are so called beach nourishments. Another nourishment strategy is adding sand to the foreshore, just outside or inside the outer breaker bar. Marine processes redistribute the sand in the cross-shore direction and gradually create a wider beach over time (M. Stive et al., 2013).

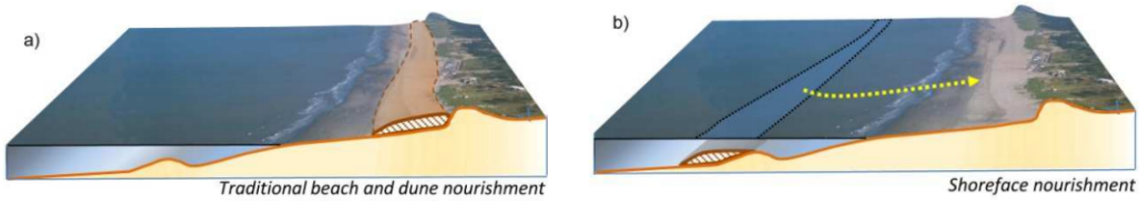

Figure 2.21: Conceptual diagram of two nourishment strategies, beach nourishments (a) and shoreface nourishments (b). (source: adjusted from M. Stive et al., 2013).

Nourishments are not a long-term solution to beach erosion as waves, storms and high water levels keep eroding the sediment alongshore and offshore (Dean, 2002). A typical nourishment has a lifetime of 3-5 years (Hamm et al., 2002). Therefore, from time to time renourishments are required to maintain the coastline at a safe position. This results in a saw-tooth shape when the volume of the sand at the beach is plotted over time. see Figure 2.22.

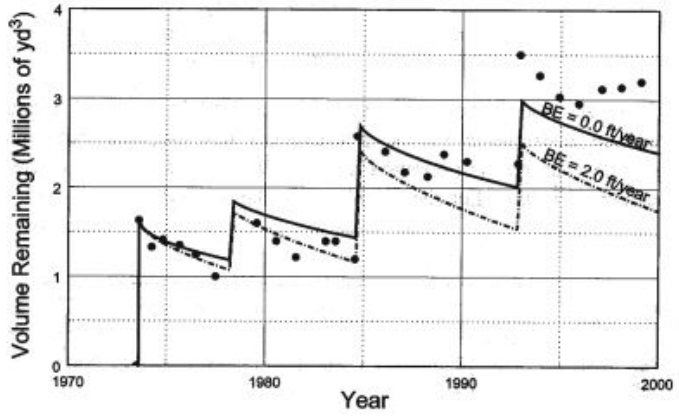

Figure 2.22: Volume of sand at Delray Beach, Florida. The solid line represents the predicted volume and the dotted line are the measured values. (source: Dean, 2005).

The CERC-formula can be used to approximate the total longshore sediment transport over the breaker zone due to the action of waves.

$$S = \frac{K}{16(s-1)(1-p)}\sqrt{\frac{g}{\gamma}}sin(2\phi_b)H_b^{2/5} \tag{2.6}$$

where
S	:	the deposited volume of sediment transported	(m^3/s)
K	:	a coefficient	(-)
p	:	the porosity	(-)
g	:	gravitational acceleration	(m^2/s)
ϕ_b	:	the wave angle of incidence at the outer edge of the breaker zone	(-)
H_b	:	the wave height at the outer edge of the breaker zone	(m)

Equation 2.6 explains that varying incident wave angles result in sediment transport gradients with coastline changes as a consequence. Figure 2.23 shows that due to a changing angle of incidence gradients arise with

erosion occurring at the beach nourishment and accretion at the nearby stretches.

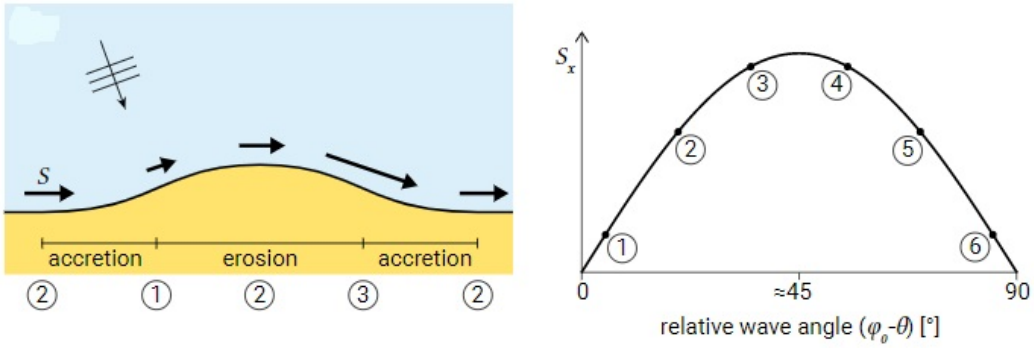

Figure 2.23: Shoreline response on a nourishment. The angle at sea indicates the direction of the incoming waves. The arrow parallel to the shoreline point out the direction and magnitude of the littoral drift. (source: Bosboom and Stive, 2012).

Nourishments are so called 'soft' measures, the natural erosion processes are allowed to continue. This is in contrast to Reclamations or shore-parallel constructions. These kind of interventions are called 'hard' measures, sediments in the alongshore and cross-shore directions of the coasts are interfered (Bosboom and Stive, 2012).

Fire Island, USA

Since the 1960s, nourishments of the beach at Fire Island have become a frequent strategy to counteract erosion from storms (Lentz and Hapke, 2011). Figure A.7 gives an overview of beach nourishments from 1930 to 2009. The nourished volumes at this location are relatively small, around 400.000 m3.

Delray Beach, USA

Since 1973, see Figure 2.24, Delray beach, located on the southeast coast of Florida, has been periodically been nourished with intervals ranging from 5 years in the past to 8 years in present days (Hartog et al., 2008; Beachler and Mann, 1996; Dean, 2005). These nourishments have been performed to secure human activities and counteract beach erosion from storms (Finkl, 1996). An overview of locations and volumes of nourishments at Delray beach can be found in Figure A.12. Volumes at this locations are in the order of 1 to 2 million m^3, corresponding to medium scale nourishments.

(a) Aerial picture of Delray beach before the beach nourishment in 1973

(b) Aerial picture of Delray beach after the beach nourishment in 1973

Figure 2.24: Delrey beach before (left) and after (right) the nourishment in 1973 (Source : Benedet, 2016)

St. Augustine, USA

Another frequent nourished beach in Florida is St. Augustine, located in the St. Johns County region. Erosion is caused by northeasters, tropical cyclones and hurricanes as well as the effects of two nearby inlets (FDEP, 2020). An overview of the nourished volumes for St. Augustine beach can be found in Figure A.13. In St. Augustine, nourished volumes are in the order of 2 to 3 million m^3 which are classified as large scale nourishments.

Mega-nourishments

The Netherlands developed an innovative intervention to stabilize the coastline and feed adjacent coastal sections. One of these mega-nourishments is the Sand Engine that was completed in 2011. This large scale nourishment project of 21.5 Mm^3 initially extended over a 2.4 kilometer stretch and up to 1 kilometer offshore (M. J. Stive et al., 2013; Luijendijk et al., 2017). With a yearly average loss of 1 Mm^3 the sand engine has an expected lifetime of 20 years (M. J. Stive et al., 2013). Another mega nourishment along the dutch coast was completed in 2015 at the coast of Hondssbosche. A total of 35.6 Mm^3 of sand was deposited on the beach at this location over a stretch of approximate 12 kilometer (de Jongh, 2017).

Figure 2.25: Aerial image of the Sand Engine in 2022, the Netherlands (source: Google Earth).

Littoral drift barriers (LDB)

A Littoral drift barrier (LDB) is an obstacle that blocks the migration of material along the shore. These barriers may be natural, such as major headlands, or man-made such as jetties or breakwaters (Channel et al., 2006). Materials are moved by longshore currents caused by waves and/or tides. In the case of one primary wave direction, one side of the LDB experiences accretion, the updrift part. The coastline at the other side of the barrier will erode due to a reduced sediment supply. This eroding part is called the downdrift side or leeside. At the downdrift part of the harbour, one area is sheltered from the prevailing wave direction. Here, set-up differences cause transport towards the breakwater such that close to the breakwater a small accreting area arises. After certain time, when the updrift part is fully developed, transportation of the sediment starts accross the barrier (bypassing). Figure 2.26 gives an overview of these morphological processes.
Figure 2.26 indicates that the accretion at the updrift part is largest near the port and decreases with distance from the port. At the leeside, erosion decreases with distance from the port but is not maximum at the structure due to the sheltering effect. In the case of a bi-modal wave climate, accretion will occur at both sides of the LDB.

Port de l'Amitie, Mauritania

The coasts in the region of Nouakchott, Mauritania, experienced strong evolution because of non-integrated coastal management. This was due to the build-up of the port de l'Amitie that was finished in 1987 (Ould Elmoustapha, 2000; Ould Elmoustapha et al., 2007; Wu, 2007). Accretion of the beach occurs in the north of the 836m long breakwater and erosion at the south. Between 1989 and 2001, the north of the beach experienced accretion of 30.44 m/yr close to the port and 12.31 m/yr 3 kilometer away from the port (Wu, 2007; Ould Elmoustapha, 2000). Wu (2007) estimated that after 2001 accretion rates at these locations would drop to 29.86 m/yr and 4.88 m/yr, respectively. At the downdrift side of the port close to the port the shoreline retreated between 1989 and 2001 with a rate of 12.76 m/yr. Downdrift the maximum retreat was observed at 1.5 kilometer to the south at a rate of 32.29 m/yr (Wu, 2007). This maximum retreat was expected to continue

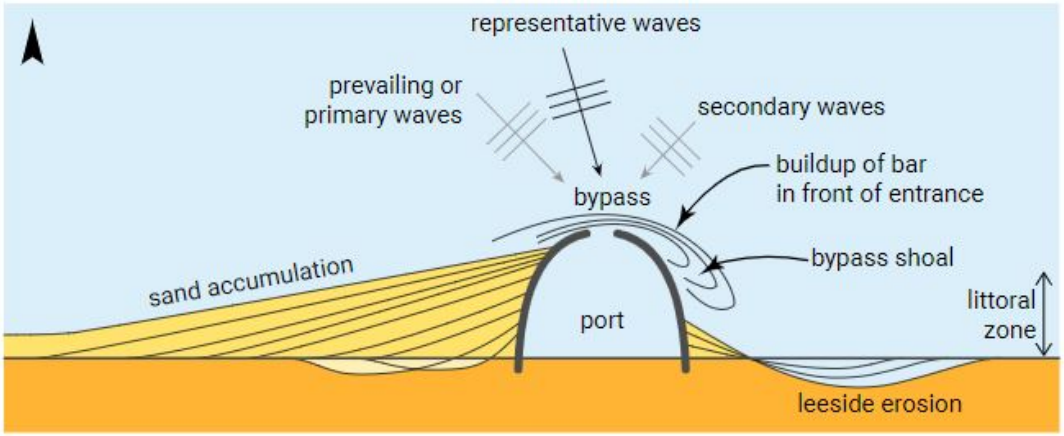

Figure 2.26: Schematic shoreline development for a port at a coast with a slightly oblique resulting wave attack. (source: Bosboom and Stive, 2012).

at the same rate after 2001 (Wu, 2007).

Port of IJmuiden, Netherlands

In the middle of the Holland coast lies the Port of IJmuiden. Around 1870 the harbour breakwaters have been constructed with an initial length of 1.5 km. In 1965 the southern breakwater was extended to about 2.5 kilometer and the northern to about 2 kilometer (Luijendijk et al., 2011), see Figure 2.27.

Figure 2.27: Port of IJmuiden in 1880 (left) and the layout of the port in 2005 (right). Accretional patterns at both sides of the port can be observed in the present layout. (source: Luijendijk et al., 2011).

Figure A.15 shows that at IJmuiden the wave climate is bimodel with waves from the south-west and north-west. This is also observed in the accretional patterns at both sides of the port. Moreover, contraction of tidal flows at the entrance of the port in combination with locally increased turbulence resulted in a scour hole in front of the port entrance. Eddies here result in flow towards both sides at the port, see Figure A.14 (Luijendijk et al., 2011; Van Rijn, 1995). At some distance of the breakwaters, erosive effects initially arised but have been migitated by means of nourishment since 1993 (Luijendijk et al., 2011). At the southern side, the coastline accreted over 200 meter between 1980 and 2000. At the northern side this is less, approximate 100 meter (Luijendijk et al., 2011).

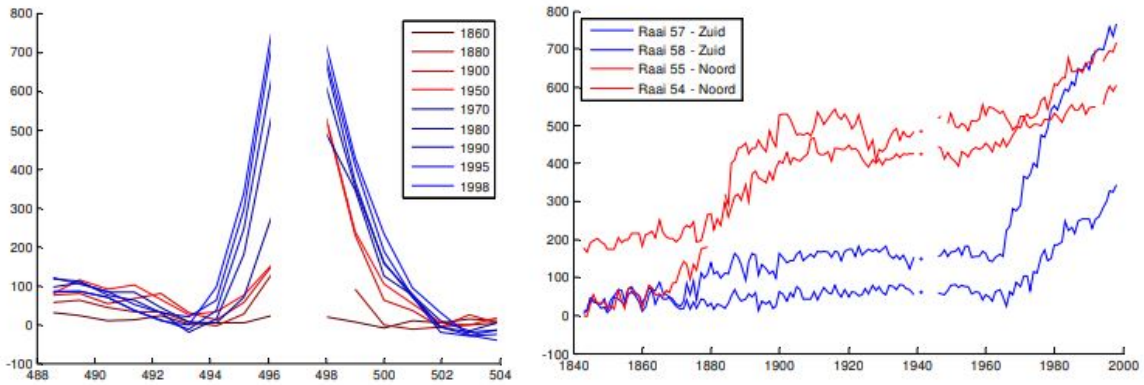

Figure 2.28: a) coastline changes after 1843 at the Port of Ijmuiden. b) Coastline position in time where red (blue) lines represent transect north (south) of the Port of Ijmuiden. (source: Luijendijk et al., 2011).

Aveiro Port

The high southward directed alongshore transport at the Portugese coast was interrupted after the construction of two breakwaters at Praia da Barra at the Port of Aveiro (Luijendijk et al., 2018; Pranzini and Williams, 2013). The northern breakwater was extended in 1985 (Earth, n.d.). Using annual SDS and a linear change rate Luijendijk et al. (2018) estimated the accretion at the updrift side at 10 m/yr. Immediate downdrift erosion was prevented by constructing a system of groins (Earth, n.d.).

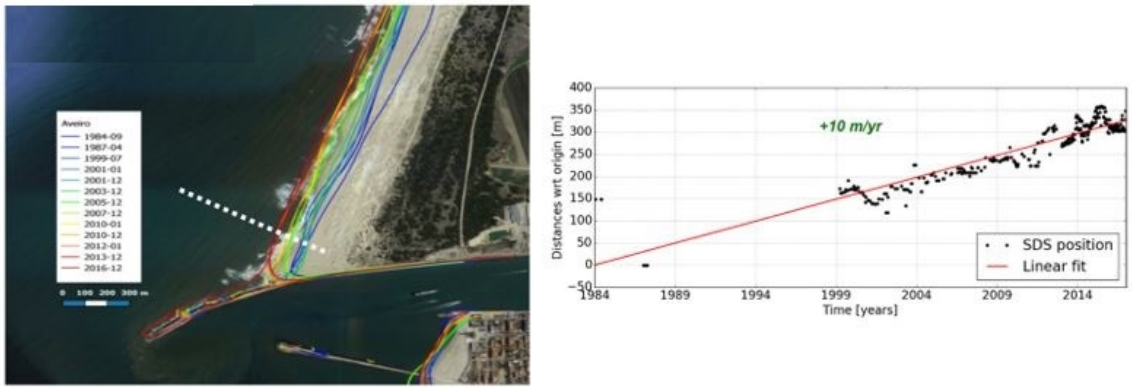

Figure 2.29: Coastline changes at Aveiro. The image at the left shows the SDS. The shoreline positions in time for the white dotted transect are plotted in the right image. (source: Luijendijk et al., 2018).

River sediment supply (RSS)

At the mouth of a river, the velocities of the water decrease and lose their capacity to carry the sediment. The coarser materials settle first, where the finer sediments settle in somewhat deeper coastal waters. Coastal change occurs where there are spatial sediment transport gradients and/or sediment sinks or sources (Bosboom and Stive, 2012). A river mouth can be seen as a source of sediment. Furthermore, waves at the river mouth can cause sediment transport. Equation 2.6 indicated that the sediment transport is proportional to $H_b^{2.5} sin(2\phi_b)$. As mentioned, when there are spatial gradients in sediment transport, coastal change occur. In other words, when the wave height and/or angle of incidence vary, the coastline will change. When the sediment supplied from a river is larger than the transported sediment by the waves, a delta will arise. If for some reason, think of river damming or sediment mining, the sediment supply decreases below the transported sediment, the delta will erode.

Ebro Delta, Spain

200 kilometer southward of Barcelona in the Mediterranean coast, lies the Ebro Delta. It has an area of 320 km^2 and a coastline of 50 kilometers long (Valdemoro et al., 2007). Intense river management that occured since the 1900s has drastically changed the sediment discharge in the ebro river. Between 1906 and 1930 some significant dams where built in the upper part of the river. During the 1940s and 1950s several reservoirs where constructed. In 1966, the largest dam, the Mequinenza Dam, was built in the lower part of the river and consequently the Ribarroja dam was built in 1969 a few kilometer downstream. These human interventions trapped more then 95% of the sediment load reducing the discharge of sediment from $17 \cdot 10^6$ in 1911 to $0.2 \cdot 10^6$ during the 1980s (Albert and Jorge, 1998). At the start of this century, the Ebro discharges less than 1% of the sediment than before the construction of the dams (Albert and Jorge, 1998). Due to this reduced sediment supply, the central part of the delta experiences much erosion whereas the spits experience accretion due to the deposition of the eroded material (Grases et al., 2020). At the mouth of the river, between 1957 and 2010 a retreat of 2 kilometer was observed which yields a rate of 40 m/yr (Somoza and Rodrıguez-Santalla, 2014). Figure A.11 shows a map with the distribution of erosion and sedimentation areas at the Ebro delta together with orders of magnitude of the shoreline evolution.

Figure 2.30: Aerial of the Ebro Delta. (source: Rocchio et al., 2018).

Subsidence (SS)

Delta's and large coastal cities are areas prone to subsidence. Delta's are soft and easily compressed (Schmidt, 2015). They're often propped up by underlying oil, gas or fresh groundwater (Ingebritsen and Galloway, 2014a; Milliman and Haq, 1996). If these resources are extracted, the sediments compress, and the land sinks. In delta's subsidence is often compounded by local flood defences within the delta and upstream dams, which reduce the sediment supply (Ericson et al., 2006; Syvitski et al., 2009; Tessler et al., 2018).
Due to insufficient water sources, cities extract water from the ground for domestic and industrial uses (Schmidt, 2015; Syvitski, 2008). Therefore, large cities also experience high subsidence rates. Besides sinking of land due to human interventions, subsidence can also occur due to compaction of sediments, natural subsidence, or sea level rise. However, rates of human induced subsidence greatly exceed rates of natural subsidence (0.1 - 1 cm/yr) and SLR (0.3 cm/yr) (Ingebritsen and Galloway, 2014b). Moreover, Wang (2018) concluded that SLR could not yet be detected by the SDS. The reason was that the time coverage of the satellites was too short to separate shoreline changes due to SLR from the natural variability of the coast. Since natural land subsidence is of the same order of magnitude, this also applies here.
Shoreline variation as a result of (human induced) subsidence can be explained using the Bruun rule (Bruun, 1954; Bruun, 1962). The Bruun rule assumes an equilibrium between the shoreface and the hydrodynamic forcing and was initially developed to make estimates of shoreline retreat due to sea level rise. A rise in sea

level (or a lowering of the land) results in a water depth too large to be in equilibrium with the forcing. In the absence of sediment sources or sinks, a new equilibrium is achieved by a landward and upward shift of the profile.
The estimated horizontal retreat can be approximated by Bruun's rule (Bruun, 1954):

$$R_{Bruun} = \frac{S_{SLR}}{tan(\alpha)} \tag{2.7}$$

where R_{Bruun} : shoreline retreat
S_{SLR} : sea level rise
$tan(\alpha)$: beach slope

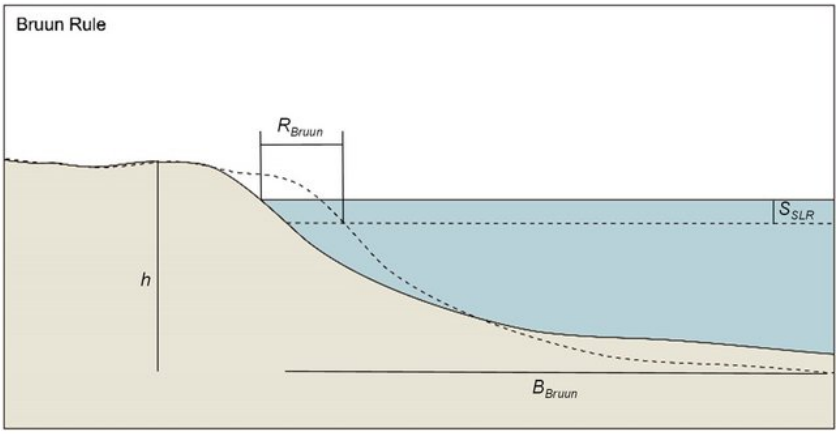

Figure 2.31: Schematization of the Bruun rule. A sea level rise with a magnitude of S_SLR causes a shoreline retreat equalt R_{Bruun} (source: Hallin, 2019).

Jakarta, Indonesia

With 9.6 million inhabitants, Jakarta is the capital of Indonesia. Urban development has increased exponentially introducing environmental problems, land subsidence being one of them (H. Z. Abidin et al., 2011). Human interventions such as groundwater extraction and load by constructions are the biggest contributers of land subsidence (H. Z. Abidin et al., 2011). Land subsidence rates exhibit spatial and temporal variations with rates up to about 1-15 cm/yr (H. Z. Abidin et al., 2011; H. Abidin et al., 2015 ;Nicholls et al., 2021). Some locations even experience rates up to about 20-28 cm/yr (H. Z. Abidin et al., 2011).

Manilla, Philippines

Manilla is the capital and second-largest city of the Philippines and has around 1.78 million inhabitants (PSA, 2016). Manila's coastal areas are sinking fast at a rate of 9 cm/yr mainly due to water extraction (Rodolfo, 2014; Nicholls et al., 2021). To counteract this subsidence, the Philippine Reclamation Authority (PRA) identified 102 near-shore reclamation projects. Figure A.16 shows the outlay of Manilla's coastal zone as proposed by the PRA in 2011.

Nile Delta, Egypt

Along the Nile Delta, highest rates of subsidence were observed over cities at the two river branches, the Damietta and Rosetta. Over the years 2014-2019, the highest rates were observed over the city of Damiat close tot the Mediterranean coastline, 12-24 mm/yr (Hassan et al., 2019).

2.2.3. Overview of the drivers

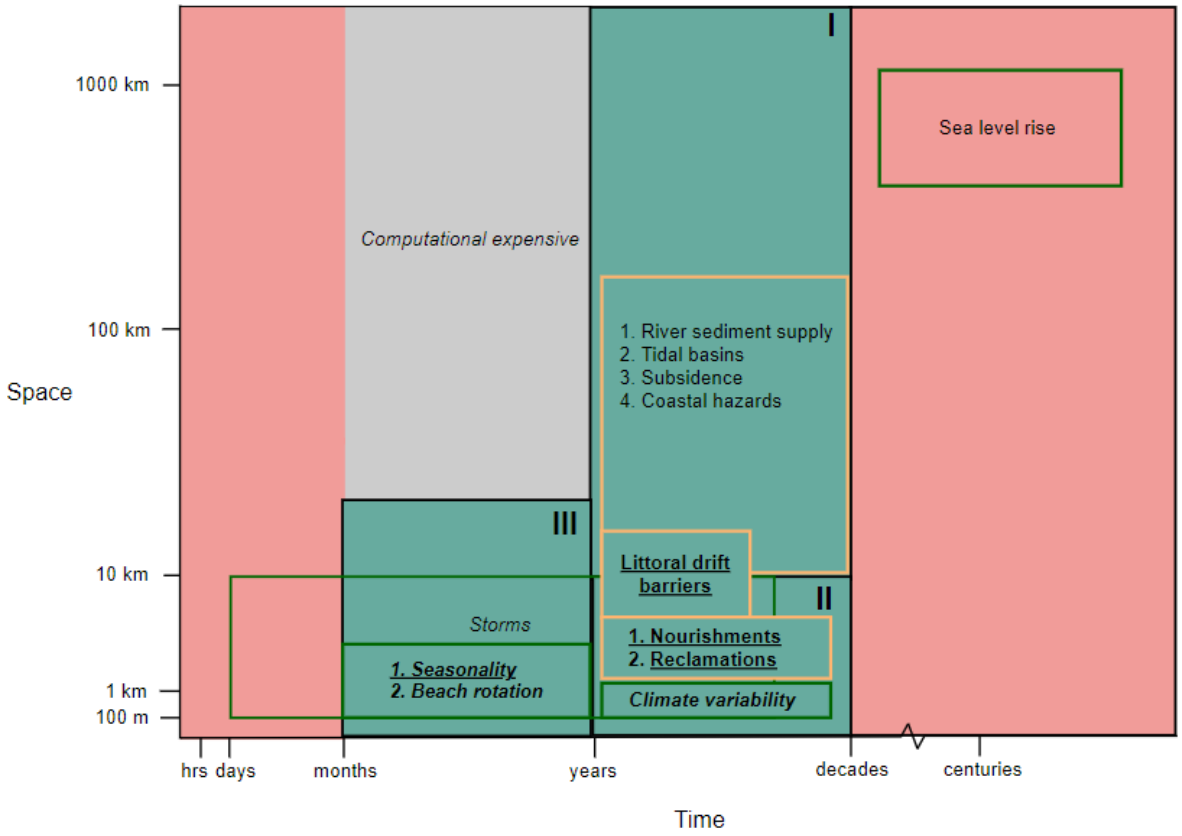

Figure 2.32: Drivers of sandy shoreline evolution with their spatial and temporal scales. The green and orange boxes indicate whether the driver is a natural or anthropogenic respectively. Furthermore, the green (red) background indicates whether the current SDS algorithm is able to detect (in a computational efficent way) the shoreline position at the corresponding spatiotemporal resolution according to Wang (2018). The drivers considered in this research are indicated with bold text. Furthermore, secondary drivers are indicated with italic text. Combinations of temporal scales and spatial scales are divided in the areas I, II and III which correspond respectively to large, moderate and small scale drivers.

Besides classifying drivers as caused by natural or anthropogenic influences, a distinction can be made between primary drivers and secondary drivers. Primary drivers have major structural effects on shoreline development, while secondary drivers do not lead to long-term changes in the coastal system. This means that hotspots can only be formed as a result of a primary driver. Figure 2.32 gives an overview of all the drivers of shoreline evolution together with their classifications and spatiotemporal scales. As mentioned in Section 2.1.4, information of shoreline variability with a temporal scale below the composite window is lost to some extent. Therefore, inter-annual variability (region III) should be studied with a composite window below 360 days.

Sea level rise is in this study ignored as a driver of shoreline evolution. The reason is that it can not yet be identified from SDS as shoreline changes due to SLR over the period 1984-2016 are within natural shoreline variability (Wang, 2018). In the future, when the temporal coverage of satellites increase, SDS might be useful to identify shoreline changes due to SLR.

This study will focus on the hotspots which were identified by Kras (2019) with rolling means of 2.5 kilometer. 95% of these hotspots have a spatial extent below 10 kilometer making them suited to study drivers with small to moderate spatial scales (region II and III).

The only driver that does not fall strictly within either region III or II are storms. As explained in Section 2.2.1, storms are characterized by a sudden shoreline change followed by a more slow process in which the beach returns to its original state. The initial response to the shoreline falls within region III, while the recovery of the beach, which can take up to several years, belongs to region II. Furthermore, studying shoreline variation

due to storms is difficult when the survey (satellite image) is taken a long time after the event, especially if beach recovery is rapid (Wang, 2018; Masselink et al., 2015). Therefore, storms will be disregarded in this study. Table 2.1 lists the remaining small to moderate scale drivers. Beach rotation and climate variability will only be treated in Section 4, where results are presented for several local case studies.

Driver	Chapter 4	Chapter 5	Chapter 6	Classification
Seasonality	X	X	X	Secondary natural
Beach rotation	X			Secondary natural
Climate variability	X			Secondary natural
Reclamations	X	X	X	Primary anthropogenic
Nourishments	X	X	X	Primary anthropogenic
Littoral drift barriers	X	X	X	Primary anthropogenic

Table 2.1: Overview of in which sections the drivers are treated. An X indicates that the driver is handled in a particular chapter.

2.3. Summary: background information

Satellite derived shorelines

The Shoreline Monitor is a dataset that identifies on a global scale, with a 500-m spaced transect system, sandy beaches and annual shoreline positions over the period 1984-2016. The shoreline position is known as the boundary between water and land. Through a series of procedures, this position can be determined from a satellite image. A Satellite Derived Shoreline (SDS) vector is derived from a satellite image as the outer edge of the pixels identified as land (Hagenaars et al., 2018). In stead of using single satellite images, composite windows can be used to identify the SDS. The technique of composing windows creates a single image from a sequence of individual images. The use of composite windows increases the accuracy to below sub-pixel precision (<15 meter for Landsat) while shoreline variability within the length of this time window is lost to some extent. Composite windows should not be confused with the temporal resolution of the SDS. A composite window of 360 days does not correspond to annual shoreline positions, but a yearly averaged shoreline position for a certain moment in time. Finally, the shoreline position is defined as the distance between the transect center (origin) and the intersection point of the SDS.

Hotspots

Using the Shoreline Monitor dataset, Kras (2019) developed an algorithm that identifies hotspots; coastal stretches with high variability containing ajdacent transects with similar characteristics both in time and space. Using a moving window of 2.5 kilometer, for each transect a moving average linear change rate is calculated, referred to as the rolling mean. The rolling mean is based on the summation of the changerates of all transects closest to a window, divided by the total summed length between these transects. Using these rolling means, the tops and bottoms are identified. A top (bottom) is a transect with a rolling mean higher (lower) than both its adjacent transects. A hotspot is defined as all transects between two bottoms. The top-bottom approach resulted in 3033 prograding and 2121 retreating hotspots. The prograding and retreating hotspots combined incorporate approximately 224 thousand transects, or 22 thousand kilometer of shoreline. This indicates that somewhat less than 22% of the transects formed a hotspot. Of all these hotspots, 95% has a length below 10 kilometer.

Drivers of shoreline evolution

The study's focus was determined by the relatively small spatial extent of the hotspots, which allowed for the analysis of drivers at small to moderate spatial scales. Shoreline evolution can be caused by natural processes or by anthropogenic (human) interventions. Besides classifying drivers as caused by natural or anthropogenic influences, a distinction can be made between primary and secondary drivers. Primary drivers have major structural effects on shoreline development, while secondary drivers do not lead to long-term changes in the coastal system. This means that hotspots can only be formed as a result of a primary driver. Below drivers with small to moderate spatial scales are shortly treated.

Seasonality	In winter, energetic waves move sediment into the surf zone, creating a narrow beach. In summer, in response to milder wave conditions, the sediment moves back to shore and eventually attaches to the beach resulting in a wider beach again (Bosboom and Stive, 2012).	Natural secondary
Climate variability	When aspects of climate such as temperature, precipitation or wind speeds differ from an average, one speaks of climate variability. The best known globally climate variations are the El-Niño-Southern Oscillation (ENSO) and the North Atlantic Oscillation (NAO). These patterns can result in seasonally elevated water levels, higher wave energy and changes in wave direction with severe erosion as a consequence	Natural secondary

2.3. Summary: background information

Beach rotation	Lateral movement of sand along the beach in response to a modification in the indicident wave direction which is observed in embayed beaches (A. D. Short et al., 2001).	Natural secondary
Reclamations	Land reclamation is the process of creating new land. For the construction of a reclamation first a vertical or mound sea dyke is build after which the inner zone is filled with sand (Stauber et al., 2016)	Anthropogenic primary
Nourishments	This is the art of placing sand in the coastal zone to maintain the sediment volume in the littoral system (Wesenbeeck et al., 2012). It is a measure to stabilize the shoreline and counter erosion. Nourishments are not a long-term solution to beach erosion as waves, storms and high water levels keep eroding the sediment alongshore and offshore.	Anthropogenic primary
Littoral drift barriers	This driver blocks the migration of material along the shore. Think of a groyne or a breakwater. This might result in sand accumulation at one side of the barrier while erosion occurs at the other side due to a deficit of sediment supply.	Anthropogenic primary

Climate variability and beach rotation are only explored locally, which is treated in Chapter 4. For the remaining drivers identification is also performed on a regional and global scale in Chapters 5 and 6 respectively.

3

Methodology

The objective of this research is to identify drivers with small to moderate spatial scales (region II and III in Figure 2.32) of dynamic sandy beach evolution using satellite derived shorelines. Chapter 2 provided background information on the SDS and the drivers of shoreline evolution. This section will elaborate on various existing and newly developed methods used to achieve the objective of this study. First, the pre-processing and generation of SDS is covered. Hereafter, methods used to identify the small to moderate scale drivers will be treated. This latter part will first explain how time series of SDS can be decomposed. Second, it will demonstrate methods that can be used to arrive at parameters that characterize a particular driver for shoreline change. Thirdly, a method and some metrics that are commonly used in predication and classification studies are explained. Finally, a method that can be used to identify regions that show similar behavior, spatial autocorrelations, is treated. To conclude, a summary of this chapter is provided in Section 3.5.

3.1. Data preparation

Before divers can be analyzed from time series, the SDS data must be generated and preprocessed. For this purpose a Python module was created. Information about this module can be found in Section 3.1.1. Further pre-processing of the data is needed as due to several environmental conditions, sensor corrections and satellite coverage (see Section 2.1.4), gaps in the data can arise. Section 3.1.2 will provide a method on how missing values in the time series are handled.

Key points

- A module is created that can be used to automatically generate satellite shorelines from a certain area of interest.
- A method is developed that fills missing values in the SDS time series.

3.1.1. SDS generation

Hagenaars et al. (2018) developed an algorithm that generates shoreline positions from satellite images, see Section 2.1.4. This algorithm consists of four steps. The current way of generating SDS is divided into four scripts, each of which separately executes one of the steps of the algorithm. To speed up the process, a module was built which runs these steps automatically. The four steps and their input are described below:

1. Find searchbox
   (a) Input:
      i. Coordinates of the area of interest (AOI).
   (b) Action: to speed up computations, the world is divided into boxes (see Appendix A.1.1). Therefore, in this step, searchboxes that contain or intersects with the AOI are identified.
   (c) Output: searchbox(es) in which the AOI falls.
2. Generate SDS

(a) Input:

i. Output from step 1

ii. Composite window: since inter-annual variability will be studied, a composite window smaller than one year should be chosen. A smaller composite window will result in more variability being captured, but contains less images and might therefore be less accurate (see Appendix A.2). In this study, composite windows of 180, 90 and 45 days will be examined to determine which window can best be used to identify small to moderate scale drivers.

iii. Cloud cover limit: this parameter determines the maximum percentage of cloud cover that a satellite image may have to be included in the composite image. A lower limit means better, but fewer images (since images above this limit are ignored).

iv. Satellite missions: images from Landsat 5, 7 and 8 or Sentinel 2 can be used to generate the SDS. Sentinel 2 has a different resolution than the Landsat images. The method does not yet allow images with different resolutions in a composite window. Therefore, Sentintel 2 is not considered. On 31 May 2003, the Scan Line Correcter (SLC) in the ETM+ instrument of Landsat 7 failed. SLC compensated for the forward motion of the spacecraft so that resulting scans are aligned parallel. The failure of the SLC has as a result that 22% of the data of Landsat can not be used (Scaramuzza and Barsi, 2005). Therefore, excluding Landsat 7 might result in better, but less images.

v. Temporal resolution: as inter-annual shoreline evolution is studied, monthly shoreline positions are generated.

vi. Period: this research will study the period from January 1984 up to July 2021.

(b) Action: methods described in Section 2.1.4 are used to generate SDS for the entire coastline that fall within the searchbox(es).

(c) Output: files containing geometries of the satellite derived shorelines at all timesteps (determined by the temporal resolution) within the study period.

3. Merge shorelines

(a) Input:

i. Output from step 2

(b) Action: merge all independent SDS files into one file containing all geometries.

(c) Output: a file containing all SDS

4. Find intersections

(a) Input

i. Output from step 3

ii. A transect system: a shoreline position is defined as the intersection of the transect with the SDS, compared to the origin of the transect, see Section 2.1.2 and 2.1.4. Similar to Luijendijk et al. (2018) a 500 meter spaced transect system is chosen in which the transects extend 1000 meter land- and seaward.

(b) Action: shoreline positions are estimated for all transects falling within the AOI. Outliers are identified and removed from the dataset. See Appendix B.1.1 for a brief explanation of how outliers are identified.

(c) Output: time series of shoreline positions.

The starting point of this module is an area of interest. Since this study focuses on dynamic sandy beaches, the coastal stretches identified by Kras (2019) with a rolling mean of 2.5 km will be the input for the module described above. For all 5154 locations, monthly shoreline positions are then automatically generated.

3.1.2. Missing values

As described in the previous section, outliers are removed from the time series, creating gaps in the data. Furthermore, missing values can also result from poor satellite coverage. Figure 3.1 illustrates step by step how missing values are filled.

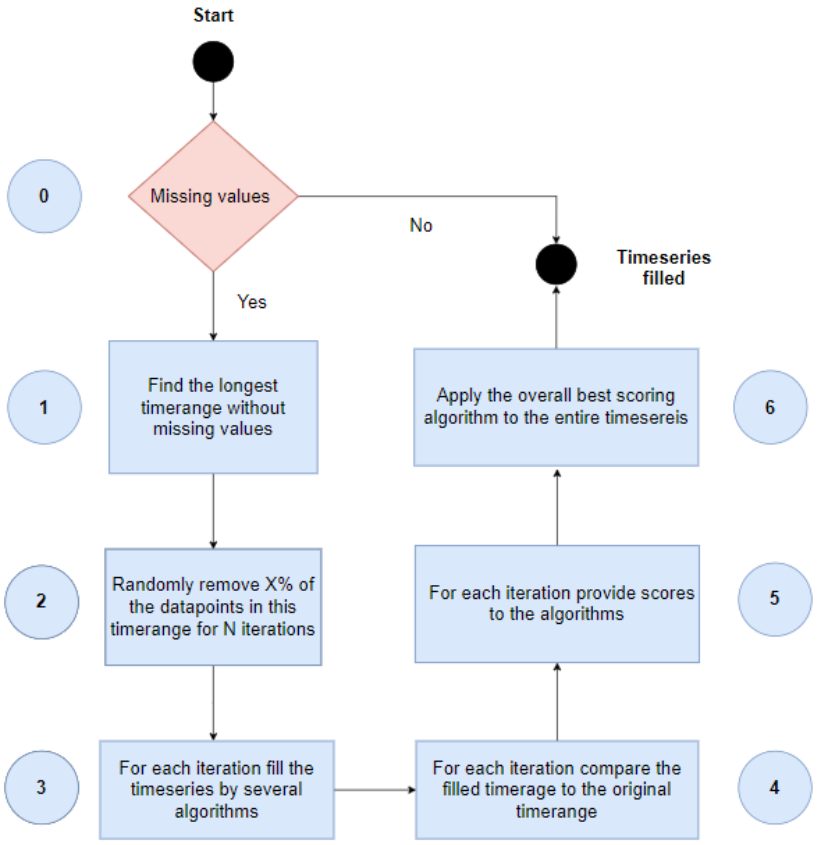

Figure 3.1: Visualization of the steps used in the developed algorithm to fill missing SDS positions. The steps are numbered 1-6 and indicated in the green blue with the descriptions in the blue boxes. The start and the end of the algorithm are indicated with black circles. The algorithm is only entered when there are missing values (red triangular box).

Below, the steps from Figure 3.1 are explained in more detail.

- Step 0: identify whether the time series contains missing values.

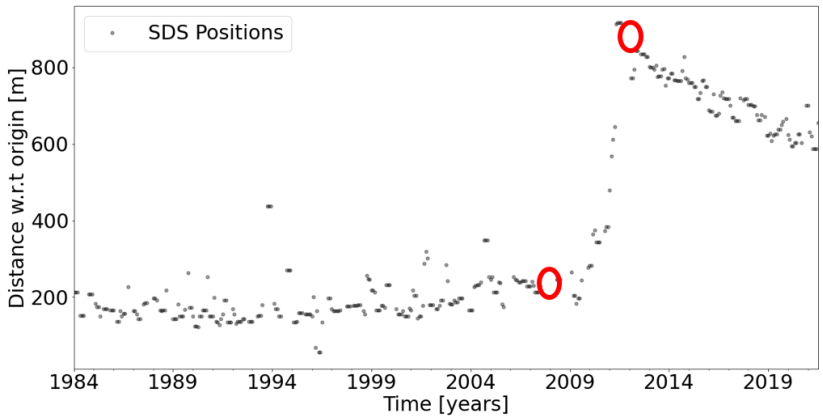

Figure 3.2: SDS positions of a transect at the Sand Engine (The Netherlands). Periods in time with missing values are indicated with red circles.

- Step 1: Find the longest timerange (T) without missing values.

- Step 2: Randomly remove X% of the datapoints within T. X corresponds to the percentage of missing values in the entire time series. This is done 100 times, generating samples of the timeranges with missing values at different timesteps. Figure 3.5 shows two samples with artificially removed shoreline positions.

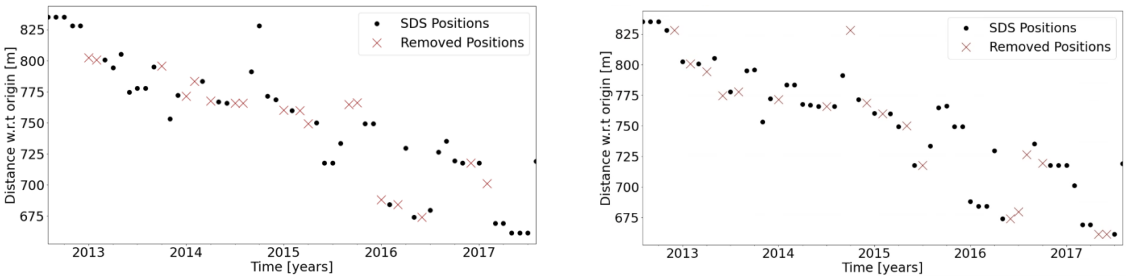

(a) Iteration i

(b) Iteration i+1

Figure 3.3: Visualization of examples of two iterations in which data is removed from the timerange.

- Step 3: For each iteration fill the time series by filling algorithms. The applied algorithms are summarized in Table B.1. Examples of how algorithms fill missing values is shown in Figure 3.4.

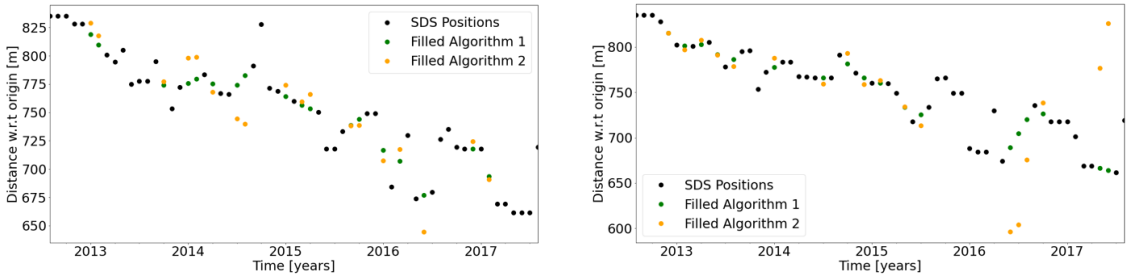

(a) Iteration i

(b) Iteration i+1

Figure 3.4: Visualization of examples of two iterations in which artificially removed data is filled by algorithms.

- Step 4: For each iteration compare the filled positions to the original positions using the coefficient of determination (R^2):

$$R^2 = 1 - \frac{\sum(y_i - a_i)^2}{\sum(y_i - \bar{y})^2} \tag{3.1}$$

where y_i : original value. Indicated in Figure 3.5 with a red cross.
a_i : predicted value with a certain algorithm. Indicated in Figure 3.5 with a coloured marker.
$\bar{y}$: mean of the original values

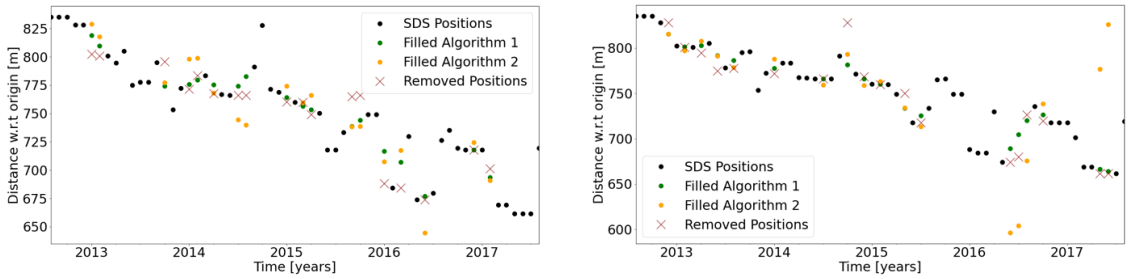

(a) Iteration i

(b) Iteration i+1

Figure 3.5: Visualization of examples of two iterations in which removed and filled data is compared.

- Step 5: Assign scores to the algorithms for each iteration. The algorithms are sorted by their R^2. The algorithm with the highest R^2 gets 4 points, the second best algorithm gets 3 points, etc. Awarded scores can not be negative. The overall performability of an algorithm is defined as the sum of the scores over the 100 iterations.
- Step 6: Finally, the overall best scoring algorithm is applied to the entire time series, see Figure 3.6.

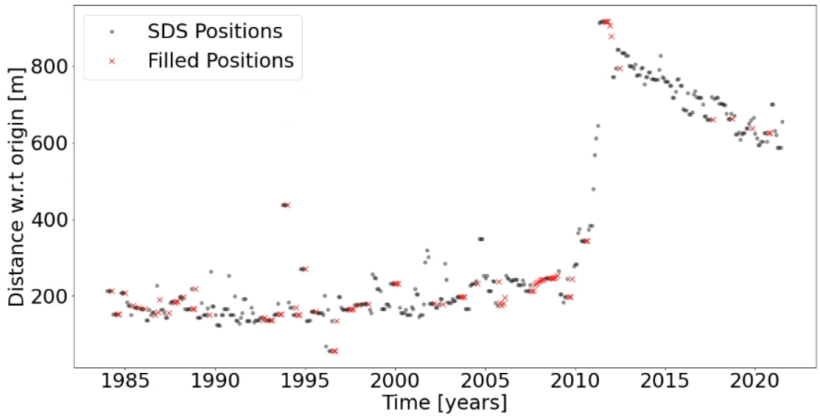

Figure 3.6: SDS positions of a transect at the Sand Engine (The Netherlands) without missing values. Red crosses indicate the positions that are filled using the overall best scoring algorithm.

3.2. Methods for identifying drivers

This section will elaborate on the methods used to identify drivers of shoreline evolution. First, fundamental methods used to decompose time signals are discussed. These methods form the basis for the identification of the drivers. Second, the methods used to identify the drivers are treated.

Key points

- Methods are presented that can be used to decompose time series into several components.
- Procedures to extract parameters from decomposed SDS time series are developed. These parameters can be used to link drivers to SDS time series.

3.2.1. Time series decomposition

Time series decompositions are used to deconstruct time series into several components (Cleveland et al., 1990). There are two principal types of decompositions. The first type is a decomposition based on rates of changes. This results in a decomposition of a trend, a seasonal component and noise. The other decomposition type is based on the idea of decomposing a time series into deterministic and non-deterministic components (Dodge et al., 2006). Below for each decomposition type, one method will be covered. Finally, the fast Fourier transform will be shortly discussed.

Seasonal-Trend decomposition with LOESS

Seasonal-Trend decomposition with LOESS (STL) is a procedure that decomposes a seasonal time series into three individual components: a trend, a seasonal and a remainder (Cleveland et al., 1990). This is thus based on the principal fundament of rates of changes. In equation-form the decomposition looks as following:

$$Y = T + S + R \tag{3.2}$$

where Y : the data
T : the trend components
S : the seasonal component
R : the remainder

In the case of Equation 3.2 the three components are summed. The decomposition is then categorized as an additive decomposition. Another form is the multiplicative decomposition:

$$Y = T \cdot S \cdot R \tag{3.3}$$

This can be used when seasonal variability changes over time. The difference between an additive and multiplicative decomposition is emphasized in Figure B.3. Figure B.4 shows an example of an additive STL decomposition from daily CO_2 concentrations.
STL has a range of advantages compared to other decomposition methods such as the classical X-11 decompositions. Compared to classical decompositions methods, STL can, except for quarterly and monthly data, also handle other seasonality types. Besides that, rates of changes of seasonality and trend smoothing can be controlled by the user. Another advantage of STL is that trend and seasonal components are not distorted by aberrant behavior in the data. Finally, due to its simplicity, the method allows for fast computation, even for long time series and large amounts of trend and seasonal smoothing (Cleveland et al., 1990).

LOESS

LOESS stands for locally weighted running line smoother. Its purpose is to recover an inherent signal from a noisy signal. The LOESS smoothening is estimated by using known neighbouring values, similar to a K-Nearest Neighbour (KNN) algorithm. In a KNN, the smoothness of the result is determined by the size of the window (k) and thus the amount of datapoints included. A larger window will result in more datapoints and more smoothening of local behavior (Cleveland and Devlin, 1988).
The following steps explain LOESS smoothing according to the method of Cleveland and Devlin (1988):

1. Find the k nearest neighbours of a datapoint x'
2. Convert the set of distances (D) into an ordered set containting weights (W). Distance weights are calculated according to a tri-cubic function:

$$w(x) = \begin{cases} (1 - |\frac{d(x,x')}{max_i d(x_i,x')}|^3)^3, & \text{if } |x| < 1 \\ 0, & |x| \geq 1 \end{cases}$$

where $d(x_i, x')$: distance between x, one of the k nearest neighbors, and x'

Neighbors at a maximum distance will have a weight of zero, whereas points at zero distance will have a weight of one.

3. Next, for every point x', the LOESS algorithm sets up a linear regression model that calculates the corresponding output y'. This calculation is based on the k nearest neighbours of x' and the distance weights. The linear regression has the form:

$$\beta = (X^T W X)^- 1 X^T W Y \tag{3.4}$$

where β : a vector of linear parameters
X : the matrix containing all x observations
W : the distance weight matrix
Y : a vector containing the predicted values

The STL procedure

STL is build out of two recursive procedures, an inner loop nested inside an outer loop. Each entire run of the inner loop consists of n_i passes, and in each of the passes the seasonal and trend components are updated once. Each pass of the outer loop consists of the inner loop followed by a computation of robustness weights. These weights are used in the next run of the inner loop to reduce the influence of transient, aberrant behaviour of the trend and seasonal components (Cleveland et al., 1990). The number of observations in each period, or cycle, of the seasonal component is $n_{(p)}$. For monthly series with $n_{(p)} = 12$, the first subseries is the January values, the second the February values, and so forth.
Each inner loop run consists of a six step update. In step 2-4 seasonal smoothing updates the seasonal component. In step 6 a trend smoothing that updates the trend component is done (Cleveland et al., 1990).

1. Detrending. A detrended series, Y_v - T_v^k, is computed.
2. Cycle-subseries smoothing. Each cycle-subseries of the detrended series is smoothed by LOESS. The collection of smoothed values for all of the cycle-subseries is a temporary seasonal series, C_v^{k+1}. consisting of $N=1 + 2n_{(p)}$ values that range from $v = - n_{(p)} + 1$ to $N + n_{(p)}$.
3. Low-pass filtering of smoothed cycle-subseries. A low-pass filter is applied to C_v^{k+1}.
4. Detrending of smoothed cycle subseries. The seasonal component from (k+1)st loop is $S_v^{k+1} = C_v^{k+1} - L_v^{k+1}$ for v=1 to N. L_v^{k+1} is subtracted to prevent low-frequency power from entering the seasonal component.
5. Deseasonalizing. A deseasonalized series Y_v-S_v^{k+1} is computed.
6. Trend smoothing. The deseasonalized series is smoothed by LOESS.

The remainder is:

$$R_v = Y_v - T_v - S_v$$

The outer loop investigates the extremeness of an outlier. Data with a very large $|R_v|$ will have a small robustness weight. The inner loop is now repeated but the distance weight in the smoothing, see Equation 3.4, is multiplied by the robustness weight (Cleveland et al., 1990).

Choosing the STL parameters

STL has 6 parameters:

1. $n_{(p)}$ = the number of observations in each cycle of the seasonal component. For yearly periodicity, $n_{(p)}$ = 12 for the monthly data and $n_{(p)}$ = 365 for daily data.
2. $n_{(i)}$ = the number of passes through the inner loop. In many cases, $n_{(i)}$ = 1 or 2 is sufficient
3. $n_{(o)}$ = the number of robustness iteration of the outer loop. A value of $n_{(o)}$ = 5 is already a very safe value.
4. $n_{(l)}$ = the smoothing parameter for the low-pass filter. $n_{(l)}$ should be equal to the least odd integer greater than or equal to $n_{(p)}$ ($n_{(l)}$ = 365 for the daily data and $n_{(l)}$ = 13 for the monthly data).
5. $n_{(t)}$ = the smoothing parameter for the trend component. $n_{(t)}$ ranges from about $1.5n_{(p)}$ to $2n_{(p)}$.
6. $n_{(s)}$ = the smoothing parameter for the seasonal component. this parameter determines the extent to which seasonal component varies from year to year. The choice depends critically on the characteristics of the series. A diagnostic graphical analysis can help in the choice of $n_{(s)}$, see Figure 3.7. According to Cleveland et al. (1990) $n_{(s)}$ should be at least 7 and odd.

From these parameters choosing the first five is straightforward. The last parameter, $n_{(s)}$, however, must be carefully tailored to each application. As mentioned, creating seasonal-diagnostic plots might help in doing so. A seasonal diagnostic (SD) plot is created using the following steps:

- calculate the mean of the seasonal component for each period ($\bar{s_k}$).
- Plot a line representing the seasonal values for the k-th month minus $\bar{s_k}$
- Plot circles representing the values of the k-th month plus the remainder minus ($\bar{s_k}$

Figure 3.7 shows an example of two seasonal diagnostic plots of the same period. The right image has a smaller seasonal smoothing parameter and thus captures more of the noise of the data. As the only reason for choice for the seasonal smoothing parameter would be to remove noise, the most optimal value would go to infinity. However, in the case of an evolving seasonal component this evolution would not be captured in the seasonality.

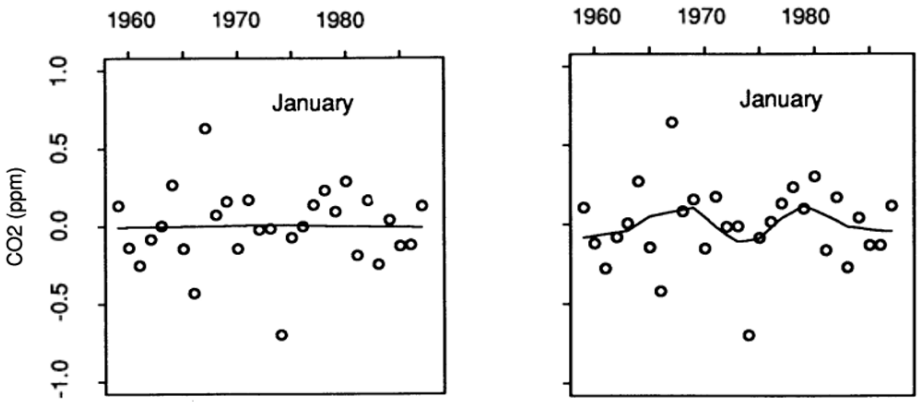

Figure 3.7: Seasonal diagnostic plots for the month January with different seasonal smoothing parameters. Smoothing is done on the data illustrated in Figure B.4. The left image shows a SD plot with a smoothing parameter of 35. The right SD plot is based on a decomposition with a seasonal smoothing parameter of 11. (Source: Cleveland et al., 1990)

The Python statsmodels package[1] provides a function for seasonal-trend decomposition using LOESS. Although, Cleveland et al. (1990) developed STL to be able to handle missing values, the statsmodels package requires complete time series. Therefore, a method to fill missing values was developed, see Section 3.1.2.

[1] www.statsmodels.org

Empirical Mode Decomposition

This method can be used to analyze non-stationary signals coming from non-linear systems. The Empirical Mode Decomposition (EMD), decomposes a signal in fast and slow oscillations. The final result is a decomposition into amplitude and frequency modulated functions and a monotonic trend (Huang et al., 1998; Colominas et al., 2014). This method is computational quite intensive, making it unsuited for a global analysis (see Figure B.5). Besides that, not all drivers are characterized by either a monotonic trend or oscillation. These two reasons make that the EMD is not suited for this study.

The Fast Fourier Transform

Fourier et al. (1822) discovered that any real world waveform can be reproduced by summing several sinusoidal waveforms. A mathematical process that converts these waveforms into individual sine components on the frequency domain, is the Fast Fourier Transform (FFT). Figure 3.8 visualizes how a complex signal is transformed by the FFT. The FFT is a computational optimized variant to the discrete Fourier transform (DFT). A discrete Fourier transform, tests the time domain waveform for discrete, or individual, frequencies based on the length of the signal (N). The computational effort is proportional to N^2 (Oshana, 2006). The DFT can be defined as:

$$F(k) = \frac{1}{\sqrt{N}} \sum_{n-0}^{N-1} e^{-j2\pi kn/N} \quad \text{where, n = 0, 1, 2, ... N-1} \tag{3.5}$$

The FFT, optimizes the DFT by the fact that to compute the Fourier transform, many of the exact same multiplications are repeated. The FFT eliminates almost all of these redundant calculations. This reduces the computational effort from N^2 to $N \cdot \log_2(N)$, outperforming the DFT by $N/\log_2(n)$ (Oshana, 2006).

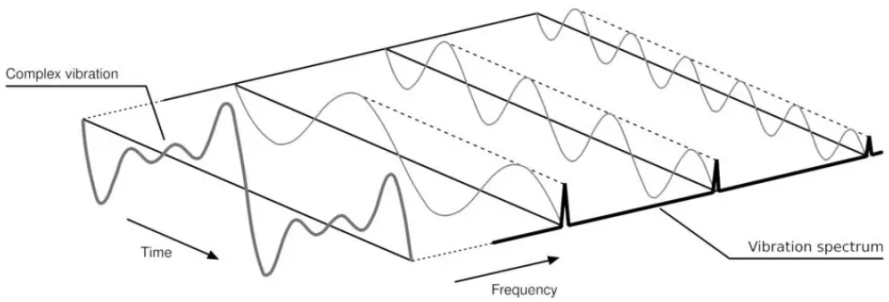

Figure 3.8: A complex signal expressed in both the time and frequency domains. (Source: Power-MI)

3.2.2. Identification methods

In this section, per individual drivers, the methods used for identification are treated. The decomposition methods from Section 3.2.1 are applied to distinguish different signals.
Figure 3.9 gives an overview with geographical locations of case studies that are used to develop these methods. Cases are used either for initial development or testing. From the identifications methods two types of parameters arise:

1. Identification parameters: used to identify a driver.
2. Informative parameters: provide extra information about (the behaviour) of a potentially identified driver.

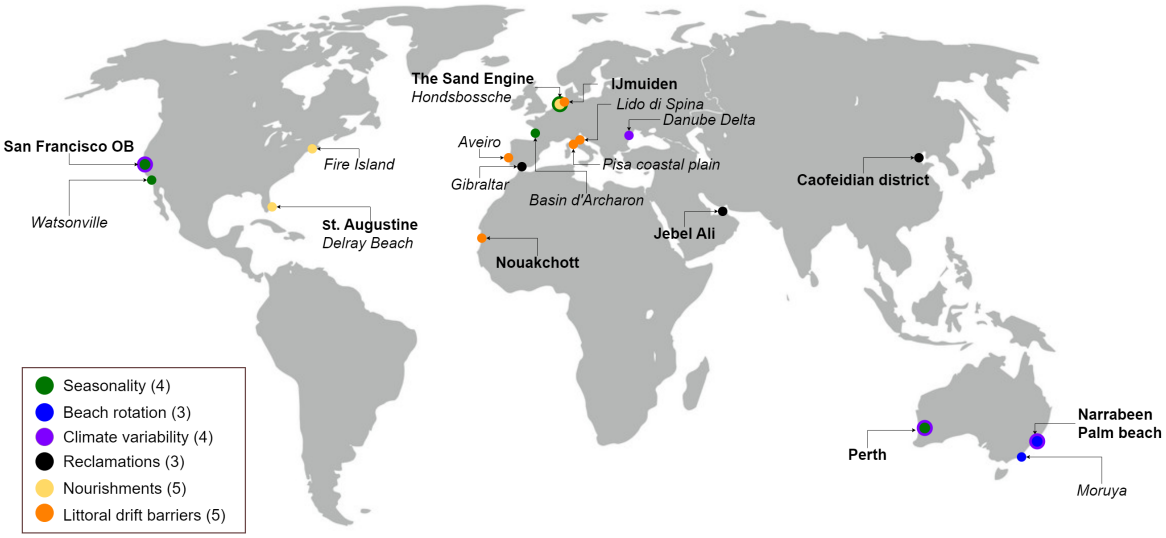

Figure 3.9: Overview of all case studies which where used to develop the methods to identify small to moderate drivers. Locations on which the methods are based are indicated in bold. Case studies used to test the method are shown in italic. Colors of the circles correspond to the driver that is verified/tested at this location. Multiple colors indicate multiple drivers. The number between brackets in the legend indicate the number of case studies used to develop a method.

Seasonality

This method for determining seasonal beach behavior was developed on three case studies and later tested on two other. These cases can be found in Figure 3.9 and are also listed in Table 3.1. For the development cases, seasonal-diagnostic plots are created to chose a value for the STL seasonal smoother ($n_{(s)}$). In the case of seasonal beach behaviour, evolution/changes in amplitudes can be allocated to climate variability (or even climate change on a longer time horizon) which is a different driver of shoreline evolution. Therefore, to separate climate variability from seasonality, a large value for $n_{(s)}$ is desired, resulting in constant seasonal amplitudes.
To identify seasonal beach behaviour, the seasonal component of STL is analyzed. As explained in Section 2.2.1, seasonality does not result in permanent changes in the shoreline position but has an oscillatory behaviour in which accretion happens during mild summer conditions and erosion because of an energetic sea climate in winter. This oscillation has thus a period of a year. Since the SDS data has a monthly frequency, the most logical choice for the STL period would be 12 months. However, since seasonality is a natural phenomenon, this period will not always be followed exactly. Therefore, outcomes based on a seasonal component of 11 and 13 months, both of which are close to a year, are also examined.

Case	Geographical location	Use
Perth North City Beach	Australia	Development
San Francisco Ocean Beach	USA	Development
The Sand Engine	The Netherlands	Development
Watsonville	USA	Test
Basin d'Archaron	France	Test

Table 3.1: Case studies used to create a method able to identify seaonal beach behaviour

From Februray 11th 2013, Landsat 5 was replaced by Landsat 8. The latter introduced a new Operational Land Images (OLI) sensor with a high spectral resolution and improved signal-to-noise ratio. This resulted in a improved image quality compared to Landsat 5 (and Landsat 7 as well) (Acharya et al., 2016). Since seasonality does not require the entire time horizon, the focus is on the period after February 2013, as image quality has improved since then. On average, based on data from almost 5000 transects, the average amount of missing values after Febrauray 2013 decreases with 8% compared to the entire time series, see Figure B.6.

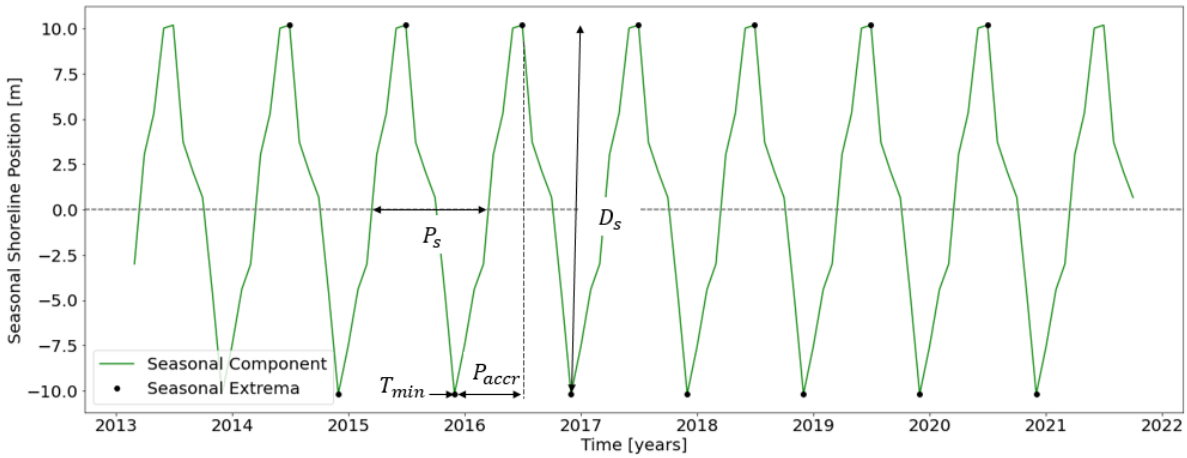

Figure 3.10: Seasonal beach oscillation derived from STL. The characterizing and informative parameters are indicated with arrows.

The following parameters are used to identify seasonality:

1. P_S: period of the seasonal component, should be more or less equal to one year.
2. D_S: seasonal displacement. As reported by Hagenaars et al. (2018), the accuracy of composite Landsat images is below 15 meters. Therefore, for reliable identification of seasonal beaches, the displacement of the oscillation should be at least 15 meters. The seasonal displacement is also a driver-characterizing parameter as it captures the magnitude of the seasonal component.

Parameters proving extra information about seasonal beach behaviour are:

1. T_{min}: the month in which the minimum shoreline position occurs.
2. P_{accr}: number of months to go from minimum shoreline position to a maximum.

Climate variability

To indicate the presence of climate variability, a fast-fourier transform is applied to the STL trend. As indicated in Section 2.2.1, ENSO has a fluctuation around 2 - 7 years. Therefore FFT peak periods in this interval might indicate El Niño and la Niña impacting shoreline variability. The method was developed on the San Francisco OB case and tested on three other cases.
A parameter used to describe the power of the peaks in the interval of 2 - 7 years, and thus the presence of ENSO, is:

Case	Geographical location	Use
San Francisco OB	USA	Development
Narrabeen	Australia	Test
Perth	Australia	Test
Danube	Romania	Test

Table 3.2: Case studies used to create a method able to identify beach rotation

- M_{ENSO}: the mean power in the interval of 2 to 7 years divided by the mean power in the remaining FFT periods. See also Equation 3.2.2 and Figure 3.11.

$$M_{ENSO} = \frac{\bar{P}_{2,7}}{\hat{P}}$$

where $\bar{P}_{2,7}$: mean power in the interval 2 to 7 years ($T_{2,7}$)
$\hat{P}$: mean power in FFT periods outside the interval 2 to 7 years

Peak periods correspond to other periods might indicate the presence of a different source of climate variability (such as the NAO).

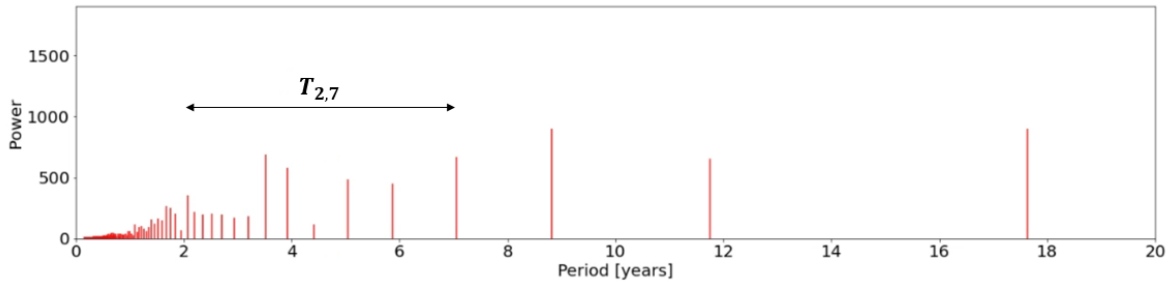

Figure 3.11: Example of a Fast-Fourier Transform with the interval corresponding to the ENSO fluctuation indicated ($T_{2,7}$.

Beach Rotation

Figure 2.2.1 shows that shoreline development of transects on the same side of the pivot are positively correlated. The figure also indicates a negative correlation between the shoreline development of transects on opposing sides of the pivot point. Therefore, to determine beach rotation, the correlation between the shoreline positions of the two outer transects in the bay are compared with those of the other transects. In the case of a rotating beach, a positive correlation is expected for neighboring transects, which decreases with distance and eventually becomes negative. This method was initially developed on two pocket beaches and tested on a third site.

Case	Geographical location	Use
Narrabeen	Australia	Development
Palm beach	Australia	Development
Moruya	Australia	Test

Table 3.3: Case studies used to create a method able to identify beach rotation

Correlation between transects is estimated with the STL trend and Pearsons correlation coefficient, see Equation 3.6. A visualization of an example of this method can be found in Figure 3.12.

$$r = \frac{\sum(x_i - \bar{x})(y_i - \bar{y_i})}{\sum(x_i - \bar{x})^2(y_i - \bar{y_i})^2} \tag{3.6}$$

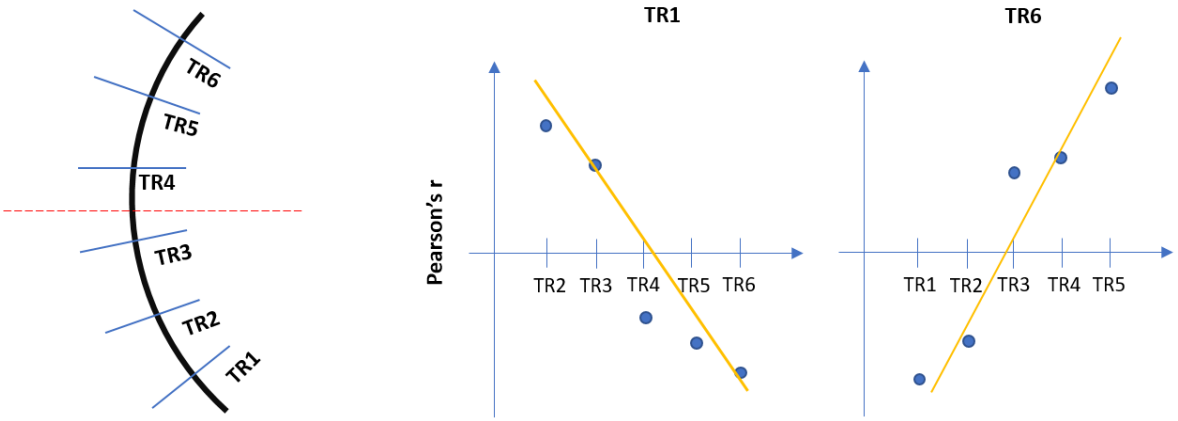

Figure 3.12: A schematization of an embayed beach subject to beach rotation. The pivot point is indicated with the red dashed line. The yellow lines in the scatter plots are FOPFs with the correlation coefficients. TR is an abbreviation for transect.

Two parameters characterize a rotating beach:

1. M_{BR}: for either one of the outer transects the correlation coefficient with the most nearest transect is divided by the correlation with the transect at the other side of the bay. From the point of view from TR1 in Figure 3.12 this is defined as:

$$M_{BR} = \frac{r_{TR1-2}}{r_{TR1-6}}$$

where r_{TR1-2} : pearson's r between TR1 and TR2
r_{TR1-6} : pearson's r between TR1 and TR6

if $M_{BR} \geq 0$: there is no beach rotation.
if $M_{BR} < 0$: there is beach rotation. The closer this value is to -1, indicating that r_{TR1-2} is 1 and r_{TR1-6} equals -1, the stronger the rotating signal is.

2. $R_{2,BR}$: the coefficient of determination between the FOPF of the correlation, the yellow line in Figure 3.12, and the correlation values.

Reclamations

Identification of a reclamation is based on the simple idea that after a coastline widening there is no shoreline variation anymore due to protection of a hard structure. Land reclamations can be identified from SDS time series as a sudden change in the shoreline position, or simply said, a shoreline jump. To clearly identify the shorelinejump consequently followed by a fixed coastline, only reclamations in the period 1987-2017 are detected. The method described in this section is generated by analyzing two case studies and tested on a third one.

Case	Geographical location	Use
Caofeidian Port	China	Development
Jebel Ali	UAE	Development
Gibraltar	UK/Spain	Test

Table 3.4: Case studies used to create a method able to identify reclamations

Section B.1.1 explains that outliers are identified by using a linear fit to the data. However, Figure 3.13 illustrates that a linear fit does not always represent the data well. Therefore, in such a case, the outlier detection

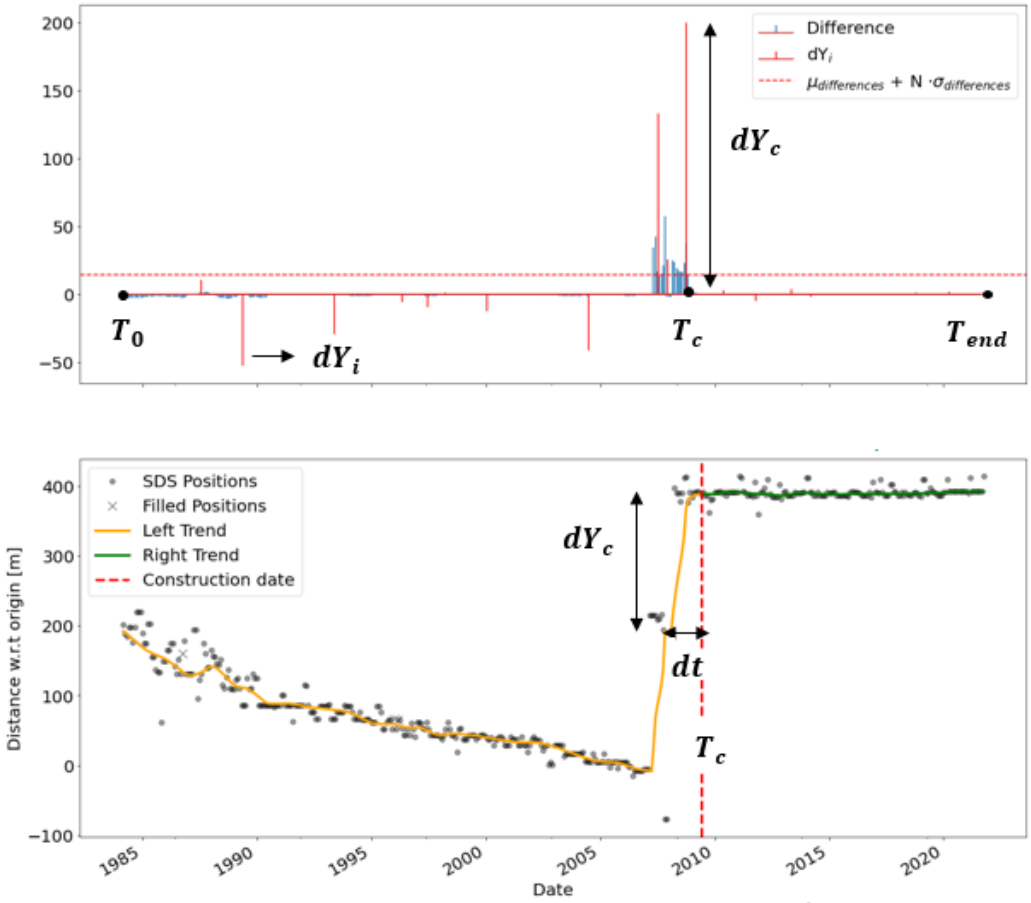

Figure 3.13: Visualization of the method used to identify reclamations. The STL trend before (after) construction is indicated in yellow (orange). Driver characterizing and informative parameters are indicated in the figure with bold letters.

method works sub-optimal. Because of this, in stead of analyzing the jumps of the individual shoreline positions, the method is based on the STL trend.
Parameters that arise from the identification method for reclamations, see Figure 3.13, are:

1. $dY_{c,dt}$: the changerate of the final shoreline jump. A Land reclamation is a sudden jump in time and is thus not characterized by shoreline positions increasing slowly over time. To arrive at $dY_{c,dt}$, the shoreline jump, dY_c, must be obtained first. This parameter is acquired with the following steps:
   (a) Calculate differences between each timestep from the STL trend
   (b) Identify the timesteps where these difference have a change in sign, so from negative to positive or the other way around.
   (c) The differences between these sign-changing timesteps are summed. These summed values are indicated with dY_i in Figure 3.13.
   (d) A shoreline jump is defined as a summed difference larger than the mean of these summed values plus N times their standard deviation (dashed line in Figure 3.13). Values for N equal to 1, 2 and 3 will be applied to the case studies to see which N best identifies reclamations.

   Then:

$$dY_{c,dt} = \frac{dY_c}{dt}$$

   where dt: duration of the shoreline jump

2. M_{RM}: shoreline evolution after construction compared to shoreline evolution up to and including construction.

$$M_{RM} = \frac{\sum_{t=T_0}^{t=T_c} dY_i}{\sum_{t>Tc}^{t=T_{end}} dY_i}$$

There are two informative parameters resulting from the identification method:

1. T_c: date at which the construction was completed. Defined as the timestep at which the shoreline jump (construction) ends.

2. dY_c: alongshore length of reclaimed land. Should be larger than 15 meters, the accuracy of Landsat.

Nourishments

As explained in Section 2.2.2, a nourishment is feeding sand to a beach system to maintain the shoreline. Nourishments are not a long-term solution to beach erosion as waves, storms and high water levels keep transporting and eroding the sediment. Time series will have the shape of a saw-tooth which shows the repetitive behaviour of sediment supplied to the system, a shoreline jump, followed by erosion. The Netherlands and the USA are countries which intensively protect their beaches by nourishments (Climate-ADAPT, 2015). Several sites located in these countries will be used to either develop or test this identification method, see Table 3.5 for an overview.

Case	Geographical location	Use
St. Augustine	USA	Development
The Sand Engine	The Netherlands	Development
Delray Beach	USA	Test
Hondsbossche	The Netherlands	Test
Fire Island	USA	Test

Table 3.5: Case studies used to create a method able to identify nourishments as a driver of shoreline evolution

Similar to reclamations, outliers are not optimal detected by a linear regression method for a shoreline subject to beach nourishments. Therefore, here too, the STL trend is analysed instead of individual shoreline positions, see Figure 3.14. Furthermore, to clearly identify the shorelinejump and the development of the beach after the widening, only nourishments in the period 1987-2017 are detected.
There are three parameters important for the identification of nourishments:

1. dY_c: shoreline jump. This is defined similar to the shoreline jump for reclamations. Different here is that not only the final jump but all shoreline jumps are analyzed. Values for N equal to 1, 2 and 3 will be applied to the case studies to see which N best identifies nourishments. Besides used for identification, dY_c also provides information on the length of beach widening. In the case of a beach nourishment this is a sudden increase where a shoreface nourishment is more characterized by a gradual increase. This shoreline jump should be larger than 15 meters, the accuracy of Landsat.

2. LT: lifetime. Time needed to erode the nourished sand. Defined as the time between two shoreline jumps, see also Figure 3.14.

3. E_{cr}: changerate of the trend after a shoreline jump. To distinguish from reclamations there must be a negative changerate after a shoreline jump. This changerate is estimated from the red line shown in Figure 3.14. This line corresponds to the STL-trend with an extra LOESS smoothening with a window corresponding to the lifetime of the nourishment.

4. N_T: number of transects in which a nourishment is observed. Accounts for the spatial scale of nourishments. This is based on how much transects have a construction date in the same period.

One other parameter gives information about the nourishment:

1. T_c: construction date. Defined as the timestep at which the shoreline jump ends rounded to the nearest year.

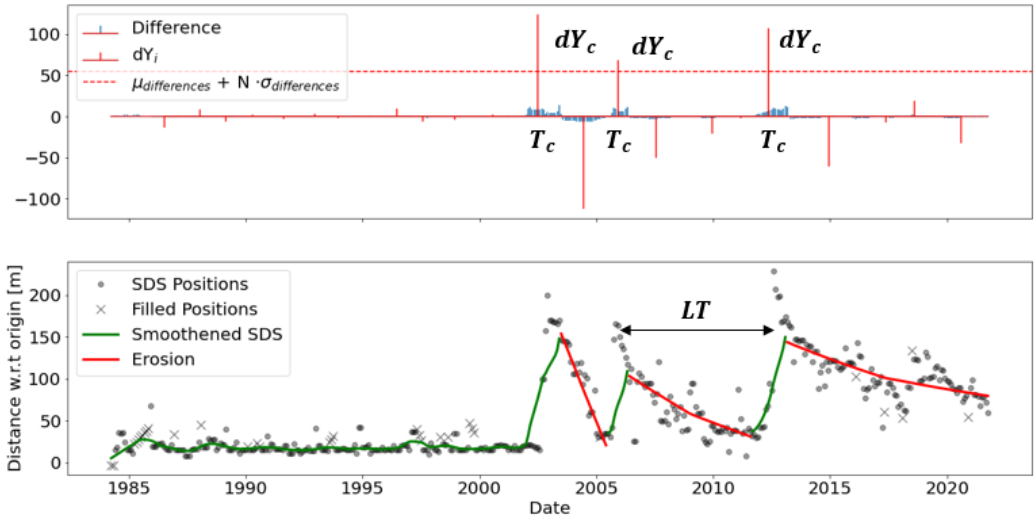

Figure 3.14: Visualization of shoreline evolution of a nourished beach. The STL trend is plotted in the lower figure in green except for the regions where erosion happens after nourishment. These erosive timeranges are indicated with a red trend. Driver characterizing and informative parameters are indicated in the figure with bold letters.

Littoral drift barriers

A typical characteristic for littoral drift barriers is large shoreline evolution near the barriers which decreases with distance. See Section 2.2.2 for more information. Therefore, for identification of LDBS, the entire coastal stretch affected by the LDB has to be identified. This is already done by Kras (2019) by extracting areas with similar (high) shoreline variability, or in other words, hotspots. For more information on the method of extraction of these hotspots, see Appendix A.1.1. A method to identify LDBs is developed on two case studies and tested on four, see Table 3.6.

Case	Geographical location	Use
Port de l'Amitie	Mauritania	Development
Port of IJmuiden	The Netherlands	Development
Pisa coastal plain	Italy	Test
Aveiro Port	Portugal	Test
Lido di Spina	Italy	Test

Table 3.6: Case studies used to create a method able to littoral drift barriers as a driver of shoreline evolution

The identification parameters are listed below and visualized in Figure 3.16. Shoreline evolution is based on the trend from the STL decomposition. Inter-annual oscillations in this trend are not caused by the littoral drift barriers. Therefore an additional smoother is applied to this trend. This additional smoothening is done by applying a LOESS smoothening on the trend and residual component with a moving window of a decade ($n_{(t)} = 120$). This moving window was only 13 months in STL. The difference between these two smoothed trends is visualized in Figure B.7.

1. $R_{2,LDB}$: coefficient of determination between changerates in space and a first-order polynomial fit (FOPF), see Figure 3.16a.

$$R^2 = 1 - \frac{\sum(y_i - f_i)^2}{\sum(y_i - \bar{y})^2} \tag{3.7}$$

where y_i : changerates in space
f_i : FOPF through changerates in space. Orange line in Figure 3.16a
$\bar{y}$: mean of the changerates

2. M_{LDB}: shoreline evolution close to the barrier compared to shoreline evolution far from the barrier.

$$M_{LDB} = \frac{Ev_{close} - Ev_{far}}{Ev_{close}} \tag{3.8}$$

   Ev_{close} (Ev_{far}) corresponds to the shoreline evolution of the averaged trends of the transects close to (far from) the barrier, see Figure 3.16b. Optimal identification is tested with respect to this metric by including the 10%, 20%, 33% and 50% closest and furthest transects.

3. N_{chars}: number of characteristics of the averaged trends of the closest and furthest transects. Characteristics are indicated in Figure 3.16b with the dashed lines. These characteristics describe the behaviour of the trend. There are multiple characteristics if the trend changes from obvious accretion to erosion or the other way around. For more information on how the number of characteristics in a trend are determined, see Appendix B.1.7.

4. N_T: number of transects to which the region of influence of the LDB extends. This parameter accounts for the spatial scale of littoral drift barriers.

The principles of how hotspots are defined by Kras (2019) introduce a difficulty to identify shoreline evolution caused by littoral drift barriers. Imagine a port protected by a breakwater which causes accretion at one side and erosion at the other. To diminish the effects of erosion near the port a groyne is constructed that interrupts the erosive pattern. This means that while erosion is still caused by littoral drift barriers, changerates are not changing linearly in space anymore. A case emphasizing this difficulty is sketched in Figure 3.15. To overcome this difficulty, the hotspot is splitted into two sub areas, the green boxes in Figure 3.15a. Appendix B.1.7 describes how such a hotspot is splitted. Hotspots are only splitted at one location to prevent over-fitting.

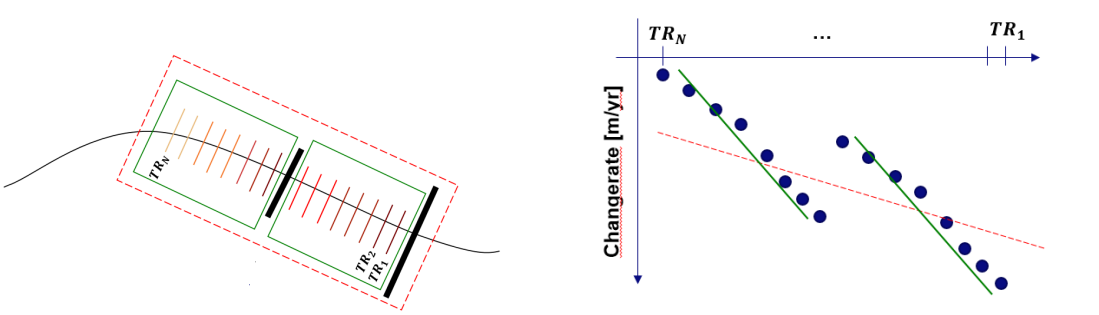

(a) Top view of a hotspot polygon that contains two littoral drift barriers. Larger shoreline evolution at the transects is indicated with darker colours. The hotspot as extracted by Kras (2019) is indicated with the dashed red polygon. Sub-hotspots are indicated with the dashed green polygons.

(b) The lines in the spatial scatter plot correspond to the FOPF for transects within a (sub-)hotspot indicated with the same color in the top view.

Figure 3.15: Example case showing how extraction of hotspots by Kras (2019) might complicate the identification of littoral drift barriers.

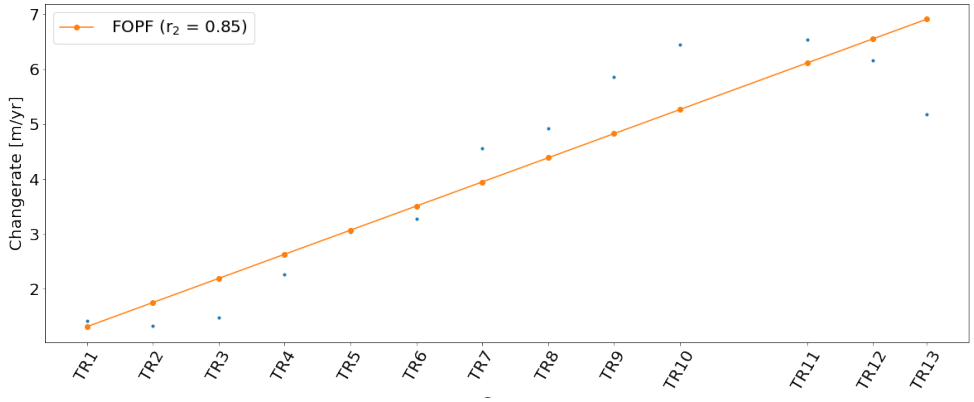

(a) Changerates of the transects plotted in space. The orange line is a first order polynomial fit through the changerates (blue markers).

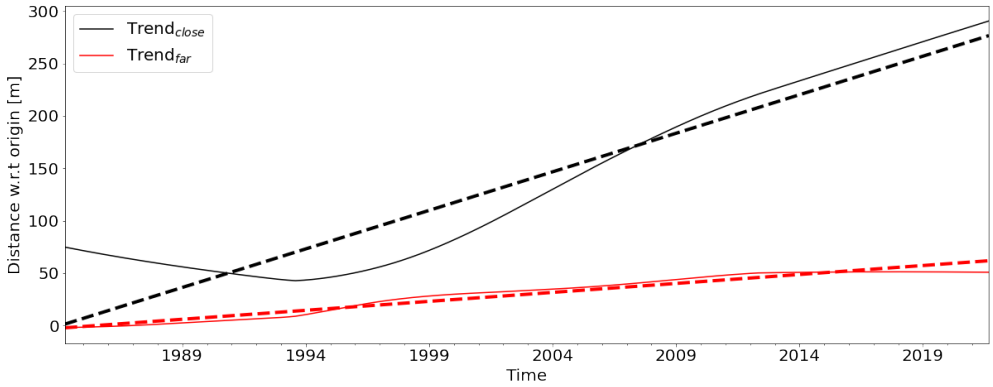

(b) Shoreline evolution of the average trend of transects close and far from the LDB. FOPFs are indicated in the dashed lines. The number of FOPF correspond to the number of characteristics, here for both trends equal to 1.

Figure 3.16: Visualization of the method used to identify littoral drift barriers.

Finally, two parameters provide extra information about LDBs:

1. LDB type, either one of:
   - Updrift: accreting hotspot
   - Downdrift: eroding hotspot
   - Double updrift: hotspot with two accreting sub-hotspots. The slopes of the FOPF of the changerates in space must be opposite. Figure 3.15 gives an example of sub-hotspots with non-opposing FOPF slopes.
2. Trend$_{Ev}$: evolution of the trend of the transects close to the LDB over the past decade compared to the decade before that. Can be classified into:
   (a) Stabilizing: meaning the change rate over the last decade has decreased compared to its previous decade.
   (b) Developing: the change rate remains equal or even increases over the last decade compared to its previous decade.

Overview of the identification methods

Table 3.7: Overview of the methods used to identify drivers of shoreline evolution

Driver	Decomposed signal	Parameters	Spatial extent
SN	Seasonal STL	• P_S: period of the seasonal component (identification) • D_S: seasonal displacement (identification) • T_{min}: month in which the minimum shoreline position is observed (informative) • P_{accr}: accretion time in months from mimimum to maximum shoreline position (informative)	Single transect
BR	STL trend with $n_{(t)}$ = 13	• M_{BR}: correlation coefficient between shoreline evolution at outer edges of the bay (identification) • $R_{2,BR}$: describes linear behaviour of correlations of shoreline evolution in space (identification)	All transects within an embayed beach
CV	FFT	• M_{ENSO}: mean power in the interval 2-7 years compared to the mean power in the remaining periods (identification)	Single transect
RM	STL trend with $n_{(t)}$ = 13	• dY_{dt}: change rate of the shoreline jump (identification) • M_{RM}: shoreline evolution after the shoreline jump compared to shoreline evolution up to and including the jump (identification) • T_C: date of construction (informative) • dY_C: length of reclaimed land (informative)	Single transect
NM	STL trend with $n_{(t)}$ = 13	• dY_C: length of reclaimed land (identification/informative) • LT: lifetime of the nourishment (identification/informative) • E_{cr}: changerate after a shoreline jump (identification) • N_T: number of transects in which a nourishment is observed (identification) • T_C: date of construction (informative)	Multiple transects
LDB	STL trend with $n_{(t)}$ = 120	• $R_{2,LDB}$: describes linearity of shoreline evolution in space (identification) • M_{LDB}: shoreline evolution close the barrier compared to shoreline evolution far from the barrier (identification) • N_{char}: number characteristics in the averaged trend over the closest transects (identification) • N_T: number of transects to which the region of influence of the LDB extends (identification) • Type: type of the LDB (informative) • $Trend_{EV}$: evolution of the averaged trend close to the LDB over the past decade compared to the decade before that (informative)	All transects within a hotspot

3.3. Methods for classification and prediction

The methods described in Section 3.2.2 result in several parameters. This Section will elaborate on how to go from the identification parameters to an accuracy of identification. A method that can be used to quantify the probability of a categorical outcome that is a function of dependent variables is discussed in 3.3.1. In this study, the categorical value is the presence of a driver (True or False), which is a function of several identification parameters. Section 3.3.2 discusses some metrics on how accuracy's of the identification of drivers can be quantified.

Key points

- Logistic regression is a method that can be used to predict categorical outcomes.
- Several metrics are presented that are used in identification studies.

3.3.1. Logistic regression

Logistic regression (LR) is a method that can be used when the dependent variable of a function is categorical. Dependent variables are the outcomes that someone is interested in and are a function of independent variables. For example, the dependent variable house price, is a function of the independent variables; location, living area, the house market etc. This is an example of a continuous dependent variable. As mentioned, LR requires categorical dependent variables. These categorical variables can be either binary (true/false, yes/no) or multinomial (non-vegan, vegan, vegetarian) (Kleinbaum et al., 2002).
The logistic function describes the mathematical form on which a logistic regression model is based. For a binomial case, this function is described as:

$$f(z) = \frac{1}{1 + exp(-z)} \tag{3.9}$$

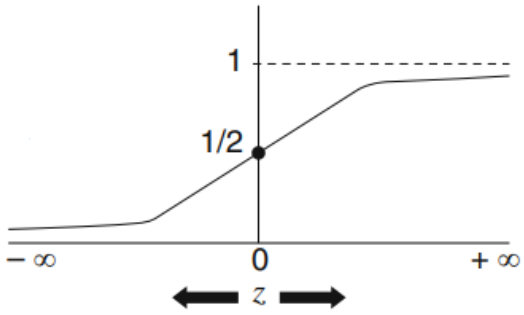

Figure 3.17: The logistic function (Kleinbaum et al., 2002)

The logistic function ranges between 0 and 1 and can therefore be used to describe probabilities. The logistic model is the combination of independent variables describing the dependent variables:

$$z = \alpha_i + \sum \beta_i X_i \tag{3.10}$$

where z : the dependent variables
α : the intersection
β_i : a coefficient
X_i : the independent variable

Suppose z is a categorical variable which either equals 0 (failure) or 1 (success). The probability that the logistic function reaches 1 is then:

$$P(1|X1, X2, ..., X_k) = \frac{1}{1 + exp(\alpha_i + \sum \beta_i X_i)}$$

α and β are called estimators and can be fitted from data on known samples of combinations of the dependent variables and outcomes. For this fitting, a limited-memory BFGS is chosen. This is an optimization algorithm in the family of quasi-Newton methods (Liu and Nocedal, 1989). For more information on this estimator optimization method see Liu and Nocedal (1989). The logit function and the logistic model in the case of a multinomial logistic regression are discussed in Section B.1.8.

There are a few key assumptions which have to be kept in mind when applying logistic regression:

1. The observations (independent variables) are uncorrelated
2. There are no extreme outliers
3. There is a linear relation between the logit of the independent and the dependent variables
4. The sample size is sufficiently large. Observational studies with large populations involving logistic regression are recommended to use a sample of size of at least 500 (Bujang et al., 2018).

3.3.2. Accuracy scores

Below several metrics are summarized that can be used to define accuracy in identification studies:

- Precision (PPV):

$$PPV = \frac{TP}{TP + FP} \tag{3.11}$$

  where TP : True positives
  FP : False positives

- Miss rate (FNR):

$$FNR = \frac{FN}{FN + TP} \tag{3.12}$$

  where FN : False negatives

- Critical succes index (CSI):

$$CSI = \frac{TP}{TP + FN + FP} \tag{3.13}$$

- False omission rate (FOR):

$$\frac{FN}{FN + TN} \tag{3.14}$$

  where TN : True negatives

3.4. Spatial autocorrelations

The method of spatial autocorrelations can be used to describe the degree two which observations at spatial locations can be similar to each other. These spatial autocorrelations are calculated using Moran's I (Moran, 1950):

$$I = \frac{n}{\sum_{i=1}^{n}(y_i - \bar{y})^2} \cdot \frac{\sum_{i=1}^{n}\sum_{j=1}^{n} w_{ij}(y_i - \bar{y})^2(y_j - \bar{y})}{\sum_{i=1}^{n}\sum_{j=1}^{n} w_{ij}} \tag{3.15}$$

where n : number of spatial units
y : variable of interest
: the mean of y
w_{ij} : matrix of spatial weight wit zeroes on the diagonal

This equation is similar to a normal calculation of correlations (see Equation 3.6) but with distance weights (w_{ij}) added. Moran's I can vary between -1 and 1. A high positive local Moran's I value implies that the location under study has similarly high or low values as its neighbors. There are four types of categories that can be extracted using Moran's I. These are visualized in Figure 3.18

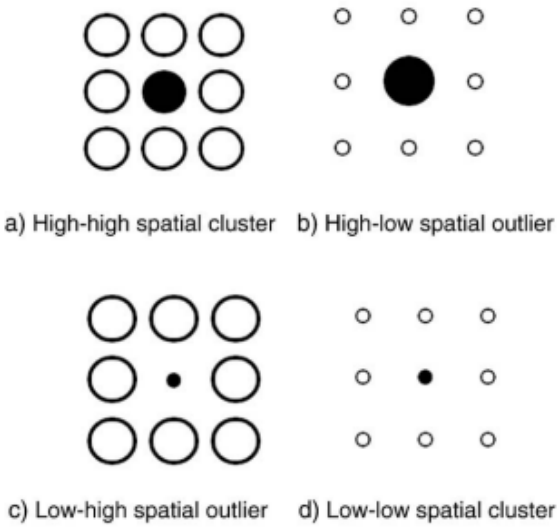

Figure 3.18: Sketch figure showing the relationship of a location and its neighbourhood. (Source: Zhang et al., 2008)

3.5. Summary: methodology

This chapter elaborated on various existing and newly developed methods used to achieve the objective of this study; to identify and characterize drivers of shoreline evolution on a global scale.

Data preparation
Before divers can be analyzed from time series, the SDS data must be generated and preprocessed. For this purpose a Python module was created. The current way of generating SDS is divided into four scripts, each of which separately executes one of the steps of the algorithm. The newly created python module links these separate steps which are then automatically executed sequentially. The input of this tool is an Area of Interest (AOI), the timestep of the satellite derived shorelines (SDS), the spatial resolution, the composite window, the maximum cloud cover limit for images and the study period. The output of this module is a time series of shoreline position for all transects within a certain AOI. Outliers and poor satellite coverage result in missing values in SDS time series. Therefore, an algorithm was developed that fills shoreline positions in these time series. This algorithm finds the longest time range in the time series without missing values and then artificially removes data from this range. Next, these missing values are filled by several filling methods (linear interpolation, rolling mean etc.) and compared to the original values. This procedure is repeated 100 times after which the best performing method, based on the coefficient of determination (R^2), is applied to the entire time series.

Time series decomposition
Time series need to be decomposed into separate signals to link the SDS to individual drivers. For this decomposition, two methods are used that are shortly explained below:

1. Seasonal-Trend decomposition with LOESS: this is a procedure that decomposes a seasonal time series into three individual components: a trend, a seasonal component and a remainder (Cleveland et al., 1990)
2. Fast-Fourier Transform (FFT): this is a mathematical process that converts waveforms into individual sine components on the frequency domain.

Driver identification methods
For each driver, several case studies are identified which are used to either develop or test a method able to link a decomposed time signal to this particular driver. From these methods two types of parameters arise:

1. Identification parameters: used to identify a driver.
2. Informative parameters: provide extra information about (the behaviour) of a potentially identified driver.

Below for each driver the key assumptions of its identification parameters are treated:

Seasonality	The seasonal component from STL is used to identify seasonality. This seasonal oscillation should have a period of about a year, along with a seasonal displacement of at least 15 meters (accuracy of Landsat satellite mission).
Climate variability	To indicate the presence of climate variability, a fast-fourier transform is applied to the STL trend. As indicated in Section 2.2.1, ENSO has a fluctuation around 2 - 7 years. Therefore FFT peak periods in this interval might indicate El Niño and la Niña impacting shoreline variability. This is indicated by comparing the mean power in the 2-7 years period to the mean power in the remaining periods.
Beach rotation	Using the trend from the STL, correlations between the shoreline positions of the two outer transects in the bay are compared with those of the other transects. In the case of a rotating beach, a positive correlation is expected for neighboring transects, which decreases with distance and eventually becomes negative.

3.5. Summary: methodology

Reclamations	This driver can be identified from SDS time series as a change in the position of the shoreline, or simply put, a shoreline jump, where the variability of the shoreline after this jump decreases significantly compared to the period before the jump. This shoreline jump should be at least 15 meters, corresponding to the accuracy of Landsat images.
Nourishments	Nourishments are identified by establishing from the trend from STL a widening of the beach followed by erosion. As nourishments are constructed along a coastal stretch, this characteristic is observed in multiple transects indicating not only a temporal but also a spatial characteristic. The beach widening should be at least 15 meters, corresponding to the accuracy of Landsat images.
Littoral drift barriers	For identification of this driver, the entire coastal stretch affected by the barrier has to be taken into account. Shoreline evolution, determined from a smoothed STL trend, increases towards the barrier.

Classification and prediction
Prediction of categorical outcomes can be done using a Logistic regression (LR) model. In this study, this is the positive or false identification of a driver. The logistic function is a combination of independent variables, the identification parameters. This function has the following form:

$$f(z) = \frac{1}{1 + exp(-z)} \tag{3.16}$$

with:

$$z = \alpha_i + \sum \beta_i X_i \tag{3.17}$$

where z : the dependent variables
α : the intersection
β_i : a coefficient
X_i : the independent variable

The logistic function ranges between 0 and 1 and can therefore be used to describe probabilities of a certain categorical outcome. Dependent on this probability, the outcome can be classified. For example, if the probability is larger or equal than 50%, the independent variables are classified as outcome A, else, outcome B is the correct classification.
A metric that can be used to assess the performability of identification, for example using logistic regression, is precision (PPV):

$$PPV = \frac{TP}{TP + FP} \tag{3.18}$$

where TP : True Positives
FP : False Positives

4

Local method validation and verification

Based on already existing and newly developed methods presented in Chapter 3, this chapter will provide results to answer the first sub-question. This sub-question can be found in Section 1.4 and relates to how drivers can be identified from SDS. For each driver, results will be presented and validated using several case studies. An overview of all the case studies can be found in Figure 3.9. Identification and informative parameters resulting from the methods described in Section 3.2.2 will be verified against existing literature from these case studies. Most of this literature is summarized in Chapter 2. A summary of this chapter can be found in Section 4.7.
First of all, the optimal settings to generate the SDS have to be determined. These settings are based on an analysis described in Appendix C.1.1 and listed below:

1. Composite window: 90 days
2. cloud cover limit: 80%
3. Satellite missions: Landsat 5, 7 and 8 (30 m spatial resolution)
4. Temporal resolution (time marching): monthly
5. Spatial resolution: 500-m spaced transect system
6. Period: 01/1984 to 06/2021

4.1. Seasonality

Identification of seasonality is based on the seasonal component from STL. Therefore, first the optimal input for the STL algorithm must be determined. The analyses for optimal inputs are based on STL decompositions with a seasonal period of 12 months since this is the most logical choice for an oscillation with a period of one year. Nevertheless, the sensitivity of STL to identification and informative seasonal parameters resulting from seasonal periods of 11 and 13 months is also analyzed. As was already mentioned in Section 3.2.2, identification of seasonality has been based on the period after February 2013.
Based on seasonal-diagnostic plots for Perth and San Francisco OB a value of 61 has been chosen for the STL seasonal smoother ($n_{(s)}$). This value results in a constant seasonal displacement over the years, see Figure C.4 and Figure C.5. As already mentioned, a constant seasonal displacement takes no shoreline evolution caused by climate variability into account. For the other input parameters ,the minimum recommended values, see Section 3.2.1, are accepted. Since SDS time series can be subject to outliers, it is necessary to run iterations of the outer loop and perform robustness iterations. This is emphasized in Figure C.6 and C.7. Visual inspection of the STL trends of these Figures confirm that a $n_{(t)}$ of 1.5 $n_{(s)}$ is a good choice.

Key points

- Identification and informative parameters resulting from a STL with a period of 12 months correspond best to literature for the case studies.
- The exact month in which minimum shoreline position can not exactly be determined if differences in shoreline positions are below the accuracy of the satellite mission. Nevertheless, a good indication can be given when shoreline positions are minimum.
- Seasonal displacements from STL can be different than values from literature. This can be caused by the fact that exact study locations do not match.

Perth North City Beach, Australia

Two transects at this location have been analysed. Figure 4.1 shows the trend and seasonal component of STL for a seasonal period of 12 months. These components follow almost exactly the original shoreline positions, implying a small STL remainder. Table 4.1 summarizes the characterizing and informative parameters for seasonality at Perth.

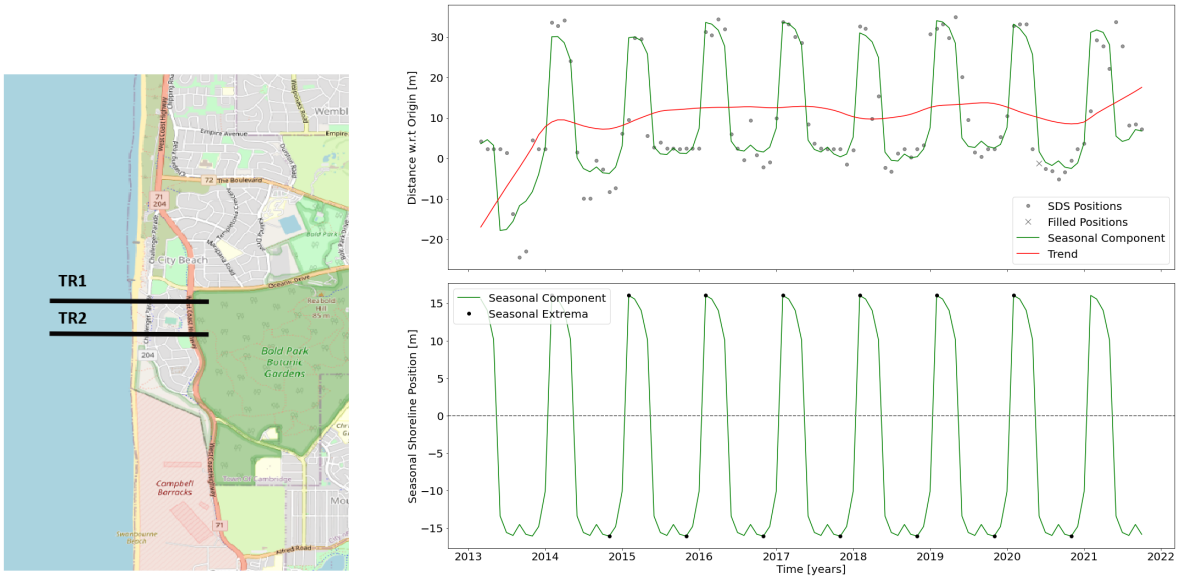

(a) Locations of the transects at Perth.

(b) STL decomposition of TR1 at Perth with a period of 12 months.

Figure 4.1: Result of the method of identification of seasonality at Perth for TR1

In the summer of 1996 and 1997, shoreline positions increased around 100 meter at Perth (Masselink and Pattiaratchi, 2001), see also Section 2.2.1. From the STL decompositions, a maximum displacement of 32 meters was observed at TR1. However, the study period here (2013-2021) is different than that from the literature in Section 2.9 (1995-1998). Moreover, the wave climate, which affects seasonal displacement, may vary locally in Perth due to reefs and sandbars. This means that differences in seasonal displacement may also have been caused by the analysis of different locations.
Figure 4.2 shows that for an analysis of the SDS with the same study period, STL produces a larger seasonal displacement, about 50 meters. A difference can still be accounted to the fact that locations at the beach do not exactly match.
According to literature, in 1997, a maximum shoreline position was reached around April where a minimum shoreline position was found around July (Masselink and Pattiaratchi, 2001). However, minimum shoreline positions resulting from STL oscillations with a seasonal period of 12 months are observed a few months later, around November. Looking at Figure 4.1 and 4.2 it can be observed that minimum shoreline positions from the SDS occur at a couple of months in stead of exactly one month. Moreover, differences between these months are below the accuracy of Landsat. As the method of identification estimates the minimum shoreline position based on the most extreme position, this might then be slightly off from literature.

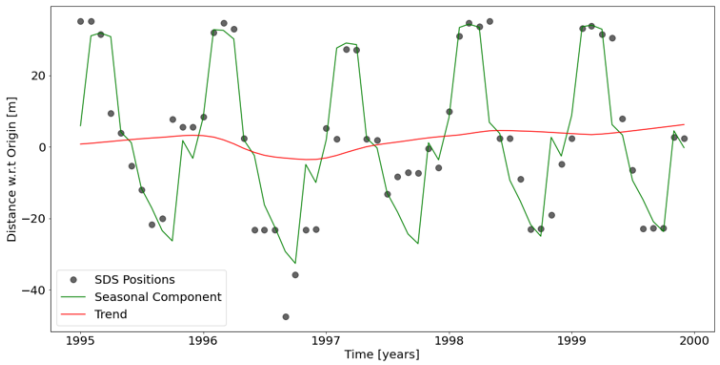

Figure 4.2: STL decomposition of TR1 at Perth with a period of 12 months from 1995 to 2000.

Table 4.1: Identification and informative parameters at Perth for various STL seasonal periods.

Transect	Method	P_S	D_S	T_{min}	P_{accr}
TR1	STL period 11 months	167	10	August	6
	STL period 12 months	365	32	November	5
	STL period 13 months	396	20	June	5
TR2	STL period 11 months	335	8	September	6
	STL period 12 months	365	18	October	7
	STL period 13 months	396	12	October	7

San Francisco Ocean Beach, USA

The results from STL at this location can be found in Table C.1. For the most northern transect (TR1), see Figure C.8 for the location, both displacements and minimum shoreline positions correspond to literature described in Section 2.2.1. For the other transect, regarding the seasonal displacement, a decomposition with a period of 13 months lies closer to the value from literature. Nevertheless, as the analyzed period from the literature from Section 2.2.1 is not equal to this study period, this is not conclusive. Furthermore, Figure C.9 shows that with a period of 12 months, the seasonal component best approximates the original SDS data at TR2.

The Sand Engine, The Netherlands

At this location, a seasonal component with a period of a year is only observed with a seasonal STL derived from a period of 12 months, see Table C.10. The minimum shoreline position from this decomposition is observed in September. According to Quartel et al. (2008), beaches in the Netherlands reach a minimal volume at the beginning of summer (May/July). The period of minimum shoreline position estimated from STL is not consistent with the literature. However, the period of accretion at this location is only four months, indicating that the maximum shoreline position is observed in December. This corresponds to the beginning of winter, which, according to Quartel et al. (2008), is the period when the maximum beach volumes are observed. Figure C.11 shows that the SDS positions are quite noisy before 2019. This also explains why the estimated period of minimum shoreline positions is so far of from literature. Figure 4.3 shows that based on a STL decomposition of the period 2019-2021, the minimum and maximum shoreline positions are more consistent with literature.

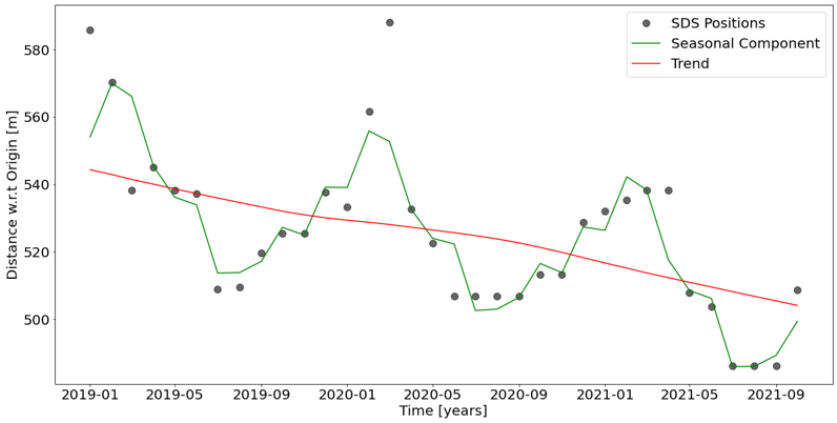

Figure 4.3: STL decomposition of at the Sand Engine with a period of 12 months for the period 2019-2021.

Watsonville, USA

Also at the analyzed transect at Watsonville, only the decomposition using a 12 month period results in the correct seasonal component. Minimum shoreline positions are observed in July which according to the geographical location of Watsonville seems logical. Moreover, Watsonville lies only at a distance of around 100 kilometers from San Francisco at which minimum beach volumes occur in July as well.

Basin d'Archaron, France

For neither of the decompositions, the period of the oscillations approximates a year. There is thus no seasonality observed at Basin d'Archaron. This lagoon is sheltered by a spit and thus is wave penetration limited. Without the presence of waves, there is no seasonal beach behavior. This is supported by the parameters from the STL decompositions.

4.2. Beach rotation

The method for identification of beach rotation is based on correlation of shoreline evolution between transects at the edges of the bay and other transects. Shoreline evolution is based on the trend from STL. For more information about this identification method, see Section 3.2.2.

Key point

- Using the trend from STL, correlations do not exactly match the values from literature. Nevertheless, negative correlations are found between transects at opposite sites of the pivot point. Therefore, the parameters resulting from the identification method are capable to capture beach rotation as a driver of shoreline evolution.

Narrabeen

Table 4.2 compares correlations from literature, see Section 2.2.1, to those derived from the identification method. There are some differences observed between the correlations from the literature and those resulting from the identification method. This might be caused by the fact that the transects in this study do not exactly match the location of the transects from literature. Nevertheless, similar to literature, the method indicates that the correlation between transects on the same side of the pivot point is positive, while there is a negative correlation between transects on opposite sides of the pivot point.

Parameter	Literature	Method
r_{TR1-2}	0.82	0.80
r_{TR1-8}	-0.19	-0.37
r_{TR8-7}	0.67	0.92

Table 4.2: Shoreline evolution correlations between transects at Narrabeen

Figure 4.4 visualizes the results for beach rotation at Narrabeen Beach.

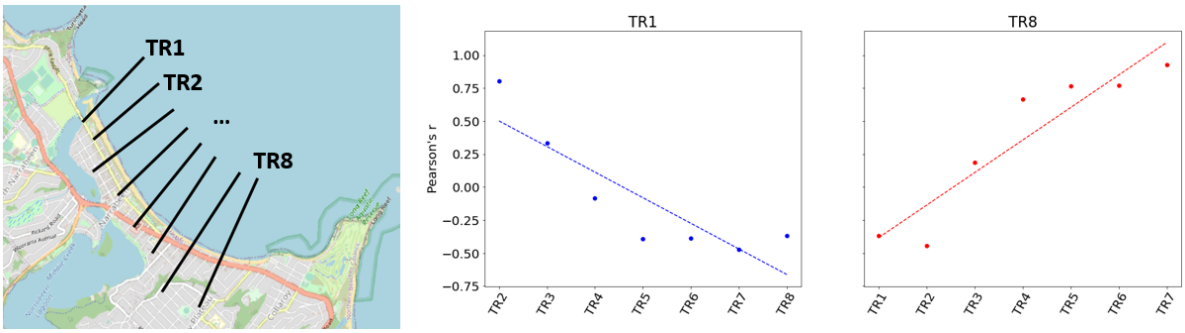

Figure 4.4: Visualization of beach rotation at Narrabeen beach. The left plot shows the locations of the transects. The two figures on the right shows correlations between the outer transects and the remaining ones. A linear fit between correlations is indicates with a dashed line.

The identification parameters at Narrabeen beach can be found in Table 4.3.

Table 4.3: Identification parameters of beach rotation at Narrabeen

Parameter	M_{BR}	$R_{2,BR}$
TR1	-2.17	0.76
TR2	-2.50	0.87

Palm beach, Australia

The resulting plot from the identification method and correlations for Palm Beach can be found in Section C.1.4. Correlations between transects at the same pivot side correspond well to literature, which was also the case at Narrabeen. However, the correlation between transects at the outer edges of the bay is significant lower than the value from literature. Again, this may be due to different transect locations between this study and literature. Table 4.4 summarizes the identification parameters for Palm beach.

Table 4.4: Identification parameters of beach rotation at Palm beach

Parameter	M_{BR}	$R_{2,BR}$
TR1	-3.56	0.97
TR2	-4.65	0.79

Besides, on the inter-annual scale effects of beach rotation are observed, it also can be seen on a seasonal scale. This is due to a seasonal varying shoreline direction. This can be seen from Figure 4.5 where the moment where the minimum shoreline position is observed differs between the two edges of the bay and converges towards the center.

Figure 4.5: Minimum seasonal shoreline positions at Palm beach

Moruya, Australia

For Moruya similar results as for Narrabeen and Palm beach were observed. However, from the parameters listed in Table C.6, it can be inferred that this pocket beach has a less rotational behaviour. For a more detailed overview of the results of Moruya see Section C.1.4.

4.3. Climate variability

Shoreline evolution caused by climate variability is identified using a fast Fourier transform (FFT) of the STL trend. More information on the FFT can be found in Section 3.2.1. Climate variability causes shoreline evolution on the inter-annual scale. The two most known phenomena causing climate variability are the El-Niño-Southern Oscillation (ENSO) and the North Atlantic Oscillation (NAO), see also Section 2.2.1. ENSO has a cyclic behaviour with a period of 2 to 7 years, see Section 2.2.1. Therefore, peak frequencies from the FFT at this interval might indicate that ENSO affects shoreline evolution.

Key points

- The fast Fourier Transform of the STL trend indicated peaks in the periods ranging from 2 - 7 years for four case studies geographically located in the equatorial Pacific Ocean. This corresponds to the period of ENSO.
- In a region dominated by NAO, peaks in the FFT periods ranging from 2 - 7 years were less prominent. In stead, a peak period of ten years was found indicating that shoreline evolution was controlled by the NAO on the decadal scale. This was confirmed by literature.

San Francisco Ocean Beach, USA

As described in Section 2.2.1, especially the northern part of the beach at San Francisco is affected by ENSO. Figure C.18 shows the fast Fourier transform of a transect at the northern part of the beach. From this Figure, peak frequencies in the 2-7 years interval can be observed.
The ENSO identification parameter has a value of:

$$M_{ENSO} = \frac{1120}{213} \approx 5.3$$

This indicates that the STL trend has periods in the 2-7 year interval that have a mean power more than 5 times larger than in the other periods.
See Figure C.8 for the exact location of the analysed transect at San Francisco OB.

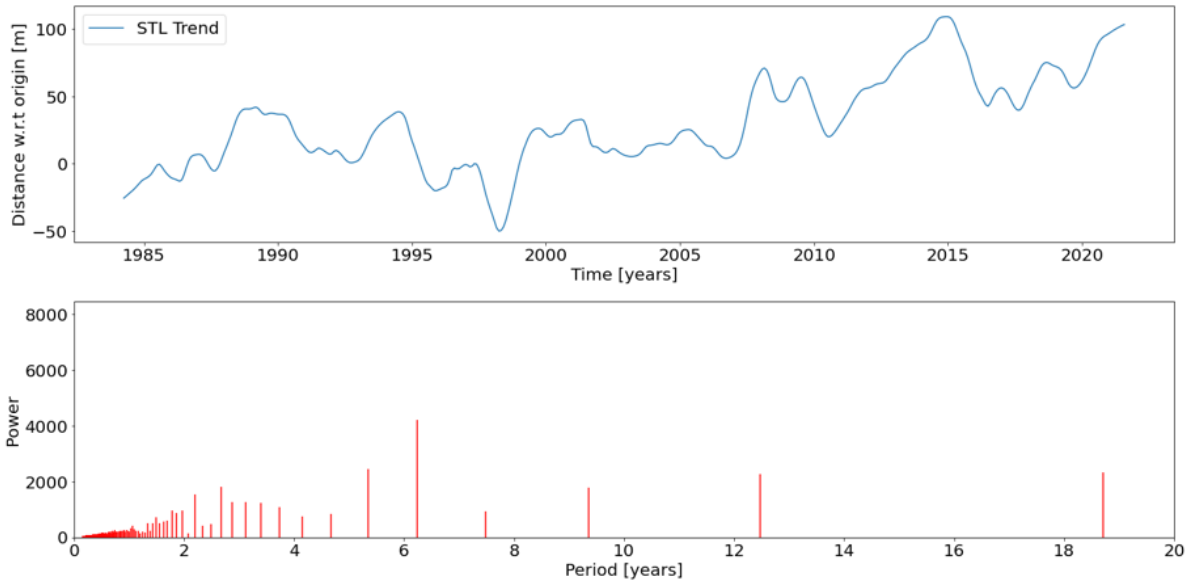

Figure 4.6: Plot of the STL trend (upper) and the fast Fourier transform of this trend (lower) of TR2 at San Francisco Ocean Beach.

Narrabeen, Perth and Palm Beach, Australia

Fast Fourier transforms for these three locations can be found in Section C.1.5. Table 3.2.2 summarizes the identification parameters. Based on the results from this table, Palm beach experiences possibly around twice as much shoreline evolution due to ENSO than the other two locations.

Table 4.5: Identification parameters of ENSO at Narrabeen, Perth and Palm beach

Location	Transect	M_{ENSO}
Narrabeen	TR2 (see Figure 4.4)	6.6
Perth	TR1 (see Figure 4.1a)	5.4
Palm Beach	TR1 (see Figure C.14)	11.0

Danube Delta, Romania

The Danube Delta is a region far from the equatorial Pacific Ocean and thus not within the area of influence of ENSO. This is also pointed out by the fact that peak frequencies from the FFT are less prominent in the interval 2 to 7 years, see Figure 4.7. Vespremeanu-Stroe et al. (2007) stated that shoreline evolution at the Danube region at a decadal scale was controlled by the NAO. Indeed, Figure 4.7 shows a peak period around 10 years. The location analysed in the FFT corresponds to one of the coastal stretches analysed by Vespremeanu-Stroe et al. (2007). For the exact geographical position of this coastal stretch, see Figure C.19.

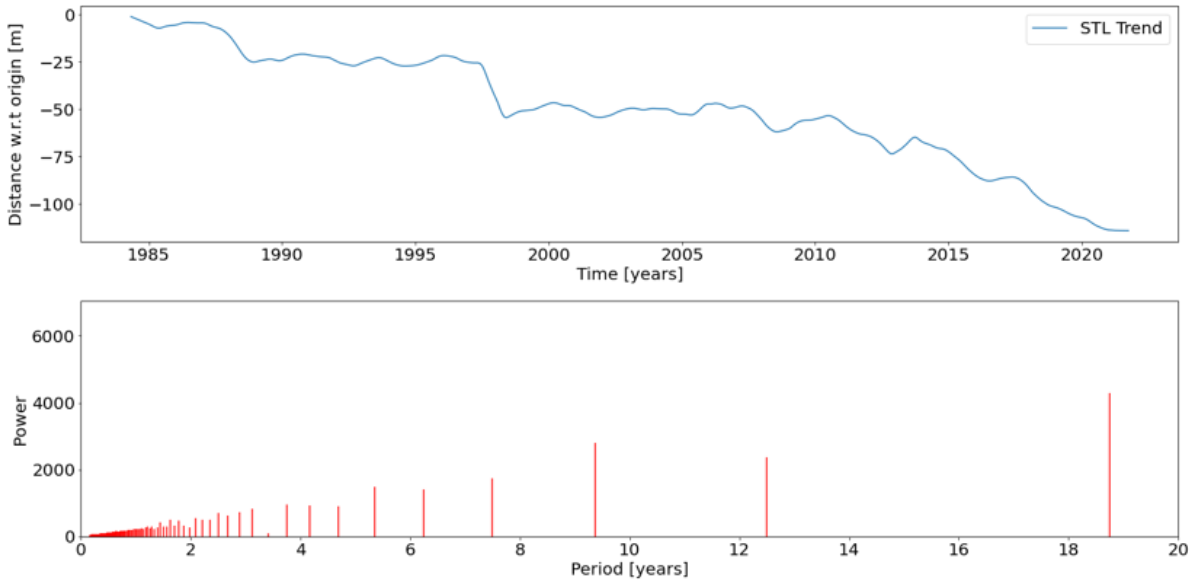

Figure 4.7: Plot of the STL trend (upper) and the fast Fourier transform of this trend (lower) of at the Danube Delta.

The identification parameter at the transect at the Danube delta has a value of:

$$M_{ENSO} = \frac{783}{255} \approx 3.0$$

4.4. Reclamations

This section presents results for three cases used to identify reclamations as a driver of shoreline evolution. The method for identification of this driver is based on the idea that after a shoreline is reinforced, coastlines positions will become fixed in time. For more information on this method see Section 3.2.2.

Key points

- The identification parameter shows that for the case studies, shoreline evolution after construction decreases by 70-90% compared to the period up to and including construction. Outliers affect the STL trend, which can influence the identification parameter.
- Construction dates resulting from the identification method correspond to literature.
- Parameters from the identification method remain the same for a varying threshold set to identify the shoreline jump (N, see Section 3.2.2). Therefore a value of N equal to 2 is chosen for the remainder of this study.

Caofeidian Port, China

For two transects the results will be given for identification of reclamations. See Figure C.20 for the exact locations of these transects.
Figure A.10 shows that at these locations, land was reclaimed during the period 2005-2010. Construction dates resulting from the identification method, see Figure 4.8 and C.21, are consistent to this reclamation period. Construction dates were found in 2007 and 2008 for TR1 and TR2 respectively. Figure 4.9 gives an overview of the identification and informative parameters. For both transects, shoreline evolution after construction is less than 10% compared to shoreline evolution before construction. Changing N has no effect on outcomes from the identification methods.

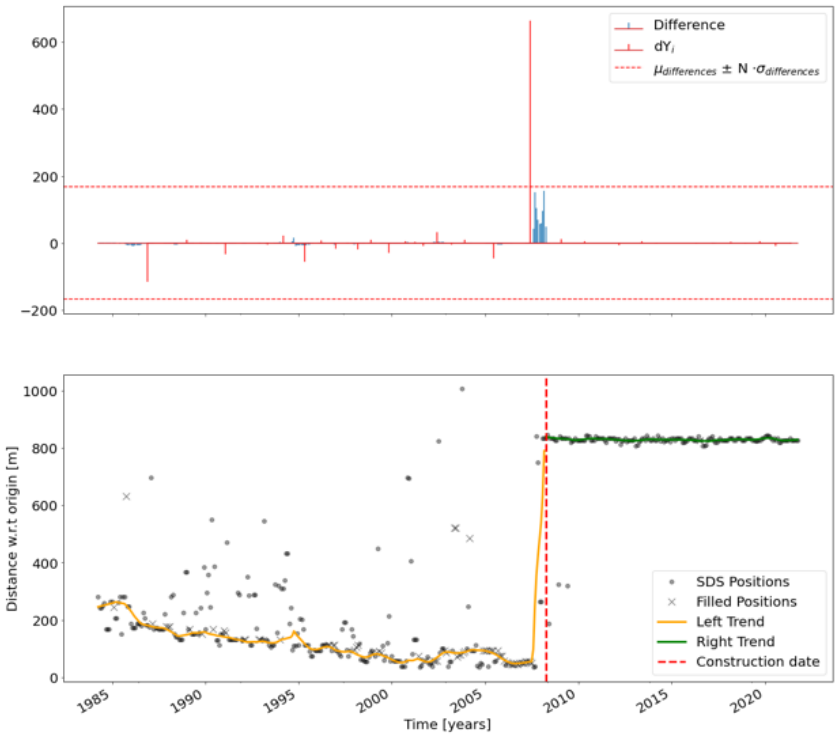

Figure 4.8: Visualization of the method used to identify reclamations for TR1 at the Caofeidian Port for N = 3. Other values of N would have resulted in the same plot, see Table 4.9.

Table 4.6: Identification and informative parameters for reclamations at the Caofeidian port.

Transect	N	$dY_{c,dt}$	M_{RM}	T_c	dY_c
TR1	1	397	0.097	2008	664
	2	397	0.097	2008	664
	3	397	0.097	2008	664
TR2	1	137	0.039	2007	330
	2	137	0.039	2007	330
	3	137	0.039	2007	330

Jebel Ali, UAE

As already mention in Section 2.2.2, expansion of the port in Jebel Ali was done in two phases. The first one started in 2005 and was completed in 2007. The second expansion was finished in 2017. Same construction dates can be observed from Figure 4.9. For the location of the analysed transect at this site, see Figure C.23.

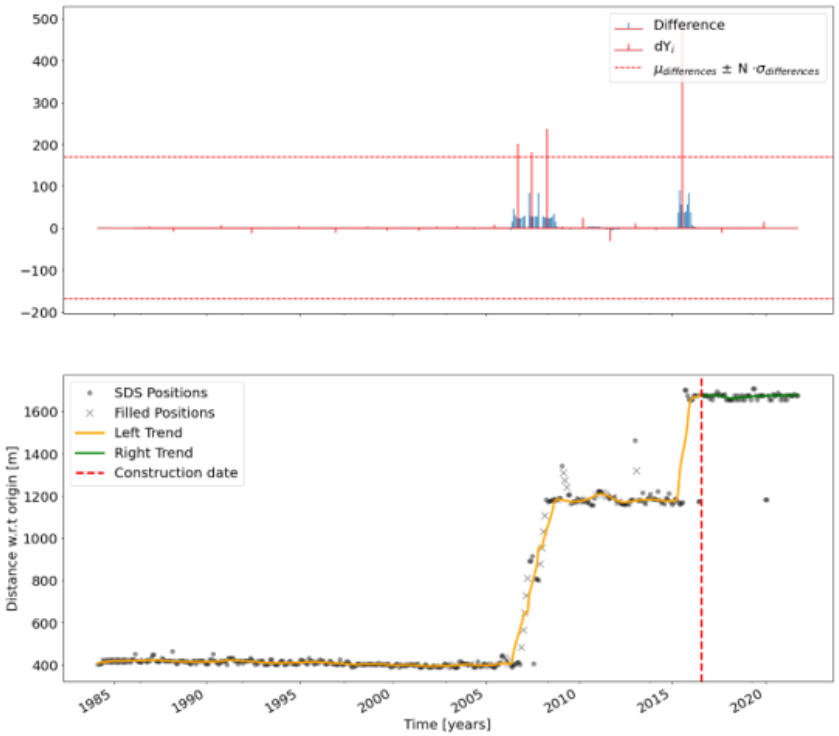

Figure 4.9: Visualization of the method used to identify reclamations at the Jebel Ali Port for N = 3. Other values of N would have resulted in the same plot, see Table 4.7

Parameters resulting from the reclamation identification method applying to this Figure are summarized in Table 4.7. Similar to the Caofeidian port, shoreline evolution decreases with around 90% after the reclamation. Also, changing N has no effect on the results.

Table 4.7: Identification and informative parameters for reclamations at the Caofeidian port.

N	$dY_{c,dt}$	M_{RM}	T_c	dY_c
1	248	0.13	2016	496
2	248	0.13	2016	496
3	248	0.13	2016	496

Gibraltar, Spain/UK

For the location of the analysed transect at Gibraltar and the visualization of the results, see Section C.1.6. Table 4.8 gives an overview of the parameters at Gibraltar used for identification of reclamations.

Table 4.8: Identification and informative parameters for reclamations at the Caofeidian port.

N	$dY_{c,dt}$	M_{RM}	T_c	dY_c
1	97	0.30	2001	259
2	97	0.30	2001	259
3	97	0.30	2001	259

At this location, M_{RM} has a much larger value compared to the other sites. Inspection of the time series, see Figure C.1.6 show that this is caused by noise.

4.5. Nourishments

This driver is characterized by a widening of the beach followed by erosion, see also Section 2.2.2. The method for identification follows this clear characteristic of nourishments, see Section 3.2.2 for more information on the method. Below results are given for two so called mega-nourishments, two sides subject to medium to large scale nourishments and finally a location where relatively smaller amounts of sand were deposited. Besides only temporal characteristics, also a spatial parameter (N_T, see Section 3.2.2) is used to identify nourishments. The areas of interest for the casestudies are determined from literature, see Section 2.2.2.

Key points

- Nourishments identified with a larger spatial correspond to literature.
- Small scale nourishments, as in the Fire Island case, are not identified by the method,
- Parameters from the identification method change for a varying threshold set to identify the shoreline jump (N, see Section 3.2.2). Nourishments are best identified with a N equal to 1.

The Sand Engine, Netherlands

Figure 4.10 visualizes the method for identification of nourishments applied to a mega-nourishment, the Sand Engine. This nourishment was completed in 2011, which can also be observed in Figure 4.10. This 2011 nourishment was observed in 8 transects. Besides the 2011 nourishments, also other periods characterised by a shoreline jump followed by erosion where identified. These were only identified at a maximum spatial scale of 2 transects.

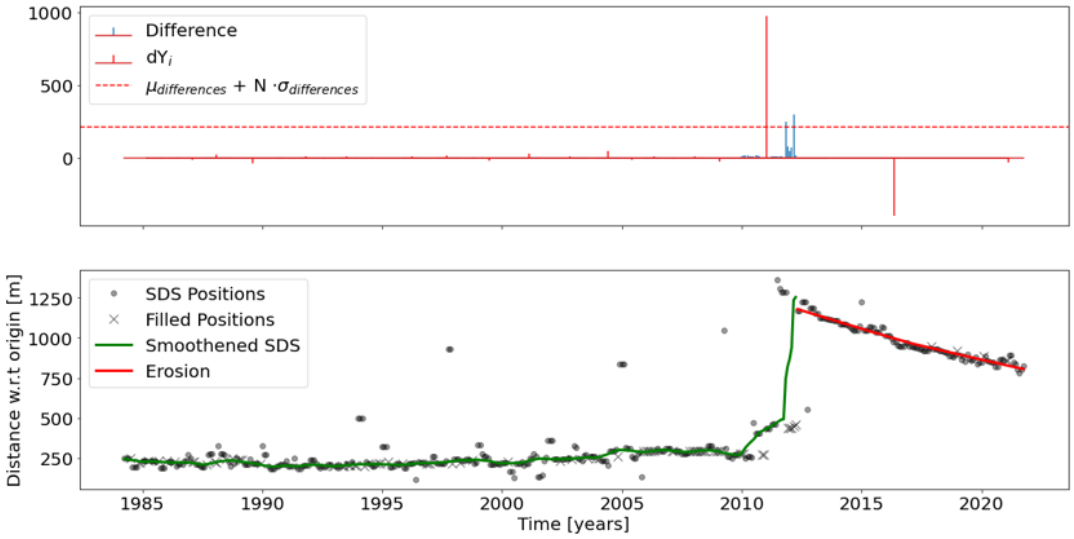

Figure 4.10: Visualization of the method used to identify nourishments at the Sand Engine (TR5) for N = 3

Figure 4.11 visualizes the 2011 nourishments for various transects. The method was not capable to identify the nourishment at all locations. This can be due to aberrant behaviour in the data, see Figure C.26. Although a nourishment can be detected from looking at this Figure, the construction date is detected much later in time.

In Figure 4.11, at transects where identification was successful, The nourished volumes follow the shape of the topview of the Sand Engine. For example, it is clear from the top image of Figure 4.11 that at TR8 more sand was deposited that TR12. This is also observed in the bottom part of the image which is the result from the identification method.

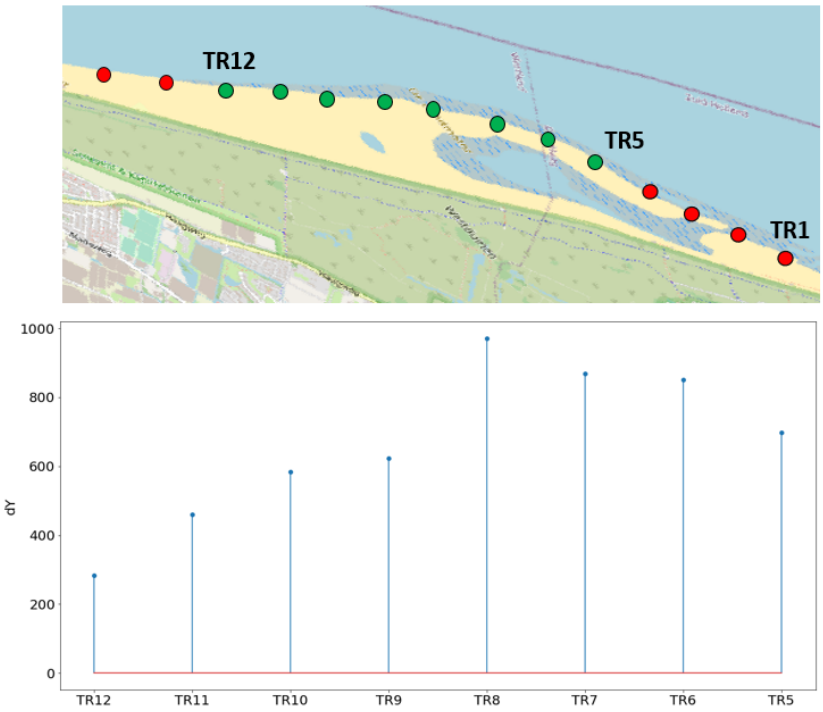

Figure 4.11: Top view of the Sand Engine (upper). Transects at which identification of the 2011 nourishment was successful (unsuccessful) are marker in green (red). The lower image visualizes the length of the widening of the beach for transects at which identification was successful.

Changing the value of N, does not affect the results at this location.

Hondsbossche, Netherlands

The mega nourishment at Hondbossche, completed in 2015, was observed in 15 transects. Beach widening was more or less constant along the transects and about 250 meters, see Figure C.27. As well as at the Sand Engine, varying N does not influence any of the results.

St. Augustine, USA

Figure A.13 gives an historic overview of the nourishments at St. Augustine. Nourishments in this area were completed in 2003, 2005, 2012 and 2018. From the identification method, these nourishments were observed in 4, 6, 5 and 0 transects respectively, see Table C.7. For the locations of the analyzed transects at St. Augustine, see Figure C.28. The volume deposited in 2018 is much smaller than in the other years, possibly explaining why this nourishment is not identified.
Finally, in 2015, a nourishment was identified in four transects. Nevertheless, Figure A.13 does not give any information about a nourishment in 2015.
At St Augustine, nourishments were identified better with N = 1 compared to N = 2, for results of the latter, see Table C.8. Performance of the identification method further worsened by increasing N to 3.

Delray Beach, USA

Delray Beach was nourished in the years 1992, 2002 and 2013, see Figure A.12. Below, shortly the results of the identification methods are summarized for N equal to 1, 2 and 3. The nourishments are best identified with N equal to 1. For the locations of the analysed transects, see Figure C.29.

Table 4.9: Identification and informative parameters for nourishments at Delray Beach.

N	Year	N_T
1	1992	3
	2002	7
	2013	9
2	1992	1
	2002	4
	2013	7
3	1992	0
	2002	1
	2003	3

Fire Island, USA

The identification method was not able to identify any of the nourishments indicated in Figure A.7. This can be explained by the fact that nourished volumes are small and fall within normal shoreline variability. As shoreline jumps are analyzed relative to the shoreline variability these nourishments are therefore not detected. The analyzed area corresponds to a region with a distance of 20 to 23 kilometer alongcoast in Figure A.7.

4.6. Littoral drift barriers

The most important characteristic that identifies littoral drift barriers is that shoreline evolution increases towards the barrier. Temporal characteristics as well as spatial ones are thus of interest for the identification of LDBs. Areas of interest are, similar to nourishments, determined based on literature. If no literature is present, it is assumed that effects of a LDB extend up to 8-10 times its length (Kudale, 2010).

Key points

- Shoreline evolution caused by littoral drift barriers increases nearly linear towards the barrier for the case studies.
- In the case of a groyne field this linear signal is interrupted. The method will in this case not be able to link the shoreline evolution to a littoral drift barrier.

Port de l'Amitie, Mauritania

The analysed areas for Port de l'Amitie can be found in Figure 4.12 and is based on Ould Elmoustapha et al. (2007). The breakwater affects shoreline evolution up to 8-10 times the breakwater length (836 meter). Table 4.10 gives an overview of the identification an informative parameters at Nouakchott. Visualizations of the method can be found in Section C.1.8.
The parameters M_{LDB} and $R_{2,LDB}$ indicate that shoreline evolution increases (nearly) linear towards the breakwater at both sides of the port.
$Trend_{Ev}$, see Table 4.10, indicates that for the updrift, as well as the downdrift part, shoreline evolution near the port is stabilizing. This is confirmed by literature, see Section 2.2.2.

Figure 4.12: Analysed transects at Nouakchott. Accreting (eroding) transects are indicated in green (red). The length up to where the breakwater affects shoreline evolution is also indicated in the figure.

Table 4.10: Identification and informative parameters at Port de l'Amitie. N_{chars} contains two values, the first corresponding to the averaged trend of transects close to the port. The other value is based on the averaged trand of transects furthest away from the port.

Type	$R_{2,LDB}$	N_{chars}	N_T	$Trend_{Ev}$	P	M_{LDB}
Updrift	0.86	(1, 1)	17	0.76	50%	4.0
					33%	7.0
					25%	8.3
					10%	14.3
Downdrift	0.97	(1, 1)	16	0.4	50%	2.3
					33%	5.3
					25%	6.9
					10%	14.2

Port of IJmuiden, The Netherlands

Figure 4.13 shows the area of interest at IJmuiden (based on Luijendijk et al. (2011)). Here the rule of thumb from Kudale (2010) does not apply as the northern and southern breakwater were extended in 1965 by 500 and 1000 meter respectively. At IJmuiden port, accretion occurs at both sides of the port, see also Section 2.2.2. Therefore, to apply the identification method, first the hotpot has to be split into two sub-hotspots. Figure 4.14 shows the location where the split was made. This corresponds to the port entrance, see Figure 4.13.
Trend$_{Ev}$, see Table 4.11, indicates that at the Northern part, close the barrier, erosion occurs. At the Southern part, accretion still continues at a constant rate. Figures of shoreline evolution close and far from the port can be found in Section C.1.8. At both sides of the breakwater, the parameters M_{LDB} and $R_{2,LDB}$ indicate that shoreline evolution increases nearly linear towards to port.

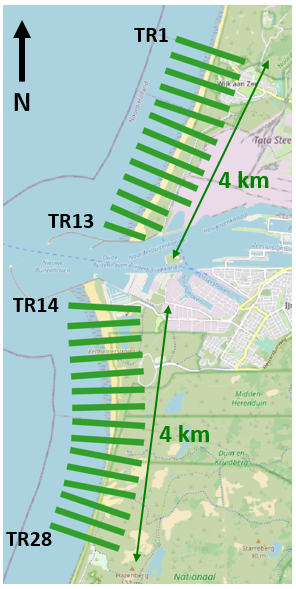

Figure 4.13: Analysed transects at IJmuiden. Accreting transects are indicated in green. The length up to where the breakwater affects shoreline evolution is also indicated in the figure.

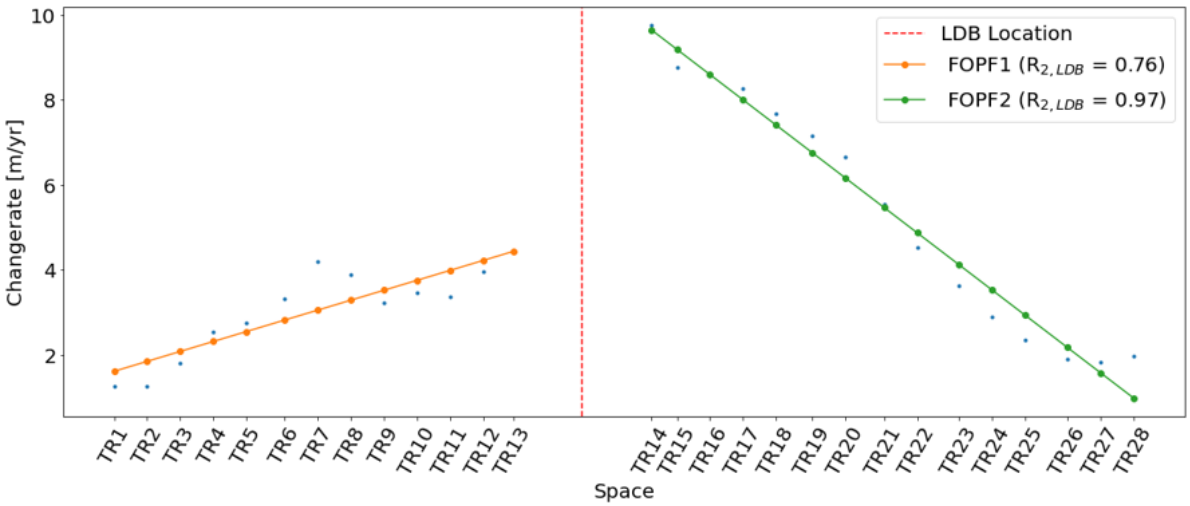

Figure 4.14: Sub-hotspots at Ijmuiden. TR1-TR13 (TR14-TR28) correspond to the southern (northern) part of the port. The red dotted line indicates the location where the hot spot was split, or equivalently, the location of the LDB.

Table 4.11: Identification and informative parameters at IJmuiden. N_{chars} contains two values, the first corresponding to the averaged trend of transects close to the port. The other value is based on the averaged trend of transects furthest away from the port.

Type	$R_{2,LDB}$	N_{chars}	N_T	$Trend_{Ev}$	P	M_{LDB}
Updrift north	0.76	(2, 1)	13	-0.42	50%	1.5
					33%	1.4
					25%	2.1
					10%	2.4
Updrift south	0.97	(1, 1)	14	1.1	50%	2.6
					33%	2.5
					25%	3.4
					10%	3.8

Pisa Coastal Plain, Italy

The erosive coastal stretch at Pisa is splitted in two sub-hotspots, see Figure 4.15. This is done using the method explain in Section 3.2.2 which is also visualized in Figure 3.15. In sub-hotspot A, the linear relation between shoreline evolution and distance to the littoral drift barrier is disturbed by 300-m spaced groynes. This also results in a relative low value of $R_{2,LDB}$, 0.49. In sub-hotspot B, erosion is caused by the construction of breakwater at a river mouth. Downdrift of this breakwater there is a linear relation between shoreline evolution and distance as there are no further constructions along this coast. This also results in a high value of $R_{2,LDB}$, 0.93. This example clearly shows the limit of this method. An option would be to create more sub-hotspots but this might lead to overfitting for other cases. Besides, the spatial resolution is less than the spacings between the groynes. This will make it impossible to extract the erosive pattern related to an individual groyne.

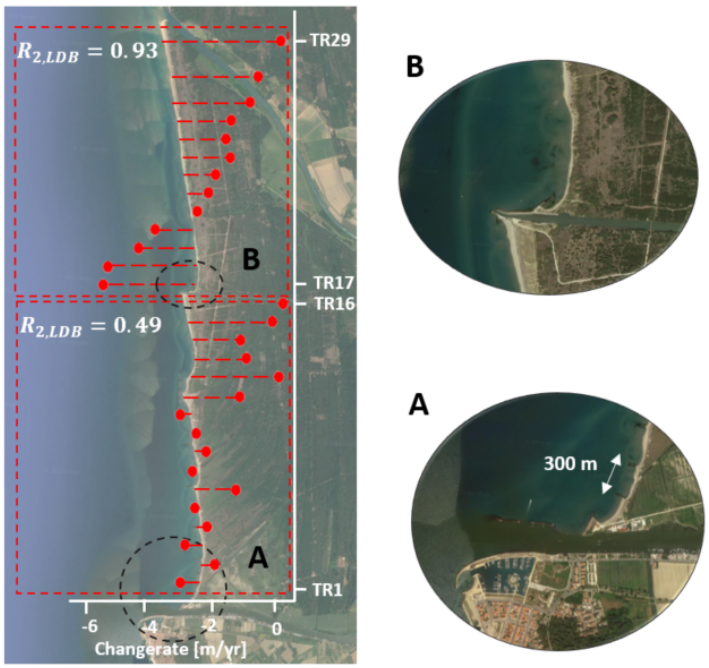

Figure 4.15: Subhotspot A and B at Pisa Coastal Plain. The red dots correspond to the changerate at a certain transect of the coast. The location of this transects is indicated with the dotted line. The black dotted circles represent the locations of the detailed maps shown on the right of the figure.

Aveiro, Portugal

For the updrift part, Aveiro Port shows similar results to both casestudies above, a strong linear relation between changerates in space. However, the eroding part does not show a linear relation. Again, this is caused

by a system of groynes interrupting this linear signal, see Figure 4.16. The results for Aveiro can be found in Section C.1.8.

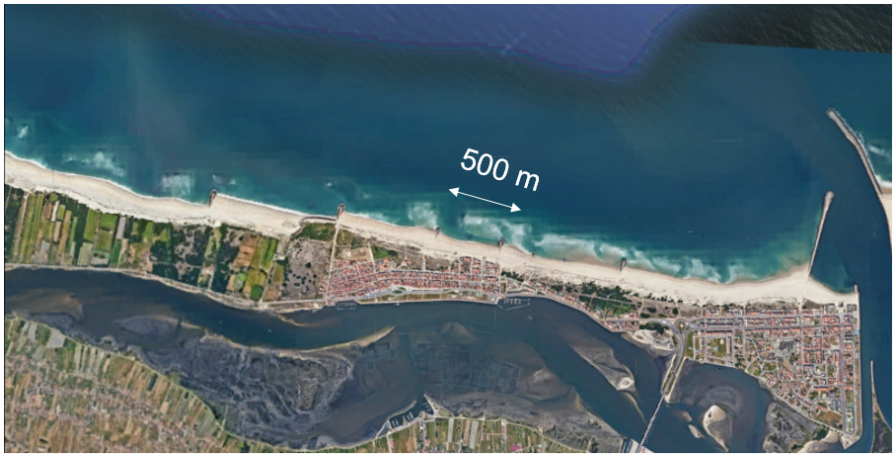

Figure 4.16: Construction of 500-m spaced groynes at a coastal stretch to the south of Aveiro port. (Source: Google Earth).

Lido di Spina, Italy

Even though at this location the linear increasing signal is interrupted by a constructed canal, $R_{2,LDB}$ is still relative high, see Figure 4.17.

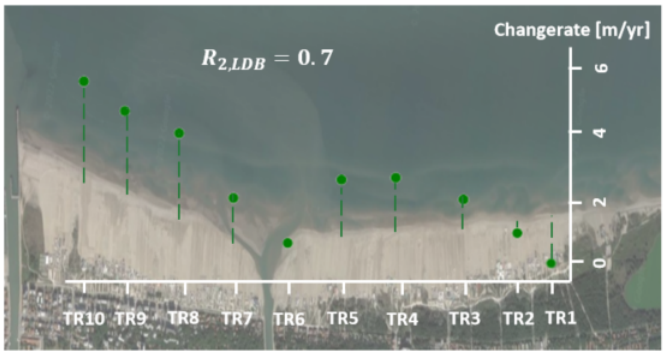

Figure 4.17: Accreting shoreline evolution at Lido di Spina. The green dots correspond to the changerate at a certain transect of the coast. The location of this transects is indicated with the dotted line.

Final remark

At all locations, even for P = 50%, the furthest transects were subject to more than twice the shoreline change than transects far away. For the rest of this study, a value for P of 33% is used, dividing a hotspots equally into transects close to the barrier, the center transects and transects far away from the barrier.

4.7. Summary: local method validation and verification

This chapter presented the results from the identification methods for several case studies. These results can be used to answer the first research question:

To what extent can existing methods be applied to link drivers to satellite derived shorelines (SDS)?

The following settings were used to generate SDS:

1. Composite window: 90 days
2. Cloud cover limit: 80%
3. Satellite missions: Landsat 5, 7 and 8 (30 m spatial resolution)
4. Temporal resolution (time marching): monthly
5. Spatial resolution: 500-m spaced transect system
6. Period: 01/1984 to 06/2021

Shoreline evolution for this case studies is linked to a driver by decomposing the SDS time series using either a Seasonal-Trend decomposition with LOESS (STL) or a Fast-Fourier Transform (FFT). Next, from this decomposed signal, two types of parameters are extracted:

1. Identification parameters: used to identify a driver.
2. Informative parameters: provide extra information about (the behaviour) of a potentially identified driver.

Overall, these case studies showed similar ranges of values for the identification parameters. This indicates that these identification parameters are well capable of capturing the behaviour of a particular driver. The informative parameters, that are site specific, differ along the case studies. Although the methods generally produced results as expected and supported by literature, some problems were also noted. These are listed below per driver:

Seasonality	The period of minimum shoreline positions and seasonal displacements are not always supported by literature. Minimum shoreline positions are determined using the most extreme minimum value from the seasonal component from STL. The difference between this extreme and the shoreline positions of nearby months may be small and below the accuracy of Landsat (15 meters). Nevertheless, a good indication of when the minimum shoreline position occurs is given. Moreover, the wave climate, which affects seasonal displacement, may vary locally due to reefs and sandbars. This makes it hard to compare the amplitudes to literature when study sites do not match exactly.
Climate variability	-
Beach rotation	-
Reclamations	Outliers have effect on the identification of reclamations.
Nourishments	Beach widening that falls within normal shoreline variability is not identified. Consequently, in these cases, nourishments can not be identified.
Littoral drift barriers	In the case of a groyne field, with spacings in the order of the distance between transects, the increasing shoreline evolution towards a barrier is not captured.

5

Regional driver verification

On a larger scale, the capability of the methods, described in Section 3.2.2, to identify the drivers will be verified and if necessary, minor refinements will be made. By increasing the sample size, accuracy scores of the identification methods can be determined. Using these accuracy scores the optimal settings for identification of the drivers can be established. These results can be used to answer the second sub-question. Verification of driver identification will be done on locations in West-Europe, or more precisely, for BOX164, BOX165, BOX186 and BOX187 (see Figure B.1). Methods will be applied only to transects within hotspots derived by Kras (2019) with a rolling mean of 2.5 km. See Figure 5.1 for an overview of the locations of hotspots in West-Europe. In Section 5.5 a summary of this chapter can be found.

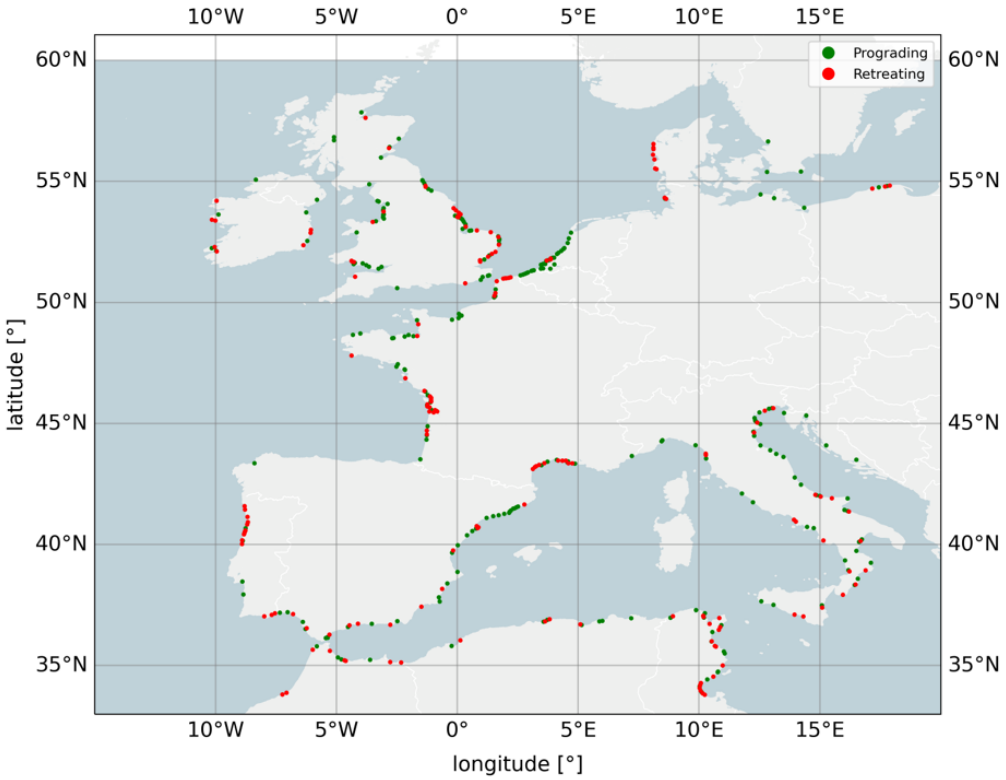

Figure 5.1: Overview of the hotspot locations in West-Europe. Prograding (retreating) hotspots are indicated with green (red) markers.

5.1. Seasonality

Key points

- A multinomial logistic regression model is applied to identify whether a beach shows seasonal beach, seasonal sandbar or non-seasonal behaviour. The dependent variables are the seasonal displacement (D_S) and the percentage of shoreline jumps of at least 100 meter (P_{dY100}). The model is fitted on a random sample of 100 transects that was verified based on location, time series and literature.
- A probability of 40% from the logistic regression model results in an identification precision of 80%. Locations with more than 30% missing data are not taken into account.
- Looking at West-Europe, the Dutch coast is primarily dominated by seasonal beach behaviour. The Belgium coast, a meso-tidal environment, is characterized by seasonal sandbar morphology. Finally, the Mediterranean is predominantly non-seasonal.

Figure 5.2 shows the resulting seasonal displacements for West-Europe for all locations which have a period of the seasonal STL of a year. This Figure shows that there are quite a few unrealistic displacements. These unrealistic values may have several causes:

A) A seasonal moving sandbar. When this sandbar reaches above the waterline, SDS is identified here as it is the outer most detected location of land. See also Figure C.35.

B) Very mild foreshores. At these locations, large horizontal tidal excursions and high water content complicate the correct detection of the shoreline (Luijendijk et al., 2018).

C) Erroneous data. For example a location with a double waterline intersection (DWI), see Section 2.1.2. Figure C.36 shows a STL decomposition from shoreline positions resulting from a DWI location.

Therefore, a logistic regression model will be applied to determine the extent to which the method correctly identified seasonality. The logistic regression will be multinomial with the following possible outcomes:

1. Non-seasonal
2. Seasonal
3. Seasonal sandbar

See Section B.1.8 for an overview of the equations for a multinomial LR. Locations for which reason A, B or C applies can be characterized by the amount of shoreline jumps equal or larger than 100 meter (dY_{100}). This amount is quantified by P_{dY100}, the percentage of dY_{100} in the data. Therefore, in addition to the seasonal displacement, D_S, the other independent variable for the LR model is P_{dY100}. For more information on P_{dY100}, see Section C.2.1.

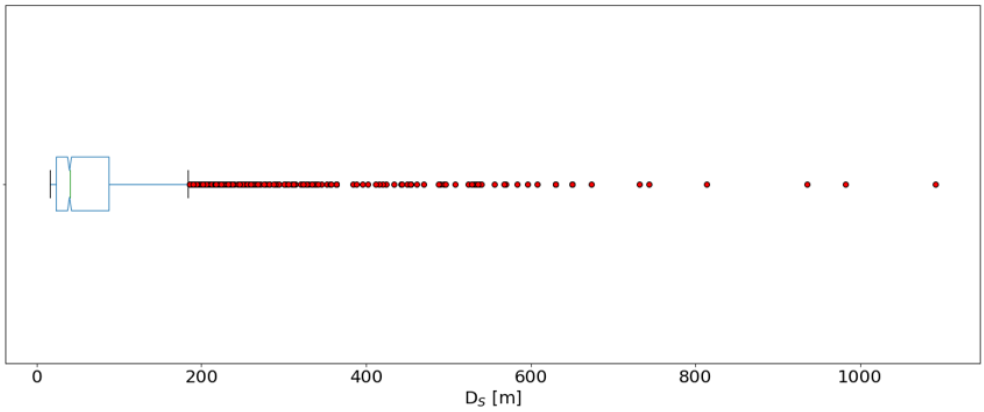

Figure 5.2: Boxplot of seasonal displacements in West-Europe.

The logistic model was trained and tested on a random sample of 100 locations in West-Europe. Verification of the sample is based on:

- Location
- Time series
- Literature

Figure 5.3 shows the verified sample, plotted against the independent variables of the logit, D_s and $P_{dY_{100}}$. This Figure shows a linear relation between the dependent and independent variables. This means that logistic regression can be applied. The logistic regression model is fitted to the sample with a train-test ratio of 80-20%. The resulting estimators and the logit model can be found in Section B.1.8.

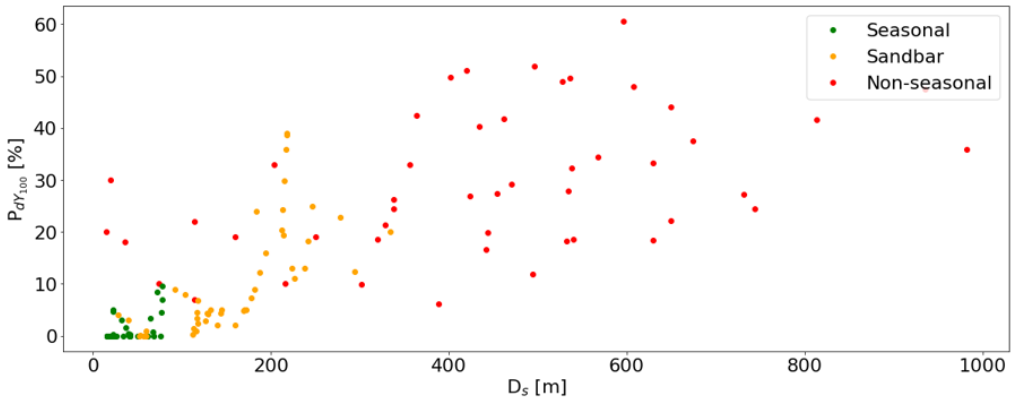

Figure 5.3: Verification of a random sample of 100 transects in West-Europe

Using the logistic regression model, probabilities of outcomes can be calculated. Based on these probabilities, an observation can be categorized as non-seasonal, seasonal or seasonal sandbar. For example, an observation can be categorized as seasonal if the seasonal probability from logistic regression exceeds 50%. The probability threshold is then set at 50%. Probability thresholds can also be set at different values, for example 40 or 60. Figure 5.4 shows PPV, FNR and CSI scores for different probability thresholds. A probability threshold of 40% is found as an optimum value. At this threshold, the precision along with the miss rate is optimal, which can be observed by a maximum CSI score. Simply said, at this threshold the highest precision is obtained with a minimum of false negatives (e.g. seasonal beaches identified as non-seasonal).

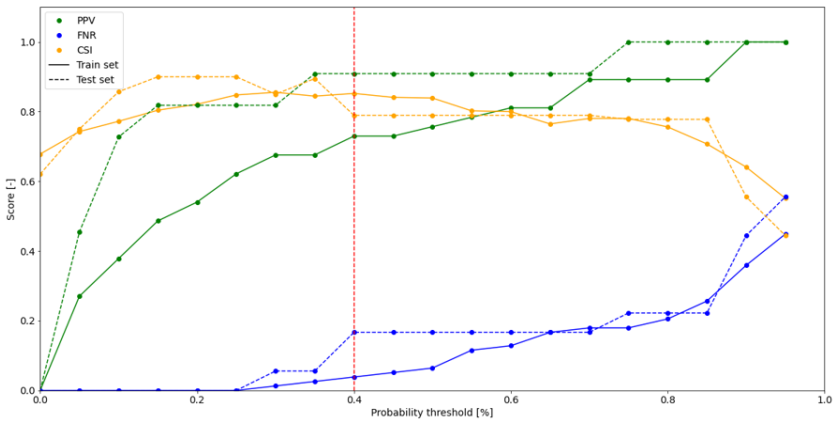

Figure 5.4: Accuracy scores for different probability identification threshold. Results for the train (test) set are indicated with a solid (dashed) line. The optimum value for the probability threshold is indicated with the red vertical dashed line.

The logistic regression model is applied to all transects within hotspots in West-Europe with the following conditions:

1. Locations with a seasonal displacement below 15 meters or a seasonal period that is not in the order of one year are categorized as non-seasonal.
2. Transects where the period of the seasonal component is not equal to one year (11 - 13 months) are categorized as non-seasonal.
3. Transects with more than 30% missing values after March 2013 are left out.
4. Locations are identified as seasonal if the probability from the LR is at least 40%, see Figure 5.4. The same procedure is applied to seasonal sandbars. The remaining transects are categorized as non-seasonal.

Figure 5.6 shows that 22.5% of the transects within hotspots in West-Europe can be identified as a seasonal beach. Looking at a more regional level, at the Dutch coast, seasonal beach behaviour is much more dominant. For this region, more than half of the transects is characterized by seasonal beach behaviour. The occurrence of identified minimum shoreline positions for seasonal beaches in the Netherlands can be found in Figure C.40. Around 78% of the transects that are categorized as seasonal have a minimum width in the months May-July which is consistent with findings from Quartel et al. (2008). Remember, transects that are categorized as seasonal beaches have a precision of 80%. This corresponds to the percentage of locations with minimum shoreline positions identified in the correct period.
The Belgium coast is more dominated by seasonal sandbar behaviour. Here, seasonal sandbars are identified at almost two-thirds of the transects. Beaches in Belgium are characterized by significant tidal ranges (over 4 meters). These meso-tidal environments are generally characterised by multiple intertidal bars (M. Chen and Montreuil, 2017), meaning these bars can rise above the waterline. This explains why at the Belgium coast seasonal sandbars is the dominant outcome of the logistic regression model. In contrary, the Dutch coast has a microtidal environment characterised by subtidal bar systems (Quartel et al., 2008). It thus makes sense that here these seasonal sandbars are detected to a lesser extent. Figure C.39 shows a detailed map of identification of seasonality along the Dutch and Belgium. From Figure 5.5 it can be observed that at a seasonal beach the shoreline positions increases more gradual, while at a beach where seasonal sandbar morphology is present the shoreline positions increases more sudden. These sudden increases are captured in the parameter $P_{dY_{100}}$.

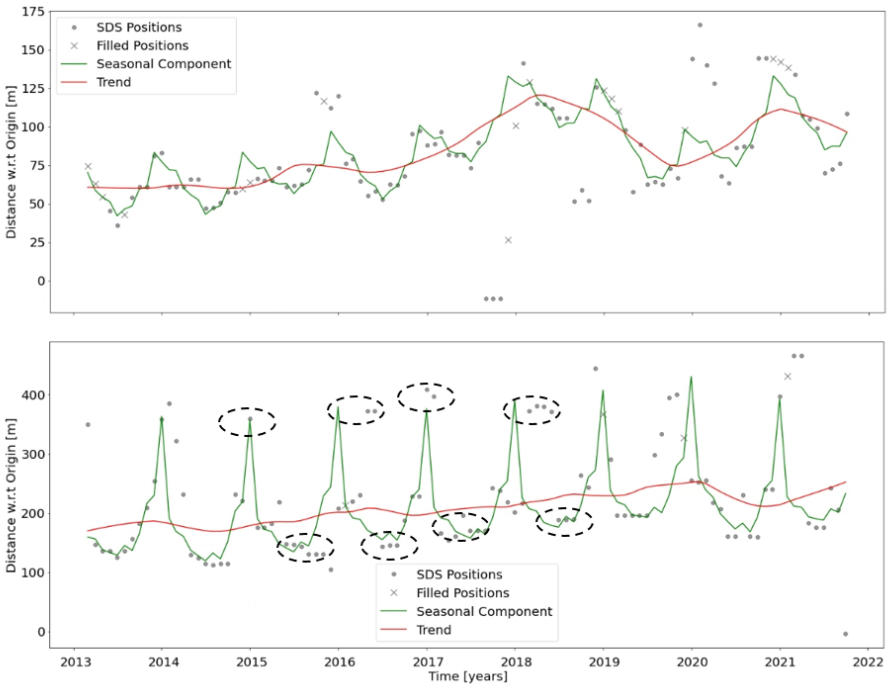

Figure 5.5: Shoreline positions of a seasonal beach at the Netherlands (upper) and of a seasonal moving sandbar in Belgium (lower). The dashed circles in the lower figure indicate the levels of the shoreline positions. The upper circles correspond to the positions of the sandbar while lower positions correspond to that of the beach.

Finally, Figure 5.6 shows that the Mediterranean coast is predominantly characterized by non-seasonal beaches.

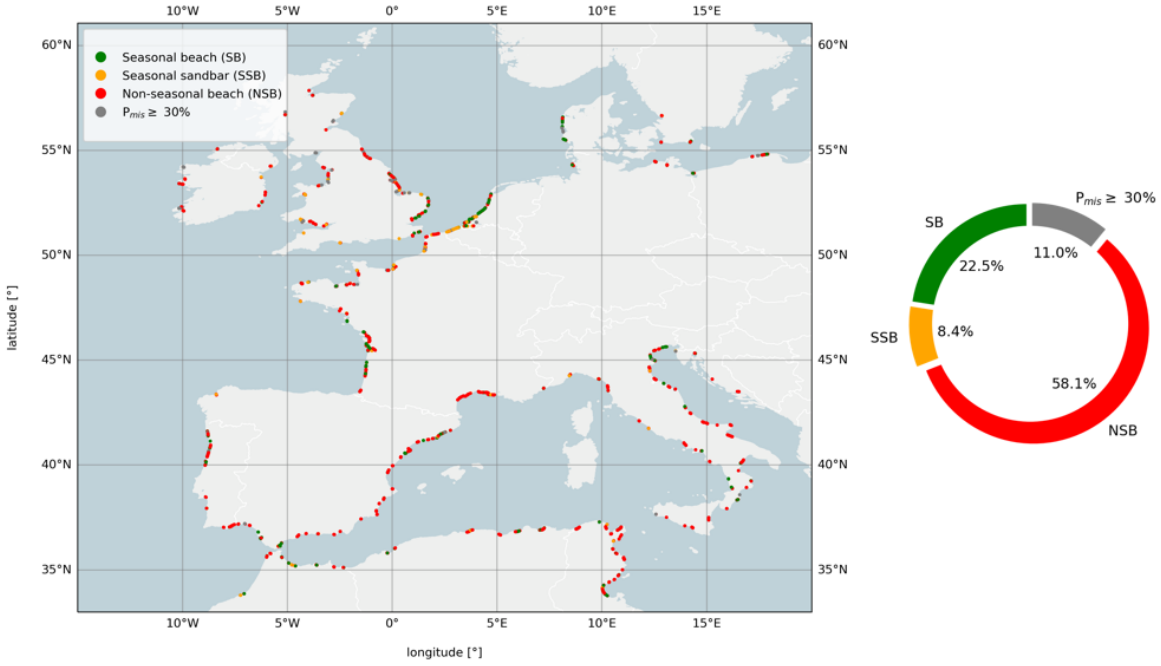

Figure 5.6: Identification of seasonal beaches, seasonal sandbars and non-seasonal beaches in West-Europe.

5.2. Reclamations

Key points

- A refinement of the method was made to correct for outliers in the data. The identification parameter describing the change rate of the positive shoreline jump (dY_{dt}) is corrected by a negative shoreline jump if possible ($dY_{dt,corr}$).
- Based on a manually verified sample of 100 locations, a threshold at 100 m/yr was set at for $dY_{dt,corr}$. With this threshold, precision increased from around 0.3 to 0.5.
- Using the manually verified sample, a sigmoid function was fitted on the precision scores resulting from the parameter M_{RM}. Locations with more than 40% missing data were not taken into account.
- Locations corresponding to a precision score of at least 70% were mostly observed in South-Europe.

A random sample of 10 transects in West-Europe with M_{RM} between 0 and 0.2 was generated to identify performability of the identification method. Verification was done by manual inspection of the locations and the time series. From this sample, 33% of the transects where a jump in the shoreline was observed followed by a fixed coastline, was caused by outliers. Figure C.41 illustrates such a case. These outliers where eliminated by correcting the positive shorelinejump by a preceding negative shorelinejump, if present. The former identification parameter dY_{dt} is replaced by $dY_{dt,corr}$, where the subscript corr is an abbreviation for corrected. This refinement of the method is further explained in Section C.2.2
After this refinement of the model, another random sample containing 100 transects was generated. This sample was, similar to the one used for refinement of the method, manually verified by inspection of the location and time series. Figure 5.7 shows that with respect to $dY_{dt,corr}$, CSI is optimal at a threshold of $dY_{dt,corr}$ equal to 100. This results in an increment of the precision from 0.3 to 0.5 and a false omission rate of only: $\frac{3}{37} \cdot 100 = 8\%$.
The remaining sample consisted of 70 transects, see Figure C.42. Some false positives where still identified in the region corresponding to low M_{RM}. By applying additional thresholds, transects with more than 40% missing values or more than 10% P_{dY100} were removed. This resulted in removal of 75% of the false positive locations with M_{RM} below 0.4, while none of the true positives were affected.

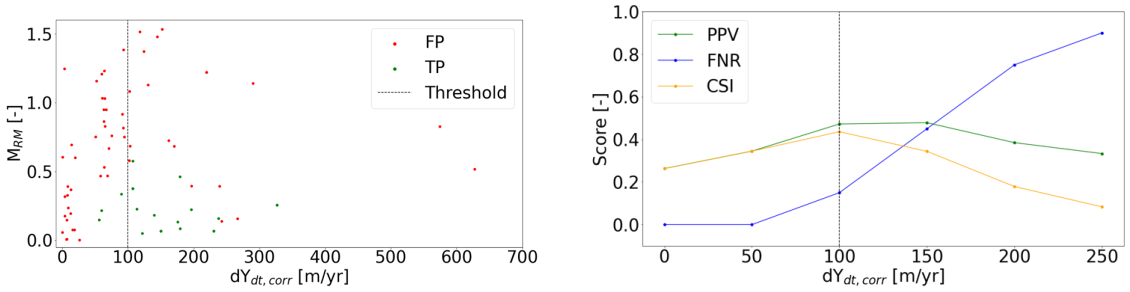

(a) Random sample of 100 transects in West-Europe.

(b) Accuracy scores for different thresholds.

Figure 5.7: Determination of the optimal threshold for $dY_{dt,corr}$ for a random sample of 100 transects in West-Europe. The sample is visualized in subfigure a). True positives (TP) (False negatives (FN)) are plotted with green (red) markers. The optimal threshold is determined with accuracy scores from subfigure b). The black dashed line is the optimal thresholds for $dY_{dt,corr}$, resulting in the maximum CSI.

Next, precision was calculated on the remaining 67 transects for M_{RM} in the intervals [-0.1, 0.1), [0.1, 0.3) etc. The precision value was assigned to the center of each interval. See the result in Figure 5.8. A sigmoid function was fitted to this probabilities. This resulted in the following equation for the precision:

$$PPV_{RM}(M_{RM}) = 1 - \frac{1}{1 + \exp(-11.73(M_{RM} - 0.50)} \tag{5.1}$$

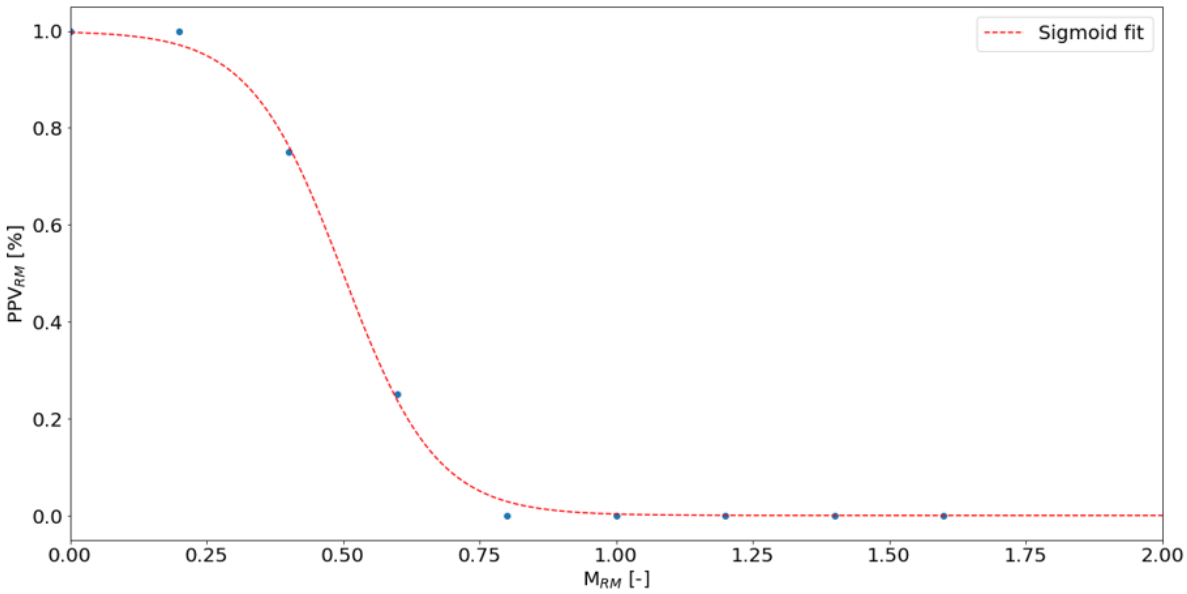

Figure 5.8: Precision (PPV) as a function of M_{RM}. A fitted sigmoid function is indicated with the red dashed line.

Equation 5.1 can be used to assess the probability that the method correctly identified a coastal reinforcement. The result of this Equation applied to all transects within hotspots in West-Europe is shown in Figure 5.9.
Transects were given zero probability if:

1. No shoreline jump was detected
2. The amount of missing values were larger than 40%
3. The amount of dY_{100} was larger than 10%

Transects where $dY_{dt,corr}$ was below 100 were given a probability of 0.08, corresponding to the FOR resulting from this threshold.
Of the 20 transects in West-Europe with the highest probability, only one transect was a false positive. This corresponds to a precision of: $\frac{19}{20} = 0.95$. In this top 20 transects, the minimum PPV_{RM} was 0.95. This shows that Equation 5.1 is a good representation of the data. From the 19 correctly locations, 17 were expansions of terminals in a port.
Figure 5.9 shows the results of identification of reclamations for West-Europe. Overall, reclamations are more common practice in South-West Europe than in the more Northern parts. In South-European ports, volumes of handled cargo's are strongly increasing while in other regions the volume remains stable (Notteboom, 2017). More cargo requires more port terminals resulting in port expansions.

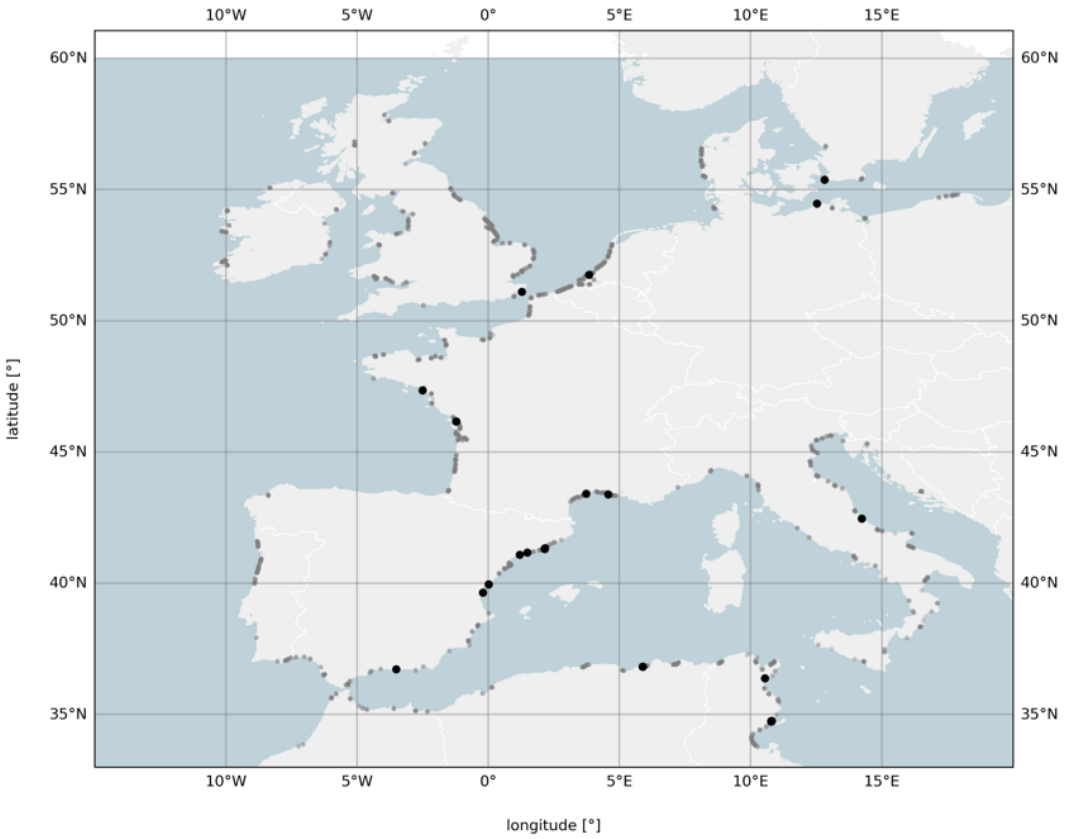

Figure 5.9: Results of identification of reclamations in West-Europe. Locations corresponding to parameters with a precision above (below) 70% are indicated in black (grey).

5.3. Nourishments

Key points

- Nourishments are verified on the Dutch coast as for this location an extensive record of nourishment projects exists. A random sample of 30 identified nourishments was verified.
- Considering only identified nourishments with a change rate after a shoreline jump below -1 m/yr and a lifetime between 3 and 11 years precision increased by 33%.
- Using the verified sample, a sigmoid function was fitted on the precision scores resulting from the spatial scale of the identified nourishments (N_T).
- Locations corresponding to a precision score of at least 70% were mostly identified in the Netherlands, Belgium and Denmark. This are also the countries in Europe were the averaged nourished volume per site are largest.

The Dutch coast has an extensive record of nourishments dating back from 1965 [1]. Therefore, identification of this driver is verified at this coast. Furthermore, since the 90's, not only beach nourishments, but also shoreface nourishments have been widely used in the Netherlands (M. Stive et al., 2013).
Nourishments are characterized by a widening of the beach followed by erosion. In the case of a beach nourishment this is a sudden increase where a shoreface nourishment is more characterized by a gradual increase. Nourishments are only identified if erosion after a shoreline jump has a minimum change rate of -1 m/yr. A threshold for the lifetime was determined with a random sample of 30 verified nourishments along the Dutch

[1] https://www.openearth.nl/coastviewer-static/

coast. A lifetime between 3 and 11 years resulted in the highest precision, see Figure C.43. Without these thresholds, precision was equal to: $\frac{10}{20} = 0.50$. With thresholds, precision increased to: $\frac{10}{15} = 0.67$. This is an increment of 33%. After applying these threshold, the FNR remained zero. Both these thresholds are also in correspondence to the results of the local case studies, see Section 4.5. Similar to reclamations, only locations with less than 40% missing values were considered.
The remaining identification parameter, N_T is further used to quantify the correctness of the identification method. That is to say, if a signal is observed in more transects, confidence of correctness increases. For the remaining 15 nourishments from the sample, precision is calculated for N_T equal to 1, 2, 3 etc., see Figure 5.10. Next, a sigmoid function was fitted to the precision outcomes. This results in the following equation that can be used to quantify the probability of the correctness of identification:

$$PPV_{NM}(N_T) = \frac{1}{1+\exp(-2.31(N_T - 3.92))} \tag{5.2}$$

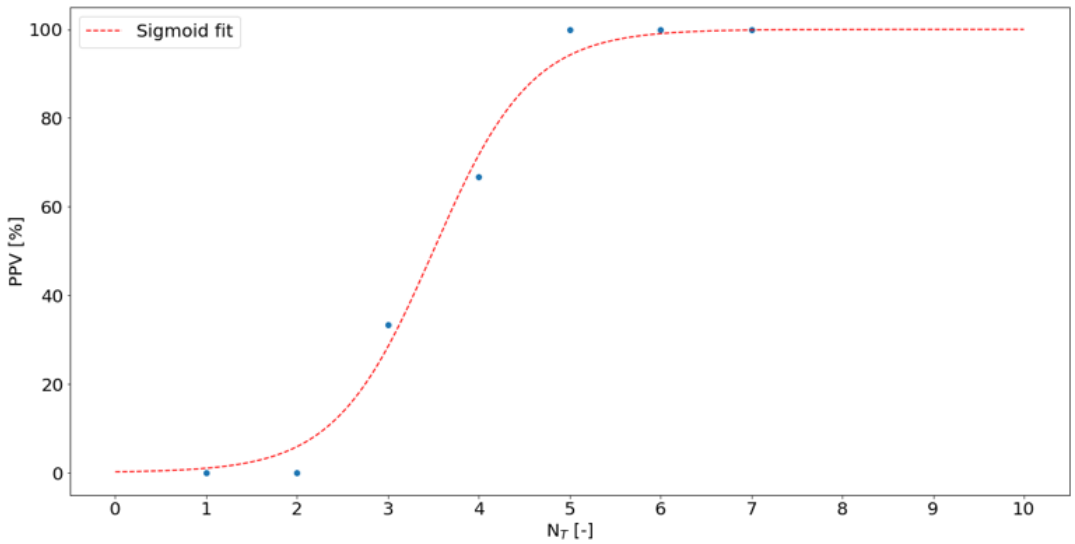

Figure 5.10: Precision ($PPV_{NM}(N_T)$) for various N_T. A fitted sigmoid function is indicated with the red dashed line.

Finally, for all transects in hotspots in West-Europe nourishment identification probabilities were calculated using Equation 5.2, see Figure 5.11. Nourishments were primarily identified on the Dutch and Belgium coast. For the Netherlands this can be explained by the fact that average nourished volumes per site (3.7 Mm^3) are much larger than in other European countries (0.5 Mm^3) (Hanson et al., 2002) and nourishments are thus more likely to be larger than normal shoreline variability. Also in Belgium, nourishments have regularly been carried out, particularly beach nourishments (Martens et al., 2007). Section 4.5 already indicated that the method was not capable of identifying nourishments that fall within normal shoreline variability. According to Hanson et al. (2002) the average lifetime of nourishments in the Netherlands is around 5 years. This is supported by the identification method, see Figure C.45.
Another European country with large average beach nourishment volumes per site is Denmark, 2.4 Mm^3. Figure 5.11 indicates two locations in Denmark with high identification probabilities for nourishments. These locations identified by the method correspond to the region in Denmark where beach nourishments are common practice, see Figure C.44.
An importance notice is that characteristics of nourishments are not similar for different regions in Europe (or the world). For example, the average return interval (lifetime) for nourishments is around 5 years in the Netherlands (as well as Spain, the UK and Denmark). In other countries, however, this value is around 25 years (Hanson et al., 2002). Nonetheless, verification and refinement of the method was based on only one region, The Netherlands.

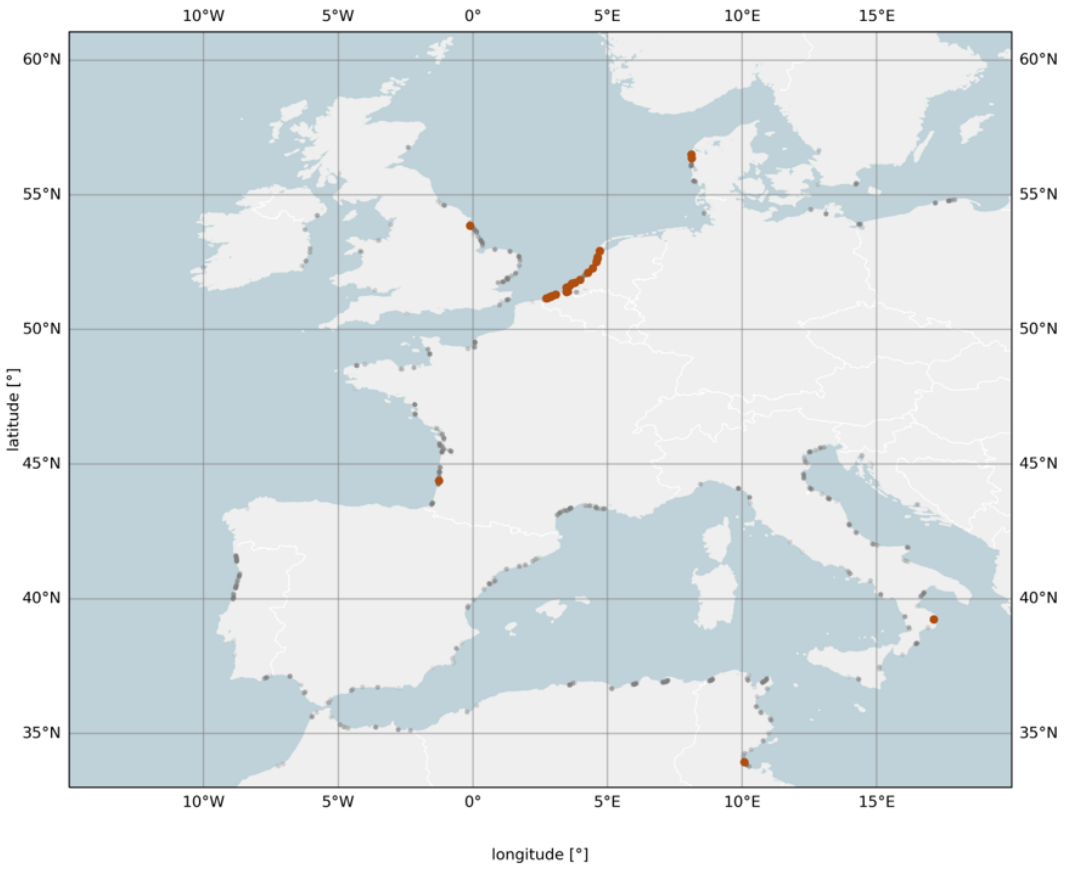

Figure 5.11: Results of identification of nourishments in West-Europe. Locations corresponding to parameters with a precision above (below) 70% are indicated in brown (grey).

5.4. Littoral drift barriers

Key points

- Verification was done on a random sample of 180 locations in West-Europe.
- Only locations where the closest 33% accreted twice the amount of the furthest transects are considered. By applying this threshold, as well as removing locations with non-linear trends, precision increased by 95%.
- Using the verified sample, precision scores were determined for combinations of the spatial scale of the identified littoral drift barriers (N_T) and the linearity of the shoreline evolution towards the barrier ($R_{2,LDB}$).
- Pairs and double updrift LDB types are sometimes incorrectly typified as single up- or downdrift.

Littoral drift barriers are characterised by three identification parameters. Two of them, M_{LDB} and $R_{2,LDB}$, describe the increasing shoreline evolution towards the barrier. The third parameter, N_T, takes the spatial aspect of LDBs into account. To identify the perfomability of the identification method a random sample of 180 hotspots was generated. For this sample, the method has a precision of: $\frac{33}{33+147} = 0.18$.
After removing locations with non-linear trends, precision increased to 0.26. Trends are characterized as non-linear when there are more than 2 characteristics (N_{chars}). Furthermore, accreting trends (updrift locations) with a final strong erosive characteristic is not assumed to be caused by a littoral drift barrier. The same applies to erosive trends (downdrift locations) with a final accreting characteristic.

For M_{LDB} a threshold was set at 1 as here the CSI is maximum, see Figure 5.12b. This threshold means that only hotspots are taken into account for identification where the closest 33% accrete at least twice the amount of the furthest transects. This resulted in a FOR of $\frac{6}{6+39} = 0.13$ while precision increased to 0.35.

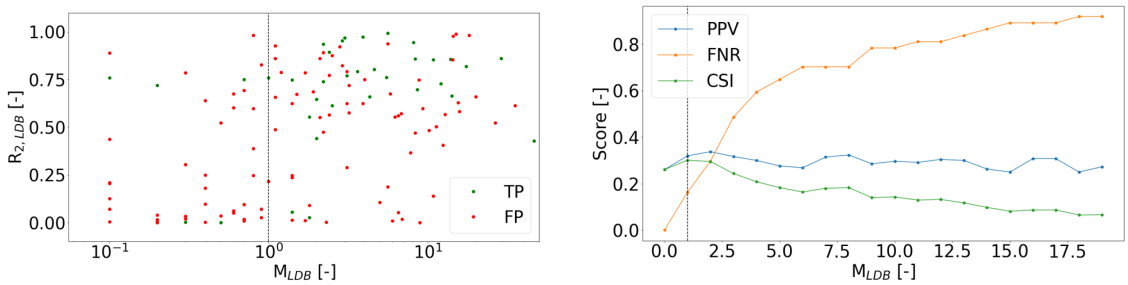

(a) Random sample of hotspots in West-Europe

(b) Accuracy scores for different thresholds

Figure 5.12: Determination of the optimal threshold for M_{LDB} for a random sample of hotspots in West-Europe. The sample is visualized in subfigure a). True positives (TP) (False negatives (FN)) are plotted with green (red) markers. The optimal threshold is determined with accuracy scores from subfigure b). The black dashed line is the optimal thresholds for M_{LDB}, resulting in the maximum CSI.

The sample points remaining after applying the threshold for M_{LDB} are divided into five regions (I-IV). The split between regions is made such that each region contains a significant amount of data, see Figure 5.13a. Here, samples are plotted with respect to the remaining two identification parameters, $R_{2,LDB}$ and N_T. Next, for each region, precision scores are calculated, see Figure 5.13b. With a linear fit precision scores between regions are interpolated. How this interpolation is done based on the two identification parameters is treated in Section C.2.4.

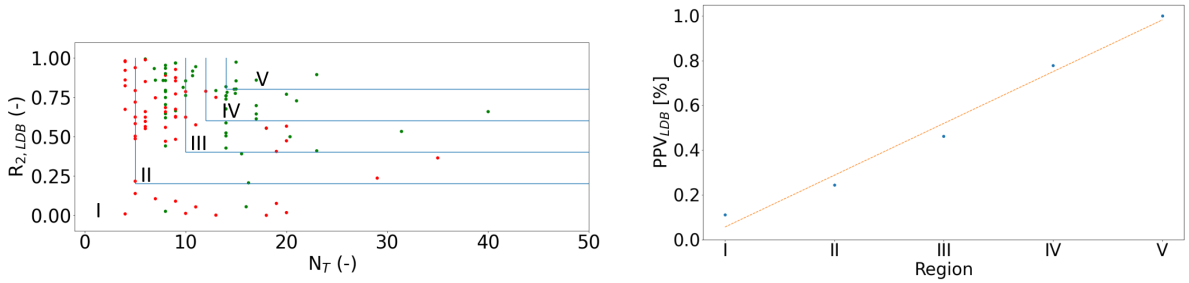

(a) Sample divided into five regions (I-IV)

(b) Precision scores per region. A FOPF is indicated with the dotted orange line.

Figure 5.13: Estimating precision scores for the sample. The sample is visualized in subfigure a). True positives (TP) (False negatives (FN)) are plotted with green (red) markers. The sample is divided into five regions (I-V). Subfigure b) shows the precision scores per region.

Finally, probability of correct identification can be calculated with the following conditions:

1. Hotspots with non-linear trends are given zero probability
2. If M_{LDB} is below 1, a probability of 0.13 is assigned. This corresponds to the FOR of this threshold.
3. If none of the conditions described above apply, probabilities are calculated using the technique described in Section C.2.4.

Figure 5.14 gives an overview of locations in Wes-Europe with a precision of at least 70%. There are 13 locations in total from which four are identified wrong, this thus corresponds to a precision of 69% for hotspots identified with a probability of correctness above 70%. The main reason for these false positive is wrongy extracted hotspots due to DWI transects. This is observed for example in the port of Castellon de la Plana in Spain.
Of the 9 locations where the method correctly identified littoral drift barriers as a driver of shoreline evolution, the type of hotspot (updrift, downdrift etc) was predicted incorrect in 3 cases. These errors are caused by the fact that down- or updrift regions were not identified as a pair or a double updrift. Below three reasons causing mistakes here are listed:

1. At only one side of the barrier the identification method captures the desired signal from a LDB. This can be for example be caused by a shoreline signal distorted by a series of groynes at the other side.

2. A hotspot is not captured in the dataset created using the method of Kras (2019).
3. The hotspot identified using the method from Kras (2019) does not correspond to the region of influence of the LDB.

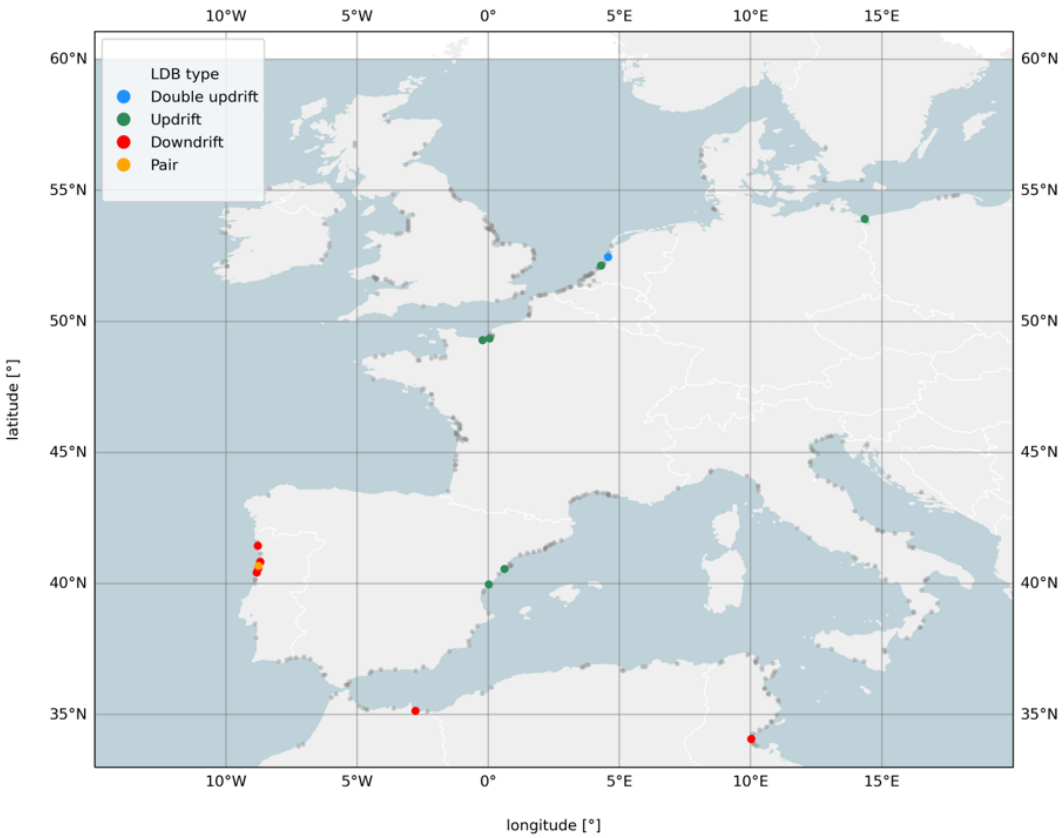

Figure 5.14: Results of identification of littoral drift barriers for West-Europe. Locations with a precision of at least 70% are indicated with a coloured marker corresponding to the LDB type. Remaining locations are indicated with a grey marker.

5.5. Summary: regional verification

In Chapter 4, the results were presented for identification of drivers on a local scale. The findings in this chapter can be used to answer the first research question. This chapter explored identification of drivers of shoreline evolution on a larger scale, the West-European coastline. Drivers are only identified for so called hotspots; coastal stretches with high variability containing ajdacent transects with similar characteristics both in time and space. Results presented in this chapter can be used to answer the second research question:

What are the optimal settings to identify drivers using regional verification?

As mentioned before, climate variability and beach rotation were only addressed at a local scale in Chapter 4 and are not considered in the remaining of this study. For the remaining drivers the results for identification on the West-European coastline are shortly summarized.

Seasonality
The seasonal displacements for the locations with a seasonal component with a period of a year resulted in quite some unrealistic values. This could be caused by either a seasonal moving sandbar that was identified as the most landward position or erroneous time series. Therefore, a logistic regression model was applied to identify whether a beach was seasonal, non-seasonal or a seasonal sandbar was present. Whereas a seasonal beach showed a more gradual increase and decrease of shoreline positions, a seasonal sandbar resulted in a sudden jump of the shoreline position. The logistic function was a combination of the seasonal displacement and a parameter describing the amount of shoreline jumps larger than 100 meter. The model was trained and tested on a mainly manual verified (random) sample of 100 locations in West-Europe. Classifying a location as a seasonal beach if the probability of the logistic regression was at least 40%, resulted in a precision of 80%. For West-Europe, the following results regarding seasonality were observed:

- The Dutch coast is primarily dominated by seasonal beach behaviour.
- The Belgium coast, a meso-tidal environment (M. Chen and Montreuil, 2017), is characterized by seasonal sandbar morphology.
- In the Mediterranean predominantly non-seasonal beaches were identified.

- - - - - - - -

The remaining three drivers were not identified using a logistic regression model. For these drivers, a random sample of locations was manually verified and precision scores were calculated for ranges of the identification parameters. Next, precision of identification for individual identification parameters were obtained by interpolating between these ranges. Remember that precision was defined as:

$$PPV = \frac{TP}{FP + TP}$$

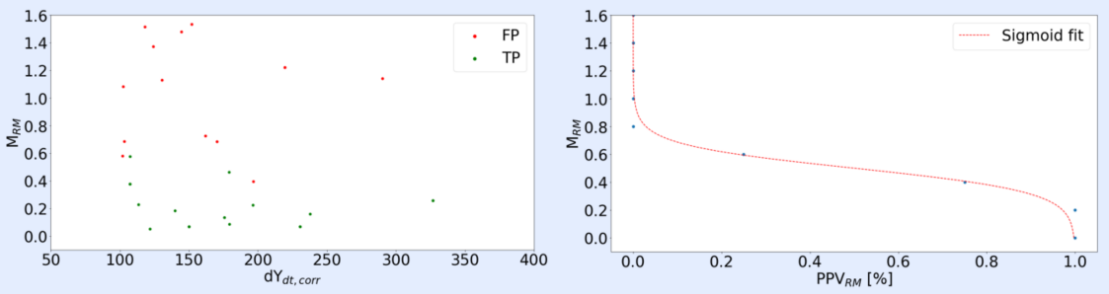

Shoreline evolution at a location was linked to a particular driver if the identification parameters corresponded to a precision score of at least 70%.

5.5. Summary: regional verification

Reclamations
Overall, reclamations are more common practice in South-West Europe than in the more Northern parts. Of the 20 locations with the highest precision for this driver, 17 were found to be an expansion of a port terminal. In South-European ports, volumes of handled cargo's are strongly increasing while in other regions the volume remains stable (Notteboom, 2017). More cargo requires more port terminals resulting in port expansions. This result indicates that a link can be made between this driver and port development.

Nourishments
Nourishments were primarily identified on the Dutch and Belgium coast. For the Netherlands this can be explained by the fact that average nourished volumes per site (3.7 Mm^3) are much larger than in other European countries (0.5 Mm^3) (Hanson et al., 2002) and nourishments are thus more likely to be larger than normal shoreline variability. Also in Belgium, nourishments have regularly been carried out, particularly beach nourishments (Martens et al., 2007).

Littoral drift barriers
In West-Europe there are 13 hotspots in which shoreline evolution is linked to a littoral drift barrier. From these 13 hotspots, four are identified wrong, thus indeed corresponding to a precision of 70%. Of the 9 locations where the method correctly identified littoral drift barriers as a driver of shoreline evolution, the type of hotspot (updrift, downdrift etc) was predicted incorrect in 3 cases. These errors are caused by the fact that down- or updrift regions were not identified as a pair or a double updrift. This may be caused by the incorrect spatial extension of an extracted hotspot and consequently the inability of the method to capture the increasing evolution of the shoreline to a barrier. Moreover, in the case of the presence of a groyne field, with spacings in the order of the distance between transects, the increasing shoreline evolution towards a barrier is also not captured. In both cases low precision scores are obtained and shoreline evolution is not linked to a littoral drift barrier.

6

Global results

The identification methods and parameters resulting from these methods were validated and verified in the Chapters 4 and 5. Based on the analyses made here, this Chapter will present the results for driver identification and characterization on a global scale in Section 6.1 and 6.2 respectively. Together, these sections will provide the results to answer the final sub-question stated in Section 1.4. Identification is done using the settings that were found from the regional verification (Chapter 5) and only for transects within a hotspot. Except for seasonality, identification and characterization is based on locations corresponding to identification parameters with a precision score of at least 70%. For seasonality, similar as in Section 5, this threshold is set at 80%. Finally, Section 6.3 provides a summary of this chapter.

6.1. Identification of drivers at a global scale

Key points

- Seasonal beaches are mostly observed in Central-America, Northern-Europe and Africa. Seasonal sandbars are most identified in Belgium, the Middle East and Australia. However, in the Middle East, identification of sandbars is actually caused by a seasonal variation of the water level together with (coral) reefs identified as the most landward position. The Mediterranean coast is characterized by non-seasonality.
- Reclamations are observed most in the Middle East and East-Asia. On a global level, the amount of constructions of reclamations has remained stable over the periods 1987-1996, 1997 - 2006 and 2007-2016.
- In the Western world, nourishments are mostly identified compared to other regions in the world. Furthermore, for the identified nourishments in the last decade, an average increase of 66% was found compared to the period 1988-2008.
- Shoreline evolution caused by littoral drift barriers is mostly observed in North-America, Africa and Europe. In Africa, hotspots are mostly identified as downdrift whereas in North-America and Europe mostly updrift regions are identified. A combination of a downdrift and updrift region, a pair, is on a global level observed in less than 2% of the cases.

6.1.1. Seasonality

Figure 6.1 shows that about one-third of the transects within the hotspots exhibit seasonal behavior (beach or sandbar). Around half of the transects are identified as non-seasonal. Nearly 20% of the locations where left out of this analysis because there where too much missing values for this method to work (≥ 30%).

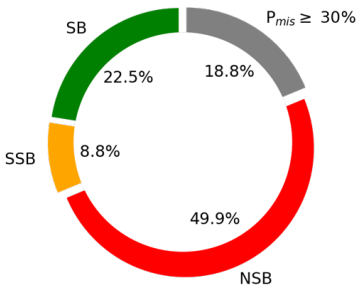

Figure 6.1: Proportions of each seasonal driver category on a global scale. Locations with more than 30% missing values were left out of this analysis and indicated in grey.

For the three categories (seasonal beach, seasonal sandbar and non-seasonal), the transects in countries that are among the top 10 where, percentage-wise, the most transects are in one of these categories are shown in Figure 6.2. Only countries containing at least 30 transects and with an average missing percentage of less than 30% are considered.

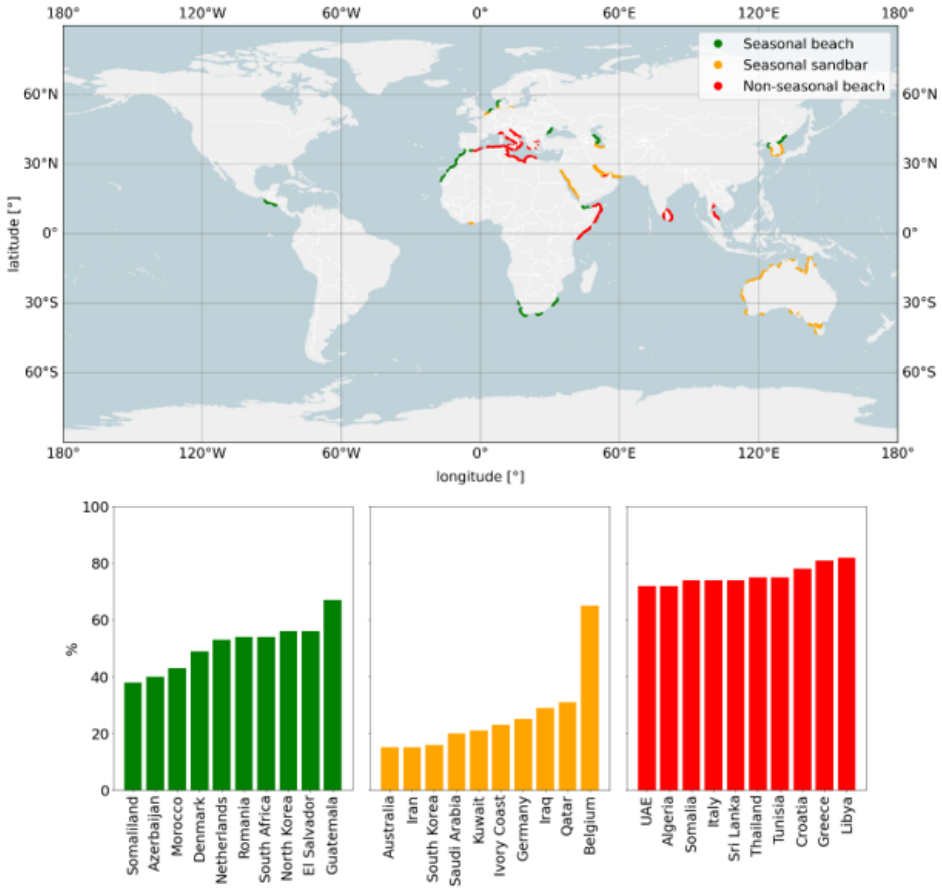

Figure 6.2: Overview of the top 10 countries per category from the logistic regression. Only countries with at least 30 transects and where the average missing percentage was below 30% are considered.

The main observations from this figure are:

1. Seasonal beaches are mostly observed in Guatemala and El Salvador. These are neighbouring countries with a geographical setting in Central-America. For Guatemala and El Salvador, 67 and 56 percent of the transects within hotspots where identified as seasonal beaches respectively. Besides one loca-

tion in Asia, the remaining top-10 countries are found in either Africa or Europe. Almost all the regions were beach seasonality is dominant are open-coasts where wave heights vary strongly with the seasons. Furthermore, Section 2.2.3 states that seasonality is a secondary cause of shoreline variability and thus not the cause of shoreline evolution resulting in hotspot formation. Therefore, seasonality is identified only in locations where shoreline evolution is dominated by another (primary) driving force. Thus, it is important to note that if shoreline evolution in hotspots at a location is primarily associated with reclamations, seasonality will not be determined here. This result is thus not representative for regions neighbouring to this hotspot. On the other hand, in the Netherlands, shoreline evolution is primarily linked to nourishments and littoral drift barriers (see Section 6.1.3 and 6.1.4). This has as a consequence a dominant identification of seasonal behavior. Moreover, the wave climate in the North Sea shows large variation between winter and summer periods, see Figure D.3. In the Caspian and Black Seas, some areas characterized by seasonal beach behavior have also been identified. In these areas, however, the wave climate is not very energetic due to a limited fetch. Here, shoreline development on a seasonal scale in these areas is not caused by a variation in wave height, but by water level elevations due to evaporation and freshwater runoff (J. Chen et al., 2017; Cazenave et al., 1997), see Figure 6.3. This type of seasonal shoreline variations can also explain identified seasonality in other small (semi-)enclosed water basins as the Red sea and the Persian Gulf.

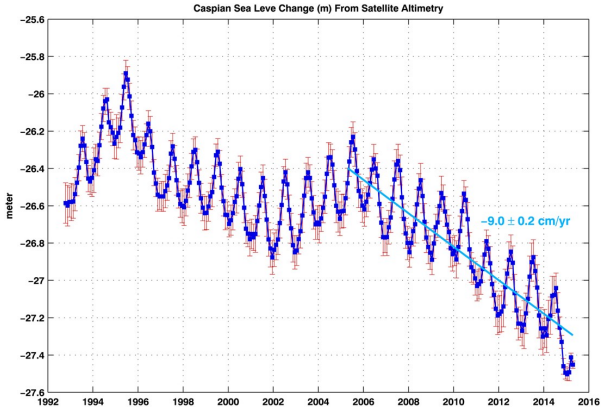

Figure 6.3: Annual and long-term water level variations in the Caspian Sea. (Source: J. Chen et al., 2017

2. Belgium is by far the leading country with transects identified as seasonal sandbars. Interestingly, of the top 10 countries with the most identified sandbanks, 6 are located around the Persian Gulf and Red Sea. In this region, seasonality is not dominated by the wave climate as this is an area with a low-energetic wave climate (Langodan et al., 2017), but similar as in the Caspian sea by water level elevations, see Figure 6.4. These are controlled in this area by steric effects, evaporation rates and long-shore wind stresses (Abdelrahman, 1997). This has large effects on the shoreline positions as the Red Sea is characterized by a shallow continental shelf (Abdelrahman, 1997). Furthermore, this region is characterized by a bathymetry with coral reefs (Fine et al., 2019). If the water level drops, these reefs might be identified as the most seaward shoreline position. Characteristics are then similar to a seasonal moving sandbar.

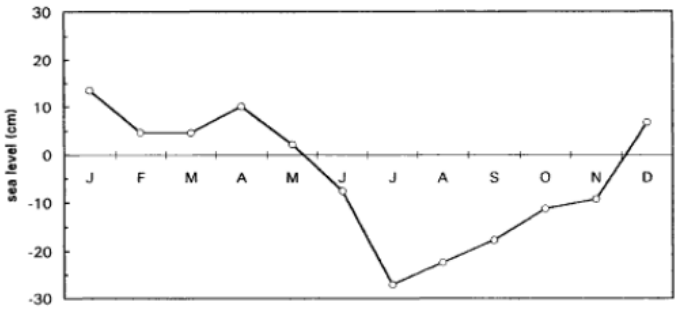

Figure 6.4: Annual water level fluctuations at Jazan, Saudi Arabia. (Source: Abdelrahman, 1997)

3. Non-seasonal beaches are mostly observed around the Mediterranean sea. Of the top 10 countries with most non-seasonal beaches, 6 of them are found in this region. An explanation for this can be found in Figure D.4, which shows that the wave height differences between summer and winter in deeper water in this region are only about 1 meter. Moreover, seasonal water level variations in the Mediterranean are small and only in the order of few centimeters (Marcos and Tsimplis, 2007). The fact that sea level fluctuations do not account for seasonality in the Mediterranean, but do in other smaller basins, can be explained in part by the fact that evaporation in a basin is inversely proportional to the surface area of the water (Linacre, 1977). In comparison, the surface area of the Mediterranean is more than 6 times as large as the red sea (Encyclopedia, 2013; Encyclopedia, 2015).

Furthermore, on a continental scale also some differences can be observed, see Figure 6.5. North America has the largest proportion of identified seasonal beaches, while the smallest proportion is observed in South America . This continent also has the largest proportion of transects with missing values above 30%. In the remaining four continents, the proportion of seasonal beach behaviour is more or less equal. Seasonal sandbanks are most commonly observed in Oceania and Asia, while this category is less dominant in Africa and South America.

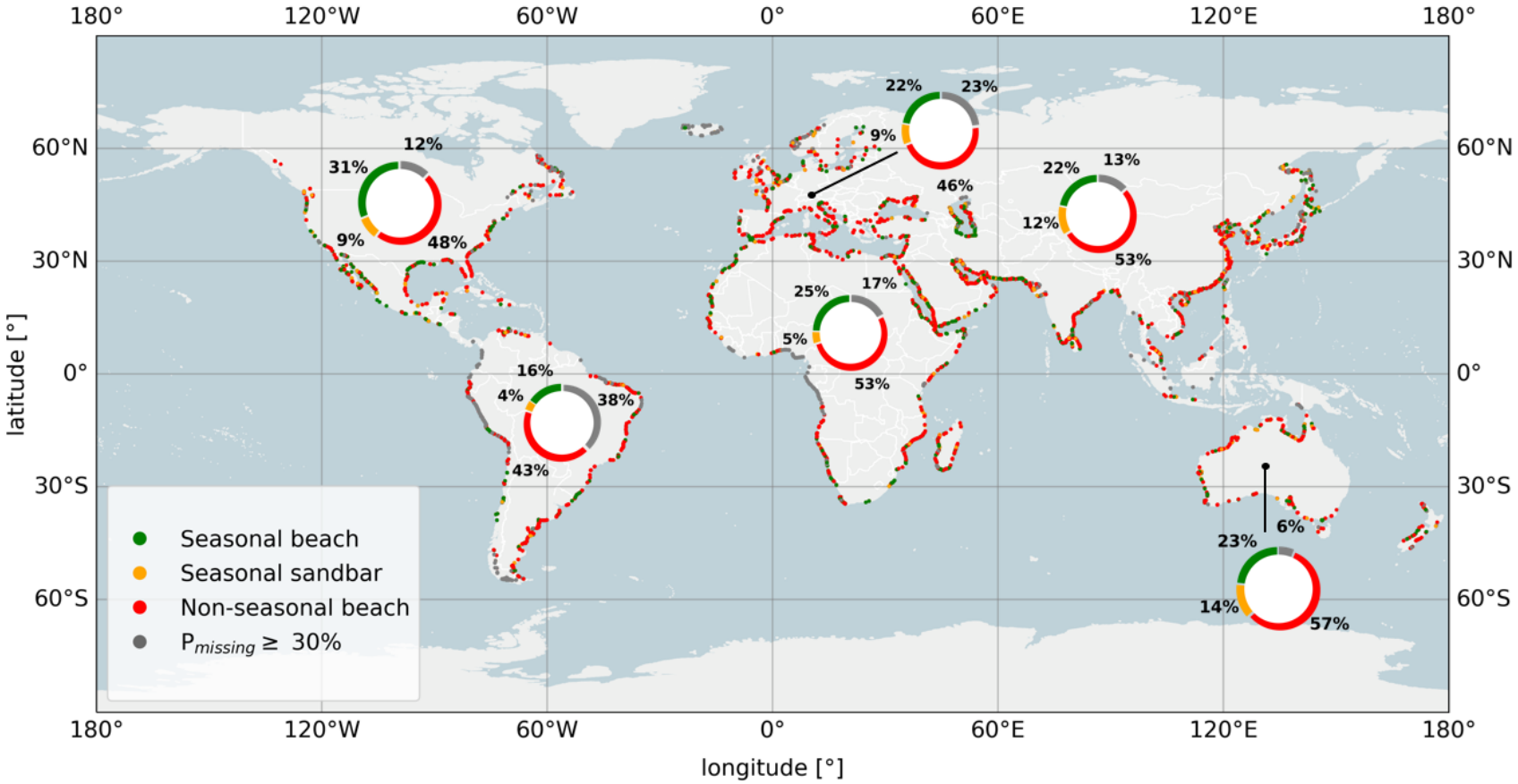

Figure 6.5: Global identification of seasonal beaches. Pie charts indicate the proportion of each category per continent. Locations with more than 30% missing values were left out of this analysis and indicated with grey.

6.1.2. Reclamations

The most reclamations occur by far in Asia, see Figure 6.6 and 6.8. In Oceania, Europe and South-America, reclamations are much less common. Looking at North-America in Figure 6.8, it becomes clear that reclamations are mostly applied in the southern United States and Central-America.

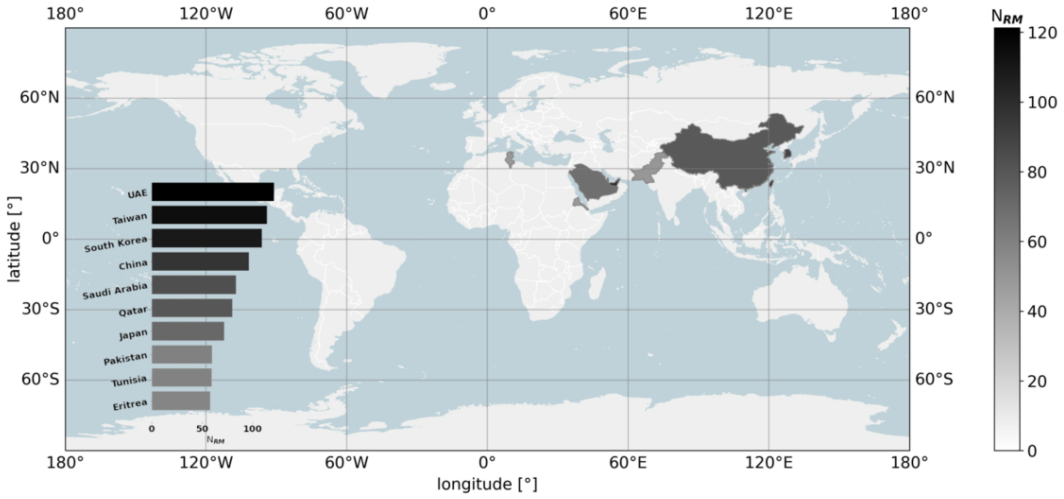

Figure 6.6: Top-10 countries with the most reclamations per 1000 transects (N_{RM}). Only countries containing at least 50 transects are considered.

The global identification map, as well as Figure 6.6 indicate that regions in the world where reclamations are most commonly applied are the Middle East and South-East Asia. The top 7 locations where relatively most reclamations are observed are located in these two geographical regions. The remaining three locations are closely located to these regions. In Section 5.4, it was already observed that most identified reclamations were found as a result of expansion of port terminals. Therefore, a link can be made between this global dataset and port development. Looking at Figure D.1, showing port development over the period 1970-2009, it can be observed that especially ports located in East-Asia are rapidly growing. Also the Middle East shows some areas where ports are increasingly developing.
Figure 6.7 indicates that the amount of constructed reclamations remained more or less constant over the periods 1987-1996, 1997-2006 and 2007-2016. Moreover, also in absolute terms, the Middle East and especially East-Asia have a large contribution on a global scale to the total amount of constructed reclamations.

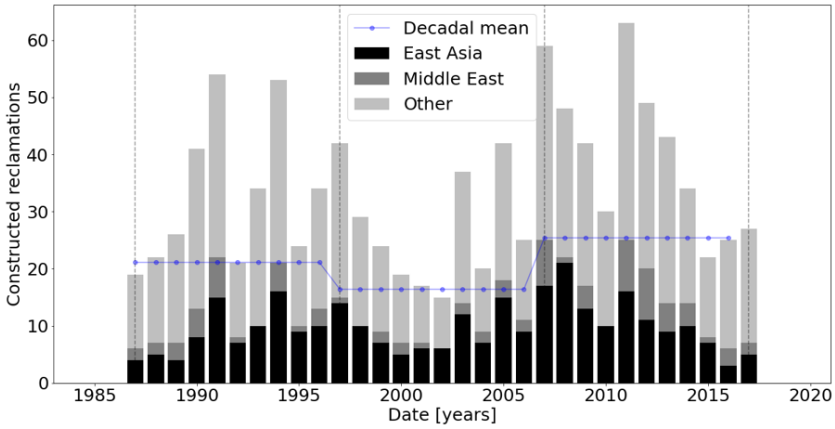

Figure 6.7: Barplot of the number of reclamations (per 1000 transects) for the period 1984-2021 on a global level. The mean in the periods 1988-1998, 1998-2008 and 2008-2018 are indicated with the dotted blue line and have a value of 49.6, 24.2 and 29.2 respectively. Dashed grey lines indicate the start and end of a period.

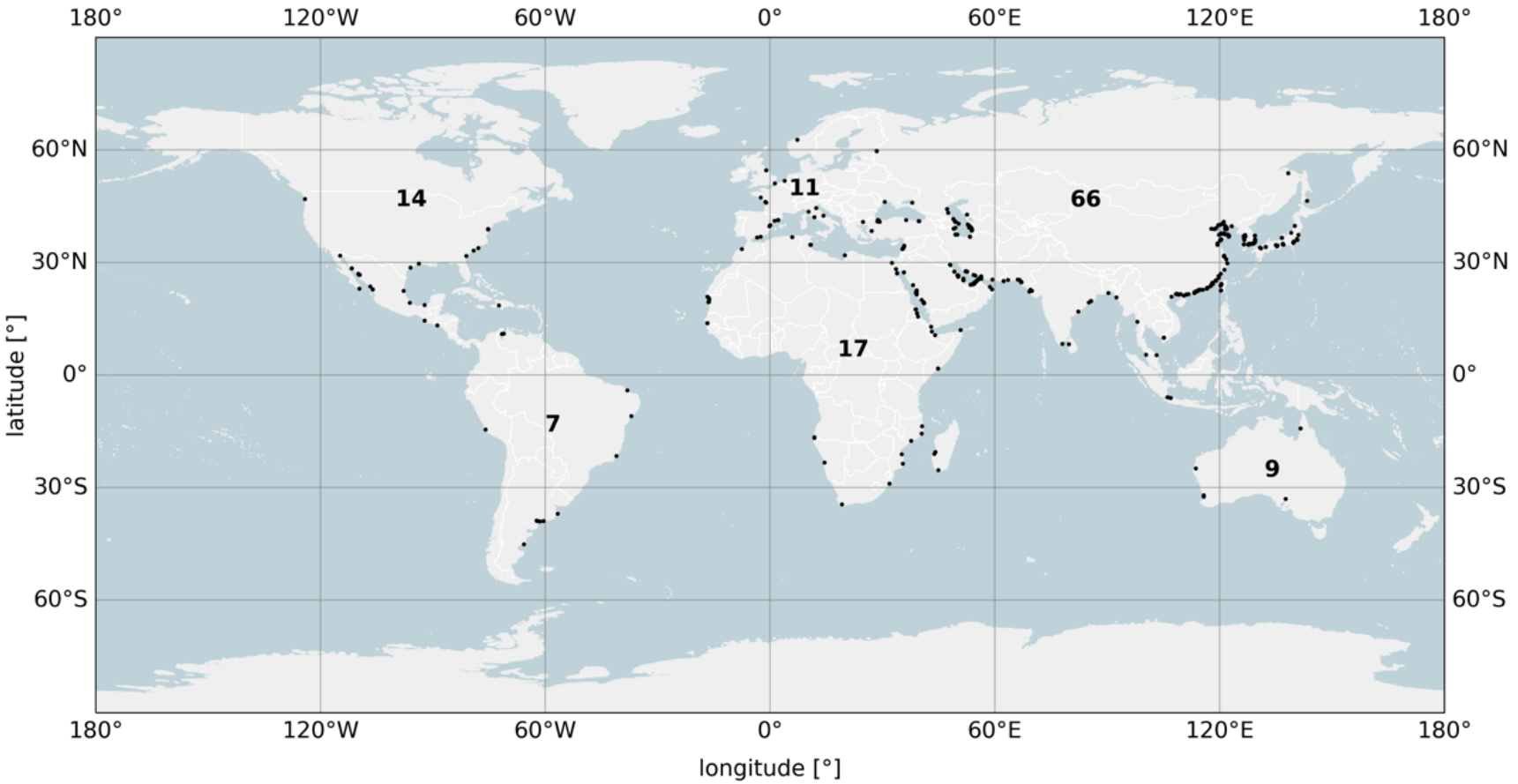

Figure 6.8: Global identification of reclamations. The black markers correspond to a transects where the identification parameters of reclamations have a precision of at least 80%. The number is bold indicate per continent the amount of reclamations per 1000 transects.

6.1.3. Nourishments

Figure 6.9 shows countries in the world were nourishments are applied most frequently. This Figure shows that more than half of these countries belong to the Western world. Countries corresponding to the Western world are indicated in Figure 6.12. Especially the Netherlands and the USA are countries well known for combating coastal erosion by applying beach nourishments (Hanson et al., 2002). This practice of artificial beach widening finds it origin in the USA in the 1920's (Massiani, 2013). Since the 1970's, nourishments were applied in Australia and New Zealand as well (Davison et al., 1992). As mentioned in Section 5.3, in Denmark nourishments are also frequently used to counter erosion. Figure 6.6 shows indeed that in these regions nourishments are often identified.

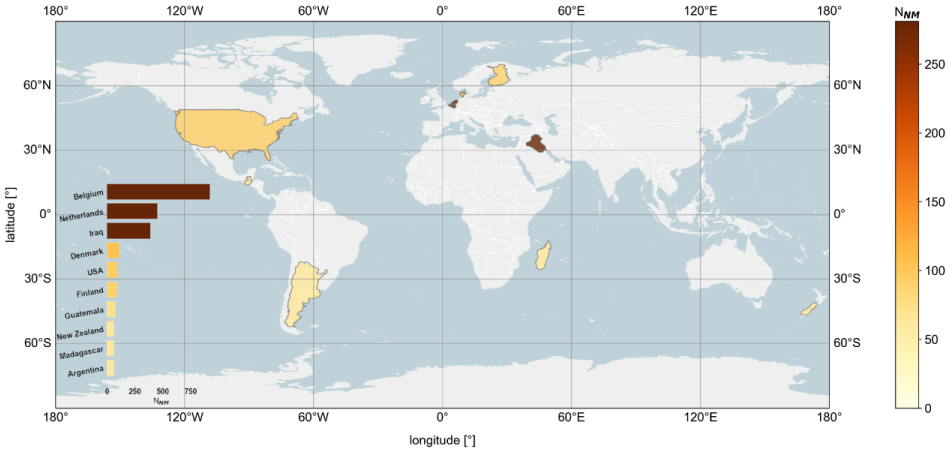

Figure 6.9: Top-10 countries with the most nourishments per 1000 transects (N_{NM}). Only countries containing at least 50 transects are considered.

For Iraq, taking a third position in this top-10, no records of nourishment projects exist. Therefore, in Figure 6.10 time series are highlighted of two transects in which a nourishment is detected in Iraq. From this figure it becomes clear that although the smoothed time series shows a behaviour corresponding to that of a nourishments, the original SDS shoreline positions do not reflect this behavior. The smoothed trend after the detected shoreline jump is thus not representative for the original shoreline positions.

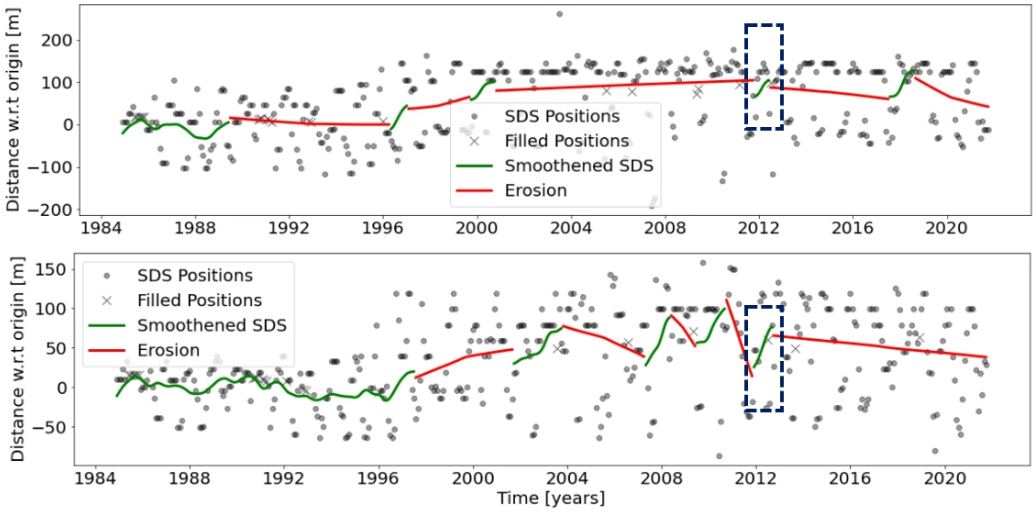

Figure 6.10: Nourishments in Iraq at BOX_145_228_60 (upper) and BOX_145_228_61 (lower). The blue dashed boxes indicate the year in which in both transects a possible nourishment is detected.

Figure 6.11 shows that in the period 2007-2016 the average amount of nourishments increased compared to its two previous decades. While in the periods 1987-1996 and 1997-2006 the number of nourishments remained more or less stable, an increment of over 66% was observed in the next decade.

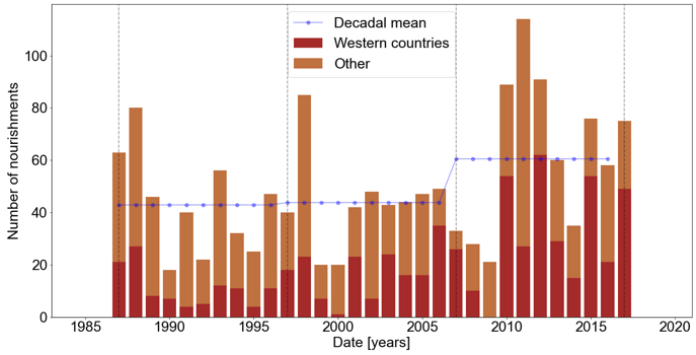

Figure 6.11: Barplot of the number of constructed nourishments per year on a global level. The mean in the periods 1988-1998, 1998-2008 and 2008-2018 are indicated with the dotted blue line and have a value of 41.1, 37.4 and 62.4 respectively. Dashed grey lines indicate the start and end of this period.

An overview of all identified nourishments on a global scale can be found in Figure 6.12. Also from this figure it can be observed that nourishments are mostly observed in Oceania, North-America and Europe.

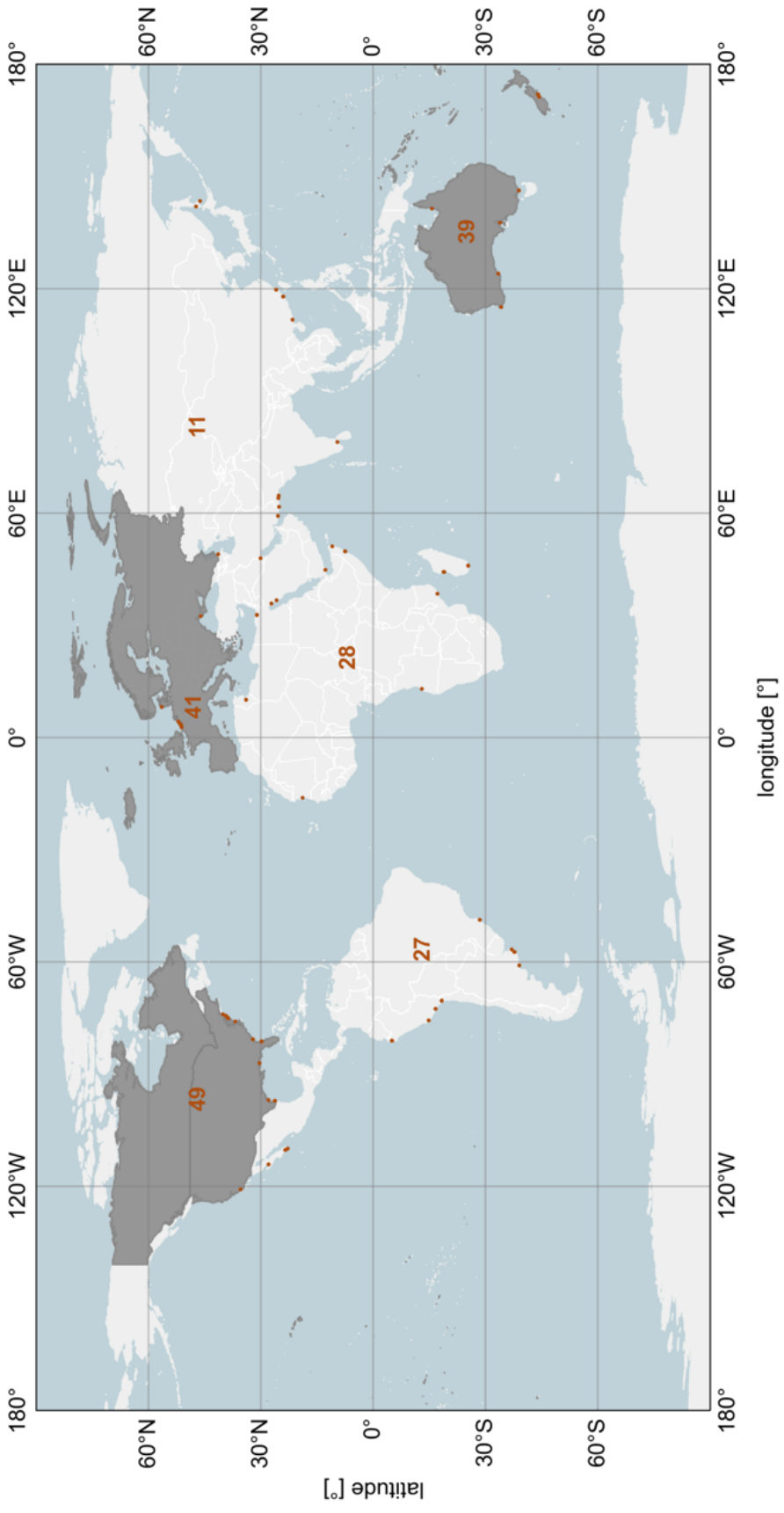

Figure 6.12: Global identification of nourishments. The brown markers correspond to a location of a nourishment with the identification parameters corresponding to precision of at least 80%. The number is bold indicate per continent the amount of nourishments per 1000 transects.

6.1.4. Littoral drift barriers

In around one in thirty hotspots (3.3%), shoreline evolution can be linked to littoral drift barriers, see Figure 6.13. These are predominantly identified as either updrift (prograding) or downdrift (retreating) LDB types. Only ten percent of the LDB hotspots is typified as double updrift, while less than 2% of the hotspots are part of a pair, a combination of an updrift and downdrift hotspot.

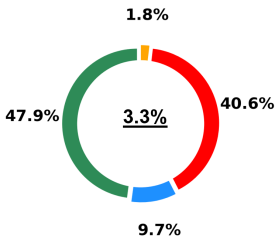

Figure 6.13: Proportions of each LDB type on a global scale. The colors green, blue, red and orange correspond to the types updrift, double updrift, downdrift and pairs respectively. The percentage of hotspots identified by characterizations of a LDB is underlined in the center of the chart

Figure 6.14 shows the top-10 countries were shoreline evolution is mostly linked to littoral drift barriers. It can be observed that particularly in Portugal, shoreline evolution is caused by littoral drift barriers. This is observed in 25% of the hotspots and these locations are predominantly typified as downdrift, see Figure 6.15. Furthermore, from the top-10 countries presented in Figure 6.14, 6 are located in the Western world.

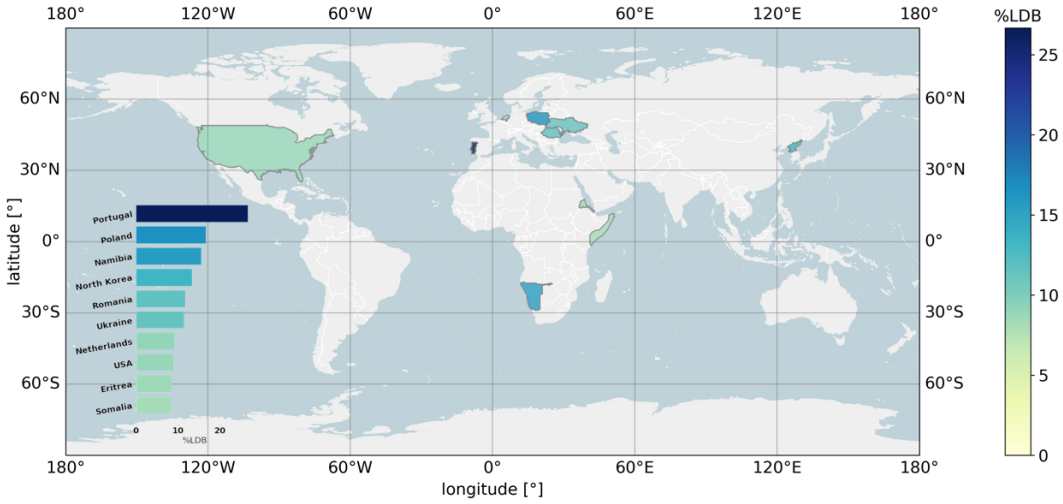

Figure 6.14: Top-10 countries with the highest percentage of hotspots where shoreline evolution is caused by littoral drift barriers. Only countries containing at least 10 hotspots are considered.

On a continental scale there are also some differences observed. These results are presented in Figure 6.15 and listed below:

1. Shoreline evolution caused by littoral drift barriers is mostly observed in the continents North-America, Europe and Africa.
2. Downdrift regions (erosive hotspots of a LDB) are mostly observed in Africa. In the remaining continents, accreting regions have the largest proportion.
3. In Oceania, more than 80% of the hotpots are typified as updrift, while the remaining locations are characterized as downdrift. Double updrift or pairs do not occur in this region.
4. Double updrift hotspots are mostly observed in North- and South-America.

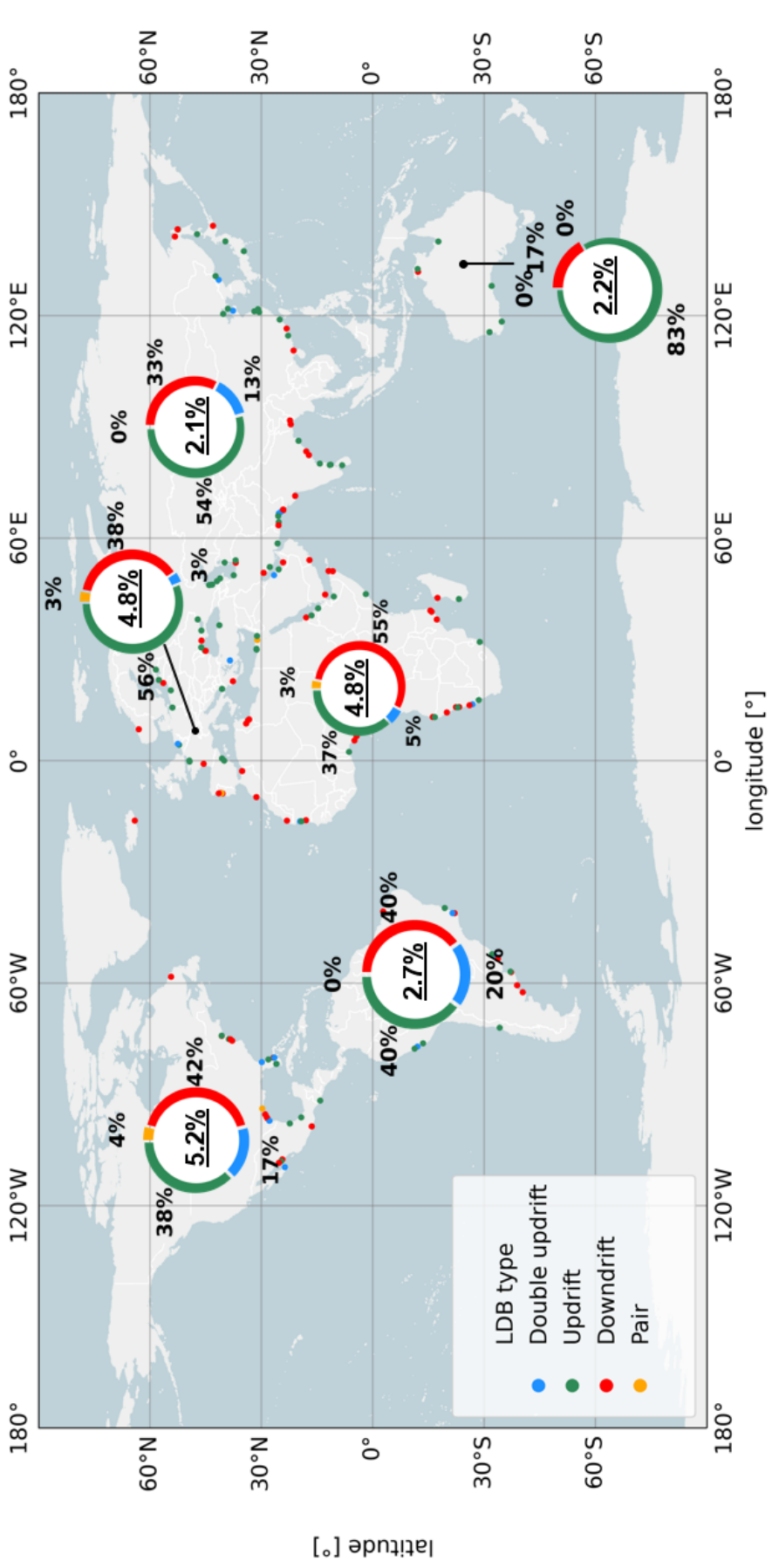

Figure 6.15: Global identification of littoral drift barriers as a driver of shoreline evolution. Pie charts indicate the proportion of each LDB type per continent. The percentage of hotspots per continent identified by characterizations of a LDB is underlined in the center of the chart.

6.2. Characterizing drivers at a global scale

Key points

- For the Northern Hemisphere, the minimum shoreline positions are mostly observed in the months June to August. In the Southern Hemisphere minimum shoreline positions are observed mostly in the months November to February.
- Although on a global level the amount of constructed reclamations remained stable, especially in East-Asia and the Middle East an increment can still be observed. In these regions, the alongshore distances of the reclaimed land are also largest.
- Over the period 1984-2021, nourishments were mostly applied in Western world countries (see Figure 6.12 for an overview of all Western world countries). However, in the entire world nourishments are gaining in popularity in the period after 2003 compared to the period 1984-2003.
- Shoreline evolution that is linked to littoral drift barriers is on a global level slightly stabilizing. This is especially observed in North-America. In Oceania, shoreline evolution in hotspots caused by littoral drift barriers is overall still developing (see Section 3.2.2 for a definition of stabilizing and developing shoreline evolution).

6.2.1. Seasonality

Minimum shoreline positions

In the Northern Hemisphere, the minimum shoreline positions are usually observed in the months June through September, see Figure 6.16. This period corresponds to the start of the summer for the Northern Hemisphere. A region above the equator that behaves completely different is observed along the Red Sea. In this region, minimum shoreline positions are observed in January and December corresponding to midwinter. In Chapter 6 it was already mentioned that seasonal shoreline positions in these area where controlled by variations in sea level height rather than the wave height. Figure 6.4 shows the water depth at Jazan (Saudi Arabia). Here, the water levels are maximum in January/December which corresponds to a minimum beach width in this period. This is indeed observed in Figure 6.16.
The Southern Hemisphere has a less peaked distribution of occurrence of minimum shoreline positions. A reason for this flattened shape can be found in the South of Australia, see Figure D.6. Here, minimum shoreline positions are observed in both summer and winter. This can be explained that in this region morphological changes are better explained by a seasonal reversal in the littoral drift direction than by variations in the incident wave energy conditions (Masselink and Pattiaratchi, 2001). Moreover, beach rotation also plays a role in pocket beaches resulting in different periods of minimum shoreline positions in a bay, see also Figure 4.5. Nevertheless, peak occurrences in the distribution for the Southern Hemisphere correspond to the beginning of the summer for this region (December - February).

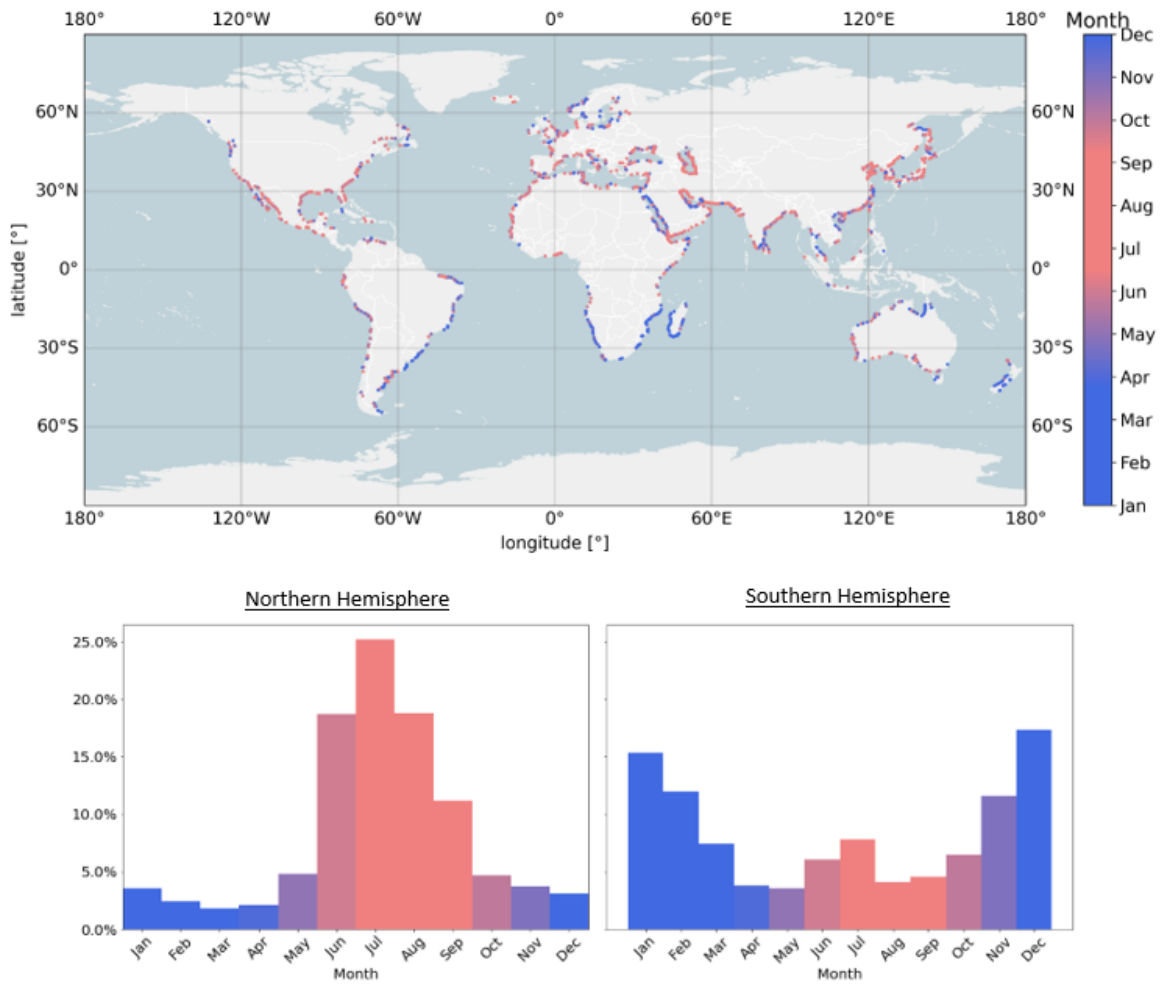

Figure 6.16: The upper part of the figure shows a global map of occurrence of minimum shoreline positions. Two histograms indicate for the Southern and Hemisphere the percentage of occurrence of minimum shoreline positions for each month.

Seasonal displacement

In Figure 6.17, regions are indicated characterized by either large or small seasonal displacements using spatial autocorrelations. The Mediterranean coast, Mexican gulf and Black Sea are predominantly characterized by small seasonal displacements. These areas have a smaller fetch (see Section 2.2.1) for a definition) resulting in lower wave heights. On the other hand, other fetch-limited regions, such as the Persian Gulf, the Red Sea and the Caspian Sea are characterized by large seasonal displacements. It was already shown that in the Middle East the frequently identified sandbar morphology was actually caused by a lowering of the water level and (coral) reefs rising above the water line. However, if these shoreline positions have jumps smaller than 100 meter, as is indicated by the parameter $P_{dY_{100}}$, these locations are identified as seasonal beaches with a large displacement. Time series emphasizing this behavior are shown in Figure 6.18.

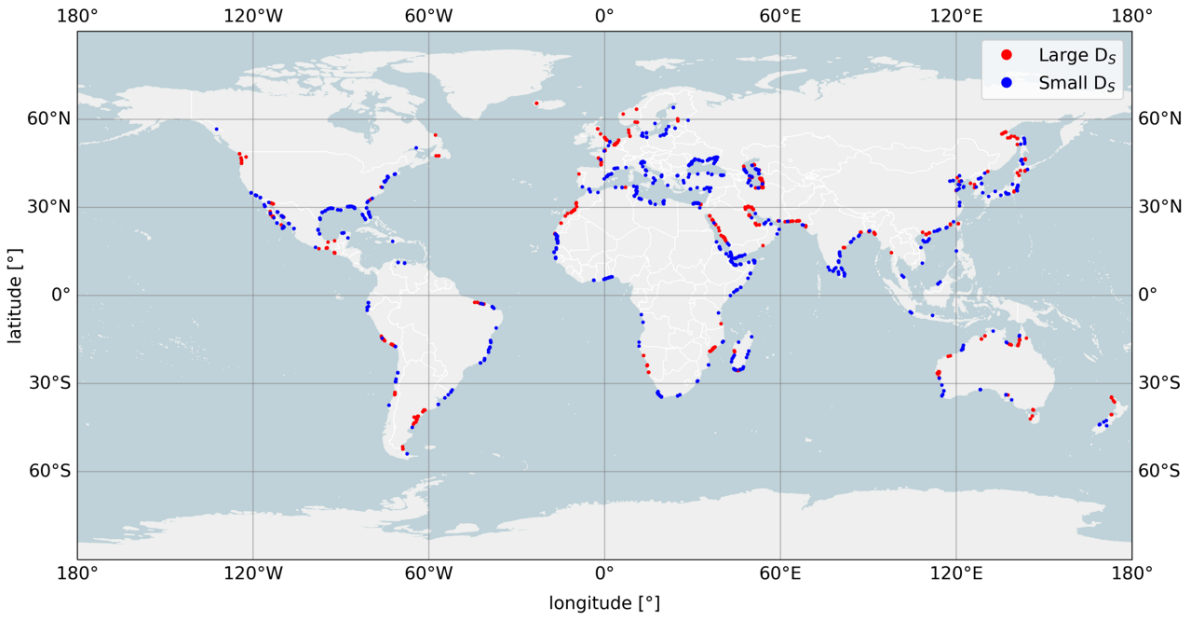

Figure 6.17: Regions characterized by either large or small seasonal displacement based on spatial autocorrelations.

Other regions where large seasonal displacements are observed are found around the North-Sea and Morocco. Wave height variations at the North sea between summer and winter are 4 meter offshore (Bonaduce et al., 2019), see Figure D.3. This is only around 2 meters in the Baltic sea which is more characterised by small seasonal displacements. In the Mediterranean these differences are even smaller, around 1 meter (Barbariol et al., 2021), see Figure D.4.

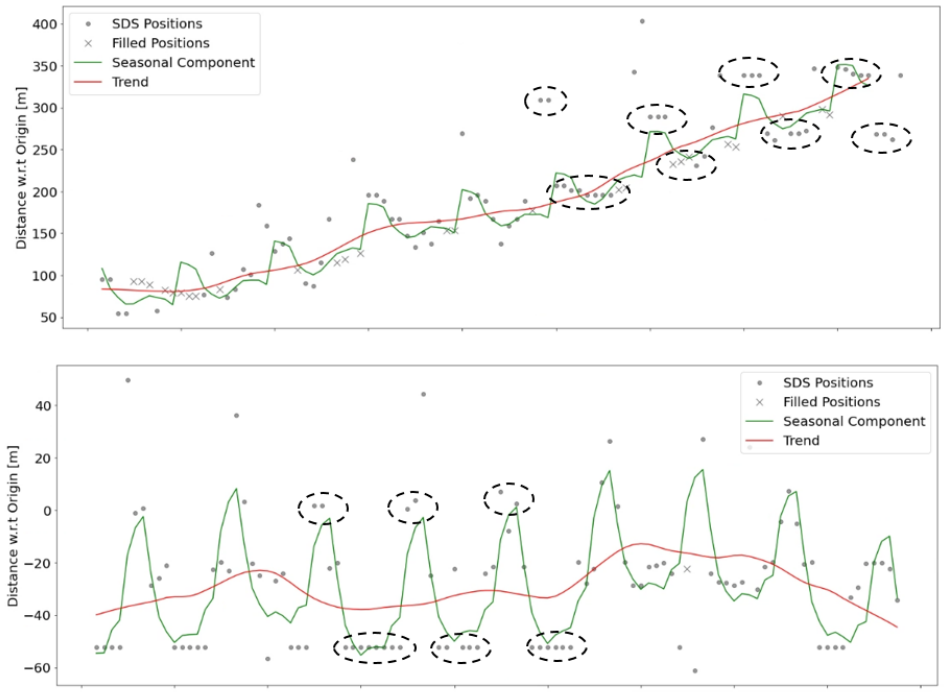

Figure 6.18: Shoreline positions at BOX_167_096_4 in Azerbaijan at the Caspian sea (upper) and BOX_145_091_49 in Saudi Arabia at the red sea (lower). The dashed circles in the lower figure indicate the levels of the shoreline positions. The upper circles correspond to the positions of the sandbar while lower positions correspond to that of the beach.

Accretion period

Regions in the world characterized by a long or short accretion period (T_{accr}) are indicated in Figure 6.19.

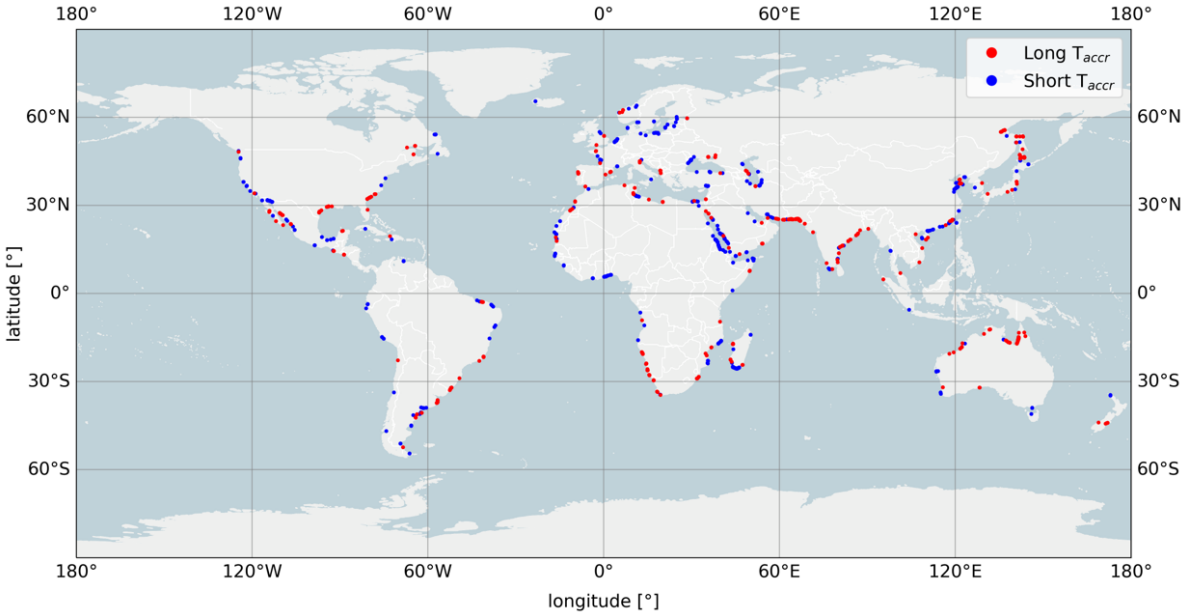

Figure 6.19: Regions characterized by either long or short accretion periods based on spatial auto-correlations.

Regions in South-West Asia are characterized by long accretion periods. Northern-Europe is more characterized by a short accretion period. The entire Dutch coast is characterized by a short accretion period. Figure 6.20 also shows that especially near this coast in the months March - May a large change in the significant wave height occurs while in the other seasonal quarters this change is more gradual (Wilson and Heath, 2019). This is explained by a short summer and a more extensive winter in the Netherlands corresponding to a short accretion period.

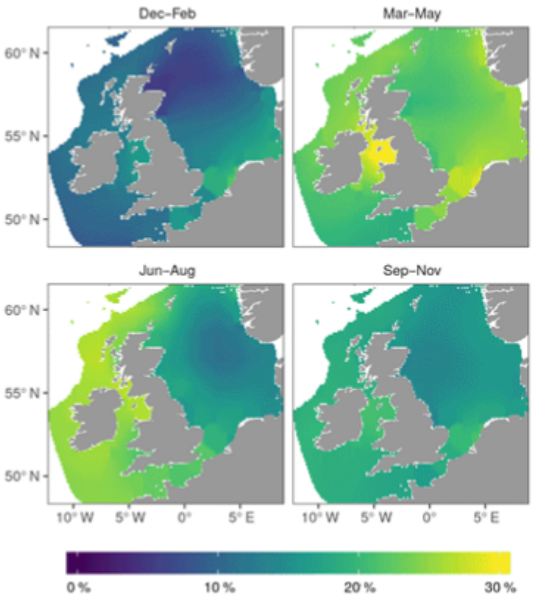

Figure 6.20: Change in significant wave height in the North sea. (Source: Wilson and Heath, 2019)

6.2.2. Reclamations

Figure 6.21 shows the construction dates of the identified reclamations. The average length of reclaimed land per continent is indicated with underline numbers in the Figure. The main takeaways regarding characterization of reclamations are:

- In Asia, Europe and Oceania reclamations occurred more after than before 2003 (center-date between 1987 and 2017). However, in Europe, reclamations are constructed very occasionally, see Figure D.7.
- In North-America, South-America and Africa, reclamations were constructed mainly before 2003.
- Alongshore lengths of reclaimed land are on average largest in Asia.
- In Europe the average alongshore length of reclaimed land is smallest.

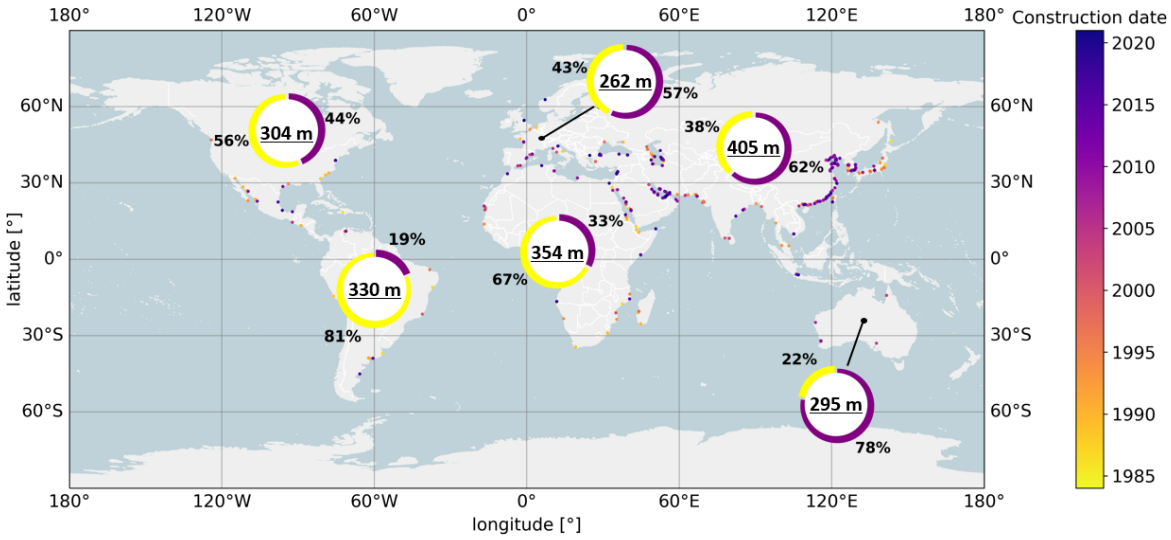

Figure 6.21: Global map of construction dates for reclamations. Piecharts indicate the proportions of constructions before 2003 (yellow) and after 2003 (purple) for each continent. In the center of each piechart is the average length of reclaimed length indicated per continent.

There are 12 countries in which construction of reclamations increased after 2003 compared to the period before that (1984 - 2003). These countries are indicated in Figure 6.22. The amount of constructions after 2003 divided by the amount of constructions before 2003 is indicated by T_{2003}. Six of these countries are located in the Middle East and three in East-Asia. Spain, the USA and Australia are three Western countries in which reclamations has been developed after 2003. Nevertheless, it should be denoted that the especially in Australia and Spain the total number of constructed reclamations is not very high.

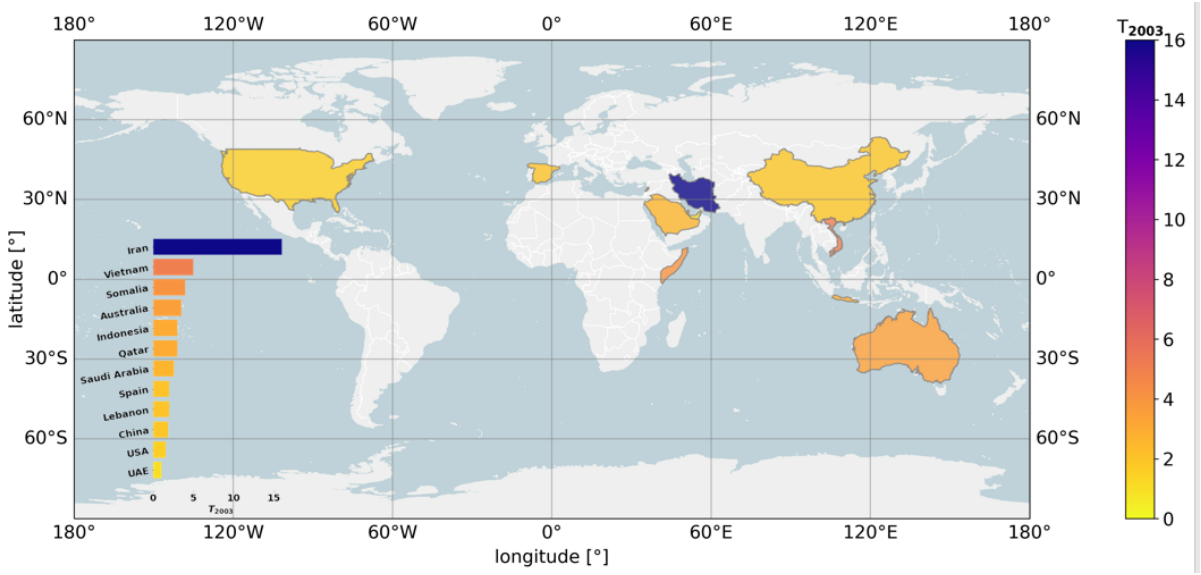

Figure 6.22: Overview of countries in which the number of constructions of reclamations has increased after 2003 compared to the period 1984-2003.

6.2.3. Nourishments

For all continents, except for North- and South America, the amount of constructed nourishments after 2003 (center of the period 1987-2017) compared to the period 1984-2003 remained approximately stable, see Figure 6.23. In North-America, the number of identified nourishments after 2003 increased by a factor 3, while South-America is the only continent where the number of constructed nourishments decreased.

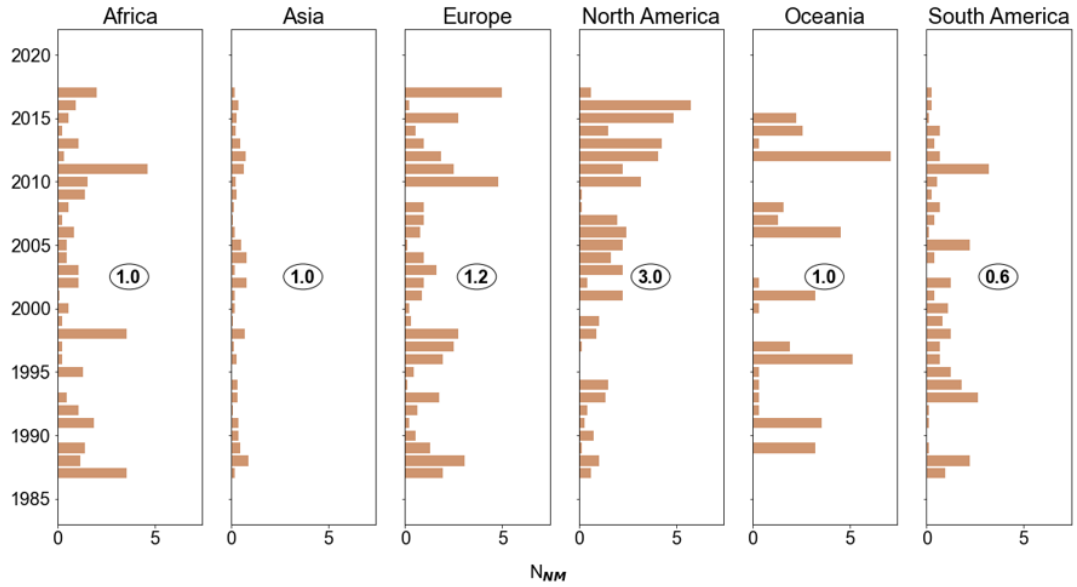

Figure 6.23: Timeline per continent regarding the amount of constructed nourishments per year per 1000 transects (N_{NM}). The proportion of the number of nourishments after 2003 compared to the period of 1984-2003 is indicated in bold for each continent.

The results presented in Section 6.1.3 point out that nourishments were mostly applied in Western countries. However, Figure 6.24 indicates that in the entire world, nourishments are increasing in popularity as a method to combat erosion.

Beach nourishments with a lifetime between 3 and 6 years are mostly observed, see Figure D.8.

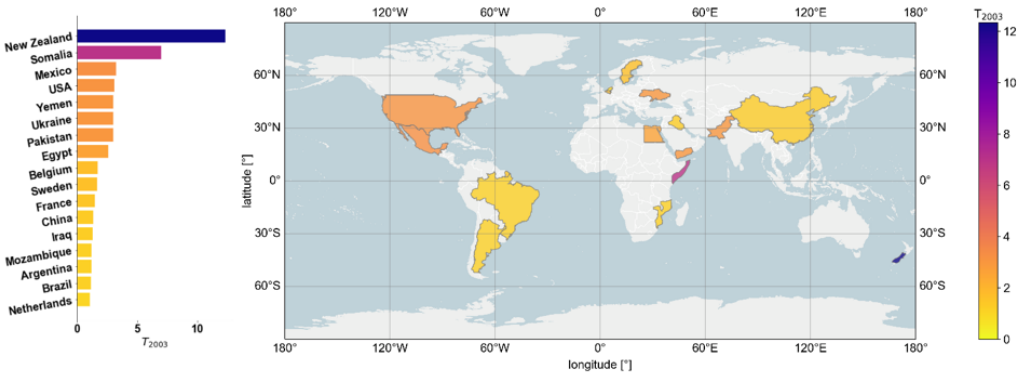

Figure 6.24: Overview of countries in which the number of constructions of nourishments has increased after 2003 compared to the period 1984-2003.

6.2.4. Littoral drift barriers

Overall, shoreline evolution in hotspots caused by littoral drift barriers is slightly more stabilizing, see Figure 6.25. On a continental scale, in North-America, the evolution in these hotspots is predominantly stabilizing while the opposite is observed in Oceania. Except in Europe, slightly more stabilizing hotspots than developing hotspots are observed in the other continents, see Figure 6.26.

Figure 6.25: Global proportions of developing (green) and stabilizing (orange) hotspots in which shoreline evolution is caused by littoral drift barriers

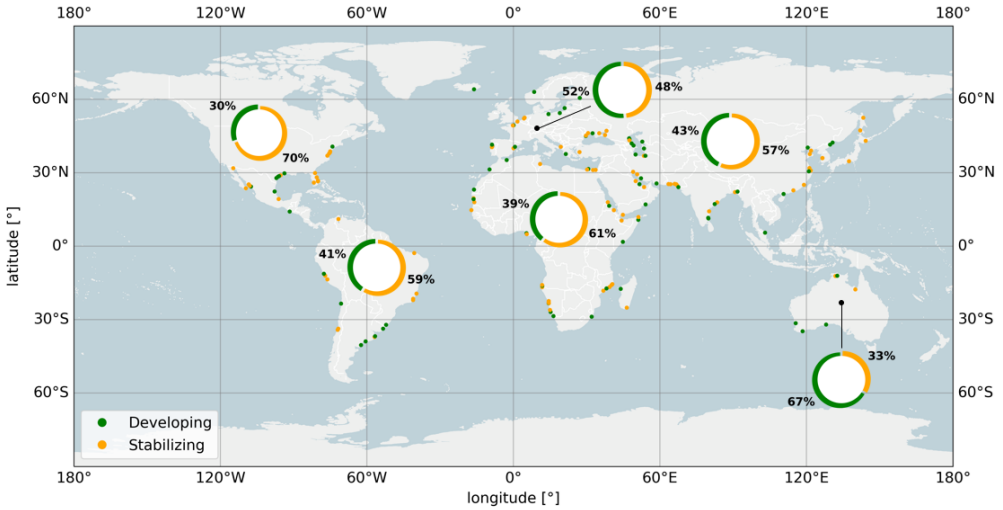

Figure 6.26: Global map of hotspots in which shoreline evolution is caused by littoral drift barriers. The green (orange) markers indicate that shoreline evolution in a hotspot is developing (stabilizing). Proportions of the categories developing/stabilizing per continent are indicated with piecharts.

6.3. Summary: global results

In this chapter the results were presented of identification on a global scale for the following drivers of shoreline evolution; seasonality, reclamations, nourishments and littoral drift barriers. Observations made here allowed to answer the final sub-question:

What is the global distribution and characterization of drivers?

In Chapter 5 the optimal settings were derived to identify these drivers. Except for seasonality, identification and characterization is based on locations corresponding to identification parameters with a precision score of at least 70%. For seasonality, classifying a location as a seasonal beach if the probability from the logistic regression model was at least 40% resulted in a precision of 80%. Below for these drivers the results using these optimal settings are summarized.

Seasonality
Seasonal beaches are mostly observed in Central-America, Northern-Europe and Africa. Seasonal sandbars are most identified in Belgium, the Middle East and Australia. However, in the Middle East, identification of sandbars is actually caused by a seasonal variation of the water level in the Red Sea (Abdelrahman, 1997) and (coral) reefs identified as the most landward position. Also in the Caspian sea, seasonal behaviour of the coast can be linked to a variation of the water level rather than a variation of the wave energy (J. Chen et al., 2017). This might also explain seasonality that is observed in other (semi-)enclosed basins such as the Black Sea and the Persian Gulf. The Mediterranean is mainly characterized by non-seasonality as this region is fetch limited and has only 1 meter difference in wave height between winter and summer (Barbariol et al., 2021). For the Northern Hemisphere, the minimum shoreline positions are mostly observed in the months June to August. In the Southern Hemisphere minimum shoreline positions are observed mostly in the months November to February. However, in Australia, minimum shoreline positions are mostly observed in July. In this region morphological changes are better explained by a seasonal reversal in the littoral drift direction than by variations in the incident wave height (Masselink and Pattiaratchi, 2001).

Reclamations
Reclamations are observed most in the Middle East and East-Asia. From the top 10 countries where relatively most reclamations are observed, 7 are located in these two geographical regions. The remaining three countries are closely located to these regions. On a global level, the amount of constructions of reclamations has remained stable over the periods 1987-1996, 1997 - 2006 and 2007-2016. Although on a global level the amount of constructed reclamations remained stable, especially in East-Asia and the Middle East an increment can still be observed. In these regions, the alongshore distances of the reclaimed land are also largest.

Nourishments
In the Western world, nourishments are mostly identified compared to other regions in the world. Furthermore, for the identified nourishments in the last decade, an average increase of 66% was found compared to the period 1988-2008. This increase is not only observed in Western countries but in the entire world.

Littoral drift barriers
Shoreline evolution caused by littoral drift barriers is mostly observed in North-America, Africa and Europe. In Africa, hotspots are most identified as downdrift whereas in North-America and Europe mostly updrift regions are identified. A combination of a downdrift and updrift region, a pair, is on a global level observed in less than 2% of the cases. Shoreline evolution that is linked to littoral drift barriers is on a global level slightly stabilizing. This is especially observed in North-America. In Oceania, shoreline evolution in hotspots caused by littoral drift barriers is overall still developing. Stabilizing shoreline evolution is defined as a trend where the changerate in the final decade is equal or smaller than the changerate of its previous decade.

7

Discussion

This chapter will reflect on the results presented in the Chapters 4, 5 and 6. First, limitations in the developed methods are taken into consideration focusing on the assumptions, decisions and restrictions. Section 7.2 will discuss what outcomes from this research might contribute to individuals and/or organizations in this field or research area. Finally, by considering the ability to solve the limitations discussed in Section 7.1, future directions are explored in Section 7.3.

7.1. Limitations

Below, four major assumptions, decisions and restrictions in the research methods and results from Chapter 4, 5 and 6 are discussed.

1. Hotspot extraction

In this research, drivers of shoreline evolution were identified for hotspots on a global scale. A hotspot is a region with high shoreline variability and with similar characteristics (both in time and space). Drivers were identified for hotspots extracted using a method developed by Kras (2019). These regions of increased shoreline variability where identified with a moving spatial window of 2.5 kilometer. This resulted in hotspots with relatively small spatial scales; 95% of the hotspots has a length of less than 10 kilometers. This method thus allowed to study shoreline evolution caused by drivers with small to moderate spatial scales (~10 kilometer, see Figure 2.32). By increasing the size of the moving spatial window it will be possible to study the drivers with larger spatial scales as well (region I).
The global and regional results for littoral drift barriers indicated that only very few pairs, a combination of an up- and downdrift location, were identified. This, and sensitivity of identification of LDBs in general, can be linked to the spatial extent of the hotspots. An example of a hotspot with an incorrect extent can be found at Contonou (Benin), see Figure 7.1. As a consequence, thresholds from the hotspot extraction method, see Section A.1.1 have to be adjusted. As these thresholds (and hotspots) were determined on the spatiotemporal resolution of the Shoreline Monitor an increase in accuracy can be expected if new thresholds are determined based on a higher spatiotemporal resolution (Kras, 2019).

Figure 7.1: Updrift (green) and downdrift (red) hotspots at Contonou, Benin. The thick shore-parallel lines indicate the spatial extent of the hotspots, while the shore-normal lines correspond to the locations of the transects. Downdrift, the spatial extent of the hotspot is incorrectly identified. The correct extent of the hotspot is indicated with the red dashed box.

2. Spatial resolution

Similar to the Shoreline Monitor, shoreline evolution was linked to drivers using a spatial resolution of 500-m spaced transects. As mentioned in Section 5.4, this made it impossible to resolve shoreline evolution caused/interrupted by a groyne field. Groynes are most effective when they are spaced 1.5 to 2 times their length (Neshaei and Biria, 2013). With groynes of typical lengths of a few hundred meters the spatial resolution of 500-m is too coarse to capture the shoreline evolution signal of a single groyne.
Furthermore, identification of other drivers improves as well with a higher spatial resolution. Whereas seasonal variations may vary over a distance of 500 meter this is expected to be more constant over 100 or 50 meters. This information can then be used to compare results of neighbouring transects and increase robustness. The same applies to identification of nourishments. Moreover, this might result in possible identification of nourishments with smaller spatial scales as well. Currently only nourishments were identified with spatial scales of at least 2000 meter (4 transects with 500 meter spacing corresponds to a precision of 70%) as identification probabilities are estimated according to the spatial scale in which a signal is observed.

3. Nourishments

Overall, identification of nourishments on a global scale showed results that could be supported by literature. Belgium was identified as countries that frequently applied nourishments as a measure to combat coastal erosion. Even though Belgium has applied nourishments in the past, it is not one of the pioneering countries in this practice (as are the Netherlands and the USA). A possible reason could be found in the attempt of this identification method to resolve shoreface nourishments as well. A shoreface nourishment is in contrast to a beach nourishment characterized by a more gradual increase of the beach width. In this research no distinguishment is made between a sudden increase, in the case of a beach nourishment, and a more gradual increase of shoreline positions, as will happen in the case of a shoreface nourishment. However, in the case of inter-annual cross-shore sandbar morphology, similar shoreline evolution in the time series to a shoreface nourishment will be observed. The sandbar gradually attaches to the beach over time after which it will move offshore again (Bosboom and Stive, 2012). Looking at Figure 6.2, Belgium is identified as a region were (seasonal) sandbar morphology is present. Thus, the identification of nourishments in these areas may actually be caused by the morphology of a sandbar on the inter-annual scale. Another word of a sandbar attaching to the shoreline is sandbar welding (Cohn et al., 2017). Figure 7.2 shows examples of timeseries of a beach nourishment, a shoreface nourishment (constructed in 2014 [1]) and sandbar welding (Ostrowski et al., 2016). In this figure, the characteristics that are already implemented in the detection method are coloured with green boxes. The characteristics that are not yet implemented, and therefore limit the detection method, are coloured in orange. These orange coloured characteristics are shortly elaborated on below:

1. Sudden/gradual shoreline increase: there is no distinguishment made between a sudden (beach) and gradual shoreline increase (cross-shore sediment supply).

2. Erosive trend represents SDS positions: it was observed from Figure 6.10 that the shoreline positions are not always supported by the smoothed erosive trend after a shoreline jump.

3. Temporal behavior: neighbouring transects should show similar erosive trends after a shoreline jump as they experience the same wave climate. The timeseries from two neighbouring locations in Iraq from Figure 6.10 do not reflect this characteristic.

The timeseries of shoreline positions of shoreface nourishments and sandbar welding as well as the physical processes behind these drivers are similar. Therefore it is recommended to make a split between beach nourishments and these latter two sediment supply drivers categorized as cross-shore sediment supply.

[1] https://www.openearth.nl/coastviewer-static/

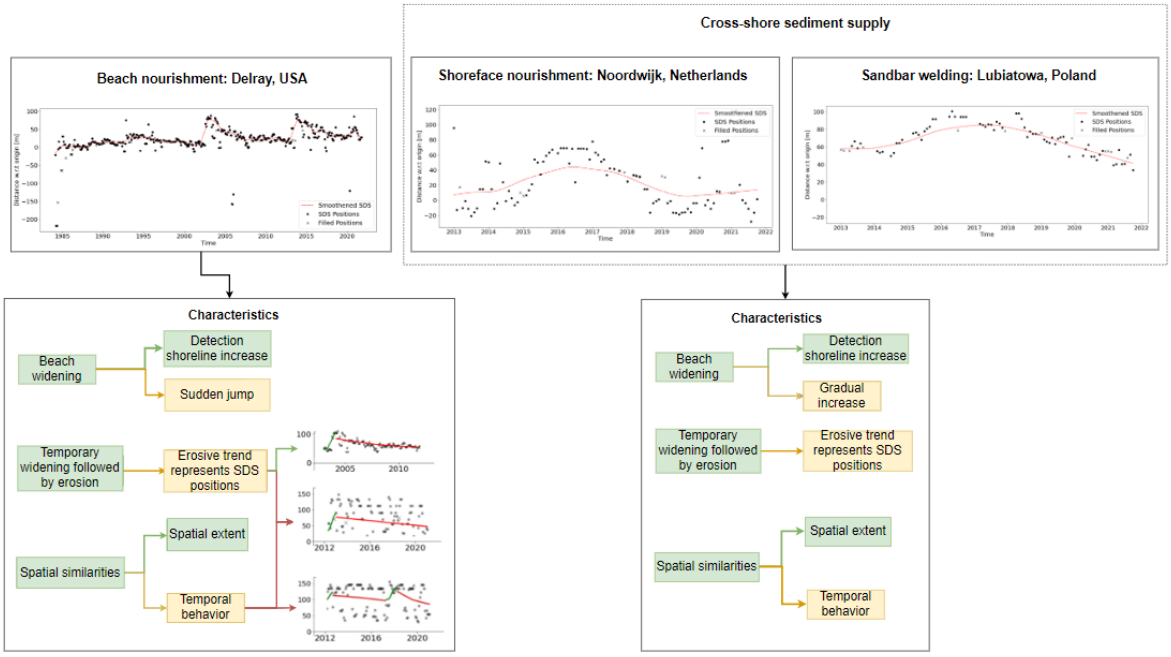

Figure 7.2: Schematic overview of current and recommended implementation of characteristics of nourishments. The characteristics that are already (not yet) implemented in the detection method are coloured with green (orange) boxes. Green (red) arrows correspond to an example which shows correct (incorrect) behaviour of the characteristic.

4. Compound drivers

In this study, drivers were identified independently from each other. Because of this, when more drivers where identified at a coastal stretch, these probabilities of identification combined do not equal 1. Therefore, instead of independent identification of the drivers, drivers should be identified taking interactions into consideration.

Five minor limitations incorporated in this research are listed below.

1. Outlier identification

Outliers are observations that lie at an abnormal distance from other values in the time series. In this study, outliers are identified using a linear regression fit of the data. As a result, in the case of non-linear shoreline evolution, as is the case for nourishments and reclamations, outliers are poorly identified. Optimizing the procedure of outlier identification will result in cleaner time series with as a consequence improved identification of drivers of shoreline evolution. This will also improve the method that was developed to fill missing values as filling algorithms do not longer interpolate on these outliers.

2. Missing values and driver identification

Less than 10 locations were used to determine the thresholds of missing values that enhance accurate identification of shoreline evolution. If these thresholds are not indicative for the complete data set, applying the identification procedures with these thresholds on a larger scale could lead to inaccuracies. Therefore, the verification sample for this analysis should be increased in order to provide a better understanding of the impact of missing data on identification of drivers. Furthermore, only the amount of missing values over the entire time series was considered. Regarding a more incidental driver, such as reclamations, missing values around the time of the shoreline jump are also important to consider. Too much missing values around this period might result in an artificial construction of time series corresponding to the characteristics of this driver, see Figure 7.3.

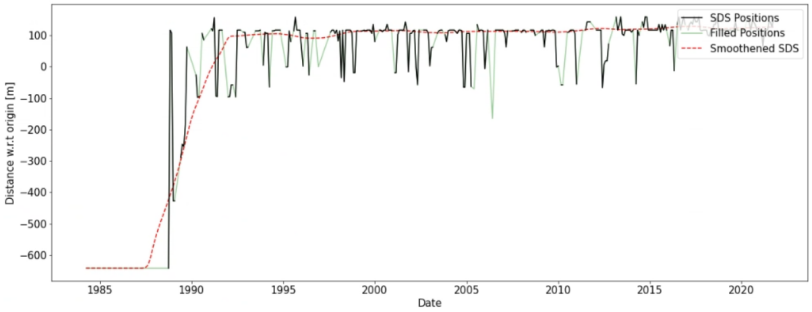

Figure 7.3: Example of SDS positions with missing values around a shoreline jump. Because of the filled positions the time series shows characteristics that can be linked to a reclamation.

3. Erroneous shoreline behavior

Especially for identification of seasonality, problems were encountered due to erroneous shoreline behaviour. This was mainly due to seasonal sandbars, mild foreshores and double waterline intersections of the transects. A logistic regression model was used to correct for incorrect identification. This erroneous shoreline behavior also results in erroneous extraction of hotspots. For a verified sample of 380 hotspots, Kras (2019) found that 25% was erroneously extracted. Van Leeuwen (2018) made two recommendations that might reduce the amount of wrong extracted hotspots. The first recommendation was to plot transects on SDS instead of the OSM shoreline. The other recommendation was to either statically or dynamically adjust the length of the transects.

4. Minimum shoreline position

This study used SDS derived from Landsat images that have an accuracy of 15 meter. If differences in shoreline positions are below the accuracy of the satellite mission, the exact month in which the minimum shoreline position occurs can not exactly be determined. Monthly changes of 15 meters are quite large and not expected to be observed quite frequently. As a result, the moment of occurrence of minimum shoreline positions that are provided in this study are more an indication than an exact estimate. This could be improved by identifying seasonality by using SDS from Sentinel-2 images. This satellite mission has an accuracy of 5 meter. Moreover, shoreline evolution with seasonal displacements between 5 to 15 meter can then also be linked to seasonality.

5. Method verification

As mentioned in Section 3.3, large classification studies require a sample size of at least 500 for reliable results of a logistic regression model. Nevertheless, the logistic model to predict seasonality outcomes was fitted on a sample with a size of 100. Furthermore, verification can be subjective as not for all locations literature was present. In those cases, verification was done using the time series and the GEE. In the case of littoral drift barriers and reclamations this subjectivity is less of a problem as these drivers can be more easily observed in aerial images for a certain location. Nevertheless, verification was done on less than 1% of all transects

in the case of reclamations and on only 2% of the hotspots in the case of littoral drift barriers. Finally, nourishments were only verified on the Dutch coast using a sample size of only 20. As mentioned in Section 5.3, characteristics of nourishments can vary between countries. Furthermore, the effect of sandbar morphology on identification of nourishments should be taken into account as this possible issue was not observed along the Dutch coast in the verified sample.

7.2. Implications

Taking into account the limitations mentioned in the section above, this section will elaborate on the main outcomes of this research and show how these can be applied to real life problems.

1. Identification of drivers.
   Local-scale studies can be supported by indicating the most probable and/or relevant driver of shoreline change.

2. More robust analysis of shoreline evolution.
   Similarities can be shown between locations where shoreline evolution can be linked to the same driver.

1. Support to local studies

This application is similar to the results presented in Chapter 6. However, as here results were presented on a global scale, identification of drivers can also be provided for a single hotspot. Furthermore, the informative parameters provide knowledge on how a driver behaves on a specific site.

2. Link shoreline evolution to the littoral drift barrier

On a global scale, locations where shoreline evolution is linked to littoral drift barriers are identified. Now, imagine the construction of a new port in Africa. In the preliminary phase, engineers want to know how far up the coast a breakwater will affect shoreline evolution and how this will evolve in time. Coupling the global driver dataset to external global patterns of wave heights, directions, currents and other environmental characteristics, similar locations can be easily and quickly identified. Shoreline evolution for these other sites can then be used to provide first order estimates for the breakwater of the new port, see Figure 7.4. Even a feedback loop can be created that changes the design of the breakwater to investigate other possible solutions.

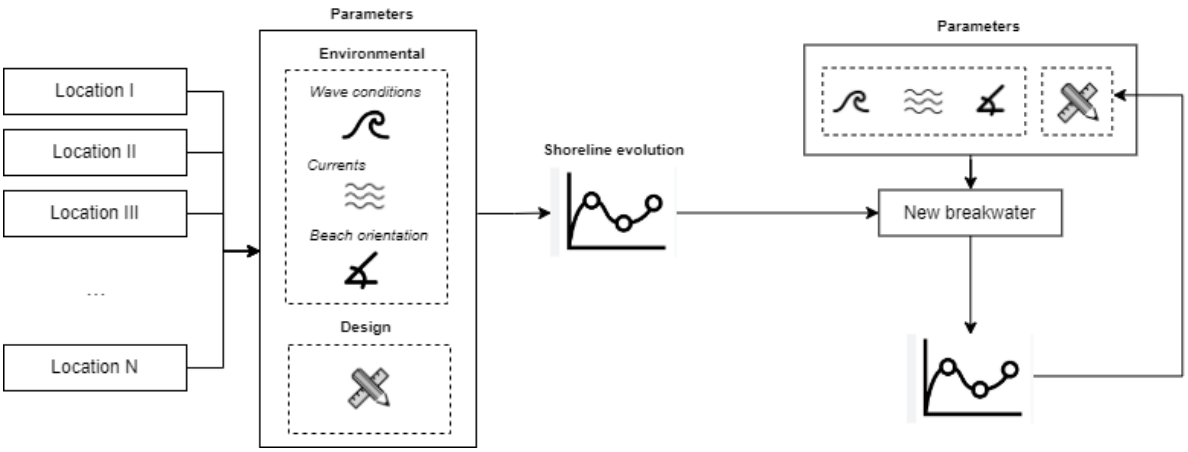

Figure 7.4: Visualization of how information from other locations can be gathered for a site where shoreline evolution is yet to be determined. A feedback loop exists between the shoreline evolution and the design of the new breakwater.

7.3. Future directions

Provided that the limitations from Section 7.1 are resolved, this section will elaborate on potential future directions for this research. Directions presented here are linked to the recommendations in Chapter 9. These future directions are already valuable to this field of research on their own, but when combined, they will enable to achieve a final goal: make (future) impact assessments of shoreline evolution and provide solutions with satellite derived shorelines as a foundation. Still, this will only serve to support detailed local studies instead of replacing them. The future directions are schematically visualized in Figure 7.5. The future directions are listed and further explained below.

1. Include unresolved drivers

There are still some drivers that were either not included in this study at all or whose identification methods have not yet been tested at larger scales. Drivers with a large spatial scale could not be identified due to the small spatial extent of the hotspots, these include the following drivers: river sediment supply, subsidence, tidal areas and coastal hazards. Furthermore, beach rotation and climate variability were only examined at a local scale, but the methods need further refinement before identification can be scaled up. All of these drivers should be included to provide better support for local case studies and a more complete analysis on a global scale. Furthermore, the identification methods for drivers considered in this study still need improved.

2. Understanding of interaction between drivers

Drivers in this study were identified independently of one another. As a result, interactions between drivers were overlooked. Nonetheless, the vast majority of hotspots are in the compound driver regime. As a result, identification probabilities should be combined to accurately represent the proportion of a specific driver for shoreline evolution at a given location.

3. Forecasting of shoreline evolution

Identification, in conjunction with driver characteristics, can be used to improve forecasting of shoreline evolution. For example, once a reclamation has been identified, the shoreline is expected to remain fixed in the future. Furthermore, shoreline evolution at developing hotspots can be predicted based on a location where shoreline evolution has already occurred. This is based on the assumption that drivers exhibit roughly similar characteristics all over the world.

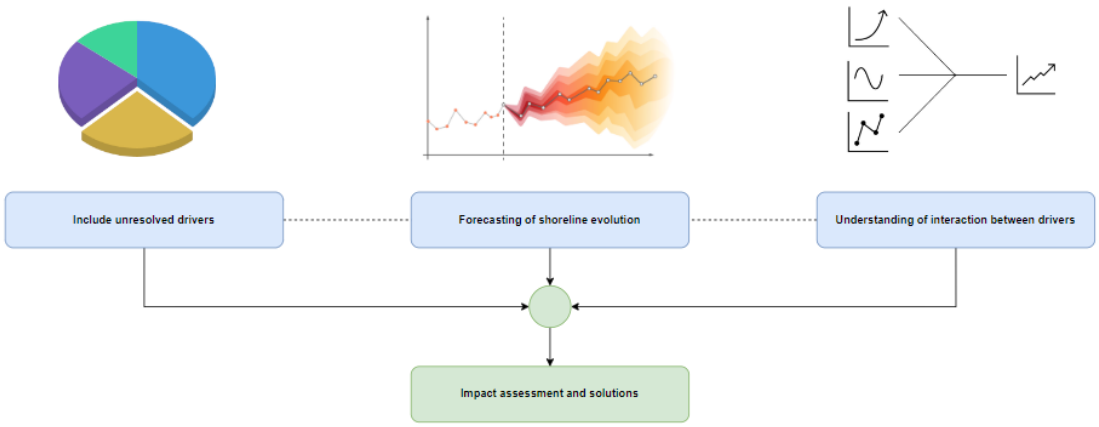

Figure 7.5: Visualization of the future directions of this study. The final goal is indicated in a green box where the future directions needed to be resolved first are indicated with blue boxes. The dotted links between future directions indicate that the outcomes of these directions can be used in conjunction with one another.

8

Conclusion

Eroding shorelines and densely populated coastal zones demand a proper management of coastal areas. As for now, solutions are mostly based on detailed local-scale studies resulting in site-specific observations. However, promising results of satellite imagery in the field of coastal engineering enhanced the possibility to increase the spatial extent of studies. By doing so, areas with similar characteristics can be identified with a methodological standardization to a problem as a result. The Shoreline Monitor (Luijendijk et al., 2018) is an application that identifies annual shoreline position of sandy beaches over the period 1984-2016 on a global scale by using satellite derived shorelines (SDS). Nevertheless, the drivers behind this shoreline evolution remain yet unknown. Therefore, the research objective in this study is to identify on a global scale the distribution and characterizations of drivers of shoreline change using SDS. This objective is translated into a research question which reads as follows:

How can satellite derived shorelines be used to identify and characterize drivers of shoreline change on a global scale?

To answer this research question, multiple sub-questions were formulated. Using already existing methods, these sub-questions are answered step-wise.

First, SDS time series were decomposed into signals that could be linked to a particular driver. Identification and informative parameters were obtained from these decomposed signals that could be used to relate the SDS to a driver. Parameters were also linked to the spatial extent of the driver. Case studies showed that drivers present at different locations showed similar results for the identification parameters. This implies that the identification parameters correctly reflect a driver's behavior. The informative parameters, that are site specific, showed differences along the case studies.

In the next two steps, the methods were applied on a regional scale to verify the methods and on a global scale to sketch a distribution of the drivers. Only transects within a hotspot were considered. A hotspot is a region with high shoreline variability and with similar characteristics both in time and space.
Verification on a regional scale was done for the West-European coastline. Hundreds of samples were verified using literature or manual inspection of satellite images. From there, optimal settings for identifying drivers were determined using precision scores, which measure the ratio of true positive cases to all cases identified. These settings resulted in a pattern of driver identification and characterization along the West-European coastline that is supported by literature.
The global dataset consisted out of 3033 prograding and 2121 retreating hotspots containing over 58 thousand transect in total. For these hotspots, SDS were generated over the period 1984-2021 with a monthly temporal resolution. This resulted in a global dataset of more than 26 million shoreline positions.
From this global dataset, it was discovered that two processes, in addition to a seasonal varying wave height, could result in seasonal variations in shoreline positions. A first phenomena could be observed at the Red Sea. Even though in this region the wave climate is low in energy (Langodan et al., 2017), the coast is characterized by seasonal behaviour. In this basin, however, this behavior was explained rather by seasonal fluctuations in water levels than by the wave climate. In addition to varying wave height and water level, seasonal beach mor-

phology can also be caused by a change in wave direction. This was observed in southern parts of Australia. Moreover, in low-energetic wave areas without any of these other two processes present, as is the case in the Mediterranean, mostly non-seasonal beaches were observed. In areas where seasonal shoreline variations are driven by wave energy, minimum shoreline positions were observed at the start of summer. However, in areas where water level variations or a change in wave direction are the drivers of seasonal shoreline behavior, the period in which minimum shoreline positions are observed may be observed in a different time of the year.
The amount of constructed reclamations remained constant over the last three decades. Nevertheless, in the Middle East and East-Asia the amount of constructions has increased over this period. In these areas also the most reclamations have been identified over the entire study period (1984-2021), along with the largest mean alongshore length of constructed reclamations. Nourishments on the other hand are increasingly identified in the period after 2003 compared to the two decades before that. Nourishments are mostly observed in Western countries. Nevertheless, nourishments have also gained in popularity in other parts of the world in the period 2003-2021 compared to the period before that.
Shoreline evolution caused by littoral drift barriers was mostly observed in North-America, Africa and Europe. In Africa the highest proportion of downdrift erosion hotspots was identified whereas in North-America and Europe mostly updrift accretion regions are identified.

Besides identification of the drivers on a global level, this study has another implication for coastal management. Using the methods and results from this study, patterns for regions with similarities can be derived. Then, these patterns can be applied to a location with comparable characteristics where the cause of shoreline evolution is still unknown. For example, seasonal variations in other (semi)-enclosed basins such as the Black Sea and Persian Gulf can be linked to water level variations based on the observations from the Red Sea.

All outcomes stated above conclude that parameters derived from decomposed signals of SDS together with spatial characteristics of a driver can be used to identify on a global scale the distribution and characteristics of drivers of shoreline evolution. Nevertheless, since the focus was on shoreline evolution in hotspots derived with a rolling mean of 2.5 kilometer, large scale drivers (region I, see Figure 2.32) could not be identified. Furthermore, beach rotation was not verified on a regional scale as the hotspots are not designed to capture this driver. Another (secondary) driver that needs more attention before it can be identified on a global scale is climate variability. Moreover, identification of the remaining drivers with small spatial scales was done independently from each other. Therefore, if multiple drivers are identified at a location, identification probabilities combined do not equal 1. More research is needed to further explore opportunities that can enhance the understanding of the unresolved drivers, interaction between drivers and further improve the obtained results.

9

Recommendations

In this chapter some recommendations are provided for the future directions of this study. These are based on the limitations and conclusion from Chapter 7 and 8 respectively.

1. Increase the spatio-temporal resolution of the dataset, The Shoreline Monitor (Luijendijk et al., 2018), which underlies the hotspot extraction method. This improves the accuracy of the spatial extent of hotspots and makes it easier to detect erroneously extracted hotspots. However, generating satellite derived shorelines (SDS) with monthly rather than annual resolution for all transects within the current derived hotspots already resulted in a large computational effort. This was only 22% of the entire global data set. On the other hand, this increases the possibility of identifying seasonality and climate variability on a global scale, two secondary drivers of shoreline evolution. Since these drivers do not lead to structural changes in a shoreline trend, they do not cause the shoreline evolution that constitutes a hotspot. Therefore, merely identifying these drivers for transects within hotspots provides an incomplete picture of these drivers. A large spatial resolution will also contribute to the identification of the other drivers. For example, it will possibly enable to solve shoreline evolution signals within groyne fields.

2. The spatial moving window that is used to identify the hotspots should be increased to be able to identify drivers with larger spatial scales. Current hotspots were extracted using a 2.5 kilometer moving spatial window which resulted in 95% of the extracted hotspots having a spatial extent below 10 kilometer. This made it impossible to study shoreline evolution caused by drivers with a large spatial scale.

3. The sample size on which the identification methods were verified should be increased. The results showed that Iraq was one of the countries where nourishments were most frequently identified. A reason for this was found in Figure 6.10 showing that smoothing of the SDS might lead to a trend that shows characteristics of a nourishments which is not supported by the original SDS. Furthermore, the large amount of identified nourishments in Belgium might actually be explained by inter-annual moving sandbars showing the same characteristic as a foreshore nourishment. Nourishments were identified on a small sample on the Dutch coast were this behavior was not observed. Furthermore, for logistic regression to yield reliable results for a study with a large population, a sample size of at least 500 must be used. In this study, a sample size of only 100 was utilized.

4. Drivers were identified independently without considering their interactions resulting in combined identification probabilities greater than 1. A good solution to this is to use the theory of expected value, a generalization of the weighted average:

$$E(X) = \sum x_i p_i(X_i) \tag{9.1}$$

where $E(x)$: expected value
X_i : the value that X takes
p_i : the probability that X takes the value x_i[%]

Here the variance is used as the expected value as from simple statistics it is known that:

$$Var(X+Y) = Var(X) + Var(Y)$$

This procedure is further elaborated using a transect at the hotspot in IJmuiden harbor. At this location, structural changes to the coast were caused by the breakwater, a littoral drift barrier. Here, this driver was identified with a probability of 0.99. Furthermore, seasonality was also identified as a driver of shoreline evolution with a probability of 0.98. The probability of identification of the other drivers equals zero.

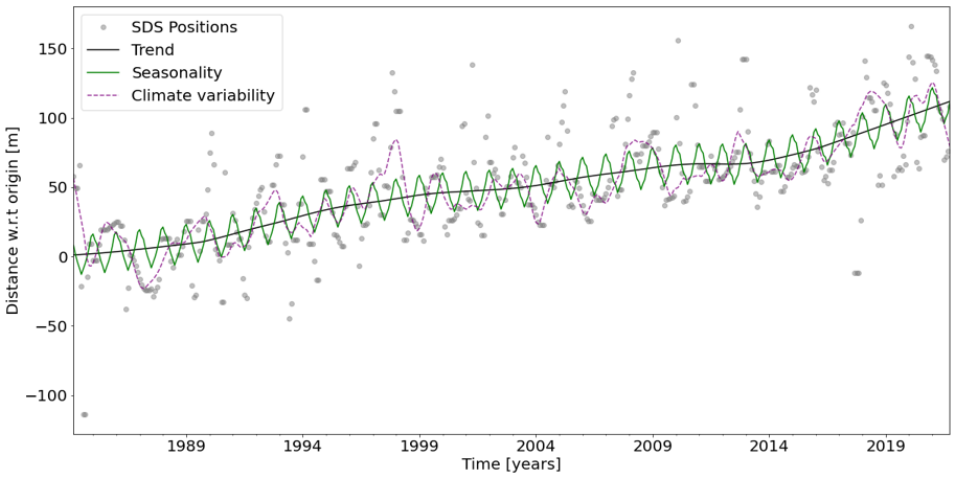

Figure 9.1: Individual signals of shoreline evolution at a transect near IJmuiden port. The identified drivers are indicated with a solid line. Another possible driver that causes shoreline evolution here, climate variability, is indicated with a dashed line.

The total variance of the SDS positions (E(x)) equals 1698 m^2 in this example. 767 m^2 and 129 m^2 of this variance could be explained by evolution due to the littoral drift barrier and seasonality respectively. Seasonality contributes to a total of the variance of $\frac{0.98 \cdot 129}{1698} \cdot 100 = 7.4\%$, while for littoral drift barriers this accounts to $\frac{0.99 \cdot 767}{1698} \cdot 100 = 44.7\%$. This means that almost 50% of the total shoreline variability at this location remains unexplained. Of course, SDS time series contain noise and outliers, making it impossible to explain 100% of the time series. Nevertheless, this location is certainly influenced by another or even several other drivers, as shown in Figure 9.1 with the dotted purple line.

5. Identifying the drivers can help finding parallels across locations where shoreline evolution is similarly influenced. These similarities can then be used to create standardization of a method to approach a certain problem. These similarities can be obtained from external data sets as well, such as wave height, wave directions, beach slopes, etc.

6. To support local case studies, not only the current or past evolution of the coastline is important, but also its behavior in the future. Forecasts using SDS have already been made in a number of studies (Vousdoukas et al., 2020; Calkoen et al., 2021), but still without knowledge of the drivers of shoreline evolution. Without this knowledge, predictions of the future behavior of the shoreline may be completely wrong, as shown in Figure 9.2. This figure shows a forecast of the shoreline behaviour at the Sand Engine which is based on a linear interpolation of the annual shoreline positions. The erosive characteristic of a nourishment after the beach widening is neglected.

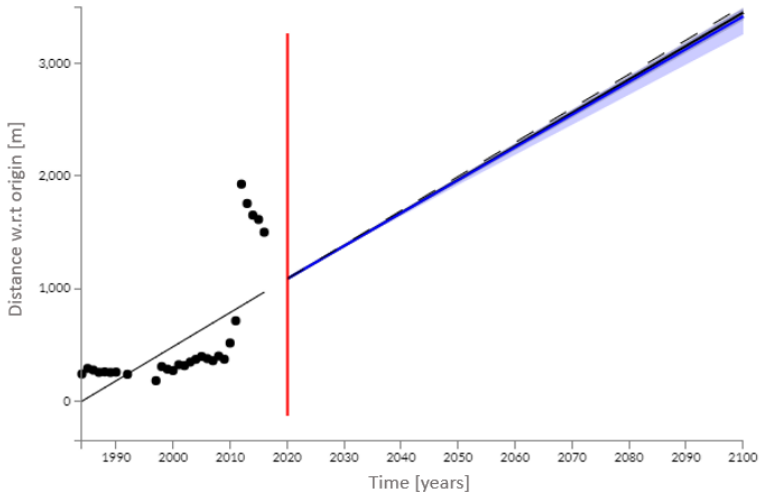

Figure 9.2: Forecast of annual shoreline positions at the Sand Engine for different emission scenario's. (Source: Vousdoukas et al., 2020)

With knowledge of the drivers, individual signals can be extrapolated and super-positioned. See Figure 9.3. In this figure the trend was linked to a nourishment, while seasonality was identified as well. These two drivers are extrapolated to the future independently and then super-positioned. Also other aspects for future projections should be taken into account. For the example of the sand engine one of this aspects is the wave angle with respect to the coast. As the volume of sand is washed away by waves, this wave angle changes (see Figure 2.23) which consequently affects the amount of sediment transported (see Equation 2.6) and thus the change rate of shoreline evolution.

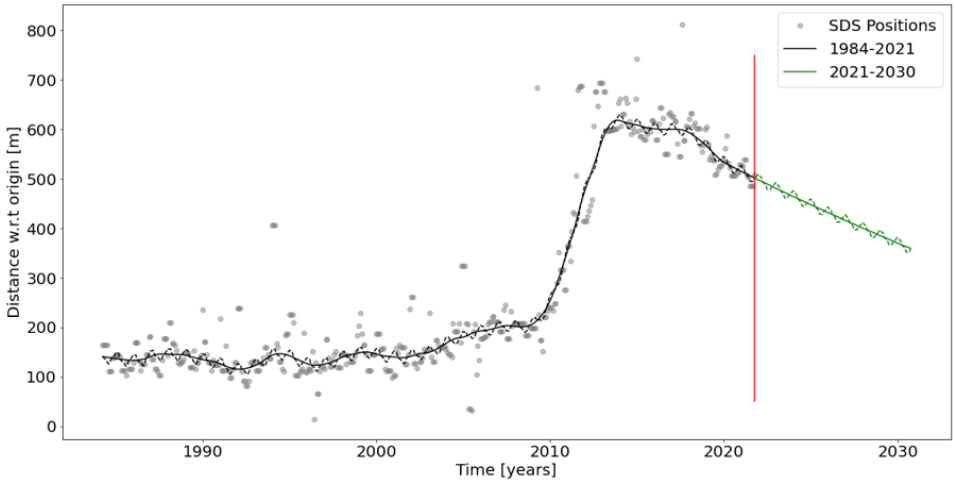

Figure 9.3: Informed forecast of monthly shoreline positions at the Sand Engine. The solid (dashed) line is the signal that is linked to nourishments (seasonality).

A

Appendix: background

A.1. Background Information

A.1.1. The Shoreline Monitor

Transect labelling

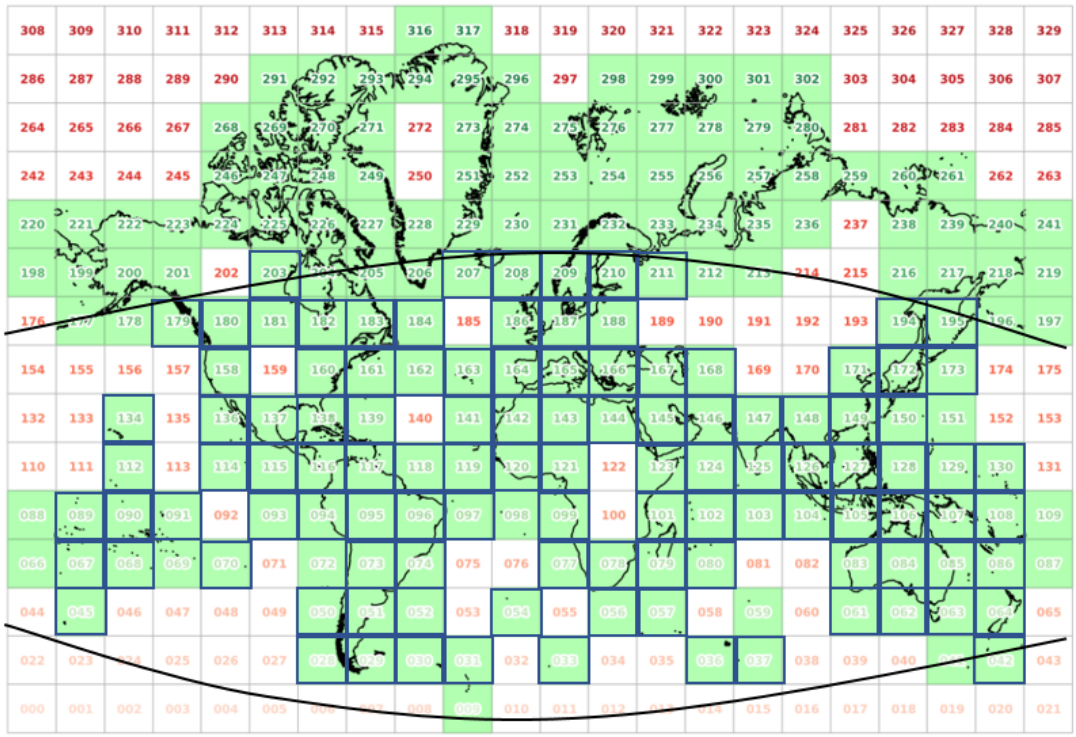

Figure A.1: Map of the world divided into boxes related to the labels of the transects in the Shoreline Monitor. Green boxes contain shorelines, whereas white boxes are either water or land. (source: Luijendijk et al., 2018).

Transects in the Shoreline Monitor are labelled as follows:

BOX_xxx_xxx_xxx

The first three x's refer to the number of the box as shown in Figure B.1. These large boxes are split into smaller sub-boxes that represent the second set of x's. The final x's consider the transect number within a sub-box.

Composite window offsets

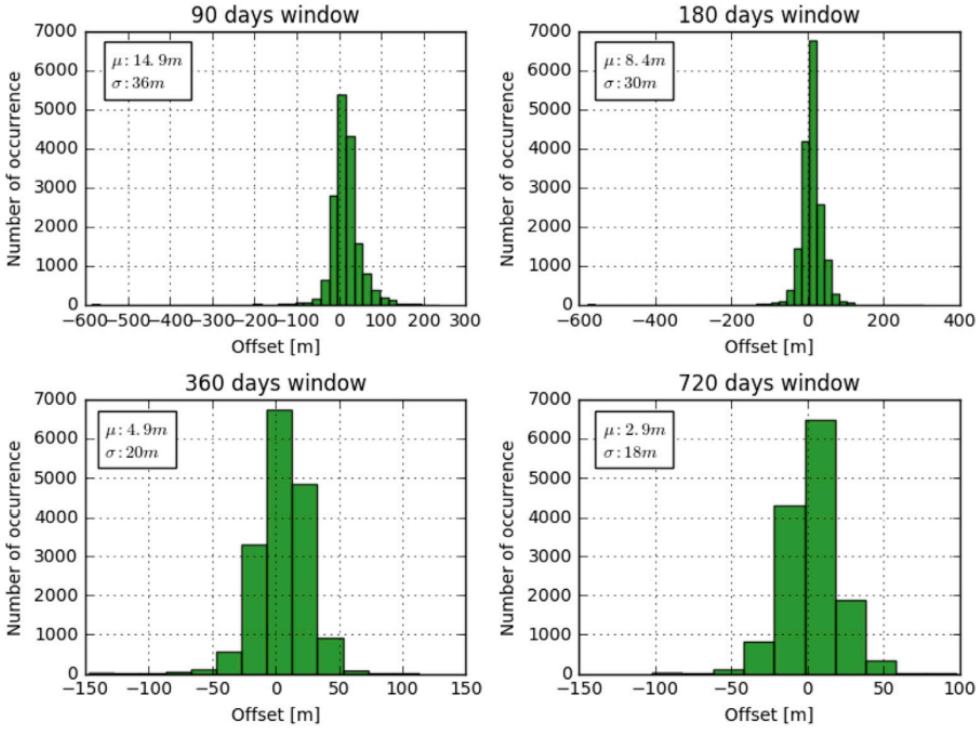

Figure A.2: Overview of the offset values for all transects per image composite window of 90, 180, 360 and 720 days. (source: Hagenaars et al., 2018).

Fault detection filter

Below situations are outlined considering situations when transects are rejected based on the recommendations of Van Leeuwen (2018) and implemented by Kras (2019). Figure A.3 shows a schematic visualization with numbers corresponding to the outlined situations.

1. a positive change rate surrounded by two much bigger positive change rates;
2. a big positive change rate surrounded by two much smaller positive change rates;
3. a big positive change rate surrounded by two negative change rates;
4. a negative change rate surrounded by two much bigger negative change rates;
5. a big negative change rate surrounded by two much smaller negative change rates;
6. a big negative change rate surrounded by two positive change rates.

Along-the-shoreline analysis

Using moving windows of 2.5, 10, 20, 50 and 100 kilometer, rolling means are calculated. A rolling mean is defined as the summation of the linear change rates of all available transects closest to a moving window divided by the total summed length between all these transects. To avoid localized hotspots or inaccuracies, the minimum available transects should be at least a fixed percentage of the total number of transects within a moving window. Rolling means are assigned to the center transect of a moving window determined by the floored center position of the first moving window of the shoreline. Figure A.4 shows a schematic visualization of the along-the-shoreline analysis for a moving window of 2.5 km. The floored position is found at the second

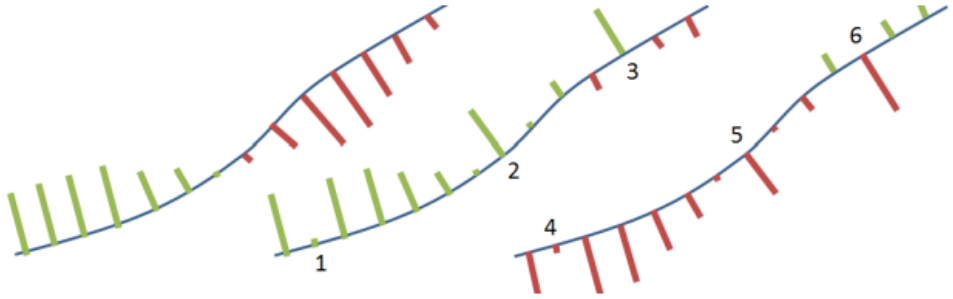

Figure A.3: Schematic visualization of a uniform shoreline with the magnitude of the changerates represented by the length of the transect. Green (red) transect represent postive (negative) linear changerates. In the center, the fault detection method excluded the transects numbered 1 to 3. On the right, transects 4, 5 and 6 are excluded, (source: Kras, 2019).

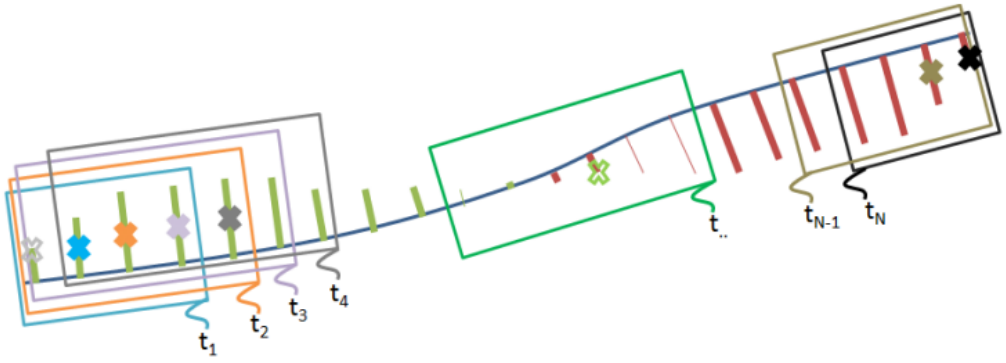

Figure A.4: Schematic visualization of the along-the-shoreline analysis applied to a uniform (blue) shoreline. The moving windows are indicated with the colored square boxes, which are labeleed $t_x x$. The thick green (red) transects refer to the magnitude of positive (negative) linear change rates, where the thin green (red) transects refer to filtered transects. Colored (empty) colored crosses represent the position and (NaN) value of the computed rolling mean. (source: Kras, 2019).

transect. Transects before the floored position of the window are appointed a NaN value for the rolling mean. Windows only start to move and compute rolling means when there are at least 6 transects from the start of the computation (Figure A.4, t_3 and t_4). At the end of the shoreline, the windows decrease in size and stop computing the rolling mean whenever the required number of available transect or the end of the transects is reached (Figure A.4, t_{N-1} and t_N). The t.. window, shows a case where the number of included transects is less than 70% of the total number of transects. In this case a NaN-value is appointed as rolling mean.
Next, with the use of these rolling means, a top-bottom approach is applied. This approach is explained using Figure A.5. First of all, all transects with a rolling mean in the stable regime (< 0.5 m/yr) are excluded. Next, all tops and bottoms are identified. A top (A.5, orange cross) has a value higher than its neighbours above the stable regime of lower than its neighbours below the stable regime. Bottoms (A.5, black cross), are identified the other way around. A top-bottom fit is created by connecting tops and bottoms by means of a linear line. Finally, by applying two final steps, this top-bottom fit is reduced:

1. Applying the c_f threshold, defined as a minimum difference between consecutive tops and bottoms and removes local maxima and minima. By connecting the remaining points, the reduced fit is obtained.

2. Applying the tb, hd and ia thresholds to obtain the feature fit:

   (a) tb: considers a minimum value between the height of a top compared to the projected linear line between two bottoms.

   (b) hd: a threshold for the minimum value for the height difference between a top and bottom after applying c_f and tb.

   (c) ia: a threshold for the number of NaN-transects compared to the total number of transects between two bottoms.

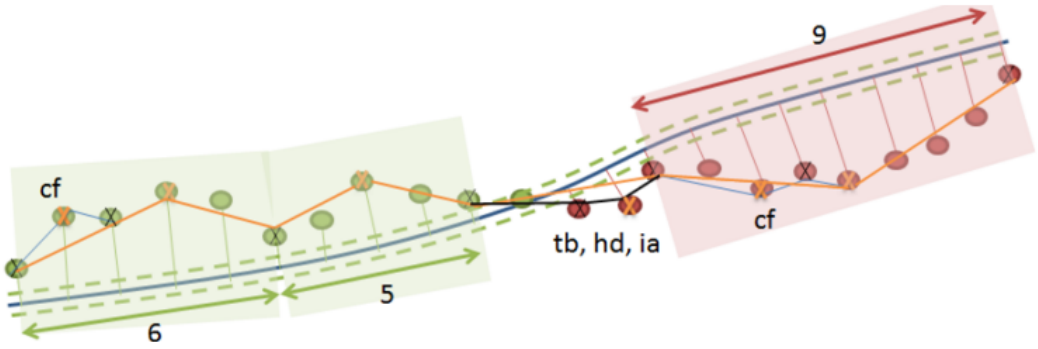

Figure A.5: Schematic visualization of a uniform shoreline (blue) where the positive (negative) rolling mean values are shown with green (red) dots and thin lines. Stable regime (+/- 0.5 m/yr) is indicated with dashed green lines. Tops (bottoms) are shown with orange (black) crosses. The top-bottom fit is represented by the thin blue line. The black line indicates the reduced fit, which is obtained after applying c_f to the top-bottom fit. The orange line shows the feature fit, after applying the threshold tb, hd and ia to the reduced fit. Hotspots characterized by a prograding (retreating) shoreline are indicated by green (red) boxes and the transects with green (red) arrows with a number. (source: Kras, 2019).

This along-the-shore analysis was validated on two small-scale and two moderate-scale shorelines. The threshold values (c_f = 1, tb = 0.5, hd = 0.5 and ia = 0.5) were iteratively found by comparison of the results on these validation cases.

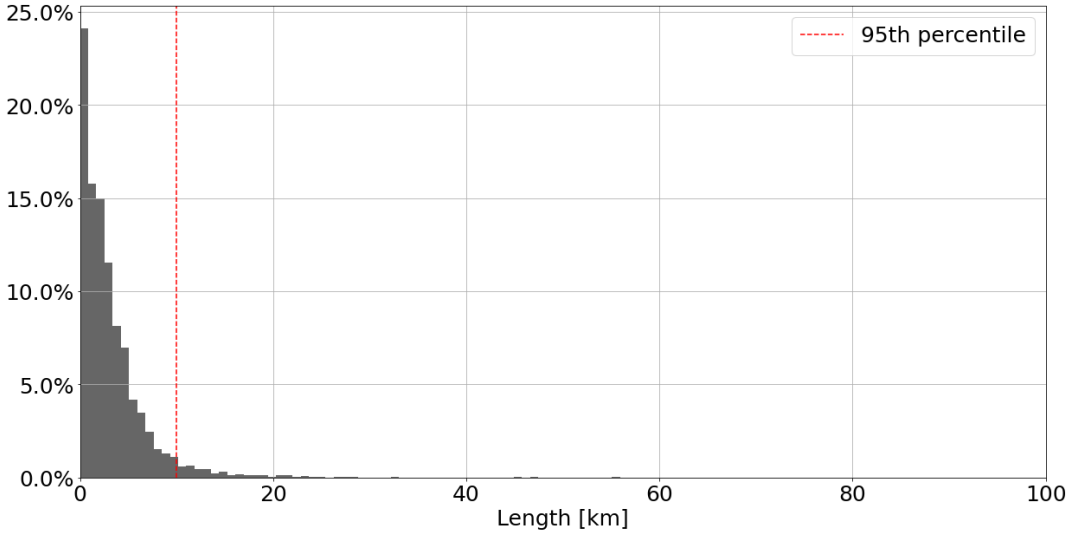

Figure A.6: Histogram of the lengths of the hotspots

A.1.2. Case Studies: Supporting Information

Fire Island: storm history

Storm	Date	Impact	Source
Halloween Storm	10-2005	Widespread erosion along the Island.	Lentz et al., 2013
Patriot's Day Nor'easter	04-2007	Substantial Beach and dune erosion particularly in the center of the Island.	Lentz et al., 2013
Nor'Ida	11-2009	Beach erosion and dune erosion after which many beaches have been renourished.	Lentz and Hapke, 2011
Hurricane Irene	08-2011	Long duration of swell and elevated water levels moved sediment towards the lower shoreface from upper beach regions.	Brenner et al., 2018
Hurricane Sandy	10-2012	Severe levels of coastal inundation and beach erosion. It even led to extensive dune overwashing and complete Island breaching.	Nelson and Hapke, 2015

Table A.1: Large storms and beach response at Fire Island from 2005 to 2012.

Fire Island: nourishment history

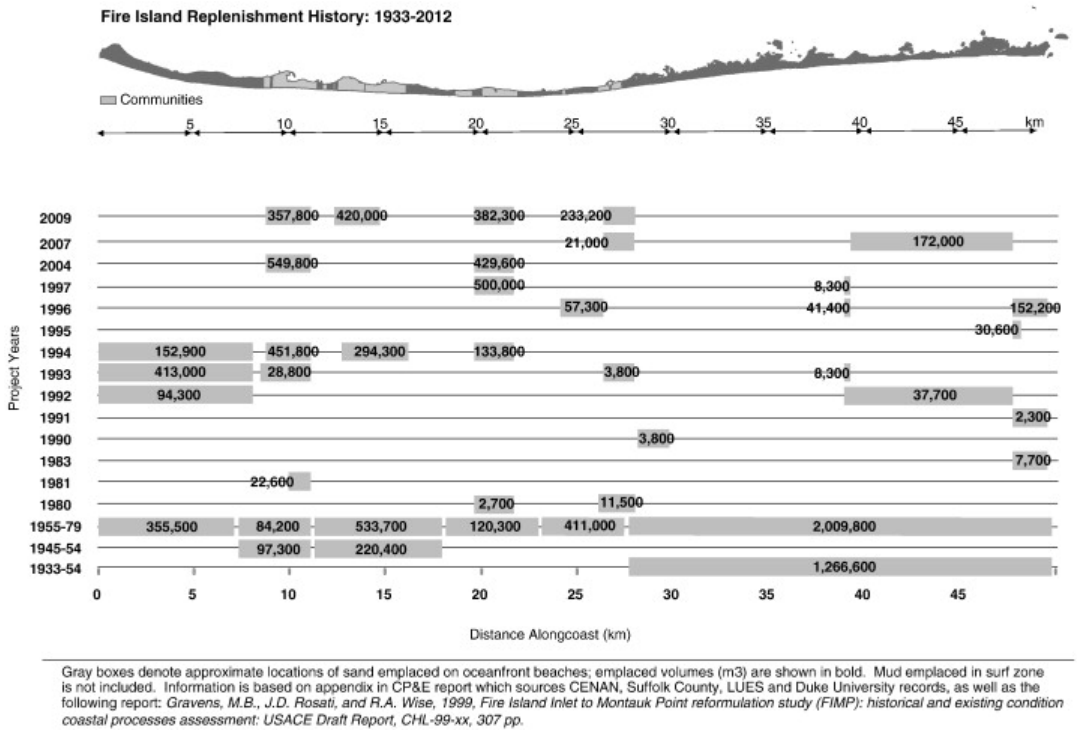

Figure A.7: Fire Island nourishment history showing apprixumate volumes and spatial locations of emplacement along shore. (source: Gravens et al., 1999).

Narrabeen: ENSO

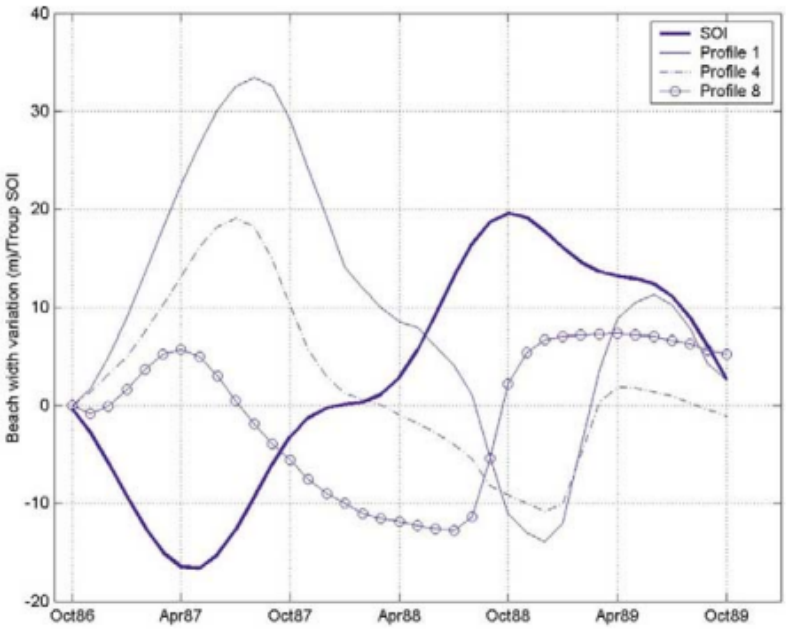

Figure A.8: Monthly beach width variation during the 1986-1989 El Niño/La Niña event. The monthly averaged SOI is also shown. Profile 1 corresponds to the Northern part of the beach where profile 8 the southern part. (source: NOAA, n.d.).

Danube Delta: NAO

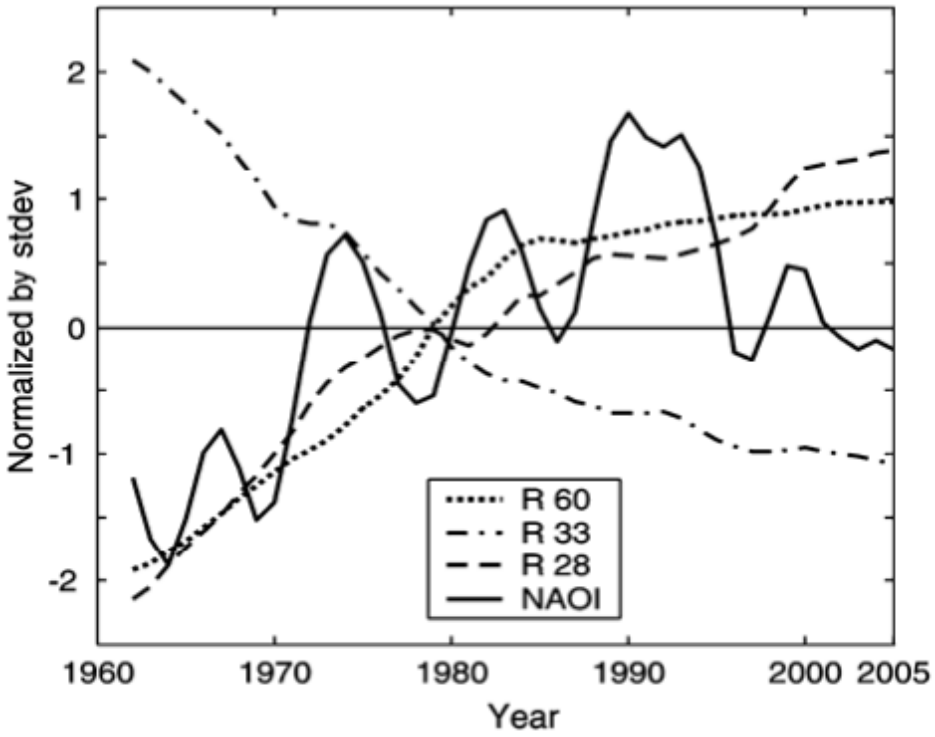

Figure A.9: Time evolution of shoreline mobility at three representative section in the Danube Delta (R60, R33 and R28) and the Hurrel's NAO index. (source: Vespremeanu-Stroe et al., 2007).

Caofedian Port: reclamation history

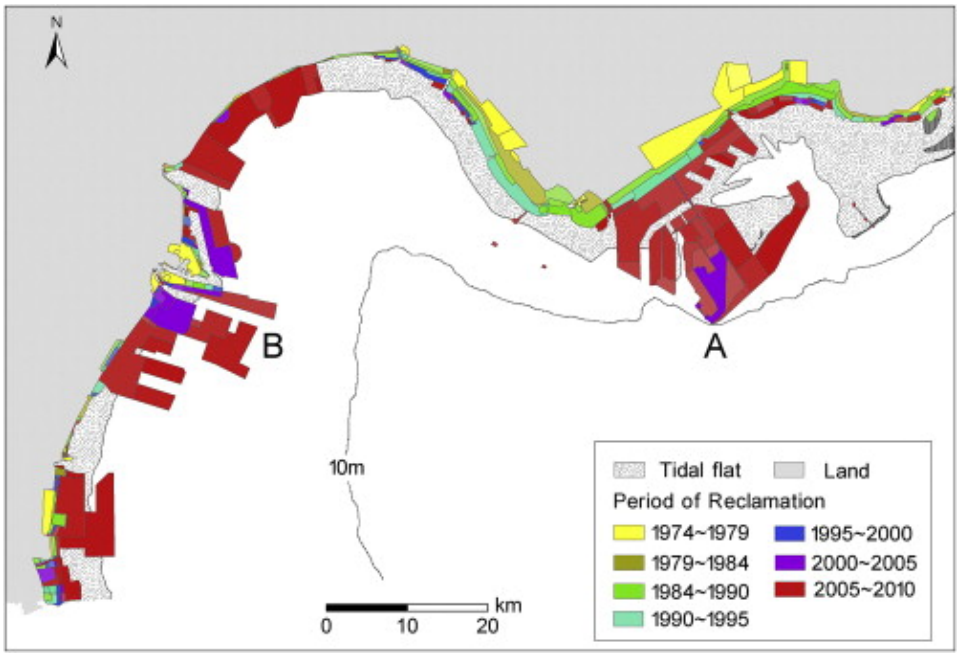

Figure A.10: Land reclamation history at the northern Bohai Bay, 1974–2010. A and B denote, respectively, the Caofeidian Industrial Complex and Tianjin New Port. (source: W. Wang et al., 2014).

Ebro Delta: shoreline evolution

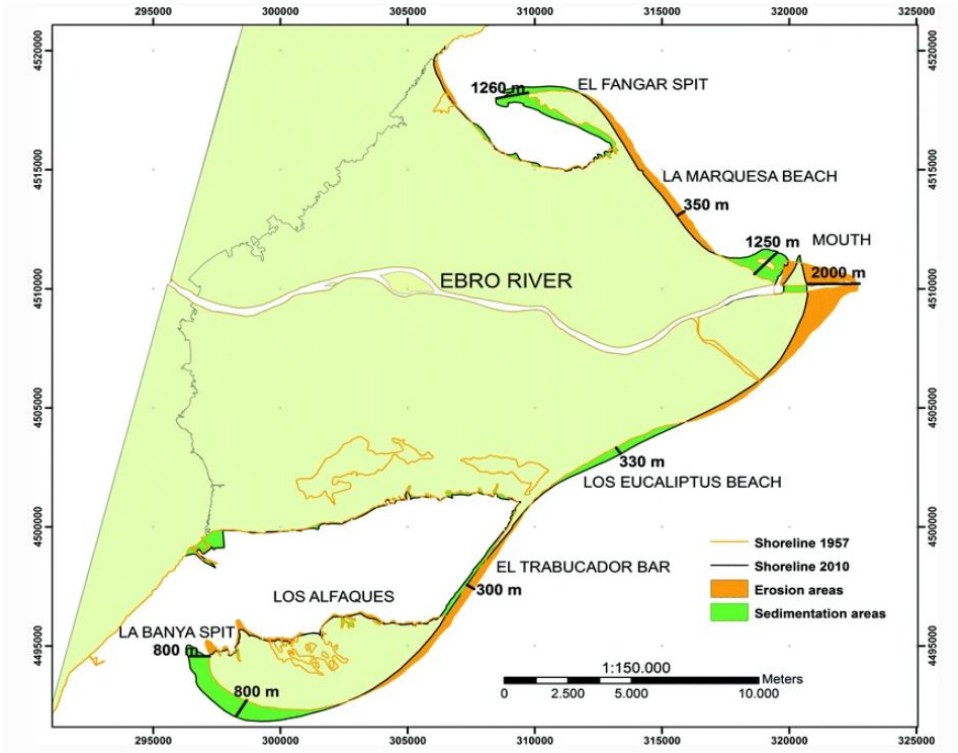

Figure A.11: Distribution of erosion and sedimentation areas for the period 1957-2010. (source: Somoza and Rodrıguez-Santalla, 2014).

Delray Beach: nourishment history

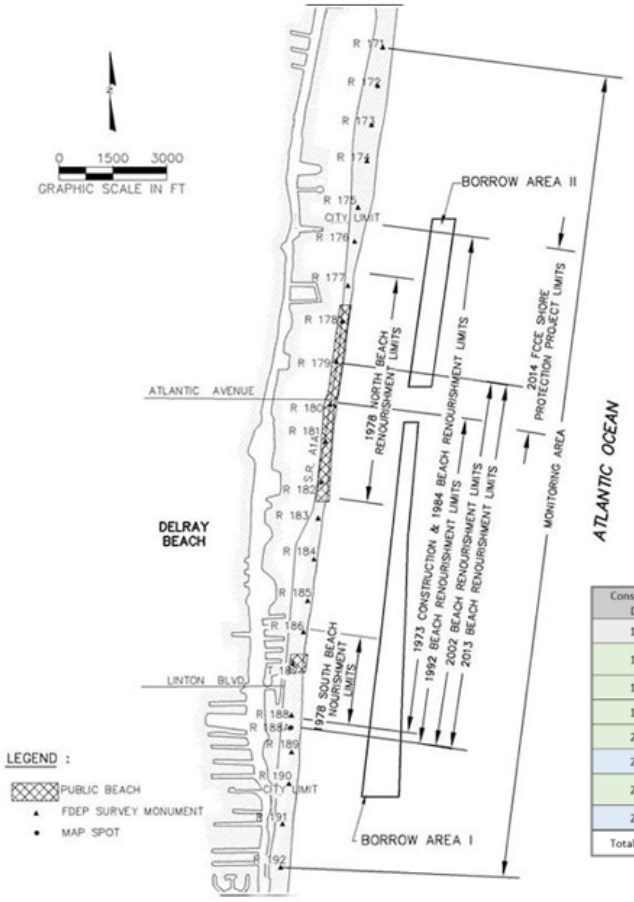

Construction Date	Placed Volume (CY)	Location	Permit Number
1973	1,634,500	R-175 to R-188	BBS 72-24
1978	701,300	R-176 to R-182 and R-186 to R-188	BBS 75-10
1984	1,311,000	R-175 to R-188	BBS 75-10M1
1992	1,196,500	R-180 to R-188.5	DBS890242 and 501662809
2002	1,230,000	R-179 to R-188A	0178582-001-JC
2005	250,000	R-175 to R-188	0178582-003-EM
2013	1,158,500	R-179 to R-188A	0303553-001-JC and 0303553-002-BV
2014	381,200	R-175+300 to R-180	0303553-001-JC
Total to Date	7,863,000	R-175 to R-188.5	-

Figure A.12: Nourishment locations and volumes at Delray Beach (Florida, US). (source: “Delray Beach Program”, 2020).

St. Augustine: nourishment history

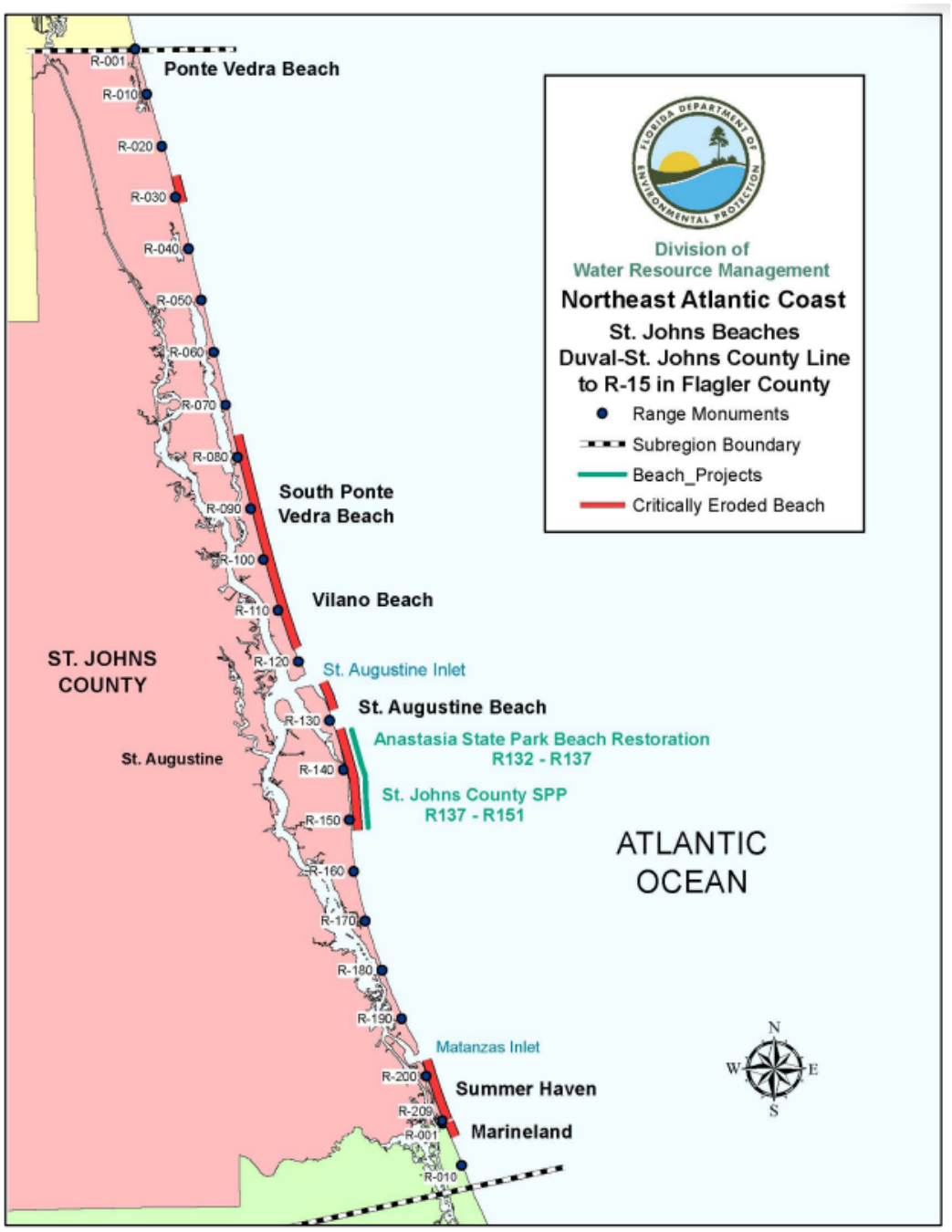

Figure A.13: Nourishment locations and volumes at St. Augustine (Florida, US). (source: FDEP, 2020).

Ijmuiden: environmental conditions

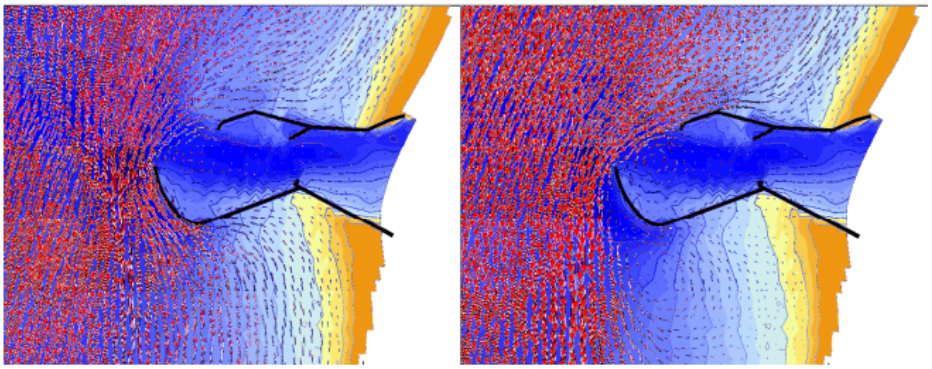

Figure A.14: Flood velocities (left) and ebb velocties (right) at IJmuiden. (source: Luijendijk et al., 2011).

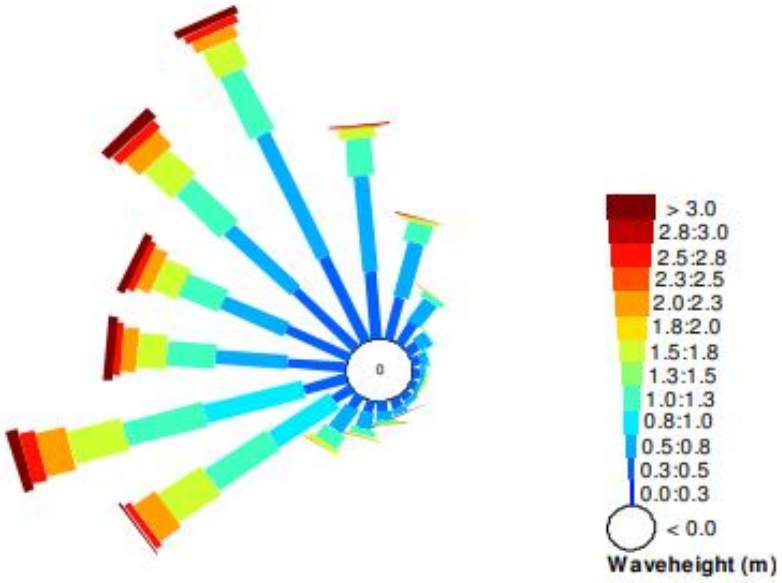

Figure A.15: Wave rose at Ijmuiden. (source: Luijendijk et al., 2011).

Manilla: reclamation plan

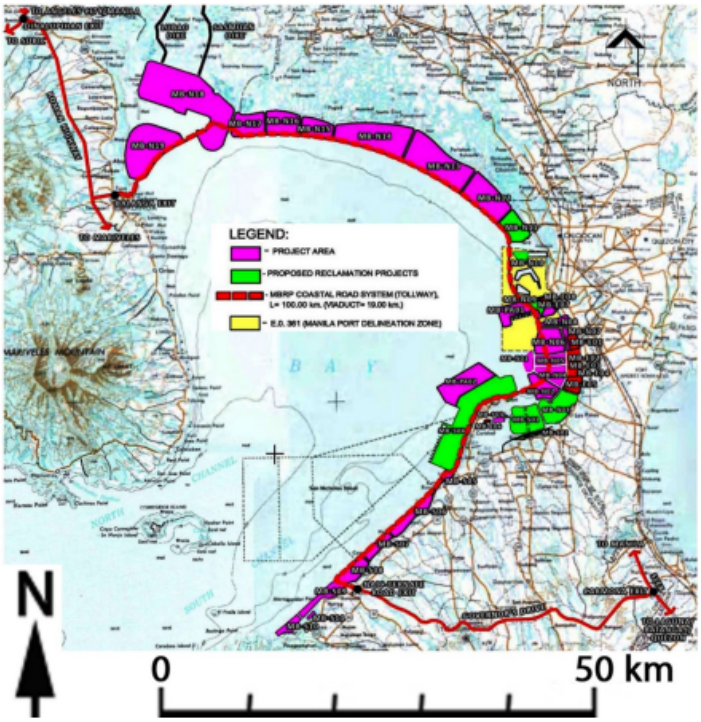

Figure A.16: The Manila Bay sector of the National Reclamation Plan. From the Philippine Reclamation Authority (2011). (source: Rodolfo, 2014).

B

Appendix: methodology

B.1. Methods

B.1.1. Outlier identification

Below in several steps is explained how outliers are identified from SDS positions:

1. A linear regression fit is made between the datapoints using Ordinary Least Squares (OLS).
2. Next, the Bonferroni Outlier Test is applied. This test uses a t-distribution to indicate at what timesteps the studentized residual value is statistically different from other observations in the model. Significant p-values indicate extreme outliers. For more information on the Bonferroni Test, see Cook and Prescott (1981).

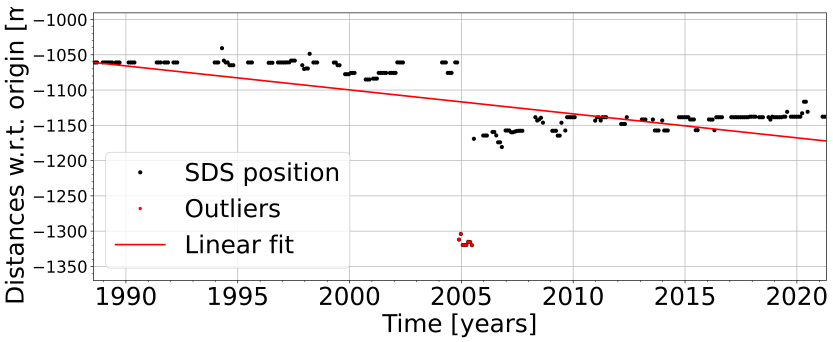

Figure B.1: SDS positions after the 2004 tsunami at the Aceh coast in Indonesia. Outlier are indicated with the red dots.

B.1.2. Timeseries filling algorithms

Filling method	Description
Neighbouring transects	A predictor is created using ordinary least squares based on training data from the targeted transect and its neighbours.
Rolling mean	mean of the timerange within a rolling window of 2 years
A rolling median	median of the timerange within a rolling window of 2 years
Polynomial interpolation	fill by a fitted polynomial with orders 1, 2, 3, 5 and 7
Spline interpolation	a piecewise polynomial fit with orders 1, 2, 4 and 5
Derivative interpolation	construct new datapoints along the curve defined by known data
Pchip interpolation	a piecewise cubic polynomial with specified derivatives at the interpolation points.

Table B.1: Methods used to fill missing values in shoreline position timeseries

B.1.3. Landsat 7: SLC failure

Figure B.2: Landsat 7 images of the San Francisco Bay area acquired before (left) and after (right) the SLC failure. (source: Scaramuzza and Barsi, 2005).

B.1.4. Seasonal-Trend decomposition with LOESS

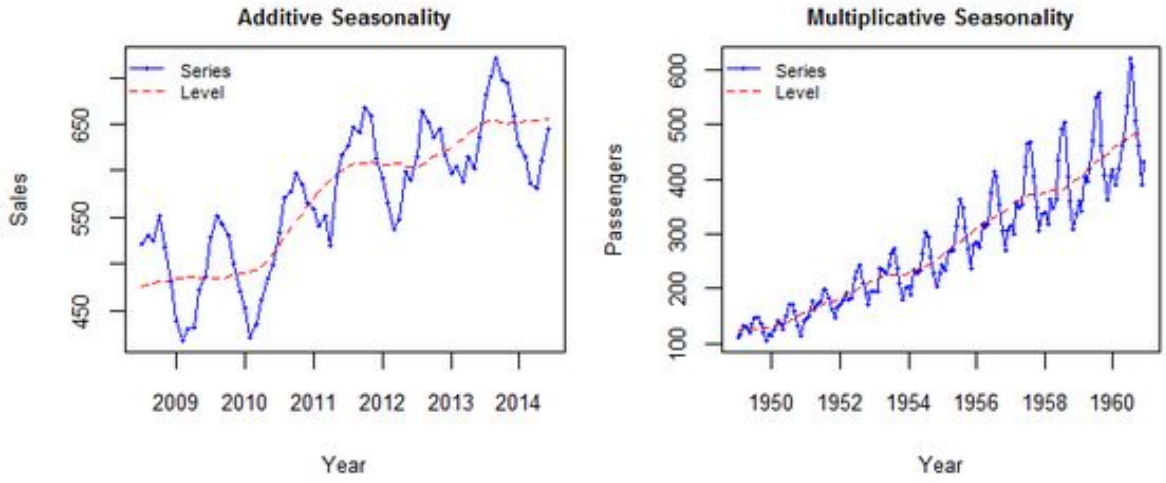

Figure B.3: Additive (left) and Multiplicative Seasonality (right). (Source: https://goo.gl/szKmgo)

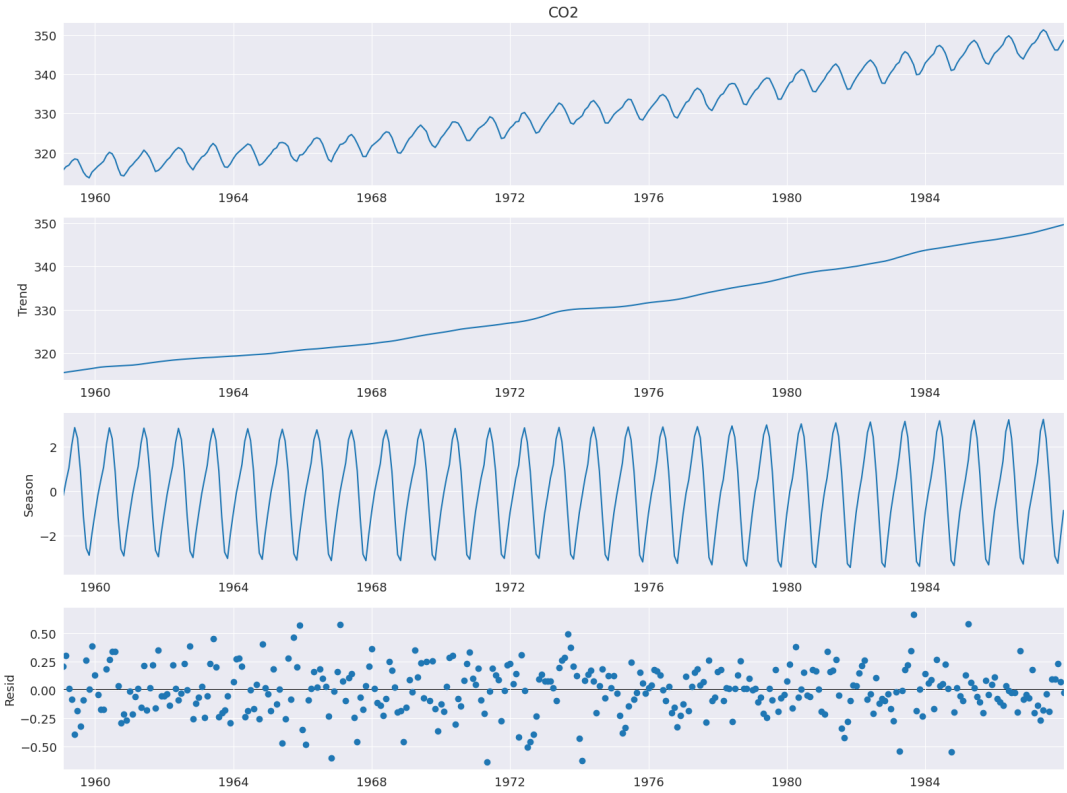

Figure B.4: STL of daily carbon dioxide data. The units on the vertical scales are ppm (source: Cleveland et al., 1990)

.

B.1.5. Empirical Mode Decomposition

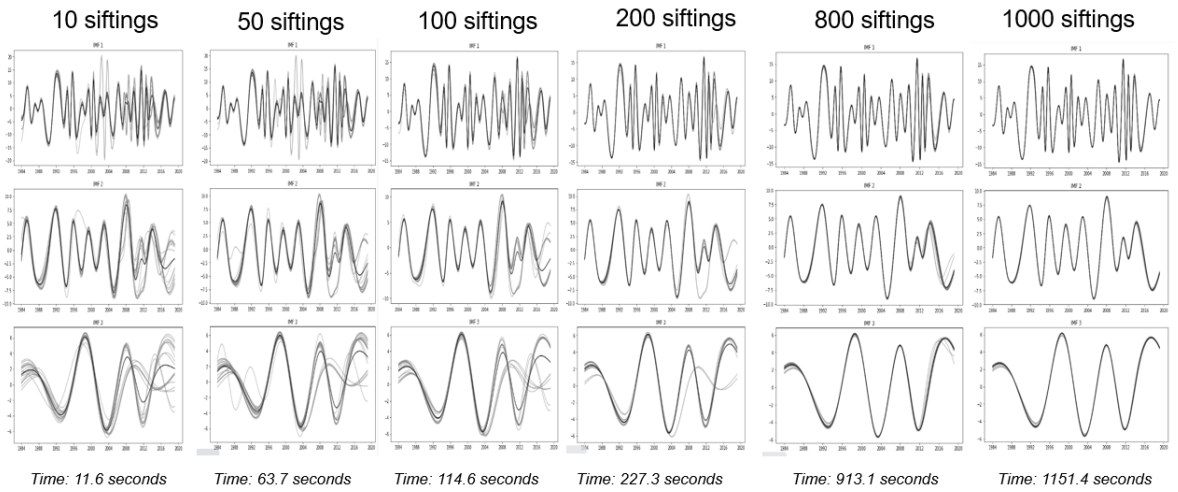

Figure B.5: EMD outcomes for several siftings (iterations) of the algorithm. The different rows represent IMFs. The grey color oscillations indicate individual output from the algorithm for a certain amount of siftings. The dark colored line represent the mean of different runs. Convergance of the runs occur after 800 siftings, at this moment the algorithm becomes computational very intensive.

B.1.6. Seasonality

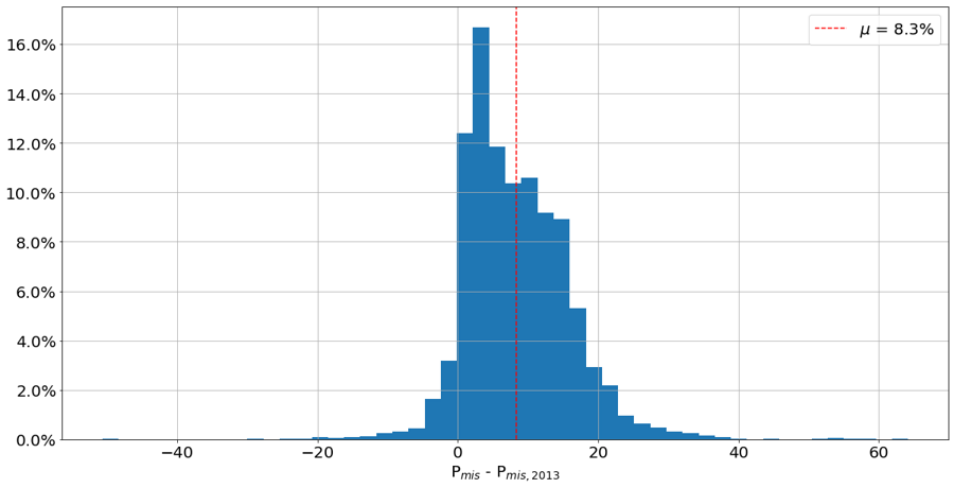

Figure B.6: Histogram of differences between missing values of the entire timeseries (P_{mis}) and only after 2013 ($P_{mis,2013}$). The mean difference is indicated with the red dashed vertical line.

B.1.7. Littoral drif barriers

Trend smoothing

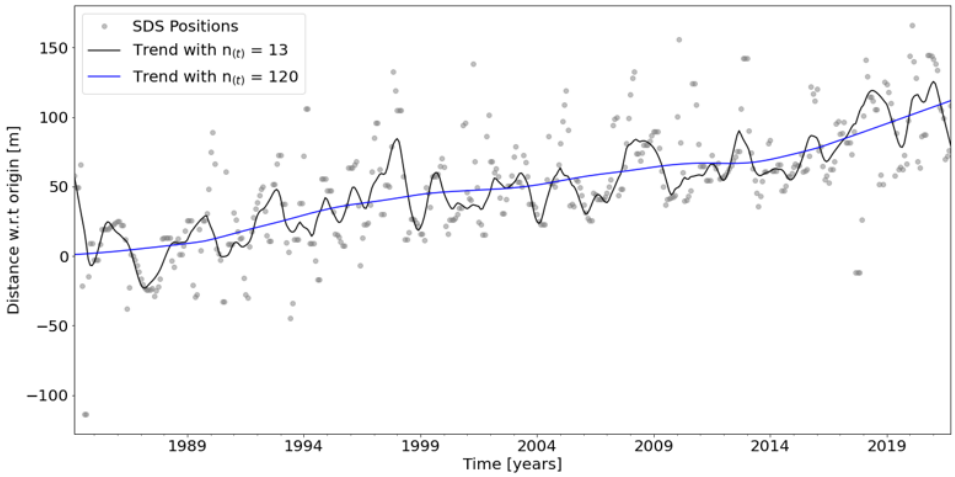

Figure B.7: Example of a trend with a smoothing window of 13 months (black line) and of a trend with a smoothing window of 120 months (blue line). The SDS positions are indicated with the grey markers.

Trend characteristics

Below the steps are explained to identify the number of characteristics in a trend:

1. A FOPF is fitted through the trend.
2. If the coefficient of determination (R_2) between the FOPF and the trend is smaller than 0.9, the following iterative process is entered:
   (a) Using a decision tree regressor the data is splitted at a location which optimized the FOPF.
   (b) FOPF are fitted to the splitted data
   (c) If all (R_2)'s are at least 0.9. The data is no further splitted. Else go back to step (a)
3. The number of characteristics is equal to the number of fitted polynomials. Fitted polynomials with a changerate in the stable regime (-1 to 1 m/yr) are not identified as a separate characteristic.

Sub-hotspots

Below the steps are explained to split a hotspot:

1. A FOPF is fitted through the changerates in space.
2. If the coefficient of determination (R_2) between the FOPF and the changerates is smaller than 0.5 (indicating a very bad fit), with a decision tree regressor the data is splitted at a location which optimized the FOPF.
3. For the changerates within the splitted hotspot, again a first order polynomial is fitted.

B.1.8. Multinomial logistic regression

In the case of multinomial logistic regression (more than 2 outcomes) the logit model has the following from:

$$f(k,i) = \beta_{0,k} + \sum_{j=1}^{j=M} \beta_{j,k} x_{j,i} \tag{B.1}$$

where k : outcome
i : observation
M : number of dependent variables

The logit function is then as following:

$$P(Y_i = K) = \frac{1}{1 + \sum_{k=1}^{K-1} e^{f(k,i)}} \tag{B.2}$$

Where K is a possible outcome.

C

Appendix: local verification

C.1. Local verification

C.1.1. SDS input

Different input combinations were tested for five test cases to see the effect on missing values in the SDS. All these locations have significant annual average cloud cover (about 50%), so the effect of different cloudcover limits on the SDS results can be tested..

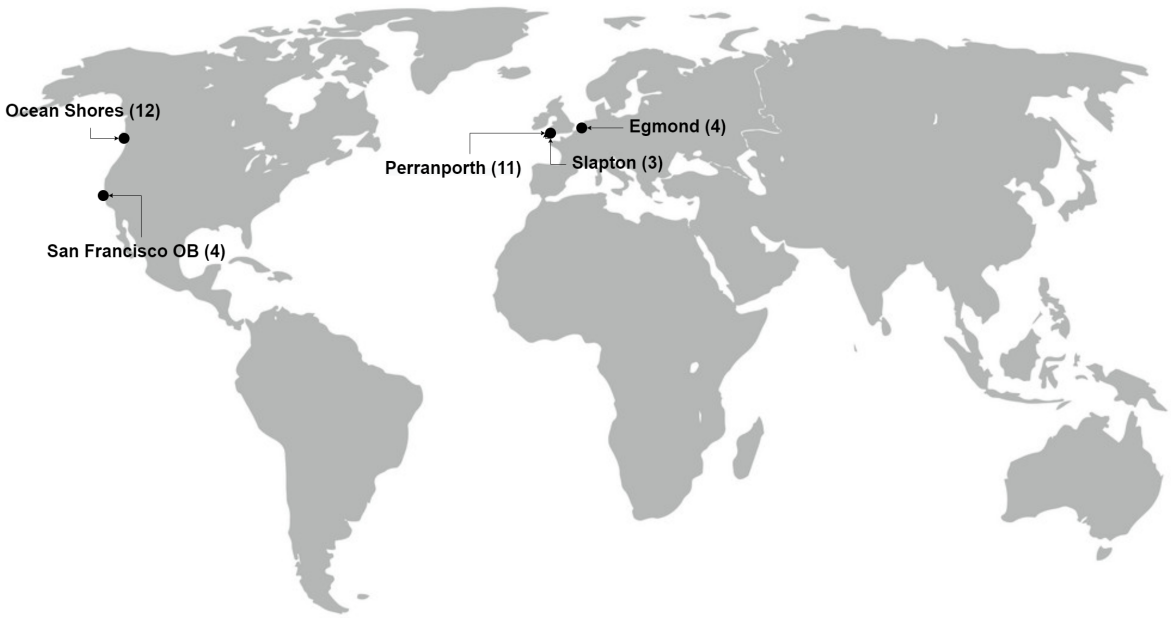

Figure C.1: Overview of all casestudies which where used to choose the optimal input parameters to generate SDS. The number of transects per location is denoted between brackets.

SDS has been generated according to the following input:

1. Composite window (CW): 90 and 180 days
2. Cloudcover limit (CCL): 20%, 40%, 60% and 80%
3. Satellite images (SI): with and without Landsat (LS) 7

4. temporal resolution (TR): monthly
5. period (P): January 1984 to July 2021

A possible combination could be: CW = 90 days, CCL = 20%, SI = LS5 and LS8, TR = monthly and P = January 1984 to July 2021.
Figure C.3 summarizes different input combinations on the effect of missing values in the generated SDS for the locations from Figure C.1. Figure C.3 shows in total 16 different combinations for 5 locations with a total of 34 transects.
The following is observed from Figure C.3:

1. Cloudcover
   (a) At Slapton, Perranporth and Egmond the amount of missing values decreases with a higher CCL
   (b) For San Francisco OB and the Ocean Shores there is no clear relation between CCL and the percentage of missing values.
2. Satellite missions.
   (a) In three of the four cases including Landsat 7 results in less missing values
   (b) In- or excluding Landsat 7 has almost no effect on the missing values at Ocean Shores
   (c) At San Francisco OB, including Landsat 7 results in more missing values
   (d) Composite window
      i. At San Francisco OB and the Ocean Shores a larger composite window results in more missing values
      ii. The remaining three locations show that the amount of missing values decrease with a composite window of 180 days compared to 90 days

Summarizing, in most cases, a composite window of 180 days with a cloud cover of 80% and including Landsat 7 results in the least missing values. However, Figure C.2 shows that for a cloudcover of 80% and by including Landsat 7, differences between the percentage of missing values between a composite window of 90 days compared to 180 days is small. Moreover, a composite window of 90 days captures more intra-annual shoreline variability than 180 days. A composite window of 45 days does result in significant more amount of missing values.

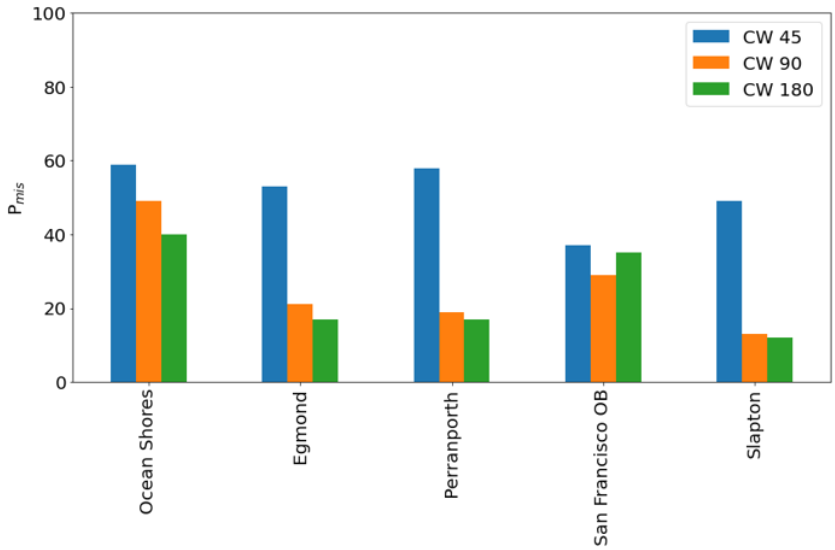

Figure C.2: Bar plot of the missing values for five cases comparing composite windows of 45, 90 and 180 days. Input is generated with a cloud cover of 80% and by including Landsat 7.

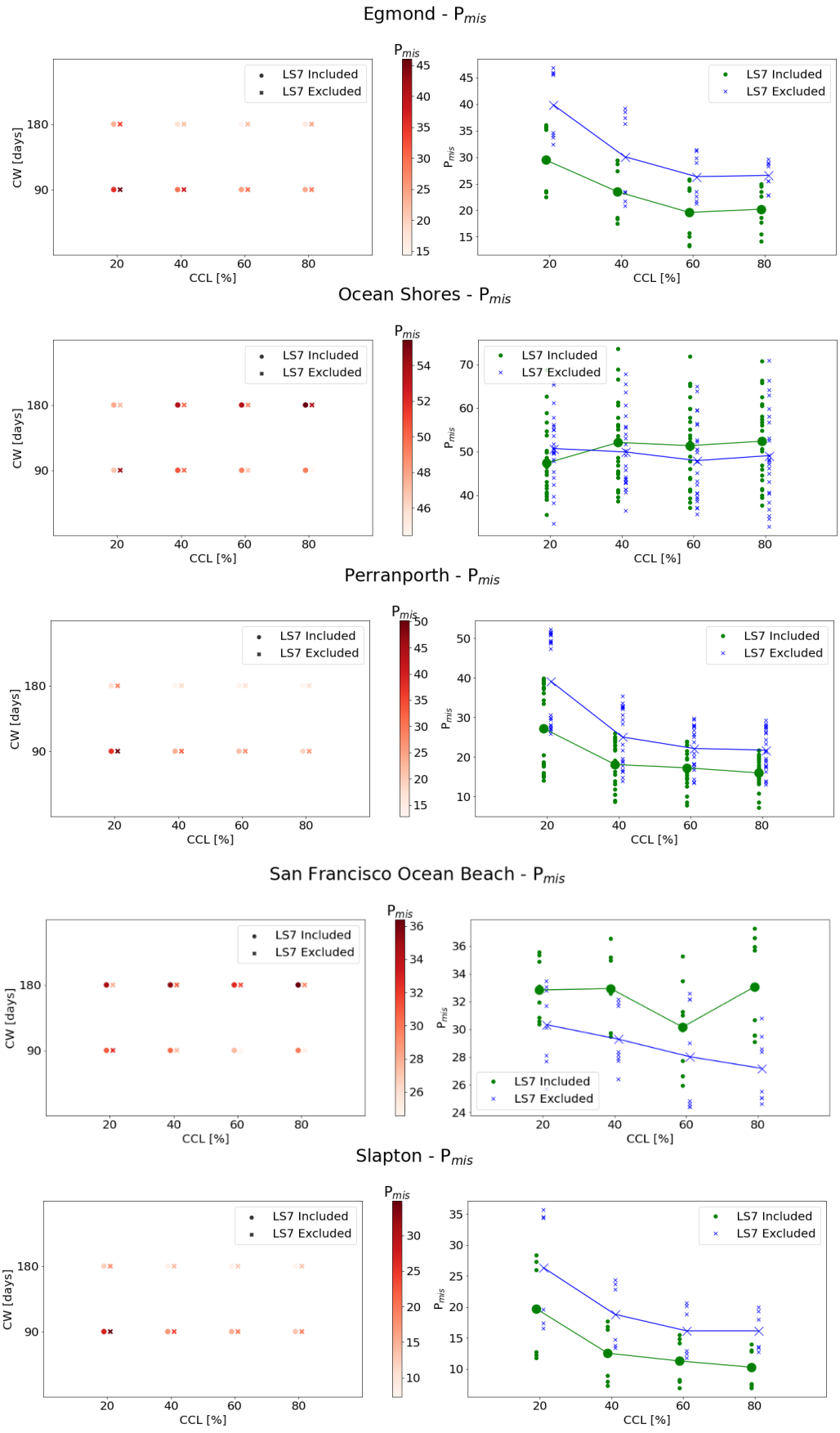

Figure C.3: Missing values analysis for five cases and several combinations of input parameters for SDS generation. P_{mis} is an abbreviation for the percentage of missing values. In the left image, only the mean P_{mis} over all transects at a location is plotted. In the right image, the markers represent the results of an individual transect for a combination of parameters. The larger side markers represent the mean P_{mis} where there is no separation made between composite windows.

C.1.2. STL input

Seasonal-Diagnostic plots

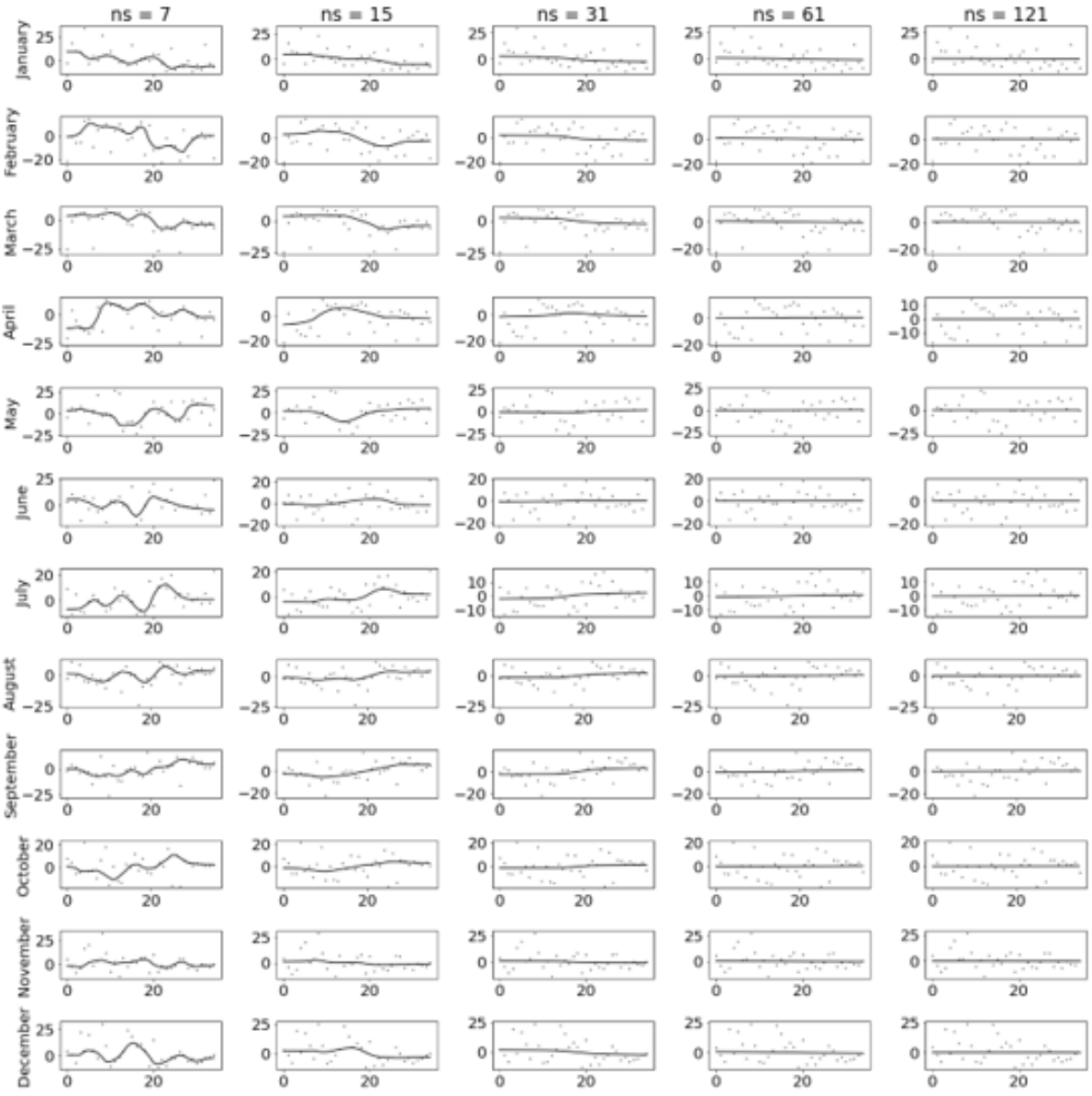

Figure C.4: Visualization of STL results, with and without an robustness iteration of TR1 (see Figure **??**) at Perth North City Beach

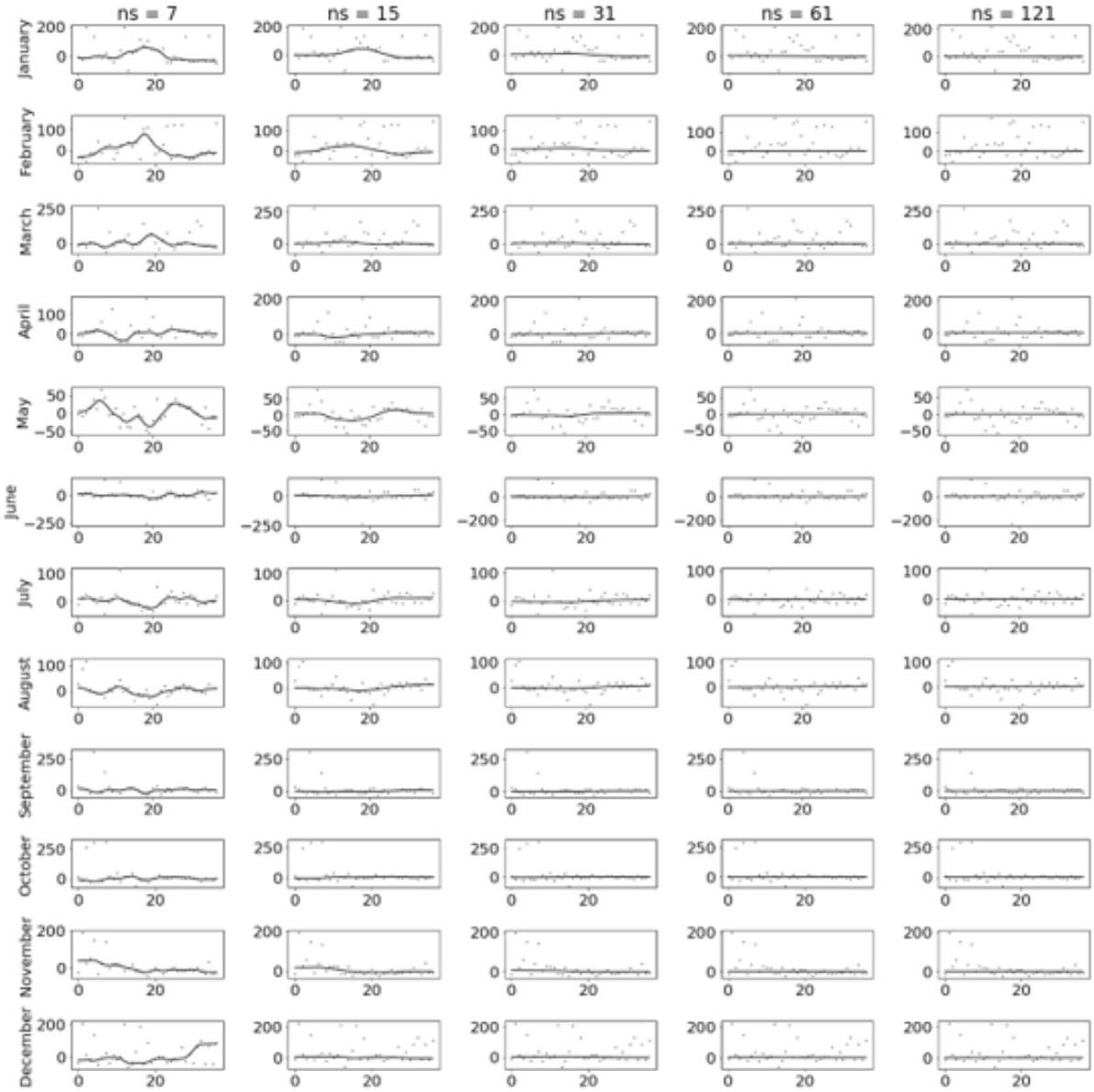

Figure C.5: Visualization of STL results, with and without an robustness iteration of TR1 (see Figure **??**) at San Fransisco OB

Both Figure C.4 and C.5 show that for a seasonal smoother of 61 (or higher) there are no changes over the years in seasonal amplitude.

Robustness

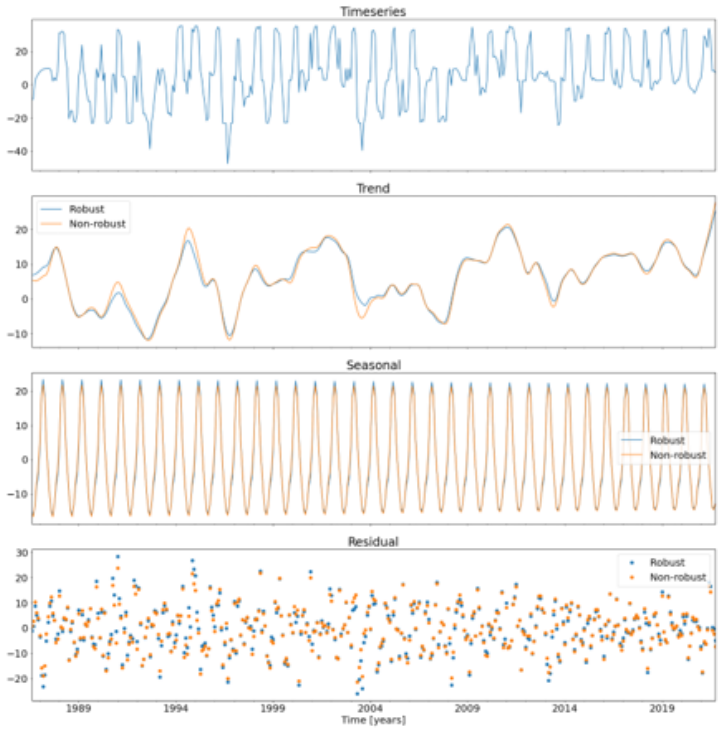

Figure C.6: Seasonal-Diagnostic plot of TR1 (see Figure **??**) at San Francisco OB

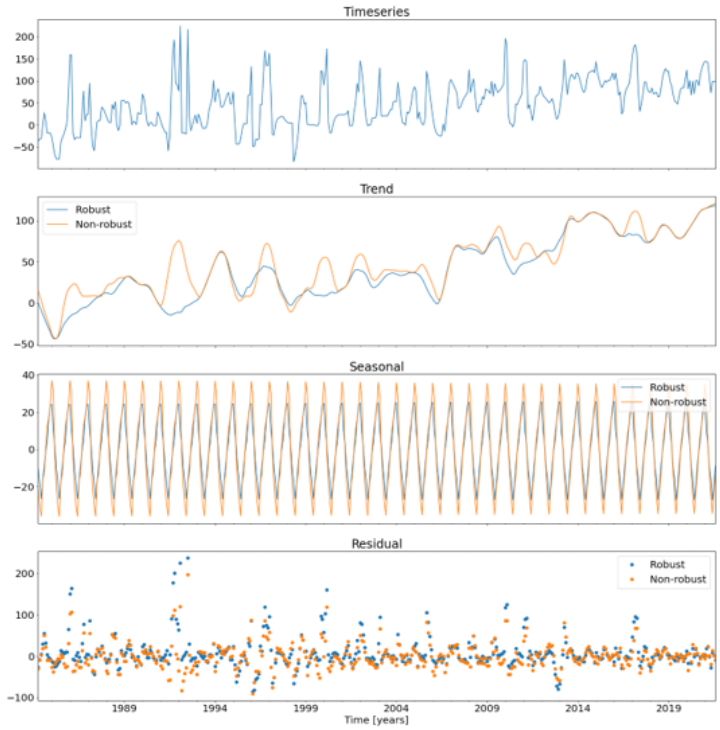

Figure C.7: Seasonal-Diagnostic plot of TR1 (see Figure C.8) at San Francisco OB

C.1.3. Seasonality

San Francisco OB

Transect	Method	P_S	D_S	T_{min}	P_{accr}
TR1	STL period 11 months	166	20	July	6
	STL period 12 months	365	54	July	7
	STL period 13 months	396	32	May	6
TR2	STL period 11 months	162	26	May	5
	STL period 12 months	365	100	July	7
	STL period 13 months	396	38	July	8

Table C.1: Identification and informative parameters at San Francisco OB for various STL seasonal periods.

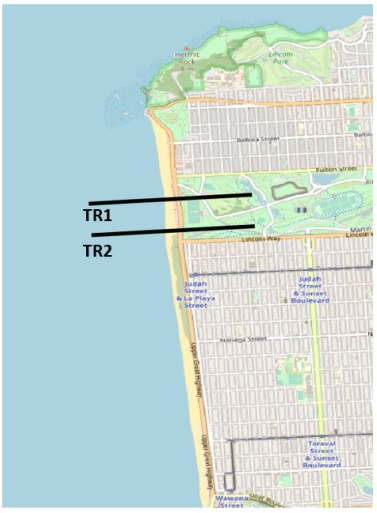

Figure C.8: Location of the analysed transects at an Francisco OB

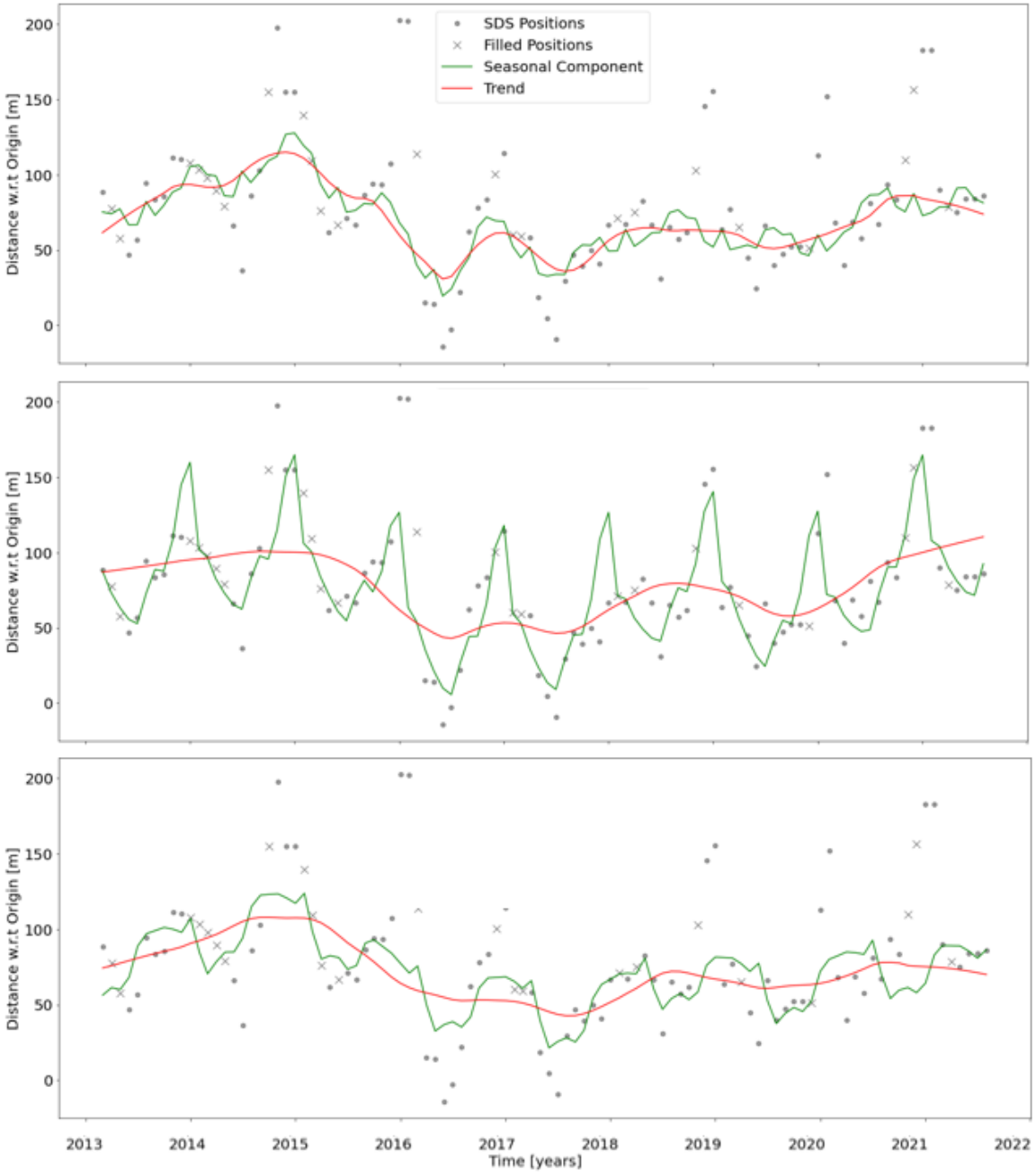

Figure C.9: Seasonal component and trend from STL with periods of 11 (upper), 12 (center) and 13 (lower) from TR2 at San Francisco OB.

The Sand Engine

Transect	Method	P_S	D_S	T_{min}	P_{accr}
TR1	STL period 11 months	167	22	October	6
	STL period 12 months	365	30	Sept	7
	STL period 13 months	200	26	May	5

Table C.2: Identification and informative parameters at the Sand Engine for various STL seasonal periods.

Figure C.10: Location of the analysed transect at the Sand Engine

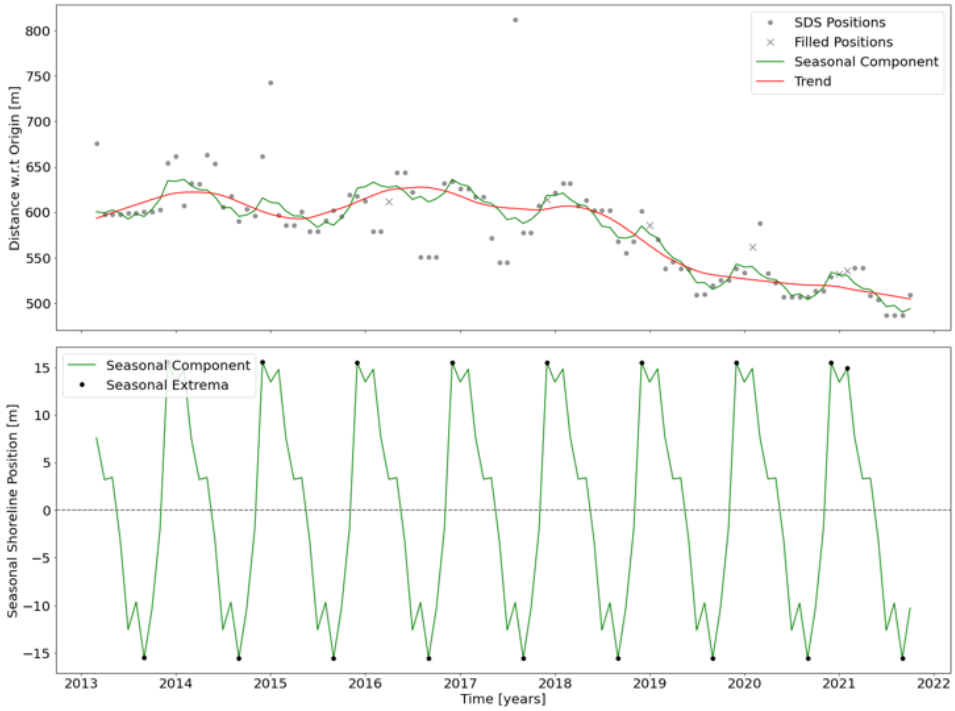

Figure C.11: STL decomposition of at the Zandmotor with a period of 12 months.

Watsonville

Transect	Method	P_S	D_S	T_{min}	P_{accr}
TR1	STL period 11 months	167	24	July	6
	STL period 12 months	365	38	July	6
	STL period 13 months	193	14	September	11

Table C.3: Identification and informative parameters at the Sand Engine for various STL seasonal periods.

Figure C.12: Location of the analysed transect at Watsonville

Basin d'Archaron, France

Transect	Method	P_S	D_S	T_{min}	P_{accr}
TR1	STL period 11 months	167	24	February	3
	STL period 12 months	183	44	July	3
	STL period 13 months	197	40	April	4

Table C.4: Identification and informative parameters at the Basin d'Archaron for various STL seasonal periods.

Figure C.13: Location of the analysed transect at the Basin d'Archaron

C.1.4. Beach Rotation

Palm Beach, Australia

Parameter	Literature	Method
r_{TR1-2}	0.62	0.60
r_{TR1-8}	-0.60	-0.16
r_{TR8-7}	0.76	0.78

Table C.5: Shoreline evolution correlations between transects at Palm beach

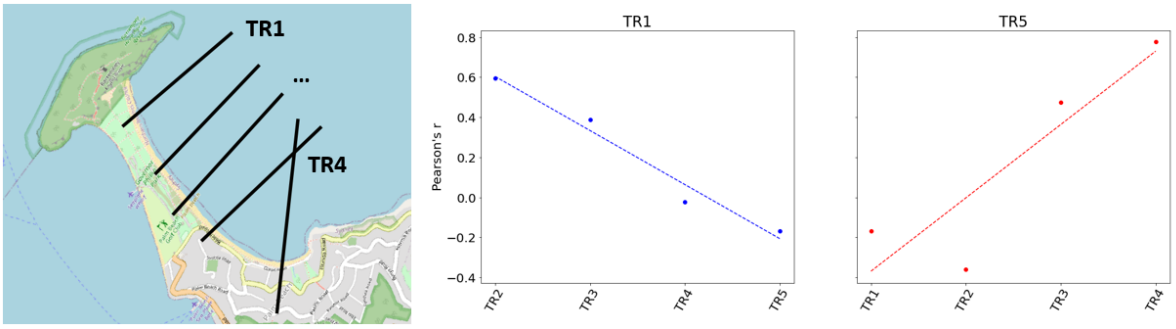

Figure C.14: Visualization of beach rotation at Palm beach. The left plot shows the locations of the transects. The two figures on the right shows correlations between the outer transects and the remaining ones. A linear fit between correlations is indicates with a dashed line.

Moruya Beach, Australia

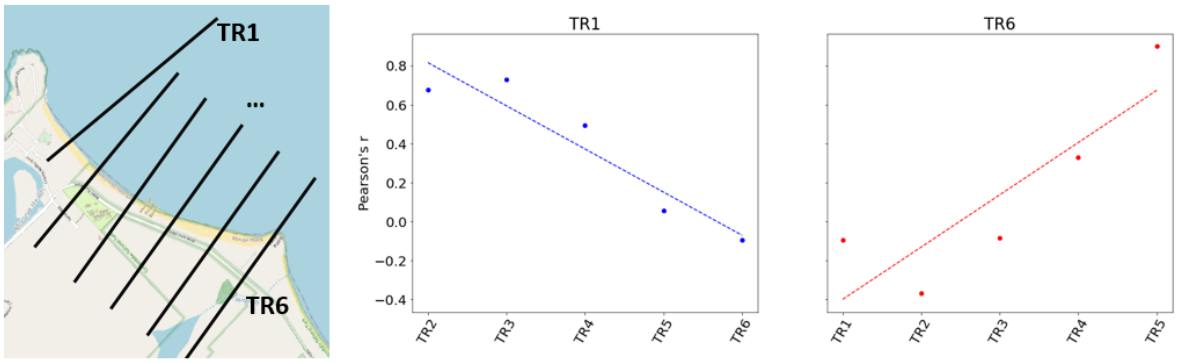

Figure C.15: Visualization of beach rotation at Moruya beach. The left plot shows the locations of the transects. The two figures on the right shows correlations between the outer transects and the remaining ones. A linear fit between correlations is indicates with a dashed line.

Parameter	M_{BR}	$R_{2,BR}$
TR1	-7.27	0.89
TR6	-9.64	0.74

Table C.6: Identification parameters of beach rotation at Moruya beach

C.1.5. Climate variability

Narrabeen

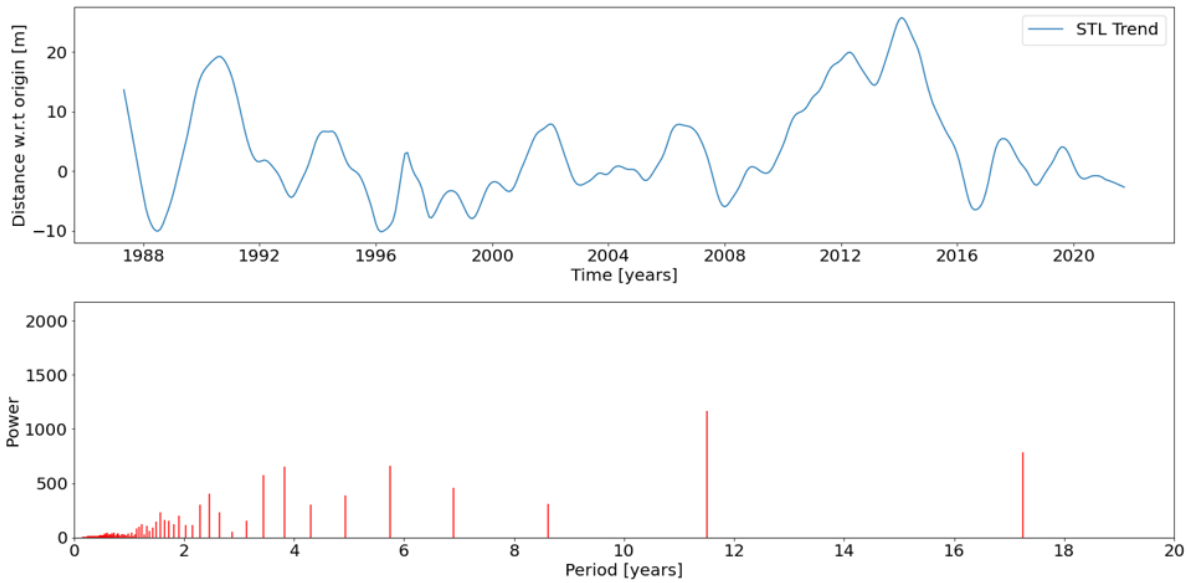

Figure C.16: Plot of the STL trend (upper) and the fast Fourier transform of this trend (lower) of TR1 at Narrabeeh.

Perth

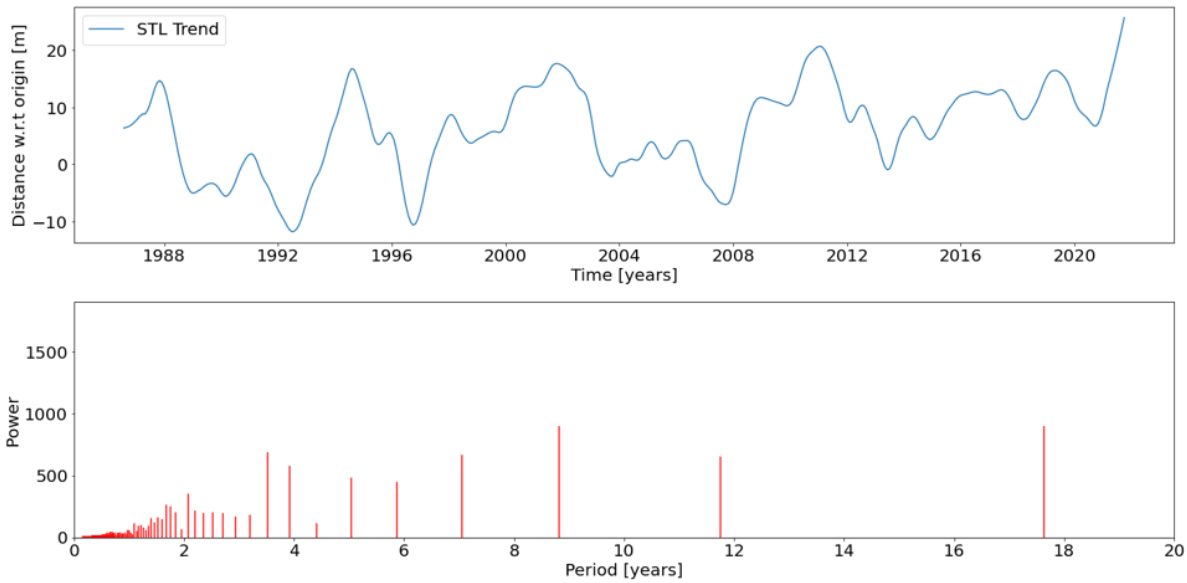

Figure C.17: Plot of the STL trend (upper) and the fast Fourier transform of this trend (lower) of TR2 at Perth.

Palm Beach

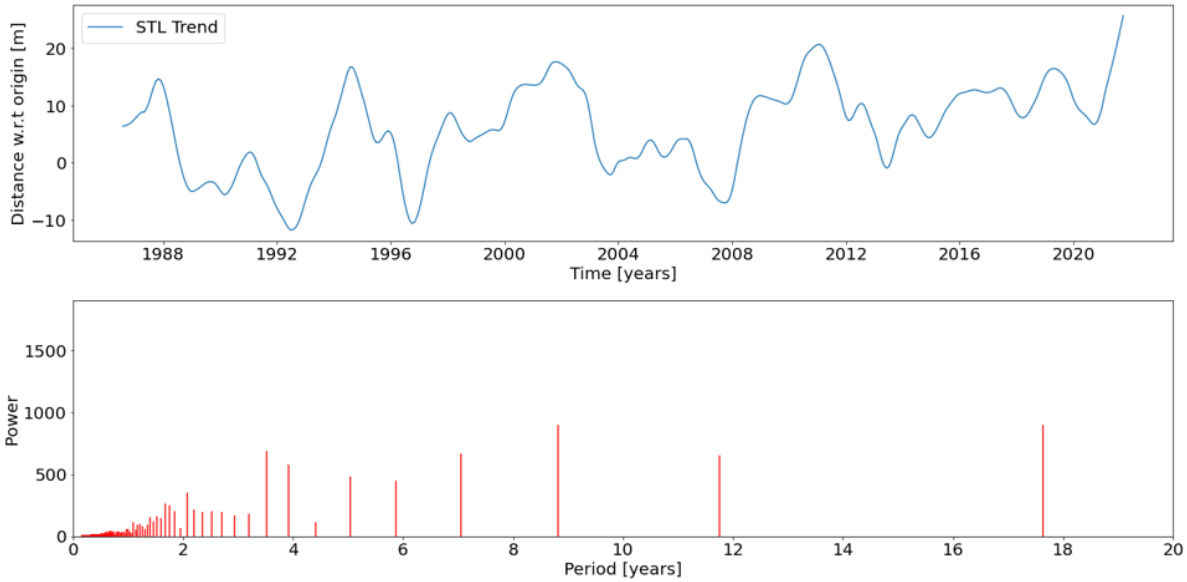

Figure C.18: Plot of the STL trend (upper) and the fast Fourier transform of this trend (lower) of TR1 at Palm beach.

Danube Delta

Figure C.19: Location of the analysed stretch of coast at the Danube Delta

C.1.6. Reclamations

Caofeidian Port, China

Figure C.20: Location of the transects at the Caofeidian port

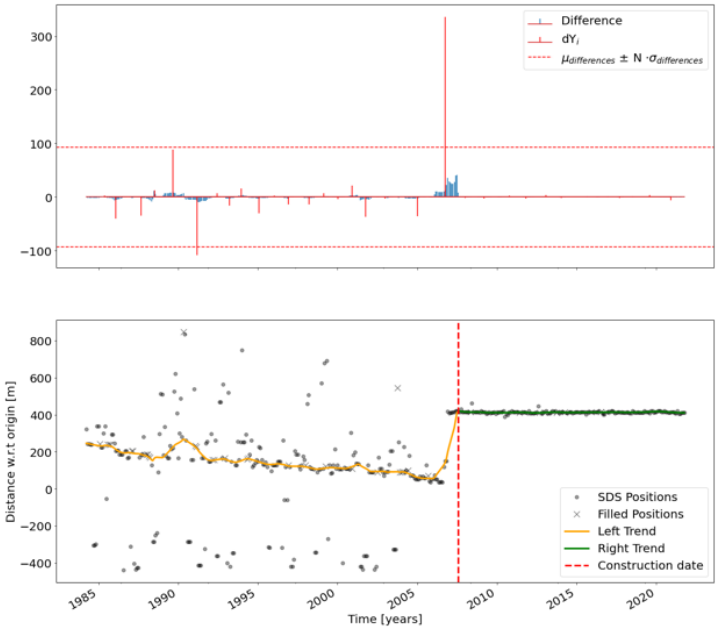

Figure C.21: Visualization of the method used to identify reclamations for TR2 at the Caofeidian Port

Jebel Ali, UAE

Figure C.22: Location of the transect at the Jebel Ali

Gibraltar, UK/SPain

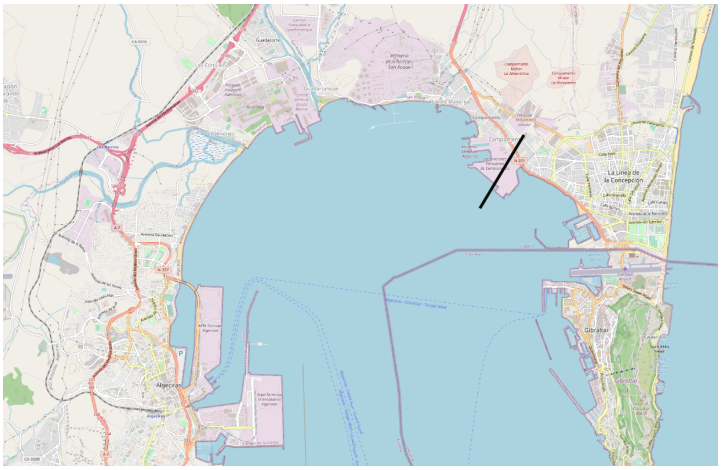

Figure C.23: Location of the transect at the Gibraltar

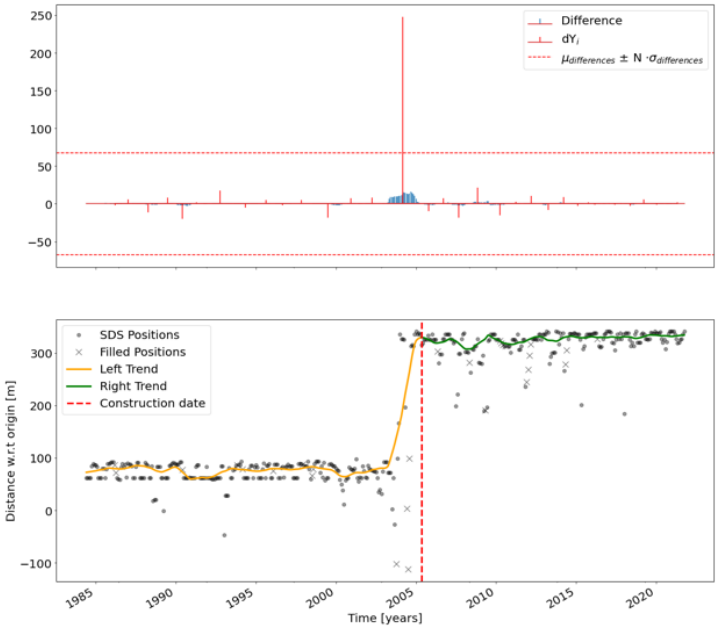

Figure C.24: Visualization of the method used to identify reclamations at Gibraltar

C.1.7. Nourishments

The Sand Engine, the Netherlands

Figure C.25: Location of the transects at the Sand Engine

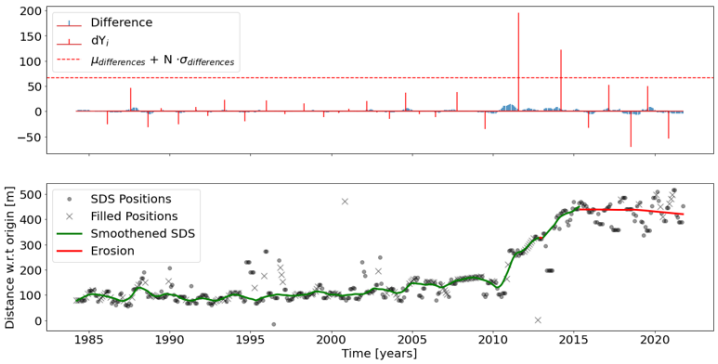

Figure C.26: Visualization of the method used to identify nourishments at the Sand Engine (TR2) for N = 3

Hondsbossche, The Netherlands

Figure C.27: Top view of the Hondsbossche coast (upper). Transects at which identification of the 2015 nourishment was successful (unsuccessful) are marker in green (red). The lower image visualizes the length of the widening of the beach for transects at which identification was successful.

St Augustine, USA

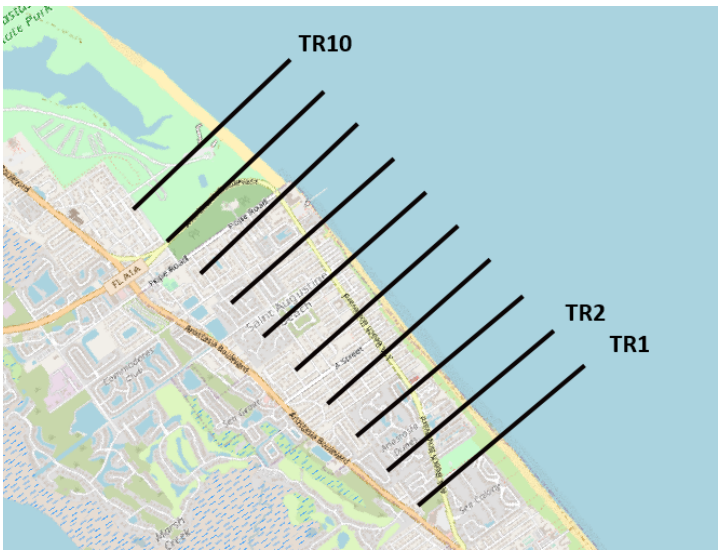

Figure C.28: Location of the transects at St. Augustine

Some notes regarding the results presented in Table C.7:

1. The 2005 nourishment is identified by the method in the year 2006, as construction dates are rounded to the nearest whole year.

2. The 2002 nourishments belong to the 2003 nourishment as parameters show the same characteristics. However, due to small differences in the data, the nourishment was identified a year earlier. This is mainly caused by rounding construction dates to the nearest whole year. Thus, it makes sense to combine identified nourishments when there is a one-year difference between construction dates. The same explanation can be given to the nourishments identified in 2013.

Nourishment year	Transect	dY [m]	LT [yr]	changerate [m/yr]
1987	TR2	22	14	-0.6
2002	TR3	74	1	-35.7
	TR4	95	1	-47.1
	TR6	126	2	-40.3
	TR8	87	2	-57.2
2003	TR1	48	2	-35.7
	TR2	51	2	-43.1
	TR5	111	2	-41.3
	TR7	123	2	-52.2
	TR9	148	2	-44.3
	TR10	95	2	-39.2
2006	TR4	51	5	-5.9
	TR5	52	5	-9.5
	TR6	81	5	-14.7
	TR7	63	5	-9.2
	TR8	76	5	-11.0
	TR9	47	5	-3.3
2006	TR5	51	5	-5.9
2012	TR5	58	9	-4.4
	TR7	107	9	-7.3
	TR8	113	9	-6.6
	TR9	115	9	-4.6
	TR10	55	9	-2.3
2013	TR1	38	0.4	-6.8
	TR2	38	0.3	-11.1
	TR6	96	8.4	-5.7
2015	TR1	39	6	-2.0
	TR2	37	6	-3.2
	TR3	30	6	-4.6
	TR4	46	6	-5.3

Table C.7: Identification and informative parameters for nourishments reinforcement at St. Augustine for N = 1.

Nourishment year	Transect	dY [m]	LT [yr]	changerate [m/yr]
2002	TR6	126	9	-8.6
2003	TR1	48	2	-29.8
	TR2	51	2	-18.5
	TR5	111	2	-30.8
	TR7	123	8	-10.8
	TR9	148	8	-7.2
	TR10	94	8	-0.4
2006	TR5	51	5	-5.9
2012	TR5	58	9	-4.4
	TR7	107	9	-7.3
	TR8	113	9	-6.6
	TR9	115	9	-4.6
	TR10	55	9	-2.3
2012	TR1	38	0.4	-11.1
	TR6	96	8.4	-5.7
2015	TR1	39	5.7	-2.0
	TR2	37	5.8	-3.2

Table C.8: Identification and informative parameters for nourishments reinforcement at St. Augustine for N = 2.

Delray Beach, USA

Figure C.29: Location of the transects at Delray Beach

C.1.8. Littoral Drift Barriers

Port de l'amitie, Mauritania

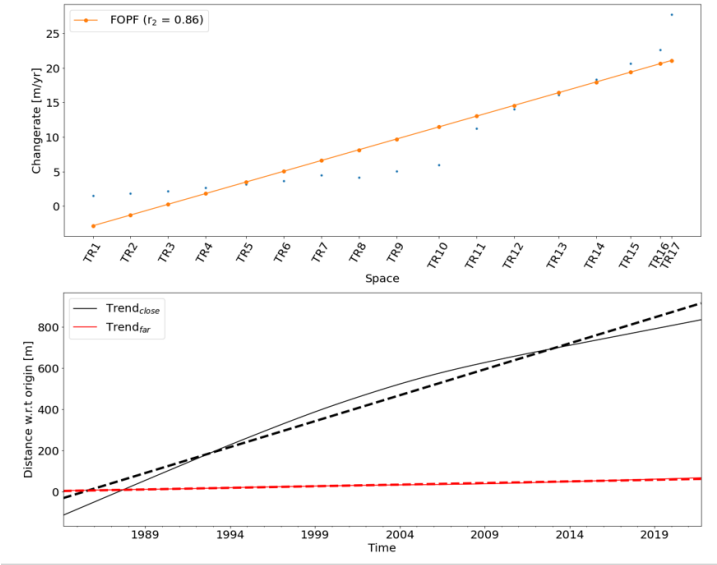

Figure C.30: Visualization of the method used to identify littoral drift barriers for P = 10% at the accreting (northern) part of Nouakchott. TR1 corresponds to the transect close to the port whereas TR17 is the transect furthest away.

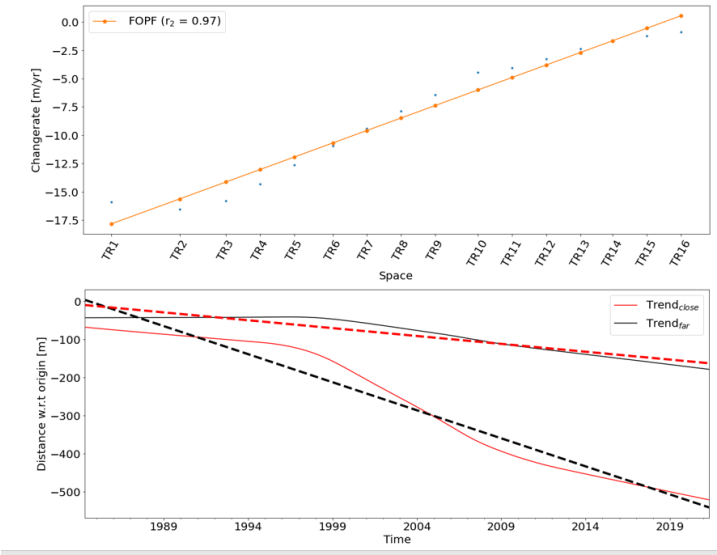

Figure C.31: Visualization of the method used to identify littoral drift barriers for P = 10% at the retreating (southern) part of Nouakchott. TR1 corresponds to the transect close to the port whereas TR16 is the transect furthest away.

Port of IJmuiden, the Netherlands

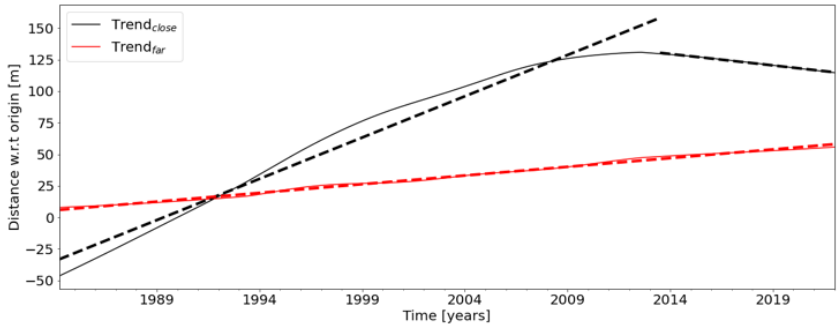

(a) Southern part

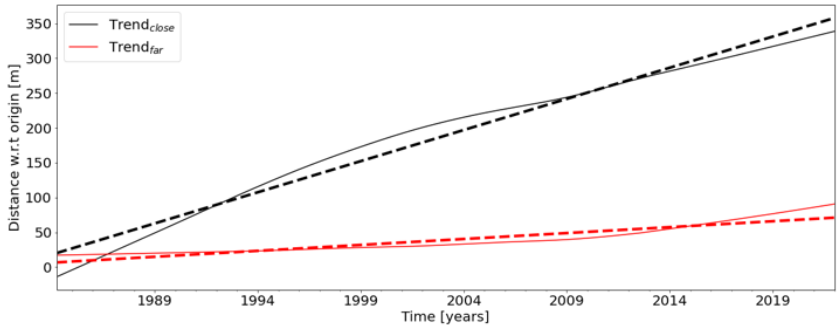

(b) Northern part

Figure C.32: Visualization of trends from the method to identify littoral drift barriers at Ijmuiden.

Aveiro, Portugal

Figure C.33: Analysed transects at Aveiro. Accreting (eroding) transects are indicated in green (red).

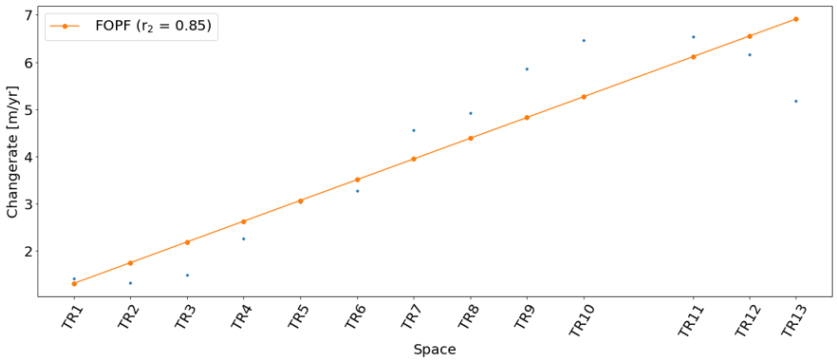

(a) Updrift

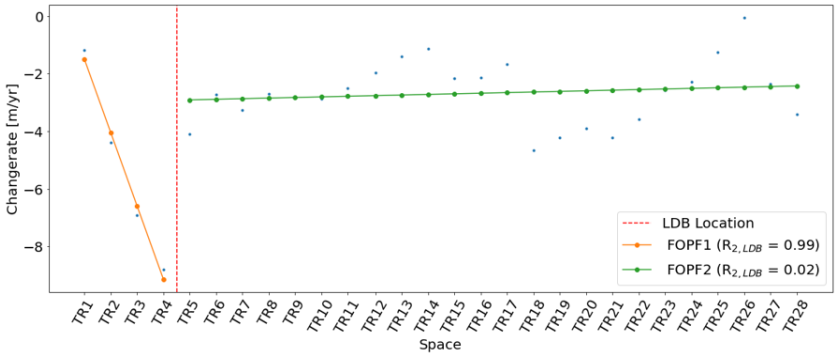

(b) Downdrift

Figure C.34: Visualization of spatial shoreline evolution from the method to identify littoral drift barriers at Aveiro port.

C.2. Regional upscaling and refinement

C.2.1. Seasonality

Unrealistic displacements

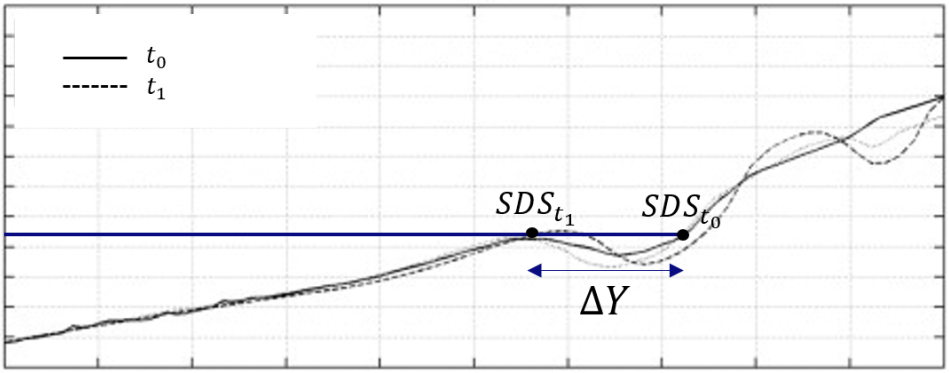

Figure C.35: Location of SDS in case of sandbar morphology near the coast.

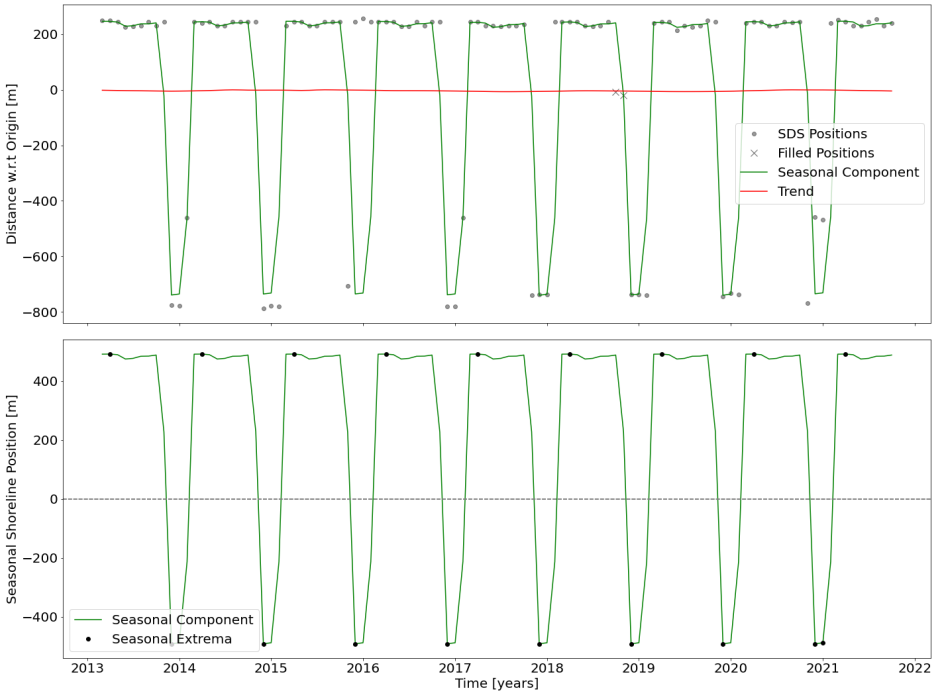

Figure C.36: Visualization of a STL decomposition at a location with a DWI.

Figure C.37 plots the differences of shoreline positions (dY) between each timestep for the same location visualized in Figure C.36. Differences larger than 100 meter are plotted in red. $P_{dY\,100}$ can be calculated with:

$$P_{dY\,100} = \frac{\#dY \geq dY_{100}}{N}$$

where dY_{100} : difference larger than 100 m
N : number of datapoints

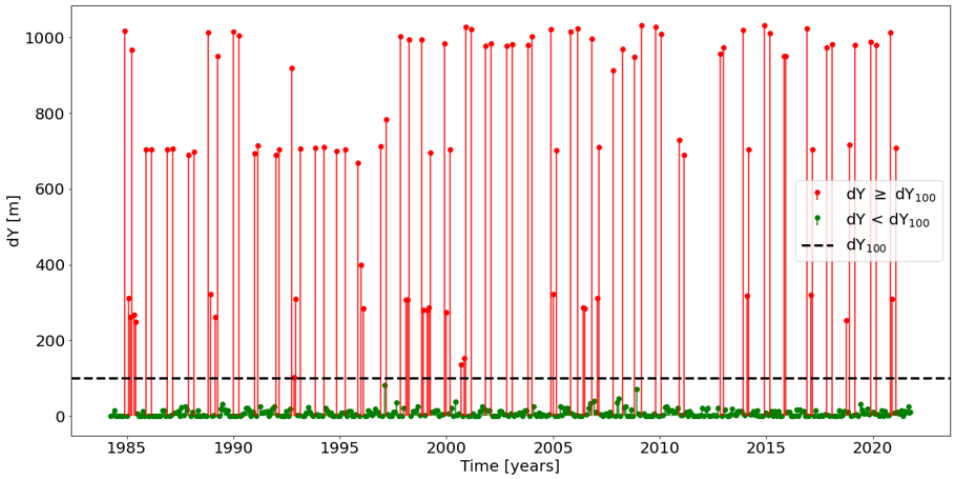

Figure C.37: Differences of shorelines positions within each timestep for a location with a DWI. Differences larger (smaller) than 100 meter are plotted with a red (green) vertical line. The 100 meter line (dY_{100} is plotted with a black dashed vertical line.

Multinomial logistic regression

Table C.9 summarizes the fitted coefficients. Equation C.1 gives an overview of the logit model with these fitted coefficients.

Estimator	Value
$\beta_{0,0}$	0.54
$\beta_{0,1}$	-1.80
$\beta_{0,2}$	1.26
$\beta_{1,0}$	2.07
$\beta_{1,1}$	-2.80
$\beta_{1,2}$	0.73
$\beta_{2,0}$	1.18
$\beta_{2,1}$	-1.45
$\beta_{2,2}$	0.27

Table C.9: Fitted estimators in the logistic regression model

$$f(i) = \begin{cases} 0.54 + 2.07 D_S + 1.18 P_{dY\,100} & \text{if i = non-seasonal} \\ -1.80 - 2.80 D_S - 1.45 P_{dY\,100} & \text{if i = seasonal} \\ 1.26 + 0.73 D_S + 0.27 P_{dY\,100} & \text{if i = seasonal sandbar} \end{cases} \tag{C.1}$$

Figure C.38 provides probabilities from the logistic regression with varying D_S and $P_{dY\,100}$ equal to either 0% (solid line) or 10% (dashed line). As expected, for an increasing $P_{dY\,100}$ the probability of the seasonal outcome decreases.

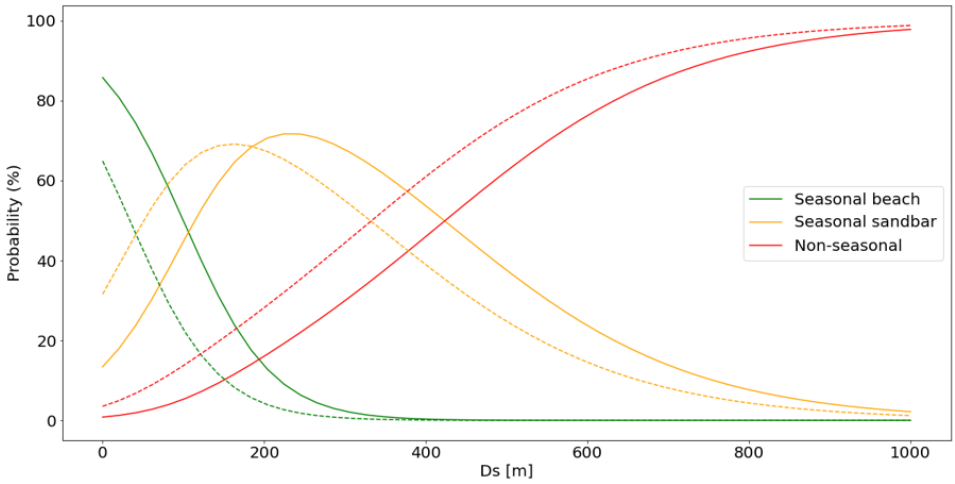

Figure C.38: Plot of the probabilities from LR regression for the three outcomes. The solid (dashed) line represents a value of $P_{dY\,100}$ equal to 0(10)%

Dutch and Belgium coast: identification

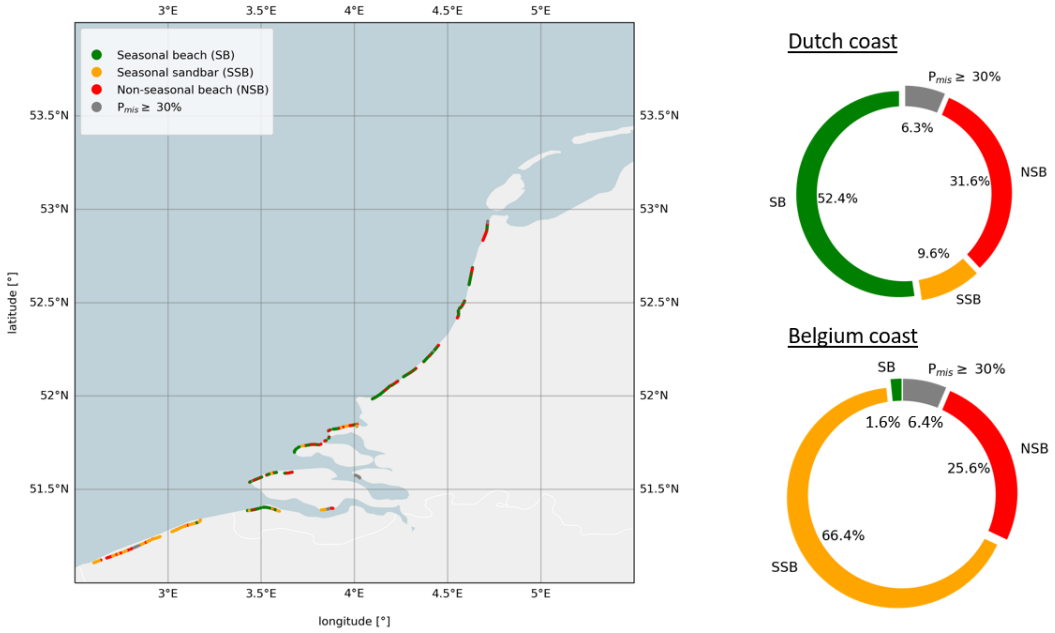

Figure C.39: Identification of seasonal beaches, seasonal sandbars and non-seasonal beaches in Belgium and The Netherlands.

Netherlands: minimum beach width

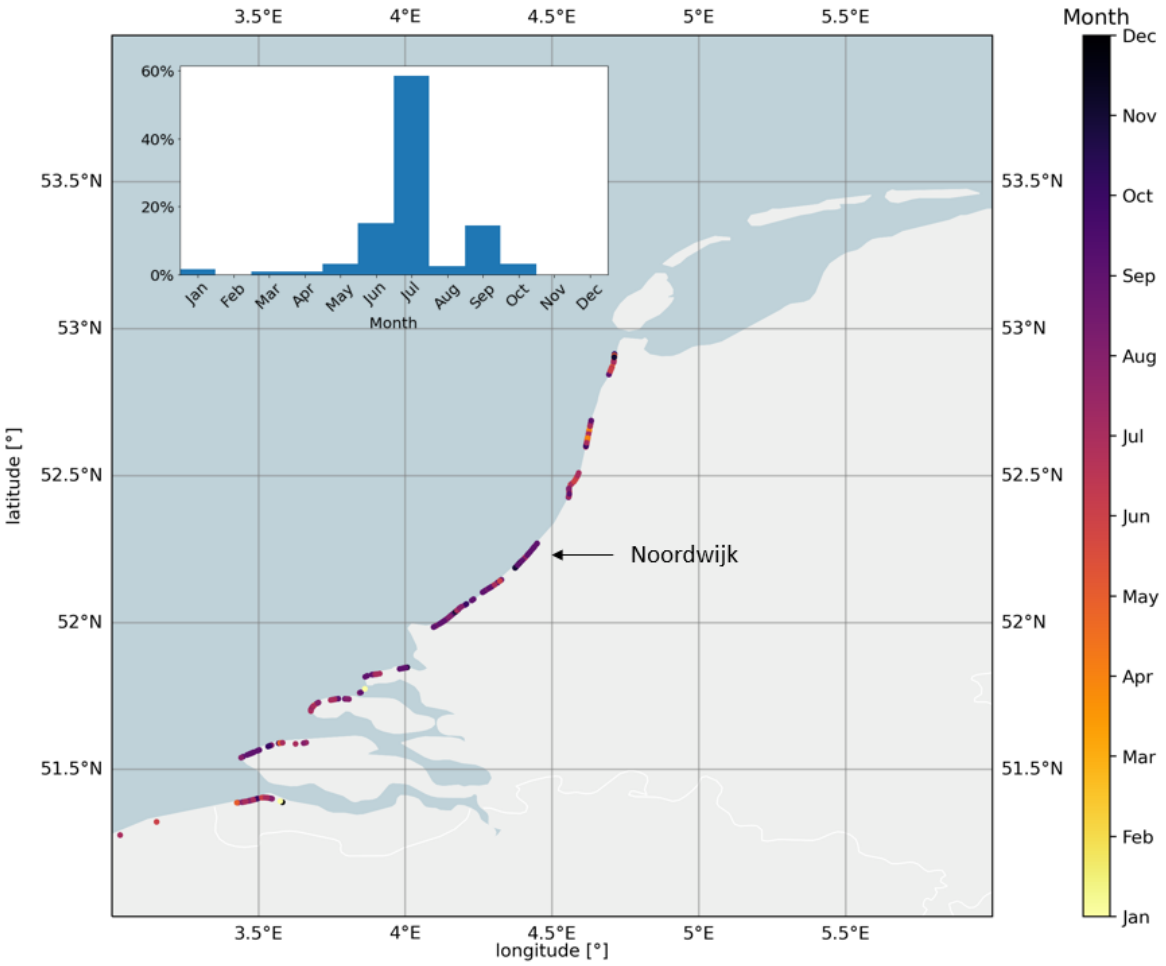

Figure C.40: Occurrence of minimum beach width in the Netherlands. The location that was analysed by Quartel et al. (2008) is indicated with an arrow.

C.2.2. Reclamations

The corrected shoreline jump is defined as:

$$dY_{c,corr} = dY_c^+ - dY_c^-$$

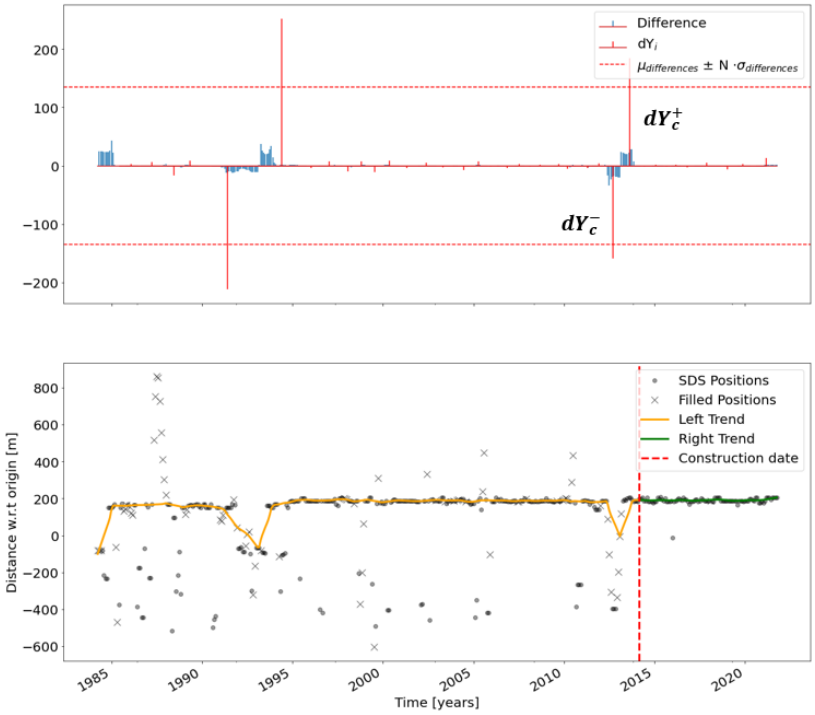

Figure C.41: Example of a case where a positive shoreline jump is caused by outliers. The positive and negative shoreline jump are indicated in the figure by dY_c^+ and dY_c^- respectively.

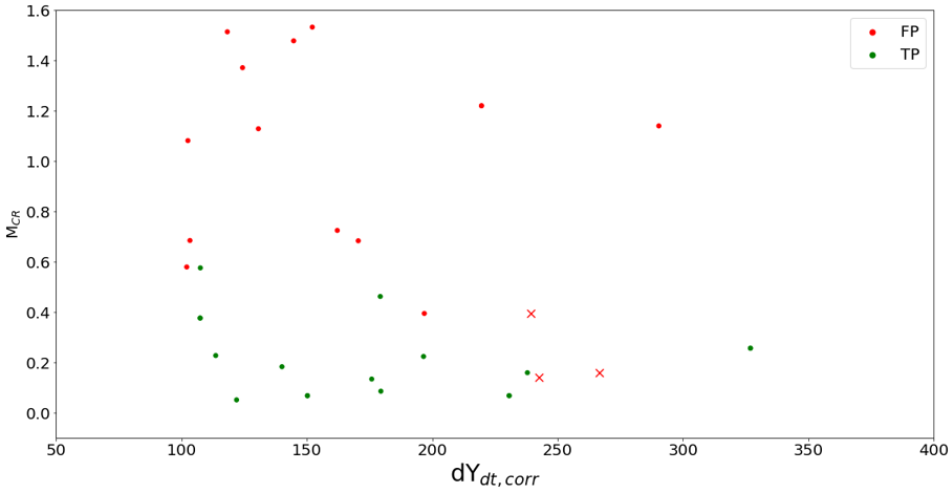

Figure C.42: Reduced sample from Figure 5.7. The positive and negative shoreline jump are indicated in the figure by dY_c^+ and dY_c^- respectively. Locations which contained less than 40% missing values and where the percentage of dY_100 is also below 10% are plotted with circles. If one of these conditions is not met, the location is plotted with a cross.

C.2.3. Nourishments

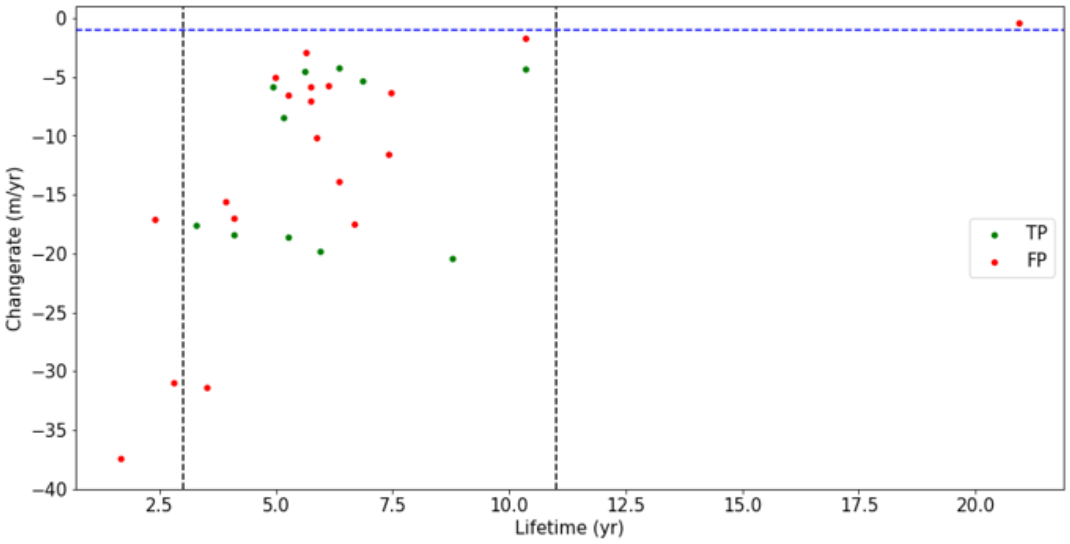

Figure C.43: Verified sample of 20 transects on the Dutch coast. The threshold for the changerate is indicated with the blue dashed line. For the lifetime, thresholds are indicates with the black dashed lines.

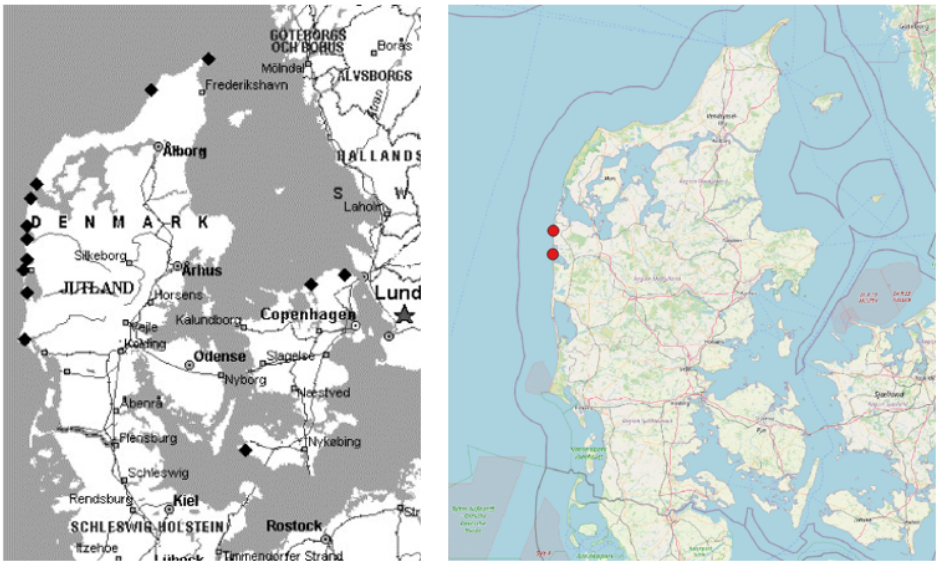

Figure C.44: Documented beach nourishment sites in Denmark (left, source: Hanson et al., 2002) and identified beach nourishment sites (right)

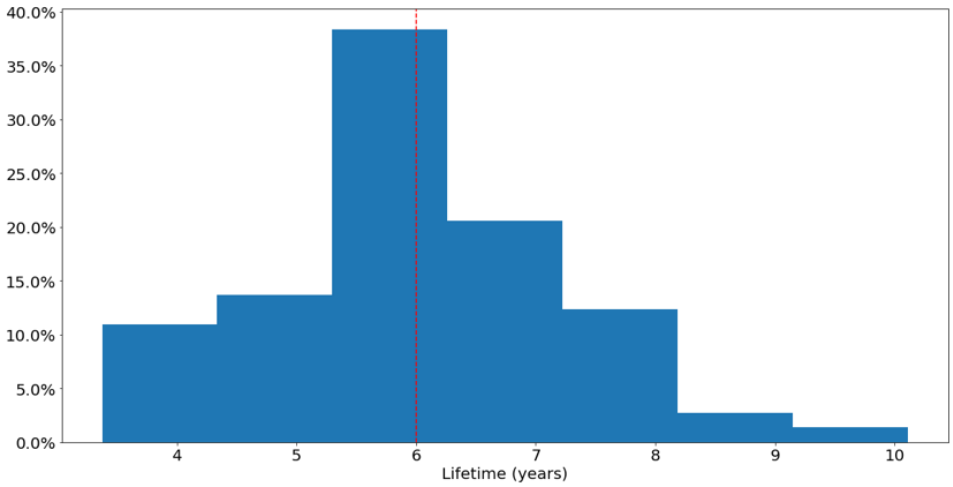

Figure C.45: Histogram of the lifetime of beach nourishments in the Netherlands based on 73 nourishments in the period 1984-2021. The red dashed line indicates the mean lifetime.

C.2.4. Littoral drift barriers

Precision scores: interpolation

With the help of two examples, below is explained how precision scores are interpolated between regions. The regions, see Figure 5.13, are defined as:

I $R_{2,LDB}$: [0, 0.2), N_T: [0, 5)

II $R_{2,LDB}$: [0.2, 0.4), N_T: [5, 10)

III $R_{2,LDB}$: [0.4, 0.6), N_T: [10, 12)

IV $R_{2,LDB}$: [0,6, 0.8), N_T: [12, 14)

V $R_{2,LDB}$: [0.8, 1.0], N_T: [14, ∞]

The fundamental idea is that precision is calculated according to the minor region of one of the parameters. Meaning that, even though as either of the parameters is already in an upper region, if the other parameter remains in a lower region, precision is calculated according to the lower region.

- Example 1: $R_{2,LDB}$ = 0.3, N_T = 8. In this example, both parameters fall in region II. Precision is thus calculated according to region II.
  Region I is entirely covered so the starting point is a precision of 0.11 (see Figure 5.13). The area in Region II covered by N_T is:

$$A_1 = \frac{8-5}{11-5} \cdot (0.46-0.24) = 0.1088$$

  For $R_{2,LDB}$:

$$A_2 = \frac{0.3-0.2}{0.4-0.2} \cdot (0.46-0.24) = 0.1088$$

  A_2 and A_2 have some overlap, A_3:

$$A_3 = \frac{8-5}{11-5} \cdot \frac{0.3-0.2}{0.4-0.2} \cdot (0.46-0.24) = 0.0544$$

  This gives a total precision of:

$$PVV(R_2 = 0.15, N_T = 8) = PVV_I I + A_1 + A_2 - A_3 = 0.24 + 0.1088 + 0.1088 - 0.0544 = 0.407 \approx 40\%$$

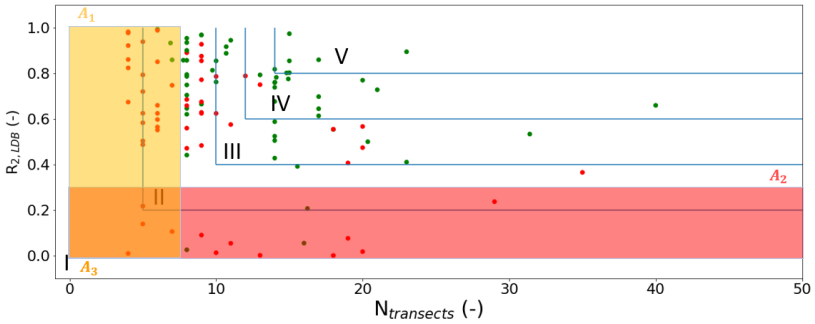

Figure C.46: Precision score interpolation for $R_{2,LDB}$ = 0.30 and N_T = 8

- Example 2: $R_{2,LDB}$ = 0.15, N_T = 8. In this example, N_T falls already in region II while $R_{2,LDB}$ remains in region I. Precision is thus calculated according to region I.
  N_T covers the entire part of region I:

$$A_1 = \frac{4-0}{5-0} \cdot (0.24-0.11) = 0.0996$$

For $R_{2,LDB}$:

$$A_2 = \frac{0.15-0}{0.2-0} \cdot (0.24-0.11) = 0.1062$$

A_2 and A_2 have some overlap, A_3:

$$A_3 = \frac{4-0}{5-0} \cdot \frac{0.15-0}{0.2-0} \cdot (0.24-0.11) = 0.0797$$

This gives a total precision of:

$$PVV(R_2 = 0.15, N_T = 8) = PVV_I + A_1 + A_2 - A_3 = 0.11 + 0.0996 + 0.1062 - 0.0797 = 0.237 \approx 24\%$$

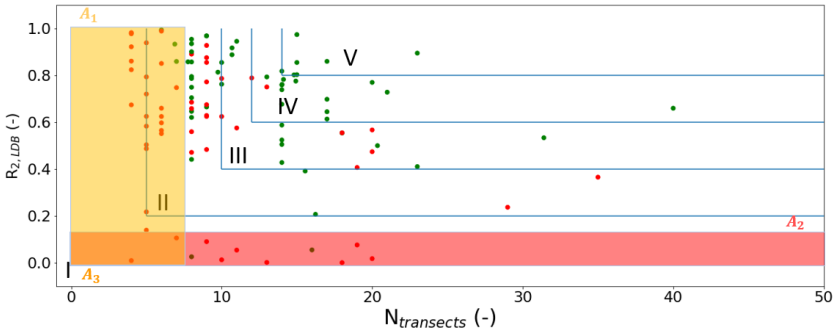

Figure C.47: Precision score interpolation for $R_{2,LDB} = 0.15$ and $N_T = 8$

D

Appendix: global analysis

D.1. Global identification

Reclamations

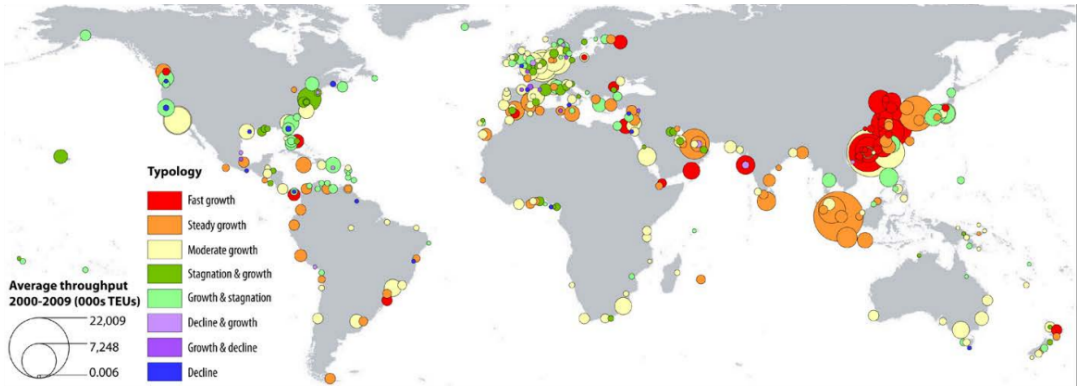

Figure D.1: Global port trajectories 1970 - 2009. (Source: Merk, 2013

D.2. Global characterization

D.2.1. Seasonality

Seasonal displacement

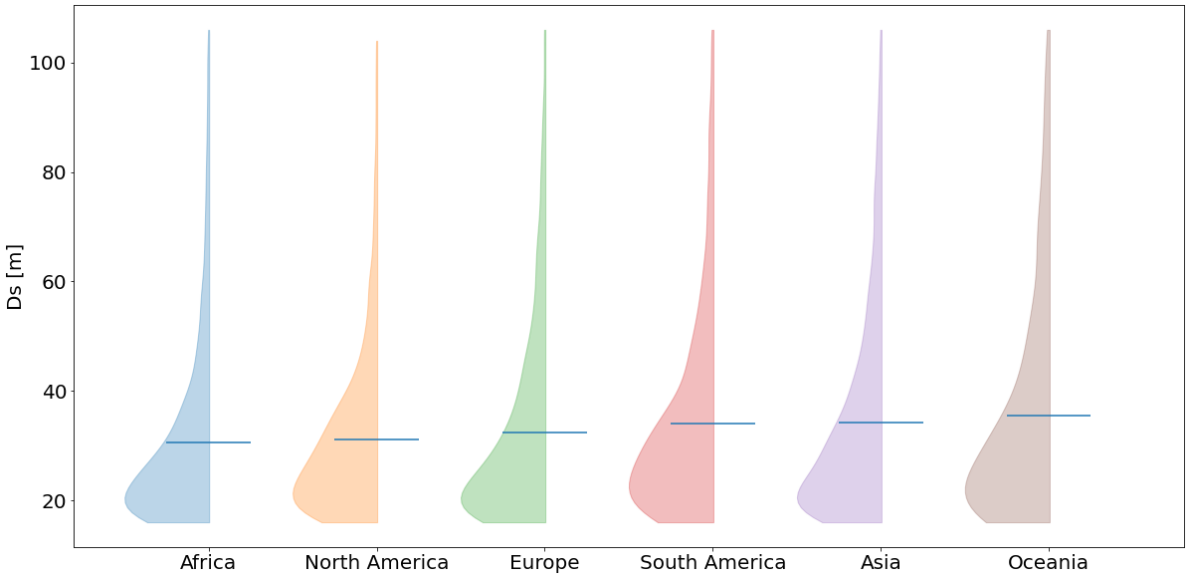

Figure D.2: Violinplot of the seasonal displacements for each continent. Thickness of the shape indicates the density of the values at a certain positions.

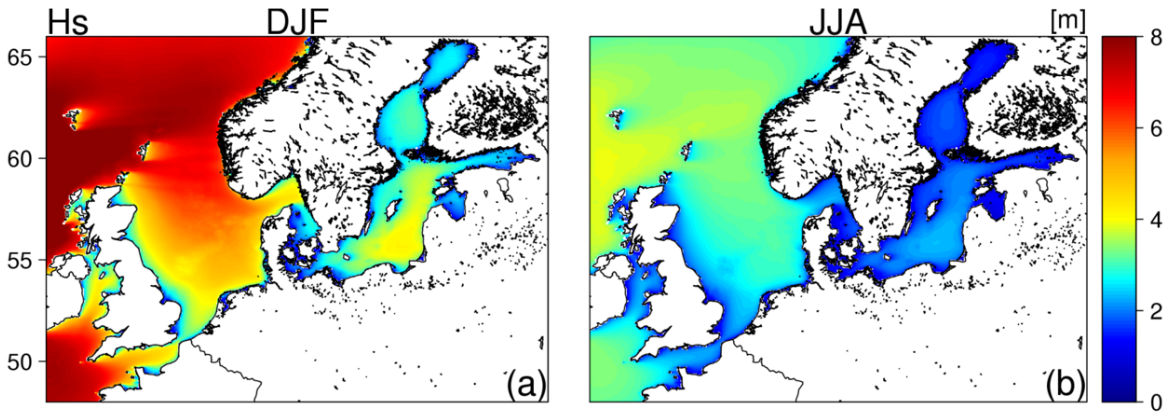

Figure D.3: Seasonal wave climate variations in the North and Baltic sea. (Source: Bonaduce et al., 2019)

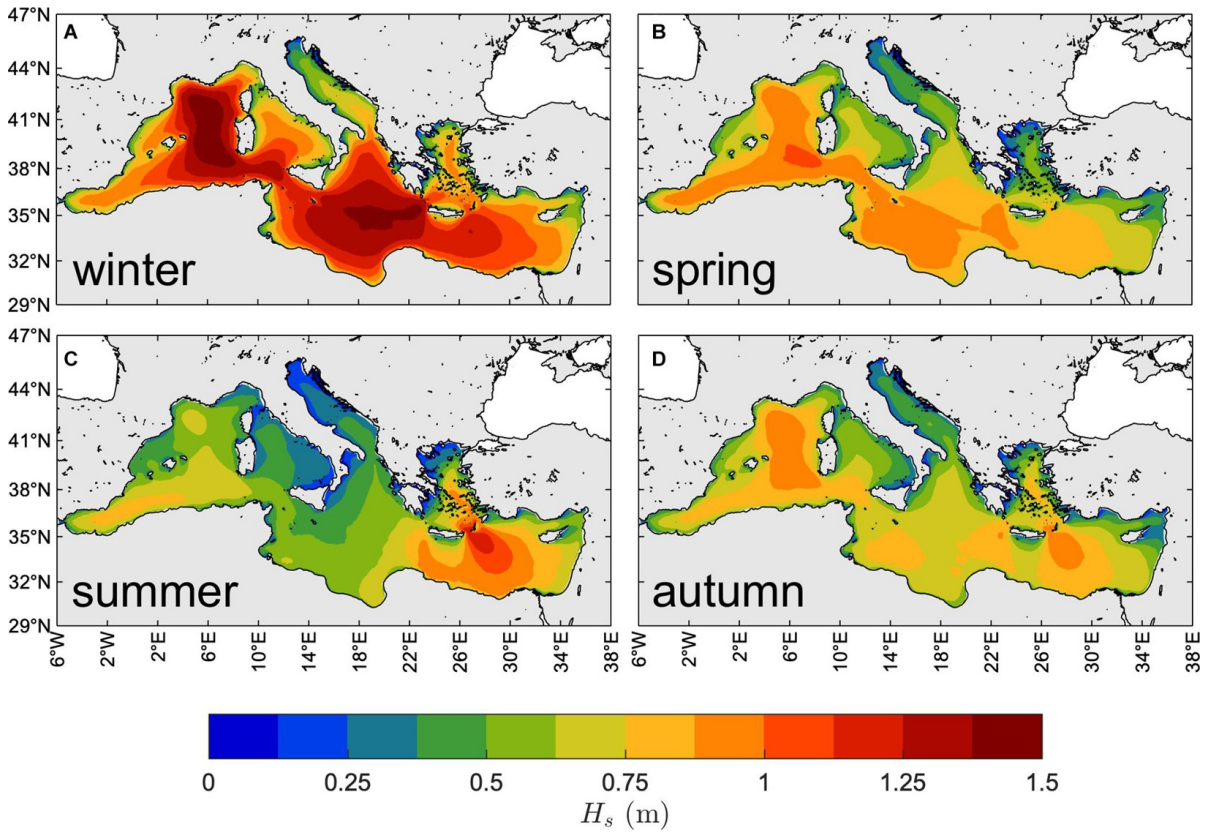

Figure D.4: Seasonal wave climate variations in the Mediterranean sea. (Source: Barbariol et al., 2021)

Accretion period

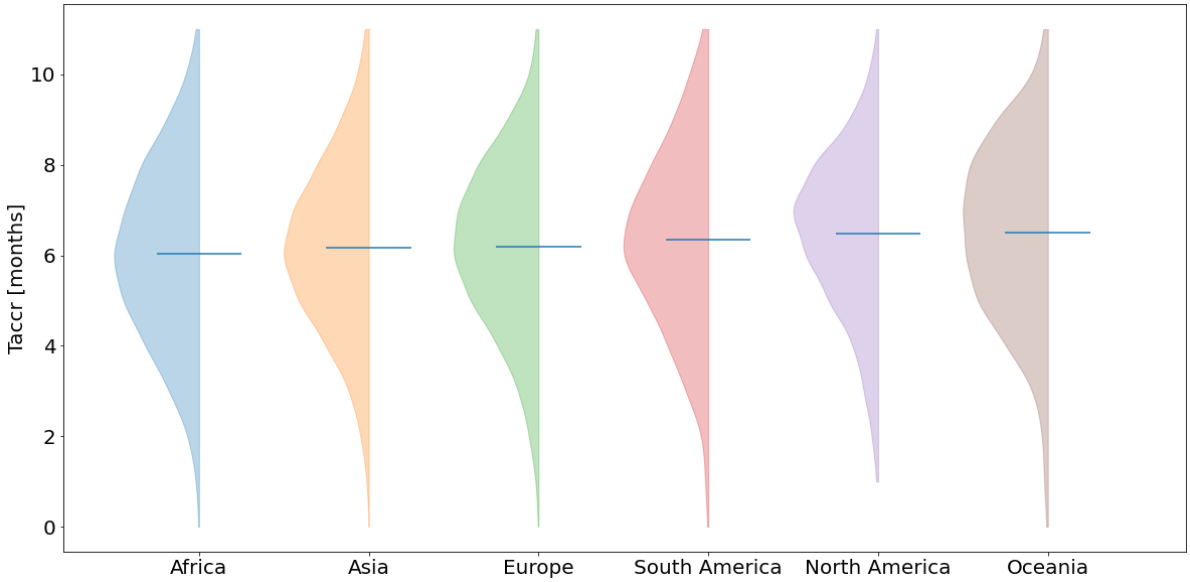

Figure D.5: Violinplot of the accretion period for each continent. Thickness of the shape indicates the density of the values at a certain positions.

Minimum beach width

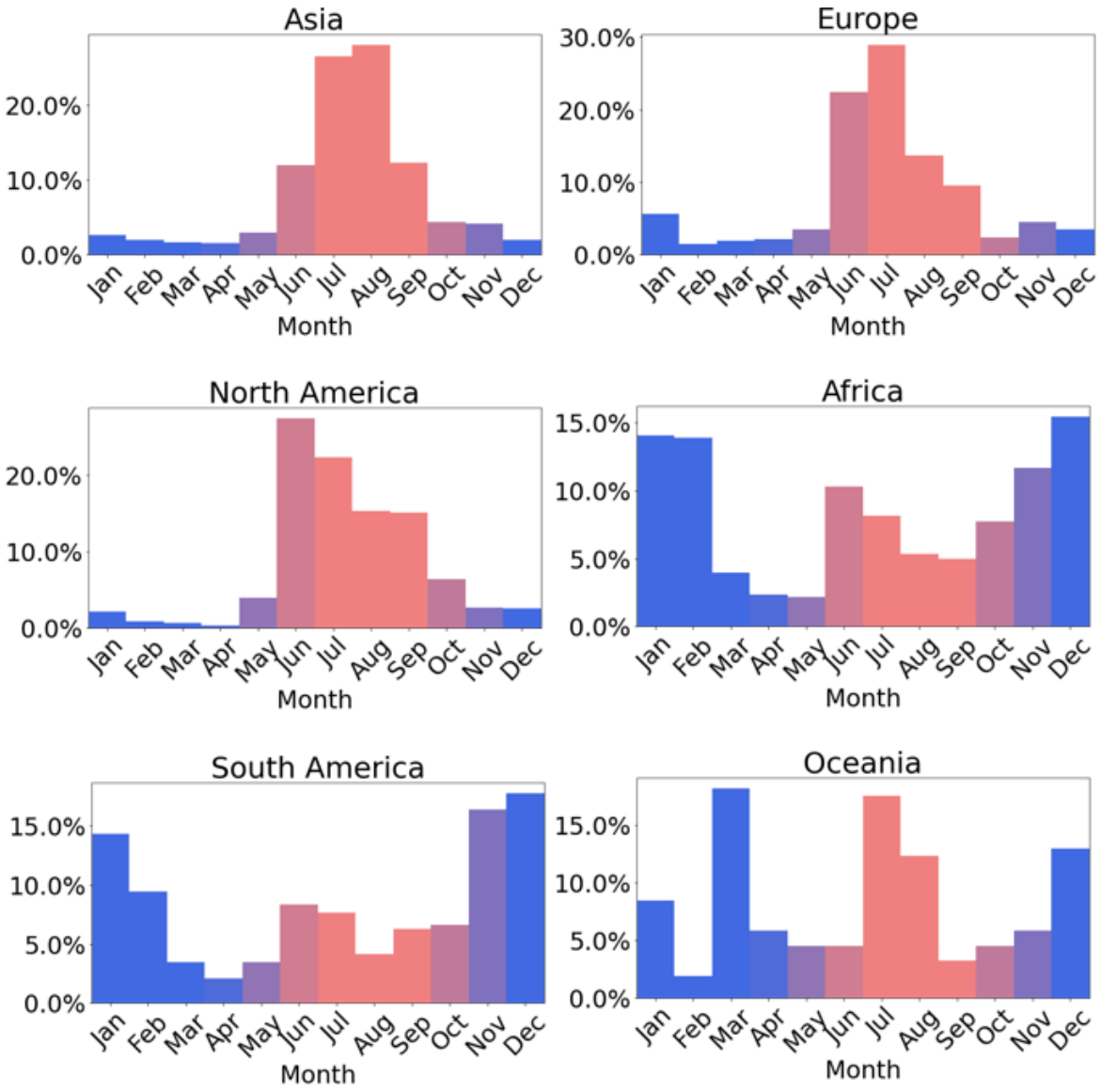

Figure D.6: Histograms of minimum beach width occurrence for each month

D.2.2. Reclamations

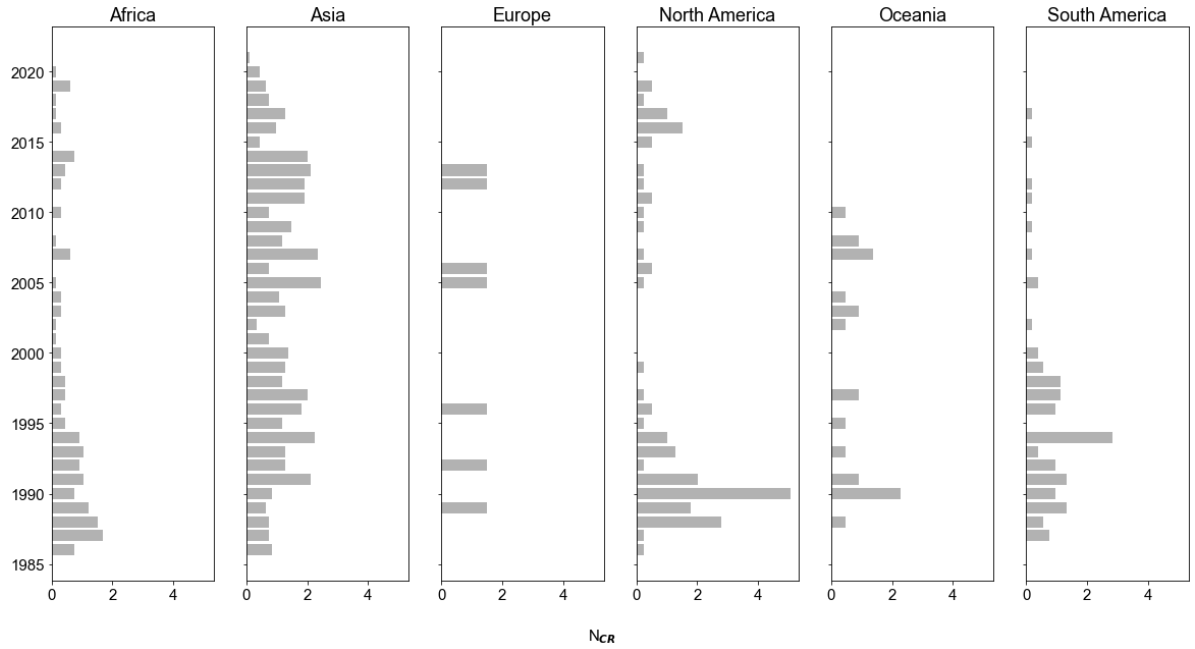

Figure D.7: Barplot per continent showing the number of reclamations per 1000 transects for each year

D.2.3. Nourishments

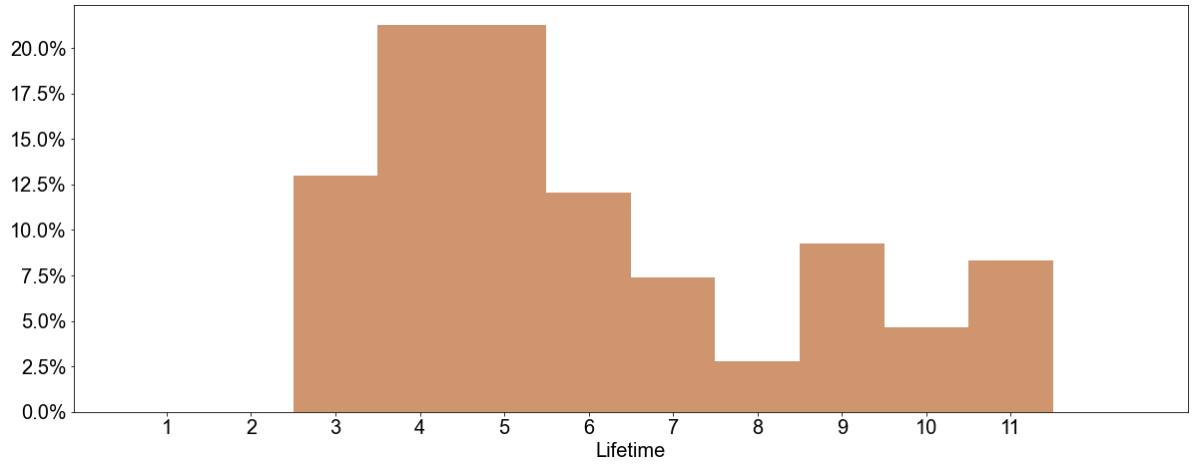

Figure D.8: Histogram of the lifetime of nourishments on a global scale

Bibliography

Abdelrahman, S. M. (1997). Seasonal fluctuations of mean sea level at gizan, red sea. *Journal of coastal research*, 1166–1172.

Abidin, H. Z., Andreas, H., Gumilar, I., Fukuda, Y., Pohan, Y. E., & Deguchi, T. (2011). Land subsidence of jakarta (indonesia) and its relation with urban development. *Natural hazards*, *59*(3), 1753–1771.

Abidin, H., Andreas, H., Gumilar, I., & Wibowo, I. (2015). On correlation between urban development, land subsidence and flooding phenomena in jakarta. *Proceedings of the International Association of Hydrological Sciences*, *370*, 15–20.

Absalonsen, L., & Dean, R. G. (2011). Characteristics of the shoreline change along florida sandy beaches with an example for palm beach county. *Journal of Coastal Research*, *27*(6A), 16–26.

Acharya, T. D., Lee, D. H., Yang, I. T., & Lee, J. K. (2016). Identification of water bodies in a landsat 8 oli image using a j48 decision tree. *Sensors*, *16*(7), 1075.

Agency, U. S. C. I. (2016). World factbook: Coastlines. https://www.cia.gov/library/publications/the-world%02factbook/felds/2060.html

Albert, P., & Jorge, G. (1998). Coastal changes in the ebro delta: Natural and human factors. *Journal of Coastal Conservation*, *4*(1), 17–26.

Allan, J. C., & Komar, P. D. (2006). Climate controls on us west coast erosion processes. *Journal of coastal research*, *22*(3), 511–529.

Barbariol, F., Davison, S., Falcieri, F. M., Ferretti, R., Ricchi, A., Sclavo, M., & Benetazzo, A. (2021). Wind waves in the mediterranean sea: An era5 reanalysis wind-based climatology. *Frontiers in Marine Science*.

Barnard, P. L., Eshleman, J., Erikson, L., & Hanes, D. M. (2007). *Coastal processes study at ocean beach, san francisco, ca: Summary of data collection 2004-2006* (tech. rep.).

Barnard, P. L., Short, A. D., Harley, M. D., Splinter, K. D., Vitousek, S., Turner, I. L., Allan, J., Banno, M., & Bryan, K. R. (2015). Coastal vulnerability across the pacific dominated by el nino/southern oscillation. *Nature Geoscience*, *8*(10), 801–807.

Beachler, K. E., & Mann, D. W. (1996). Long range positive effects of the delray beach nourishment program. *Coastal Engineering Proceedings*, (25).

Benedet, L. (2016). *Process controlling beach nourishment performance at delray beach, florida, usa* (Doctoral dissertation). Delft University of Technology.

Bonaduce, A., Staneva, J., Behrens, A., Bidlot, J.-R., & Wilcke, R. A. I. (2019). Wave climate change in the north sea and baltic sea. *Journal of Marine Science and Engineering*, *7*(6), 166.

Bosboom, J., & Stive, M. J. (2012). *Coastal dynamics i: Lectures notes cie4305*.

Brenner, O. T., Lentz, E. E., Hapke, C. J., Henderson, R. E., Wilson, K. E., & Nelson, T. R. (2018). Characterizing storm response and recovery using the beach change envelope: Fire island, new york. *Geomorphology*, *300*, 189–202.

Bruun, P. (1954). *Coast erosion and the development of beach profiles* (Vol. 44). US Beach Erosion Board.

Bruun, P. (1962). Sea-level rise as a cause of shore erosion. *Journal of the Waterways and Harbors division*, *88*(1), 117–130.

Bryant, E. (1983). Regional sea level, southern oscillation and beach change, new south wales, australia. *Nature*, *305*(5931), 213–216.

Bujang, M. A., Sa'at, N., Bakar, T. M. I. T. A., Joo, L. C., et al. (2018). Sample size guidelines for logistic regression from observational studies with large population: Emphasis on the accuracy between statistics and parameters based on real life clinical data. *The Malaysian journal of medical sciences: MJMS*, *25*(4), 122.

Burke, L., Kura, Y., Kassem, K., Revenga, C., Spalding, M., McAllister, D., & Caddy, J. (2001). *Coastal ecosystems*. World Resources Institute Washington, DC.

Calkoen, F., Luijendijk, A., Rivero, C. R., Kras, E., & Baart, F. (2021). Traditional vs. machine-learning methods for forecasting sandy shoreline evolution using historic satellite-derived shorelines. *Remote Sensing*, *13*(5), 934.

Cazenave, A., Bonnefond, P., Dominh, K., & Schaeffer, P. (1997). Caspian sea level from topex-poseidon altimetry: Level now falling. *Geophysical Research Letters*, *24*(8), 881–884.

Channel, F., Indicate, V., & Flood, I. (2006). Bypassing at littoral drift barriers. *Encyclopedia of Coastal Science*, *32*, 210.

Charlier, R. H., Chaineux, M. C. P., & Morcos, S. (2005). Panorama of the history of coastal protection. *Journal of Coastal Research*, *21*(1), 79–111.

Chen, J., Wilson, C., Tapley, B., Save, H., & Cretaux, J.-F. (2017). Long-term and seasonal caspian sea level change from satellite gravity and altimeter measurements. *Journal of Geophysical Research: Solid Earth*, *122*(3), 2274–2290.

Chen, M., & Montreuil, A.-L. (2017). Remote sensing data for investifgating the morphodynamic of the belgium multi-barred macro-tidal beach. *Belgian Earth Observation*.

Chen, W.-W., & Chang, H.-K. (2009). Estimation of shoreline position and change from satellite images considering tidal variation. *Estuarine, Coastal and Shelf Science*, *84*(1), 54–60.

Cleveland, Cleveland, W. S., McRae, J. E., & Terpenning, I. (1990). Stl: A seasonal-trend decomposition. *J. Off. Stat*, *6*(1), 3–73.

Cleveland & Devlin, S. J. (1988). Locally weighted regression: An approach to regression analysis by local fitting. *Journal of the American statistical association*, *83*(403), 596–610.

Climate-ADAPT. (2015). Beach and shoreface nourishment. https : / / climate - adapt . eea . europa . eu / en / metadata/adaptation-options/beach-and-shoreface-nourishment

Cohn, N., Ruggiero, P., de Vries, S., & Garcıa-Medina, G. (2017). Beach growth driven by intertidal sandbar welding. *Proceedings of coastal dynamics*, 12–16.

Colominas, M. A., Schlotthauer, G., & Torres, M. E. (2014). Improved complete ensemble emd: A suitable tool for biomedical signal processing. *Biomedical Signal Processing and Control*, *14*, 19–29.

Cook, R. D., & Prescott, P. (1981). On the accuracy of bonferroni significance levels for detecting outliers in linear models. *Technometrics*, *23*(1), 59–63.

da Fontoura Klein, A. H., Benedet Filho, L., & Schumacher, D. H. (2002). Short-term beach rotation processes in distinct headland bay beach systems. *Journal of coastal research*, 442–458.

Davidson, M., Lewis, R., & Turner, I. (2010). Forecasting seasonal to multi-year shoreline change. *Coastal Engineering*, *57*(6), 620–629.

Davison, A. T., Nicholls, R. J., & Leatherman, S. P. (1992). Beach nourishment as a coastal management tool: An annotated bibliography on developments associated with the artificial nourishment of beaches. *Journal of Coastal Research*, 984–1022.

De Viron, O., Dickey, J., & Ghil, M. (2013). Global modes of climate variability. *Geophysical Research Letters*, *40*(9), 1832–1837.

Dean, R. G. (2002). *Beach nourishment: Theory and practice* (Vol. 18). World scientific.

Dean, R. G. (2005). Beach nourishment: Benefits, theory and case examples. In *Environmentally friendly coastal protection* (pp. 25–40). Springer.

de Jongh, L. (2017). Initial morphological evolution of a mega nourishment: The hondsbossche dunes one year after construction.

Delray beach program. (2020). http://www.resilientdelray.com/beach-program-2/

Di, K., Ma, R., Wang, J., & Li, R. (2003). Coastal mapping and change detection using high-resolution ikonos satellite imagery. *Proceedings of the 2003 annual national conference on Digital government research*, 1–4.

Dodge, Y., Cox, D., & Commenges, D. (2006). *The oxford dictionary of statistical terms*. Oxford University Press on Demand.

Dolan, R., Hayden, B. P., May, P., & May, S. (1980). The reliability of shoreline change measurements from aerial photographs. *Shore and beach*, *48*(4), 22–29.

Donchyts, G., Baart, F., Winsemius, H., Gorelick, N., Kwadijk, J., & Van De Giesen, N. (2016). Earth's surface water change over the past 30 years. *Nature Climate Change*, *6*(9), 810–813.

Duxbury, A. C., Duxbury, A. B., & Sverdrup, K. A. (1997). Introduction to the world's oceans, an.

Earth, G. (n.d.). Map showing location of praia da barra. earth.google.com/web/.

The economist. (n.d.). https://www.economist.com/middle-east-and-africa/2015/06/04/growing-up

Elias, E. P., Van der Spek, A. J., Wang, Z. B., & De Ronde, J. (2012). Morphodynamic development and sediment budget of the dutch wadden sea over the last century. *Netherlands Journal of Geosciences*, *91*(3), 293–310.

Elsayed, M. A., Younan, N. A., Fanos, A. M., & Baghdady, K. H. (2005). Accretion and erosion patterns along rosetta promontory, nile delta coast. *Journal of Coastal Research*, *21*(3), 412–420.

Encyclopedia, N. W. (2013). Mediterranean sea — new world encyclopedia [[Online; accessed 6-December-2022]]. %5Curl%7Bhttps://www.newworldencyclopedia.org/p/index.php?title=Mediterranean_Sea&oldid=971160%7D

Encyclopedia, N. W. (2015). Red sea — new world encyclopedia [[Online; accessed 6-December-2022]]. %5Curl%7Bhttps://www.newworldencyclopedia.org/p/index.php?title=Red_Sea&oldid=989212%7D

Ericson, J. P., Vörösmarty, C. J., Dingman, S. L., Ward, L. G., & Meybeck, M. (2006). Effective sea-level rise and deltas: Causes of change and human dimension implications. *Global and Planetary Change*, *50*(1-2), 63–82.

FDEP, F. D. o. E. P. (2020). *Strategic beach management plan: Northeast atlantic coast region*.

Fine, M., Cinar, M., Voolstra, C. R., Safa, A., Rinkevich, B., Laffoley, D., Hilmi, N., & Allemand, D. (2019). Coral reefs of the red sea—challenges and potential solutions. *Regional Studies in Marine Science*, *25*, 100498.

Finkl, C. W. (1996). Potential impacts of a federal policy promoting "no new beach replenishment activities"on us shorelines: Iterations from se florida. *Proceedings of the 1996 National Conference on Beach Preservation Technology (St. Petersburg, Florida)*, 281–296.

Foody, G. M., Muslim, A. M., & Atkinson, P. M. (2005). Super-resolution mapping of the waterline from remotely sensed data. *International Journal of Remote Sensing*, *26*(24), 5381–5392.

Fourier, J. B., et al. (1822). *Théorie analytique de la chaleur* (Vol. 504). Didot Paris.

Frihy, O., Nasr, S., El Hattab, M., & El Raey, M. (1994). Remote sensing of beach erosion along the rosetta promontary, northwestern nile delta, egypt. *International Journal of Remote Sensing*, *15*(8), 1649–1660.

Gorelick, N., Hancher, M., Dixon, M., Ilyushchenko, S., Thau, D., & Moore, R. (2017). Google earth engine: Planetary-scale geospatial analysis for everyone. *Remote sensing of Environment*, *202*, 18–27.

Grases, A., Gracia, V., Garcıa-León, M., Lin-Ye, J., & Sierra, J. P. (2020). Coastal flooding and erosion under a changing climate: Implications at a low-lying coast (ebro delta). *Water*, *12*(2), 346.

Gravens, M., Rosati, J., & Wise, R. (1999). Fire island inlet to montauk point reformulation study (fimp): Historical and existing condition coastal processes assessment. *prepared for the US Army Engineer District, New York*.

Hagenaars, G., de Vries, S., Luijendijk, A. P., de Boer, W. P., & Reniers, A. J. (2018). On the accuracy of automated shoreline detection derived from satellite imagery: A case study of the sand motor mega-scale nourishment. *Coastal Engineering*, *133*, 113–125.

Hagenaars, G. (2017). Accuracy assessment of coastline dynamics based on satellite images: Application to the holland coast.

Hallin, C. (2019). *Long-term beach and dune evolution: Development and application of the cs-model* (Doctoral dissertation). Lund University.

Hamm, L., Capobianco, M., Dette, H., Lechuga, A., Spanhoff, R., & Stive, M. (2002). A summary of european experience with shore nourishment. *Coastal engineering*, *47*(2), 237–264.

Hanson, H., Brampton, A., Capobianco, M., Dette, H. H., Hamm, L., Laustrup, C., Lechuga, A., & Spanhoff, R. (2002). Beach nourishment projects, practices, and objectives—a european overview. *Coastal engineering*, *47*(2), 81–111.

Hanson, H., Gravens, M. B., & Kraus, N. C. (1989). Prototype applications of a generalized shoreline change numerical model. In *Coastal engineering 1988* (pp. 1265–1279).

Hartog, W. M., Benedet, L., Walstra, D.-J. R., Van Koningsveld, M., Stive, M. J., & Finkl, C. W. (2008). Mechanisms that influence the performance of beach nourishment: A case study in delray beach, florida, usa. *Journal of Coastal Research*, *24*(5), 1304–1319.

Hassan, S. R., Sultan, M., Emil, M. K., Zahran, K., Issawy, E., Abdeldayem, A., Kamh, S., & Emam, E. (2019). Monitoring recent land subsidence in the nile delta of egypt using sentinel-1 insar time series. *AGU Fall Meeting Abstracts*, *2019*, G13B–0534.

Hinkel, J., Nicholls, R. J., Tol, R. S., Wang, Z. B., Hamilton, J. M., Boot, G., Vafeidis, A. T., McFadden, L., Ganopolski, A., & Klein, R. J. (2013). A global analysis of erosion of sandy beaches and sea-level rise: An application of diva. *Global and Planetary change*, *111*, 150–158.

Horikawa, K. (1988). *Nearshore dynamics and coastal processes: Theory, measurement, and predictive models*. University of Tokyo press.

Huang, N. E., Shen, Z., Long, S. R., Wu, M. C., Shih, H. H., Zheng, Q., Yen, N.-C., Tung, C. C., & Liu, H. H. (1998). The empirical mode decomposition and the hilbert spectrum for nonlinear and non-stationary time

series analysis. *Proceedings of the Royal Society of London. Series A: mathematical, physical and engineering sciences*, *454*(1971), 903–995.

Hurrell, J. W. (1995a). Decadal trends in the north atlantic oscillation: Regional temperatures and precipitation. *Science*, *269*(5224), 676–679.

Hurrell, J. W. (1995b). Decadal trends in the north atlantic oscillation: Regional temperatures and precipitation. *Science*, *269*(5224), 676–679.

Hurrell, J. W., Kushnir, Y., Ottersen, G., & Visbeck, M. (2003). An overview of the north atlantic oscillation. *Geophysical Monograph-American Geophysical Union*, *134*, 1–36.

Ingebritsen, S. E., & Galloway, D. L. (2014a). Coastal subsidence and relative sea level rise. *Environmental Research Letters*, *9*(9), 091002.

Ingebritsen, S. E., & Galloway, D. L. (2014b). Coastal subsidence and relative sea level rise. *Environmental Research Letters*, *9*(9), 091002.

Kamdi, S., & Krishna, R. (2012). Image segmentation and region growing algorithm. *International Journal of Computer Technology and Electronics Engineering (IJCTEE)*, *2*(1), 103–107.

Katsman, C. A., Sterl, A., Beersma, J., Van den Brink, H., Church, J., Hazeleger, W., Kopp, R., Kroon, D., Kwadijk, J., Lammersen, R., et al. (2011). Exploring high-end scenarios for local sea level rise to develop flood protection strategies for a low-lying delta—the netherlands as an example. *Climatic change*, *109*(3), 617–645.

Kleinbaum, D. G., Dietz, K., Gail, M., Klein, M., & Klein, M. (2002). *Logistic regression*. Springer.

Kras, E. (2019). Planetary-scale classification of natural and human-induced sandy shoreline evolution: A semi-automated method that employs machine learning and satellite derived shorelines over the past decades.

Kudale, M. (2010). Impact of port development on the coastline and the need for protection.

Langodan, S., Cavaleri, L., Pomaro, A., Vishwanadhapalli, Y., Bertotti, L., & Hoteit, I. (2017). The climatology of the red sea–part 2: The waves. *International Journal of Climatology*, *37*(13), 4518–4528.

Larson, M., Capobianco, M., Jansen, H., Rózyński, G., Southgate, H. N., Stive, M., Wijnberg, K. M., & Hulscher, S. (2003). Analysis and modeling of field data on coastal morphological evolution over yearly and decadal time scales. part 1: Background and linear techniques. *Journal of Coastal Research*, 760–775.

Lentz, E. E., & Hapke, C. J. (2011). Geologic framework influences on the geomorphology of an anthropogenically modified barrier island: Assessment of dune/beach changes at fire island, new york. *Geomorphology*, *126*(1-2), 82–96.

Lentz, E. E., Hapke, C. J., Stockdon, H. F., & Hehre, R. E. (2013). Improving understanding of near-term barrier island evolution through multi-decadal assessment of morphologic change. *Marine Geology*, *337*, 125–139.

Liew, S. C., Gupta, A., Wong, P. P., & Kwoh, L. K. (2010). Recovery from a large tsunami mapped over time: The aceh coast, sumatra. *Geomorphology*, *114*(4), 520–529.

Linacre, E. T. (1977). A simple formula for estimating evaporation rates in various climates, using temperature data alone. *Agricultural meteorology*, *18*(6), 409–424.

Liu, D. C., & Nocedal, J. (1989). On the limited memory bfgs method for large scale optimization. *Mathematical programming*, *45*(1), 503–528.

Luijendijk, A., Hagenaars, G., Ranasinghe, R., Baart, F., Donchyts, G., & Aarninkhof, S. (2018). The state of the world's beaches [Luijendijk, Arjen Hagenaars, Gerben Ranasinghe, Roshanka Baart, Fedor Donchyts, Gennadii Aarninkhof, Stefan eng Research Support, Non-U.S. Gov't England 2018/04/29 Sci Rep. 2018 Apr 27;8(1):6641. doi: 10.1038/s41598-018-24630-6.]. *Sci Rep*, *8*(1), 6641. https://doi.org/10.1038/s41598-018-24630-6

Luijendijk, A., De Vroeg, H., Winkels, C., & Walstra, D.-J. (2011). Coastal response on multiple scales: A pilot study on the ijmuiden port. In *The proceedings of the coastal sediments 2011: In 3 volumes* (pp. 602–615). World Scientific.

Luijendijk, A., Ranasinghe, R., de Schipper, M. A., Huisman, B. A., Swinkels, C. M., Walstra, D. J., & Stive, M. J. (2017). The initial morphological response of the sand engine: A process-based modelling study. *Coastal engineering*, *119*, 1–14.

Marcos, M., & Tsimplis, M. (2007). Variations of the seasonal sea level cycle in southern europe. *Journal of Geophysical Research: Oceans*, *112*(C12).

Martens, C., Verwaest, T., Spanhoff, R., Skou, A., Trouw, K., De Wolf, P., & Gysens, S. (2007). Lifetime estimation of beach nourishments in belgium: A practical guide for the use of one-line models and comparison

with the dutch practices. In *Coastal engineering 2006: (in 5 volumes)* (pp. 4231–4243). World Scientific.

Masselink, G., Scott, T., Conley, D., Davidson, M., & Russel, P. (2015). Regional variability in atlantic storm response along the southwest coast of england. In *The proceedings of the coastal sediments 2015*. World Scientific.

Masselink, G., & Pattiaratchi, C. (2001). Seasonal changes in beach morphology along the sheltered coastline of perth, western australia. *Marine Geology*, *172*(3-4), 243–263.

Massiani, J. (2013). How to value the benefits of a recreational area? a cost-benefit analysis of the conversion of a brownfield to a public beach in muggia (italy). *Review of Economic Analysis*, *5*(1), 86–102.

McFeeters, S. K. (1996). The use of the normalized difference water index (ndwi) in the delineation of open water features. *International journal of remote sensing*, *17*(7), 1425–1432.

Merk, O. (2013). The competitiveness of global port-cities: Synthesis report.

Milliman, J. D., & Haq, B. U. (1996). Sea-level rise and coastal subsidence: Towards meaningful strategies. In *Sea-level rise and coastal subsidence* (pp. 1–9). Springer.

Moran, P. A. (1950). Notes on continuous stochastic phenomena. *Biometrika*, *37*(1/2), 17–23.

Nelson, T. R., & Hapke, C. J. (2015). Shoreface response and recovery to hurricane sandy: Fire island, ny. In *The proceedings of the coastal sediments 2015*. World Scientific.

Neshaei, M. L., & Biria, H. A. (2013). Impact of groyne construction on beach; case study anzali & astara coasts. *7th National Congress on Civil Engineering*, 7–8.

Nicholls, R. J., Lincke, D., Hinkel, J., Brown, S., Vafeidis, A. T., Meyssignac, B., Hanson, S. E., Merkens, J.-L., & Fang, J. (2021). A global analysis of subsidence, relative sea-level change and coastal flood exposure. *Nature Climate Change*, *11*(4), 338–342.

NOAA. (n.d.). El niño/southern oscillation (enso). https://www.ncei.noaa.gov/access/monitoring/enso/soi

Notteboom, T. (2017). Porteconomics. https://www.porteconomics.eu/portgraphic-top-eu-container-port-regions-2007-2016-the-rise-of-south-europe/

Ojeda, E., & Guillén, J. (2008). Shoreline dynamics and beach rotation of artificial embayed beaches. *Marine Geology*, *253*(1-2), 51–62.

Oshana, R. (2006). Overview of digital signal processing algorithms. *DSP Software Development Techniques for Embedded and Real-Time Systems*, 59–121.

Ostrowski, R., Schönhofer, J., & Szmytkiewicz, P. (2016). South baltic representative coastal field surveys, including monitoring at the coastal research station in lubiatowo, poland. *Journal of Marine Systems*, *162*, 89–97.

Otsu, N. (1979). A threshold selection method from gray-level histograms. *IEEE transactions on systems, man, and cybernetics*, *9*(1), 62–66.

Ould Elmoustapha, A. (2000). *Influence d'un ouvrage portuaire sur l'équilibre d'un littoral soumis à un fort transit sédimentaire l'exemple du port de nouakchott (mauritanie)* (Doctoral dissertation). Caen.

Ould Elmoustapha, A., Levoy, F., Monfort, O., & Koutitonsky, V. G. (2007). A numerical forecast of shoreline evolution after harbour construction in nouakchott, mauritania. *Journal of Coastal Research*, *23*(6), 1409–1417.

Pontee, N. (2013). Defining coastal squeeze: A discussion. *Ocean & coastal management*, *84*, 204–207.

Pranzini, E., & Williams, A. T. (2013). *Coastal erosion and protection in europe*. Routledge London, UK.

PSA. (2016). https://psa.gov.ph/content/philippine-population-density-based-2015-census-population

Quang, D. N., Ngan, V. H., Tam, H. S., Viet, N. T., Tinh, N. X., & Tanaka, H. (2021). Long-term shoreline evolution using dsas technique: A case study of quang nam province, vietnam. *Journal of Marine Science and Engineering*, *9*(10), 1124.

Quartel, S., Kroon, A., & Ruessink, B. (2008). Seasonal accretion and erosion patterns of a microtidal sandy beach. *Marine Geology*, *250*(1-2), 19–33.

Ranasinghe, R., McLoughlin, R., Short, A., & Symonds, G. (2004). The southern oscillation index, wave climate, and beach rotation. *Marine Geology*, *204*(3-4), 273–287.

Reeve, D., & Spivack, M. (2001). Stochastic prediction of long-term coastal evolution. *WIT Transactions on The Built Environment*, *58*.

Röbke, B., & Vött, A. (2017). The tsunami phenomenon. *Progress in Oceanography*, *159*, 296–322.

Rocchio, L., Taylor, M., & Stevens, J. (2018). The sculpting of ebro delta. https://earthobservatory.nasa.gov/images/91832/the-sculpting-of-ebro-delta

Rodolfo, K. S. (2014). On the geological hazards that threaten existing and proposed reclamations of manila bay. *Philippine Science Letters*, *7*(1), 228–240.

Scaramuzza, P., & Barsi, J. (2005). Landsat 7 scan line corrector-off gap-filled product development. *Proceeding of Pecora, 16*, 23–27.

Schmidt, C. W. (2015). Delta subsidence: An imminent threat to coastal populations.

Schwartz, M. L. (1973). *Barrier islands* (Vol. 9). Dowden, Hutchinson & Ross.

Seale, C., Redfern, T., Chatfield, P., Luo, C., & Dempsey, K. (2022). Coastline detection in satellite imagery: A deep learning approach on new benchmark data. *Remote Sensing of Environment, 278*, 113044.

Seas, U. R., & Plans, A. (2011). Percentage of total population living in coastal areas.

Shadrin, N., et al. (2013). Coupling of shoreline erosion and biodiversity loss: Examples from the black sea. *International Journal of Marine Science, 3*.

Ship technology. (2019). https://www.ship-technology.com/projects/jebel-ali-port-dubai/#:~:text=Jebel$%5C%$20Ali$%5C%$20Port$%5C%$20had$%5C%$20an,further$%5C%$20to$%5C%$2019$%5C%$20million%5C%20TEU.

Short, A., Cowell, P., Cadee, M., Hall, W., & Van Dijk, B. (1995). Beach rotation and possible relation to the southern oscillation. *Ocean Atmosphere Pacific Conference*, 329–334.

Short, A. D., Trembanis, A. C., & Turner, I. L. (2001). Beach oscillation, rotation and the southern oscillation, narrabeen beach, australia. In *Coastal engineering 2000* (pp. 2439–2452).

Somoza, L., & Rodrıguez-Santalla, I. (2014). Geology and geomorphological evolution of the ebro river delta. In *Landscapes and landforms of spain* (pp. 213–227). Springer.

Stauber, J., Chariton, A., & Apte, S. (2016). Global change. In *Marine ecotoxicology* (pp. 273–313). Elsevier.

Stive, M. J., De Schipper, M. A., Luijendijk, A. P., Aarninkhof, S. G., van Gelder-Maas, C., Van Thiel de Vries, J. S., De Vries, S., Henriquez, M., Marx, S., & Ranasinghe, R. (2013). A new alternative to saving our beaches from sea-level rise: The sand engine. *Journal of Coastal Research, 29*(5), 1001–1008.

Stive, M., De Schipper, M. A., Luijendijk, A., Ranasinghe, R., Van Thiel De Vries, J., Aarninkhof, S., Gelder-Maas, V., De Vries, S., Henriquez, M., Marx, S., et al. (2013). The sand engine: A solution for vulnerable deltas in the 21st century? *Coastal Dynamics 2013: 7th International Conference on Coastal Dynamics, Arcachon, France, 24-28 June 2013*.

Syvitski, J. P. (2008). Deltas at risk. *Sustainability science, 3*(1), 23–32.

Syvitski, J. P., Kettner, A. J., Overeem, I., Hutton, E. W., Hannon, M. T., Brakenridge, G. R., Day, J., Vörösmarty, C., Saito, Y., Giosan, L., et al. (2009). Sinking deltas due to human activities. *Nature Geoscience, 2*(10), 681–686.

Taveneau, A., Almar, R., Bergsma, E. W., Sy, B. A., Ndour, A., Sadio, M., & Garlan, T. (2021). Observing and predicting coastal erosion at the langue de barbarie sand spit around saint louis (senegal, west africa) through satellite-derived digital elevation model and shoreline. *Remote Sensing, 13*(13), 2454.

Tessler, Z. D., Vörösmarty, C. J., Overeem, I., & Syvitski, J. P. (2018). A model of water and sediment balance as determinants of relative sea level rise in contemporary and future deltas. *Geomorphology, 305*, 209–220.

Turner, I. L., Harley, M. D., Almar, R., & Bergsma, E. W. (2021). Satellite optical imagery in coastal engineering. *Coastal Engineering, 167*, 103919.

UCAR. (n.d.). Center for science education. https://scied.ucar.edu/learning-zone/how-climate-works/climate-variability

Valdemoro, H. I., Sánchez-Arcilla, A., & Jiménez, J. A. (2007). Coastal dynamics and wetlands stability. the ebro delta case. *Hydrobiologia, 577*(1), 17–29.

Van Leeuwen, D. (2018). Global shoreline dynamics; a revision of the shoreline monitor.

Van Rijn, L. (1995). Sand budget and coastline changes of the central coast of holland between den helder and hoek van holland, period 1964-2040. *H2129*.

Vespremeanu-Stroe, A., Constantinescu, Ş., Tătui, F., & Giosan, L. (2007). Multi-decadal evolution and north atlantic oscillation influences on the dynamics of the danube delta shoreline. *Journal of Coastal Research*, 157–162.

Vousdoukas, M. I., Ranasinghe, R., Mentaschi, L., Plomaritis, T. A., Athanasiou, P., Luijendijk, A., & Feyen, L. (2020). Sandy coastlines under threat of erosion. *Nature climate change, 10*(3), 260–263.

Wang. (2018). Unravelling the sandy shorelines dynamics derived from satellite images.

Wang, W., Liu, H., Li, Y., & Su, J. (2014). Development and management of land reclamation in china. *Ocean & Coastal Management, 102*, 415–425.

Wesenbeeck, B., Kumar, R., Patnaik, P., Paimpillil, J., Nair, S., & Ven van de, F. (2012). Green adaptation and flood risk in south-east asia. *Natural hazards, 65(1)*, 947–966.

Wilson, R. J., & Heath, M. R. (2019). Increasing turbidity in the north sea during the 20th century due to changing wave climate. *Ocean Science, 15*(6), 1615–1625.

Wu, W. (2007). Coastline evolution monitoring and estimation—a case study in the region of nouakchott, mauritania. *International Journal of Remote Sensing, 28*(24), 5461–5484.

Yin, Y. (2007). Thinking on large area reclamation in caofeidian, tangshan city, hebei province. *Mar. Geol. Lett, 23*, 1–10.

Zhang, C., Luo, L., Xu, W., & Ledwith, V. (2008). Use of local moran's i and gis to identify pollution hotspots of pb in urban soils of galway, ireland. *Science of the total environment, 398*(1-3), 212–221.

Zhao, B., Guo, H., Yan, Y., Wang, Q., & Li, B. (2008). A simple waterline approach for tidelands using multi-temporal satellite images: A case study in the yangtze delta. *Estuarine, Coastal and Shelf Science, 77*(1), 134–142.

Zhu, H., Zuo, L., Reyns, J., Lu, Y., Dastgheib, A., & Roelvink, D. (2020). Morphologic modelling of tidal inlet on a barrier-lagoon coast: Case study of the laolonggou tidal inlet in the bohai bay. *Applied Ocean Research, 94*, 101967.